STUDY OF STRUCTURAL, MAGNETIC AND ELECTRICAL PROPERTIES OF AS PREPARED AND GAMMA IRADIATED RARE-EARTH DOPED NANOPARTICLE FERRITE MATERIAL

A Thesis Submitted to **Goa University** for the Award of the

Degree of

DOCTOR OF PHILOSOPHY

In

PHYSICS

By

Pranav Pandurang Naik

Research Guide

Prof. R. B. Tangsali

DEPARTMENT OF PHYSICS

GOA UNIVERSITY

TALEIGAO PLATEAU

GOA-403 206

July 2017

Dedicated to my
Family

&

Ishu

DECLARATION

I hereby declare that this thesis entitled "STUDY OF STRUCTURAL, MAGNETIC AND ELECTRICAL PROPERTIES OF AS PREPARED AND GAMMA IRADIATED RARE-EARTH DOPED NANOPARTICLE FERRITE MATERIAL" leading to the degree of Ph. D in Physics is my original work and that it has not been submitted to any other University or Institution for the award of any Degree, Diploma, Associateship and fellowship or any other similar title.

Date: Mr. Pranav Pandurang Naik

(Candidate)

CERTIFICATE

As required under the University ordinance, I certify that thesis entitled “STUDY OF STRUCTURAL, MAGNETIC AND ELECTRICAL PROPERTIES OF AS PREPARED AND GAMMA IRADIATED RARE-EARTH DOPED NANOPARTICLE FERRITE MATERIAL” submitted by **Mr. Pranav Pandurang Naik** leading to the degree of Doctor of Philosophy in Physics is a record of research done by him during the study period under my guidance and that it has not previously formed the basis for the award of any Degree, Diploma, Associateship and fellowship or any other similar titles.

Date:

Prof. R. B. Tangsali
Research Guide
Department of Physics
Goa University

ACKNOWLEDGEMENT

I wish to express my deepest gratitude to my guiding teacher, Prof. Rudraji B. Tangsali for introducing current research topic in the field of magnetic nanomaterials and encouraging me to pursue research work. The continuous guidance provided by him during my entire research period comprising of time spans in experimental work and subsequent data analysis immensely helped me in completing the set goals and arriving at logical conclusions.

I thank Dr. Bhagatsingh Sonaye and Mr. S. Sugur, Department of Radiology, Goa Medical College, Bambolim Goa, for providing Gamma Radiation facility.

I am grateful to Dr. Pramod Bhatt and Mr. Sher Singh Meena, Solid State Physics Division, Bhabha Atomic Research Centre, Mumbai, for providing Mossbauer facility and their valuable guidance in analyzing the experimental data.

I also thank

1. All the faculty and non teaching staff of Department of Physics, Goa University for extending co-operation and facilities throughout my research work.
2. University Grants Commission, Govt. of India, for awarding Basic Scientific Research (BSR) fellowship and funding my research work.

3. Mr. M. G. Lanjewar, University Science Instrumentation Centre (USIC), Goa University, for extending his help at Scanning Electron Microscope facility.

I am grateful to my teachers and senior researchers Dr. Satish H. Keluskar, Dr. Girish Kundaikar, Dr. Shraddha Ganorkar, Dr. Kapil Ingle, Dr. Manoj Kothwale, Dr. Jaison Joseph, for their constant support and valuable guidance throughout my period of research work. I would also like to thank The Principal and the faculty, Department of Physics, Ravi Sitaram Naik College of Arts & Science for their constant support and encouragement.

I thank all my research colleagues Elaine Dias, Bhargav Alavani, Chetana Gaonkar, Rukma Nevgi, Kapil Salkar, Mr. Manoj D. Salgaonkar, Arundhati Prabhudessai, M. Jeya Kanthan, Samiksha Malik, Vaishali Gaonkar Dessai, Manjunath Nayak and Dr. K. C. Bhamu for all the cheerful moments we had during my research tenure.

Last but not the least, I wish to thank my family and Ishu for their constant support and for being patient with me throughout the period of my research.

Pranav Pandurang Naik

TABLE OF CONTENTS

LIST OF FIGURES

LIST OF TABLES

CHAPTER 1

INTRODUCTION

1.1 Nanomaterials and nanotechnology

Currently enormous interest in the research and potential use of materials with dimensions that are effectively defined in terms of nanometers are under consideration. It has been observed that materials made of nanoparticles exhibit several and previously unnoticed properties, depending on the particle size. Recent research has shown that consolidated nano-materials in addition to structural, chemical, transport and magnetic properties exhibit improved mechanical properties, such as increased hardness, increased ductility, plasticity and many more. The distinctive properties of nano scale particles and nano grain bulk materials can be attributed to two several prominent aspects. These materials possess large surface area by virtue of their grain size. Moreover the ratio of number of atoms in the core of the grain to the number on the surface is relatively small. This particular aspect is responsible in governing the physical and chemical properties of these materials. This class of nanomaterials are broadly addressed as materials with core-shell type of particles where in the core of the particle behaves differently than the shell of the particle. Yet another class of particles with ultra small dimensions are known to reveal a phenomenon that is known as the “quantum size effect” or quantum confinement effect.

On a large scale, nanomaterials are classified as materials where at least one of the three dimensions is less than approximately 100 nanometers. A nanometer is approximately 100,000 times smaller than the diameter of a human hair. The history of nanomaterials started straight away after the big bang when Nanostructures were formed in early meteorites. Nature later evolved many other Nanostructures like seashells, skeletons etc. Nanoscaled smoke particles were formed during the use of fire by early humans [1-3]. If we analyze carefully, we will see that numerous organisms and plants in our neighborhood have gained unique features that are at the nanoscale level. A moth's eye surface comprises of very small bumps. They have a hexagonal shape and are a few hundred nanometers tall and apart. As these patterns are much smaller in dimension than the wavelength of visible light (350-800nm), there is no reflectance for the visible light so the moth's eye can absorb more light. This feature allows a moth to have much better than humans in low light conditions as nanostructures absorb light very efficiently. In the lab, scientists have used similar man-made nanostructures to enhance the absorption of infra-red light (heat) in a type of power source (a thermo-voltaic cell) to make them more efficient. The surface of a butterfly's wings is made up of multilayer nanoscale structures which are capable of filtering the light and reflect single wavelength, resulting in single bright color.

More precisely, the nanostructures on the butterfly's wings are about the same size as the wavelength of visible light and because of the multiple layers in these structures optical interferences are created. There is constructive interference for a given wavelength (around 450nm for the Morpho Rhetenor) and destructive interferences for the other wavelengths, so we see a very bright blue color [4].

Figure 1.1.1 Rhetenor Blue Morpho

Numerous scientific instruments use this technique to analyze the color of light. Scientists working with nanomaterials have been getting inspiration from nature and are manifesting these ideas in the developing new technology. Polarizing technologies used in telecommunications, microscopy and multimedia are constructed from naturally available crystals. These work for linearly polarised light but not circularly polarised light. However researchers have produced the first photonic crystal that can split both left and right circularly polarized light by inheriting the ideas from butterflies. Nano-optical technology for enhanced security (N-otes), a new anti-counterfeiting product is another application that is derived from butterfly. Spider silk is strong (five times stronger than steel by weight), stretchy and lightweight the same silk can be used as optical fiber as it is a hollow helix type in nature.

A new product with similar properties found in spider silk, a peel-off adhesive tape that doesn't damage the underlying surface when removed has been produced for medical applications. The spider silk strands are perfectly cylindrical, smooth, transparent and extremely strong with same characteristics as glass-based fibers. These are currently being explored as detectors for molecular level detection. Being light and strong these are being explored for making bulletproof clothing. There are large numbers of nano applications right from vegetables, fruits, insects, etc. the scientists have been trying to harness these ideas to reality with manmade nanofibers and nanomaterials.

At present there is an enormous interest in the potential for use of materials with dimensions that are effectively defined in terms of nanometers derived using various methods of material synthesis. On attaining nano dimensions it is reported that the electronic and optical behavior of several type of materials is significantly altered due to introduction of defects in the lattice.

During the last decade, nanotechnology has emerged as a prime research field due to its enormous promise for novel applications to diverse fields of human endeavour such as biomedical sciences (drug delivery, therapy, hyperthermia, advanced imaging), defence (smart and light systems), aerospace (engineered surfaces and composites), agriculture, energy (solar cells, fuel cells, batteries), environment (gas, humidity, bio-sensors), consumer electronics and advanced device systems. Modern day research is now in progress, to fulfill this promise via controlled nano-synthesis, necessary functionalization of nano-materials, self assembly or template assembly of nanostructures, integrations of nano-materials with other materials to generate functional nano-composites, development and implementation of novel device concepts highlighting the special quantum features of nano-materials etc. It has been observed that in the current scenario nanomagnetic materials is a forefront research field even though magnetism has been a old concept being investigated for last several centuries. With the advent of nanomaterial idea research in magnetic materials has grown in to a multifold arena of newer concepts and ideas never proposed in the past. When it comes to magnetism and magnetic materials ferrites forms an important and a vast area in which research is by itself can never be exhaustive. Every new idea pumped in to this concept/area opens up a new field for research. Ferrite material has always posed new challenges and has always fascinated researchers since last several centuries and will still continue doing so as the origin of magnetism is associated with nuclear particles, electrons and atoms which happens to be the smallest particle constituting matter around us.

1.2 Ferrites

Ferrites are materials with very simple composition belong to a class of ferromagnetic ceramic material with general formula AB_2O_4, where, A is a divalent metal ion usually belonging to transition series such as Mn^{2+}, Fe^{2+}, Co^{2+}, Ni^{2+}, Cu^{2+}, Zn^{2+}, Mg^{2+} or Cd^{2+} and B is generally Fe^{+3}. Magnetite (Fe_3O_4) is a typical example of naturally occurring ferrite, a well known important magnetic oxide since ancient time. Some other important ferrite materials that were developed later are $Co Fe_2O_4$, $MnFe_2O_4$, $Ni Fe_2O_4$, $ZnFe_2O_4$, $Mg Fe_2O_4$ etc.

1.2.1 Classification of ferrites

Ferrites are generally ferrimagnetic in nature with iron oxide as their main component along with the metal oxides. These materials are classified into three categories namely spinel ferrites, garnets and hexa-ferrites on the basis of crystal structure. In these the cation distribution varies according to the crystal structure bringing wide variation in the properties. Accordingly the structural and other property based investigations differ and their application avenues are also different to a large extent.

1.2.2 Spinel ferrite

Spinel ferrites are the materials with a general formula MFe_2O_4 where M stands for divalent metal ions like Cu, Ni, Mg, Mn, Co, Zn, Cd etc. M can be replaced by other divalent metal ions. Fe^{3+} can be substituted by other ions in +3 oxidation state such as Al, Cr, Ga, In etc. The compound $MgAl_2O_4$ crystallizes in cubic spinel structure with two interstitial sites namely tetrahedral (A) site and octahedral [B] site. The unit cell is made up of eight units (cube) and may thus be written as $M_8Fe_{16}O_{32}$. The structure was first determined by Bragg and Nishikawa [5].

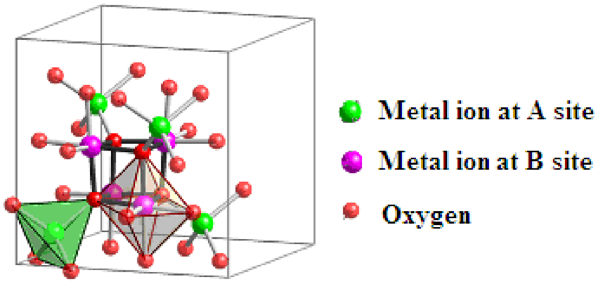

Figure 1.2.1 Spinel structure

Ferrites with spinel structure are categorized into three types on the basis of the cation distribution in the two sites, tetrahedral site (A) and octahedral site [B] [6], namely

1. Normal spinel ferrite
2. Inverse spinel ferrite
3. Mixed spinel ferrite

a) Normal spinel

In the case of normal spinel the divalent metal ion occupy the tetrahedral (A) site while 2Fe^{3+} ions occupy octahedral [B] site. The best examples of normal spinel ferrites are zinc (ZnFe2O4) and cadmium ferrites ($CdFe_2O_4$), in which the divalent metallic ions Zn^{2+} or Cd^{2+} are at the (A) site, while Fe^{3+} ions are at [B] site. The cation distribution can be represented as in general

$$(M)^A\ [Fe_2]^B\ O_4 \tag{1.1}$$

b) Inverse spinel

In inverse spinel ferrite, the divalent metal ion M^{+2} occupy octahedral site along with one of the Fe^{3+} ion while the remaining ferric ion occupy tetrahedral site. Nickel ferrite, Cobalt ferrite are known to have inverse spinel structure [7]. The distribution on cations in inverse spinel ferrite can be written as

$$(Fe)^{A}\ [MFe]^{B}\ O_4 \qquad 1.2$$

c) Random spinel (mixed spinel)

When the divalent metal ions M^{2+} and trivalent Fe^{3+} ions are distributed at both tetrahedral A site and octahedral [B] site, the ferrite is termed as random spinel or mixed spinel ferrite. Such distribution of ions between two sites is controlled by a delicate balance of various factors, such as the magnitude of ionic radii, electronic configuration and electrostatic energy of the lattice [8, 9]. The general cation distribution in random spinel can be written as

$$(M_{1-x}Fe_x)^{A}\ [M_xFe_{2-x}]^{B}\ O_4 \qquad 1.3$$

1.2.3 Cubic garnets

The general formula for cubic garnets is $REFe_5O_{12}$ where RE is yttrium or rare earth ions like Dy, Gd, La, Nd, Er etc. The structure is cubic and consists of three interstitial sites namely dodecahedral (C), octahedral (A) and tetrahedral (D) sites. The cubic crystal structure consists of 160 atoms per unit cell and 8 molecules of $REFe_5O_{12}$. The ions are arranged on a b.c.c. lattice with c and d- ions lying on cube faces [10].

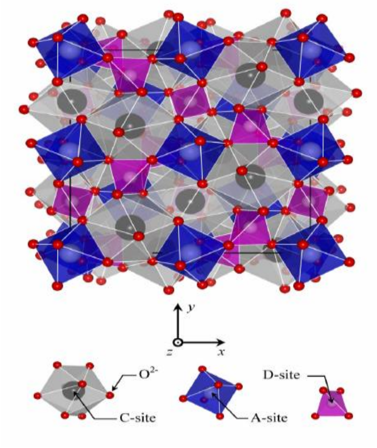

Figure 1.2.2 Cubic garnet structure

There are 24 C- ions, 16 A-ions and 24 D-ion embedded in eight sub units within the unit cell. Inside a unit cell A-ions, C- ions and D-ions are caged by six, eight and four oxygen ions to form an octahedral, dodecahedral and tetrahedral sites respectively.

1.2.4 Hexagonal ferrite

Hexagonal ferrites have general formula $MeFe_{12}O_{19}$ (Me = Ba, Sr, or Pb). These were first reported by Went, Rathenau, Gorter & Van Ostershout and Jonker, Wijn & Braun.

These materials have hexagonal crystal structure and the unit cell is made up of two unit formulae. The metal ions occupy three different sites namely tetrahedral, octahedral and trigonal bi pyramid. The oxygen lattice with f .c. c. structure comprises of a sequence of hexagonal layers of oxygen perpendicular to the (111) direction and with layer arranged SRS, SR*S. The hexagonal ferrites depending upon the composition are classified as M, W, Y, Z, X and U type [11].

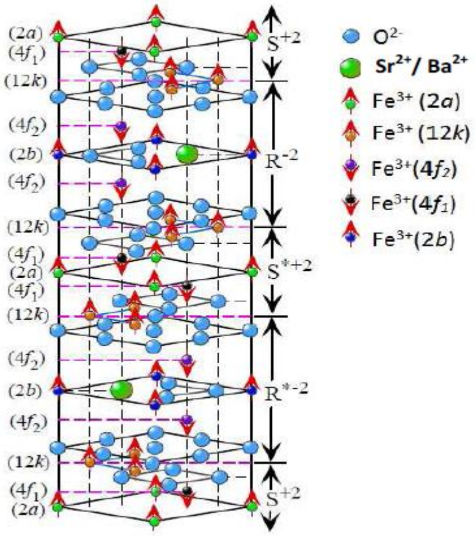

Figure 1.2.3 Crystal structure of M-type hexagonal

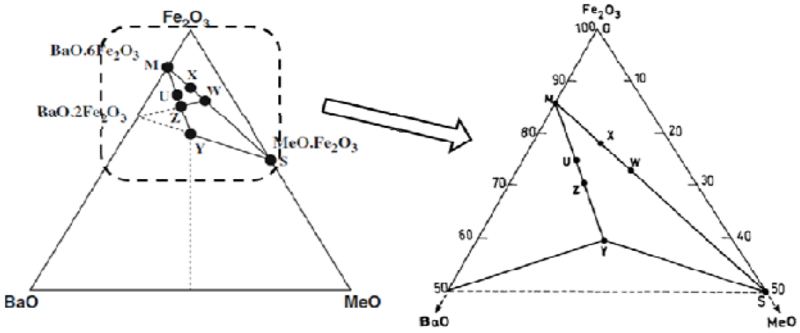

Figure 1.2.4 Chemical compositional BaO-MeO-Fe_2O_3 ternary phase diagrams showing how the different hexagonal ferrites are derived

Their crystal and magnetic structures are different from one another and are remarkably complex. Since the direction of magnetization rigid and cannot be shifted easily to another axis, these ferrites are also termed as “hard” ferrites.

Spinel ferrite is the most important class of ferrite finding a special place in the field of academic work and arenas of research all over the globe

1.2.5 Applications of ferrites

Ferrite materials have a wide range of applications. These are ceramic materials with a strong magnetic character and usually composed of oxides of iron and metals. Ferrites having semiconductor nature are technologically the most important materials.

Soft ferrites are employed in the cores of transformers, inductor devices, SMPS, inductors, convertors, electromagnetic interference filters etc. They are extensively and frequently used in energy transfer systems, telecommunication, space research, military devices and include variety of industrial applications [12-17]. They are mixed ferrite having a combination of two metals like Mn, Zn, Mg, Cu and Ni. They are useful at high frequencies due to their low losses, high resistivity, low values of remnant, flux density and low values of coercive force. They have high permeability.

Hard ferrites are used for permanent magnets. Barium ferrites are the most special and important type of ceramic material which are used as permanent magnets. They are used in producing better transformer core with minimum eddy current dissipations at high microwave frequency. They possess high value of coercivity force in comparison with Alnico alloys along with high opposition to demagnetization. Barium hard ferrites are employed in TV tubes for the role of focusing magnets and also in small dc motors and compact torque devices. Hard ferrites are commonly employed for magnetic latch and magnetic levitation purpose. Ferrites play a vital role in high frequency application and find their use in rotators, phase shifting circuits, circulator, radar technologies, aircraft and satellite navigations systems, space technologies etc. They are powerful magnetic protecting material. So, radar absorbing paint containing ferrite materials have been developed to render an aircraft or submarine invisible [18,19].

Ferrites are useful as computer memory devices. Magnetic recording media, these ferrites possess rectangular hysteresis loop. Garnets and ferrites find their applications in the components of electronic filter circuits, microwave based devices, magnetic switches and important applications such as memory storage for computers. Ferrites are used in the form of thin films for memory and switching device circuits. Ferrites are extensively used in fabrication of radio frequency coil, rod antenna etc [20-23]. Sensors made from ferrites having sharp and definite Curie temperature are used for temperature control. Position and rotational angle sensors (proximity switches) have also been designed using ferrites [24]. Ferrite materials with greater surface area, enhanced charge density on the surface and with open pore formed on bulk surface presents these materials as a strong contender for their use for humidity sensitivity [25,26]. Targeted drug delivery, hyperthermia cancer therapy, radiotherapy, AC magnetic field assisted cancer therapy are among some of the medical applications of ferrite nano materials. The magnetic nanoparticles can be injected in the patient’s body and translocate to the tumor cells. Then energy for magnetic moment is provided by external magnetic field applied. This causes a dissipation of energy and generates heat in the tumors. The cancerous cells have high temperature (45^{oC}-50^{oC}) sensitivity and so, will be destroyed. Super paramagnetic nanoparticles do not have remenance and thus the harm of thrombosis is avoided. Magnitude of magnetization, coercivity, magnetocrystallinity, and shape anisotropy of ferrite nano material used plays an important role in this therapy [27-29].

1.2.6 Manganese zinc ferrite (MZF)

Research work carried out in ferrites in last several decades has shown that Mn-Zn ferrites have been the subject of intensive experimental and theoretical investigations. In general Ferrite is magnetic ceramic containing iron oxide as its main component. The presence of trivalent ion (Fe^{3+}) having five unpaired d shell electrons compels ferrites to show their magnetic characteristics. An interaction with cations in the neighborhood is necessary to gain high magnetic moment. Mn-Zn Ferrite retain strong ferrimagnetic coupling among its constitutional cations because of possessing spinel structure. The unit cell of Mn-Zn Ferrite lattice consists of eight face centered cubic (fcc) sub unit cells. Each fcc subunit cell is formed by oxygen ions called anion. There are 64 tetrahedral sites (A-site) out of which 8 are filled and there are 32 octahedral sites (B-site) out of which 16 are filled. There are total 56 ions per unit cell of spinel structure in which each oxygen ion is bonded to one tetrahedral and three octahedral sites.

Particle size and grain morphology of Mn-Zn Ferrite powders strongly depend upon adopted synthesis route as well as set of conditions that prevail during sample preparation. The method of synthesis plays a crucial role in preparing a highly crystalline monophasic nanoparticle material, possessing desired perfect chemical, electrical and magnetic properties.

1.2.7 Effect of Mn inclusion

The element Mn plays a significant role in deciding several properties of the nanoparticle ferrite. Mn^{+2} is an interesting divalent cation which can drastically alter the curie temperature and initial permeability of a ferrite material. It also affects the grain size and electromagnetic properties. Reports suggest that the element Mn plays a crucial role in deciding the structural parameters, magnetic character like initial permeability, magnetization (M_S), and remnant magnetization (M_R), and physical aspects like grain size and material's densification in nanoparticle Mn-Zn ferrite.

1.2.8 Effect of Zn incorporation

The occupancy Zn^{2+} usually at tetrahedral site gives rise to enhanced electromagnetic properties and also results in the densification of the ferrite material. It also lowers magnetostriction and anisotropy in ferrites [30]. It has been also observed that Zn enhances initial permeability and brings down the hysteresis loss which is essential parameter in any good quality ferrite material. However lowering of Curie temperature, a technically unwanted effect also occurs due to presence of Zn. Heavy Zn substitution at 'A' site can dilute A-B interaction to a great extent, affecting the overall magnetic properties. Weakening of magnetic interactions could weaken the spin coupling or could more easily destroy the spin alignment even at low thermal energy vibrations thereby decreasing the Curie temperature.

1.3 Literature Review

Last two decades has seen a tremendous upward surge in research on magnetic materials. A large fraction of this work is based on ferrites and nanoferrite materials. This is essentially due to increasing demand for improved performance materials for various types applications ranging from simple to most sophisticated electronics as well as in variety of medical, sensors and host of other application in the emerging technologies [31].

Among these materials, Mn-Zn ferrites are one of the most important materials for their high magnetic permeability, high saturation magnetization, and low core losses and other interesting properties. These Mn-Zn ferrites were formally reported by J. L. Snoek in 1947 [32]. Theoretical work on Mn-Zn Ferrite was initiated by L. Neel in 1948. This article explains about the impact of addition of zinc in ferrite which may be helpful to attain very high values of saturation magnetization.

Reports show that nanoparticle Mn Zn ferrites can be prepared through various methods like solid state reaction method [33]; high energy ball milling method; sol-gel method [34]; chemical co-precipitation method [35]; microwave sintering method [36]; auto combustion method [37], conventional ceramic technique [38], conventional two-step synthesis method [39] etc.

Lan et al [40] synthesized Mn-Zn Ferrite nanoparticles by co-precipitation and reported decreased particle size with increase of zinc content against manganese which conversely affected Curie temperature, blocking temperature and coercivity of Mn-Zn Ferrites.

Keluskar et al [41] prepared nanoparticle $Mn_xZn_{1-x}Fe_2O_4$, (with ‘x’ from 0.35 to 0.65) by combustion method using nitrilotriacetate precursor and sintered these compositions at various temperatures ranging from 950°C to 1350°C in nitrogen atmosphere to obtain bulk materials with improved properties wherein high initial permeability values were reported. Janghorban et al [42] synthesized Mn Zn ferrites with top-down method using ball milling and sintered the powders with V_2O_5 at (1100°C). Addition of V_2O_5 failed to show any encouraging results on initial permeability, saturation flux density and Curie temperature on Mn-Zn Ferrites.

Mathur et al [43] prepared nanocrystalline Mn-Zn Ferrites (comprised of Indium oxide *0.5 mol %* against iron oxide) by employing co-precipitation technique and prepared torid cores. These toroids were found to maintain initial permeability of 1000 up to Curie temperature *(152°C)* with minimum loss tangent *(<0.1)* upto30 MHz frequency.

Xuan et al [44] synthesized Mn-Zn Ferrites from metal sulfate salts and ammonia solution by employing hydrothermal precipitation approach. Reports show that the quality and size of powder particles was greatly dependent on pH of the solution, reaction time and temperature. The effect of Zn concentration was strongly observed on magnetic properties of Mn-Zn Ferrites. Nalbandian et al [45] employed hydrothermal process using low sintering temperature to get nanosized Mn-Zn Ferrites in the range of 5- 25 nm having the surface area 60-110 gm/m2. The nanoparticles so obtained showed superparamagnetic behavior.

Kikukawa et al [46] synthesized Zn substituted M-Zn Ferrites, where M = Mg, Mn, Co, Ni, Cu, (Li, Fe) using glycerin- nitrate process. They suggested that glycerin to nitrate ratio (G/N) would be 0.5 to develop Mn-Zn Ferrite system with good stiochiometery and nano crystallinity.

Jeyadevan et al [47] employed co-precipitation technique to synthesize Mn-Zn Ferrites and conducted an extended X-ray absorption study to determine the ionic distribution. It was reported that variation in electromagnetic properties of Mn-Zn Ferrites synthesized by different processing routes were not only due to different particles sizes but it was also due to the cationic distribution on octahedral and tetrahedral sites. They further stated that Fe3+, Mn2+ and Zn2+ ions had zero crystal field stability energy (CFSE) for both interstitial sites. Therefore, these ions could be accommodated with a certain cation that has a non-zero CFSE for a particular site.

Mn-Zn Ferrite was also synthesized by Makovec et al [48] having better properties using hydrothermal process which were compared with commercially available Mn-Zn Ferrite powder. They inferred that the uniformity in magnetic powder could be gained by evading the agglomeration of phases (Mn-rich) during the aqueous surrounding. They also observed that the particle shrinkage rate in inert atmosphere was high due to increase of oxygen lattice diffusion at low partial pressure.

Hessien et al [49] examined the effect of Mn substitution on the annealing temperature, microstructure and magnetic properties of Mn-Zn Ferrite prepared by conventional mixed oxide method. They explained that pure spinel phase could be obtained at 1300°C and further increased in temperature dropped the saturation magnetization due to internal grain porosity.

Hu et al [50] prepared fine powder of Mn-Zn Ferrite (MZF) by nitrate-citrate auto combustion process and studied the effect of heat treatment on its magnetic properties. They observed that Mn-Zn Ferrite decomposed into Mn_2O_3 and Fe_2O_3 at 550°C during annealing in air. However, these oxides again diffused with rise of temperature. Finally monophasic Mn-Zn Ferrite was prepared after annealing at 1200°C. In addition they studied that saturation magnetization of Mn-Zn Ferrite could be increased to to a high value keeping the coercivity value low by argon atmosphere annealing at 600°C.

Mn-Zn Ferrites were synthesized in ultrafine form by Praveena et al [51 by employing microwave-hydrothermal method and observed that these ferrites have performance range of 10 Hz to 1 MHz frequency range with minimum power loss.

Joseyphus et al [52] prepared nanosized powder of Mn-Zn Ferrites using a uniquely modified oxidation method. They found an enhancement in magnetic anisotropic constant with the reduction particle size to nano range from bulk dimentions. They also inferred that critical particle size for superparamagnetic response is less than 25 nm.

E. Auzans et. al. [53] employed coprecipitation method for the synthesis of Mn-Zn ferrites. Material preparation methods like hydrothermal precipitation process, Sol-gel synthesis [54] and the microemulsions approach [55] have been often used to synthesize the Mn-Zn ferrite nanosized materials. Xian- Ming Liu et.al [56] has synthesized Mn-Zn ferrites by precursor method. Shunli Hao et.al [57] has used citrate precursor method to synthesize Mn-Zn ferrites. Daun and co-workers [58-60] have designed novel synthesis route of pure MFe2O4 (M=Mg, CO, Ni) spinel ferrites using a single molecular precursor.

Yamamoto et al [61] employed Spark plasma sintering method to prepare Mn- Zn Ferrite cores. The platelet ferrite cores showed good magnetic properties with high saturation magnetization. They reported that fabricated cores could be used as substrate materials for hard disks.

Venkataraju et al [62] synthesized nanocrystalline manganese zinc Ferrite by employing co-precipitation method where in Ni was substituted in the place of manganese content. The lattice constant was found to reduce in comparison with that of bulk material with increasing Mn/Ni substitutions. Magnetization was also seen to reduce (except for x=0.3) due to the alteration from normal cationic distribution. They also reported that Ni substitution had increased the spin canting effect on B-site, as the cause of lower magnetization.

Dasgupta et al [63] examined the effect of sintering environment on grain size and magnetic properties of Mn-Zn Ferrites synthesized by mechanical alloying technique. They reported that milling and annealing in air prohibits the formation of Mn- Zn Ferrites and only Zn-Ferrite was confirmed by XRD analysis. While the precursor reactants were mixed and subjected to annealing under inert atmosphere (Ar), monophasic Mn-Zn ferrites were synthesized. They also reported that blocking temperature could be decreased by annealing at low temperature (500°C).

Ahmed et al [64] used flash combustion method to synthesized nanosized manganese zinc ferrites and studied the impact of rare earth oxides like as Tb, La, Ce and Th on their properties. Improvement in magnetic susceptibility was observed with these additions. It is reported that rare earths having larger radius and +3 valance states were ideal substitutions to enhance the electrical and magnetic properties of nanosized Mn-Zn Ferrites.

Ateia et al [65] also examined the impact of rare earth elements (Dy, Gd, Sm, Ce, and La) on the magnetic properties of Mn-Zn Ferrites and inferred that the rare earth substitutions enhanced the electrical resistivity by increasing the activation energy of Mn-Zn Ferrites. Rezlescu et al. [66] examined the effect of Fe replacement by RE (Yb, Er, Sm, Tb, Gd, Dy and Ce) ions on the properties of $Ni_{0.7}Zn_{0.3}Fe_2O_4$ ferrite. The results showed that the electrical resistivity of a ferrite increased by substituting a small quantity of $Fe_2O_3$with RE_2O_3. Zhao et al. [67] investigated the effect of Gd on magnetic properties of $(Ni_{0.7}Mn_{0.3})\ Gd_xFe_{2-x}O_4$ ferrites. It is reported that the crystallite sizes decreased when Gd ions were doped into Ni-Mn ferrites. With Gd-substitution, with $x > 0.06$ all Gd ions could not enter into the ferrite lattice but resided at the grain boundary. X=0.06 was found to show optimum penetrability of Gd^{+3} ions in the Ni-Mn framework. Costa et al. [68] investigated the effect of Samarium on the microstructure, relative density and magnetic properties of $(Ni_{0.5}Zn_{0.5})$ $SmxFe2_{-x}O_4$ ferrites. A increase in relative density, decreased average grain size along with increase in coercive field and decrease in permeability with increase in rare earth substitution has been reported in this work. Zhao et al. [69] examined the effect of substitution of Fe^{3+} by Nd^{3+} ions on structure and magnetic properties of $CoFe_{2-x}Nd_xO_4$ ferrites. It is reported that there is a decrease in saturation magnetization, the value of which is less than pure cobalt ferrite, with increase in coercivity with increasing value of Nd^{3+} concentration in the doped samples. Mahmoud et al. [70] investigated the cation distribution and spin canting angles variation in Sm and Nd doped $Cu_{0.5}Zn_{0.5}Fe_2O_4$ using Mossbauer spectroscopy. A marginal decrease in saturation magnetization M_s for the sample doped with Nd and significant increase in M_s for the sample doped with Sm have been reported.

Darwish et al.[71] as well as Hemeda et al.[72] examined the effect of gamma-rays irradiation using a ^{60}Co source on the structural and the electrical properties of Co-Zn ferrites. It was observed that XRD peaks were shifted after irradiation. The γ-radiation changed the ferric ions to ferrous ions having a larger ionic radii of 0.69 Å compared to that of ferric ions 0.59 Å. The values of dielectric constant were found to increase after irradiation due to increase of ferrous ions at the octahedral sites as a result of γ-radiation.

Hamada [73] and Dalal [74] investigated the effect of gamma irradiation on the structure and the diffusion coefficient of Co- Zn-Mn ferrites. A shift was observed in the XRD peak position. The diffusion coefficient of electrons was found to increase for the irradiated samples. The activation energy of hopping electrons decreased after irradiation in the first stage of rising temperature. At high temperature, the holes were the majority carriers in this system.

A similar study on Co-Zn-Ce-Fe_2O_4 ferrites was reported by Ateia [75]. It was found that, the crystallite size for unirradiated samples was greater than irradiated one, while the estimated micro strain values for irradiated samples was greater than unirradiated ones. Also, the dielectric constant increased after irradiation. This increase in dielectric constant was attributed to the production of Fe^{2+} after irradiation and the generation of some vacancies at different depths which acted as trapping centers.

Ahmed et al. [76,77] studied the effect of gamma irradiation on the structural and electrical properties of Mg-Ti-Er-Fe2O4 system. It was found that, noticeable shift for the

XRD peaks occurred after irradiation. This was attributed to the γ-irradiation may change the ratio of Fe^{2+}/Fe^{3+} on the octahedral sites

This led to decrease in the crystal size. It is also noticed that, there was distinct increase in the dielectric constant. The conductivity was found to increase with increase in γ -dose increases. This increase in σ was attributed to the increase in the ratio of Fe^{2+}/Fe^{3+} on the octahedral sites as a consequence γ -dose increases. The values of the activation energy decreased with increasing γ – radiation dose.

Okasha [79] achieved an enhancement of magnetization of Mg–Mn nano ferrite by γ -irradiation. An increase of lattice constant (*a*) for the irradiated samples observed was explained on the basis of the ionization of the ferric ions of smaller ionic radius to ferrous ions of larger ionic radius. An absence of hysteresis, saturation, remanence, and coercivity was also observed at a higher applied magnetic field of 6 kOe indicating superparamagnetic behavior. Moreover, the values of saturation magnetization (Ms) for irradiated samples were higher than these obtained of the un-radiated samples. This behavior was explained according to the small particle surface effect and the internal cation disorder.

Gamma irradiation induced damage creation on the cation distribution, structural and magnetic properties in Ni-Zn ferrite was investigated by Karim et al. [80]. It was found that, the positions of XRD peaks were shifted to higher 2θ values and the peak intensities were decreased. In addition, the width of the peaks was increased from that of the unirradiated samples. The value of lattice constant decreased after irradiation. This was attributed to the lattice vacancies generated after irradiation caused distortion and deviation from the spinel cubic structure. The cation distributions indicated the redistribution of the cations in the A and B-sites. The change in cation distribution data was attributed to the formation of Fe^{2+} ions at octahedral sites after irradiation. An increase in the saturation magnetic moment and Curie temperature after irradiation was observed also after irradiation. It was attributed to the partial formation of ferrimagnetic centers and rearrangement of cations in the lattice and ion induced disorder.

1.4 Motivation

Manganese zinc ferrites have been more extensively examined and investigated over last several decades for their various properties, to alter their properties, to obtain more efficient material and nanoparticles. These materials have a tremendous impact in the field of science and new emerging technology. Manganese Zinc ferrites find place in wide range of technological and scientific application in the area of electronics, opto-electronics, refrigeration, magnetic recording media, magneto caloric applications, sensors etc. These are also used in temperature sensitive ferrofluids for applications in heat transfer enhancement, energy conversion devices and power devices especially for electromagnetic interference suppression (EMIS) [81-84]. In addition to onsite application on earth these materials also find applications in, aviation electronics, satellite communication, spacecrafts, electronic applications in space ships like Moon mission, Mars mission etc. The electronics used in space are exposed to various types of radiations coming from the solar system and outer space. As per the reports available and examined in literature review it is seen that the high energy radiation produces an irreversible effects in these materials thereby modifying the properties of these materials. Thus it will not be surprising if the same set of electronics that behaved /worked in a particular way on earth would behave differently in space when exposed to radiant energy.

Secondly, It has been observed from the reports that the structural, electrical, dielectric, magnetic properties of these ferrite materials can be altered and refined or redefined by appropriate addition of dopant material, as well as by use of external factors such as control of pressure, optimizing annealing temperature in some preparative methods. Moreover Gamma radiation exposure is also emerging as an excellent novel method for control of sample properties. Indeed this could be an a unique and essential tool for altering sample properties both structural, physical, chemical, electrical and magnetic [85-88] not only for the purpose of producing fine quality samples but this would also address the much required issue of understanding the behavior of electronics in the radiation environment .

In current times it is observed that rare earth substituted ferrites are becoming promising materials for several applications [89,90]. Addition of small percentage of rare earth ions to ferrite material can produce a significant variation in their structural, magnetic and electrical properties depending upon the type and the amount of rare earth added [89].

One can classify rare earth ions into two categories: one with the radius closes to Fe ions while the other with ionic radius larger compared to that of Fe ions [90]. This difference in ionic radii can develop micro strains in the material, which can be the cause of producing deformation in the spinel structure with can result in domain wall perturbation or movement [91]. The rare earth ions tend to occupy the octahedral sites by replacing Fe^{3+} ions and have limited solubility in the spinel lattice, restricting large concentrations, due to their large ionic radii [92].

In ferrites, ferrimagnetism is prominently governed by Fe-Fe interaction (the spin coupling of the 3d electrons). On the inclusion of the rare earth ions in the spinel lattice, interactions of the type RE-Fe also appear (4f-3d coupling), which can lead to changes in the magnetization and Curie temperature [93]. Rare earth oxides have high resistivities that are greater than 10^6 Ω-cm at room temperature [94]. Moreover occupation of RE ions at 'B' sites in a doped ferrite impedes the motion of Fe^{2+} in the conduction process, causing an additional increase in resistivity [95]. Available reports suggest that investigations have been carried out to study the influence of different rare earth ions (La, Sm, Gd, Nd, Dy, Tb, Ce, Th, Y, Eu) on electrical, magnetic and structural properties of different types of ferrites. However the variations in the prescribed properties, depends on the percentage content and the type of Rare earth substitution [96-99].

In the past several researchers have examined crystallographic and magnetic changes induced in bulk ferrite samples by bombarding the same with different kind of atomic particles, such as fast neutron, low energy ions, high energy ions for different kinds as well as radiating these materials with different energy photons.

Reports suggest that gamma radiation has the energy to bring about a permanent change in structural property of the material thereby affecting the transport and magnetic properties of ferrite material [100-102]. This changes in the properties of the materials depends upon the extent to which they are exposed to gamma radiation. Interaction of radiant energy with matter, especially gamma irradiation, is extremely important problem from the viewpoint of theory and practice. The study of gamma irradiation on magnetic insulators such as ferrites has shown that it can lead to modifications in their physical, magnetic and electrical properties. This method of materials modification sounds interesting and a wide class of materials like metals, semiconductors, and ceramics has been found sensitive to gamma radiation [101].

Gamma (γ rays) radiation with high energy (1.17MeV to 1.33MeV) interacts with an electronic shell or the atomic nuclei of the substance when exposed. These interactions results in an elastic and inelastic scattering of the particles causing excitation and ionization of the atoms, initiation of nuclear reactions and also disturbance in the structure of the matter, termed as radiation damage. As Mn-Zn ferrite nanoparticles as well as bulk material are extensively in use in various fields including in areas of gamma radiation abundance like nuclear reactors, satellites in outer space, satellite launch vehicles and medical application it becomes important investigate the response of Mn-Zn ferrite nanoparticles to gamma radiation with respect to the affected properties [102-105] as the performance of the devices using these materials in the radiation environment can be ascertained [106,107].

Thus from the reviews undertaken it is clear that essentially both the rare earth doping as well as gamma radiation has the potential to bring about improvements or enhancements in the materials. Therefore it was felt that one could augment both these techniques and produce better performing nanoparticle Mn-Zn ferrite material. As expected the new material produced would bestrew new challenges to explore, understand and develop co-relations between the control parameters and observed novel properties.

Again it is worth stressing at this point that producing nanoparticle materials with rare-earth doping concentration at ease is not at all a easy task. One of the major difficulties associated with such doping is limited solubility of rare earth ions in Mn-Zn ferrite host material mainly due to large size of rare-earth ions. However lower amounts of rare earth material could be integrated in the host matrix by employing conventional simple methods of material preparation. Much of the ability to do so would also depend on the materials preparation method adopted, as every method has its own pros and cons.

Thus a detailed investigation of rare-earth doped $Mn_yZn_{(1-y)}Fe_{(2-x)}Nd_xO_4$ nanoparticle ferrite (with y=0.6,0.65; x=0.04,0.05,0.06,0.07,0.08,0.09,0.1) and gamma irradiated $Mn_yZn_{(1-y)}Fe_{(2-x)}Nd_xO_4$ nanoparticle ferrite materials was taken up and successfully completed in the entire course of the present research work.

1.5. Aim and objectives of the research work

Having done the literature review of large number of published research articles it was found that majority of the workers had worked on either a single or a small number of samples. The work is a fragmentation of findings that cannot be applied for large ensemble of samples or materials. Therefore preparation of a series of materials encompassing a larger range of materials was felt necessary as this would broaden the knowledge base on the series of materials selected.

The aim of present work was to prepare Nd doped nanoparticle Mn-Zn ferrite materials, investigate their properties as a function of Nd doping concentration, radiate the materials with different doses of gamma radiation and carry out further investigations on the properties of the irradiated samples.

The objective of the work was to develop a standardized procedure/method to prepare nanoparticle functionalized Mn-Zn ferrite material with better properties. It is worth emphasizing there that the existing methods of materials preparation loses control over the material properties no sooner it is prepared. However the radiation method adopted in the current investigations shows that the material properties can be subjected to change even after the materials preparation process is completed. Moreover it has been found that the changes produced in material properties are of permanent nature. The work was carried out as mentioned below.

Rare earth (Nd^{+3}) doped nanoparticles with composition $Mn_yZn_{(1-y)}Fe_{2-x}Nd_xO_4$ with y= 0.6, 0.65 and x=0.04, 0.05, 0.06, 0.07, 0.08, 0.09 and 0.1 were prepared using auto-combustion method. Composition with y= 0.6, 0.65 was preferred as previous reported work in which samples were prepared by auto-combustion method showed optimum magnetic properties for these concentrations of Mn. Each sample in the series prepared was divided in to two parts after characterization, thus making two subsets of each series. One set of each series which formed the pristine set of samples was studied for the properties whereas the second set of both the series was used for irradiating with gamma radiation and corresponding investigations. The ultimate work and the investigative findings are presented in form of thesis that is divided in to seven chapters.

1.6 Organization of Thesis

Following gives the overall synopsis of the **seven** chapters that are incorporated within the thesis.

- **Chapter 1** gives preliminary details of introductory topics like nanotechnology, magnetic nanoparticles, ferrites and manganese zinc ferrite nanoparticles. It includes a general discussion on impact of rare earth doping on structural, morphological, magnetic and electrical properties of manganese zinc ferrite nanomaterials. A flavor of use of high energy radiation in materials is discussed here by including the reports available on the topic. This chapter also consists of an in-depth literature review on the research work reported by researchers on different ferrite materials in nano form, methods of preparation and the various factors governing the properties of these materials. A review of the recent advancement in the field and modern day applications of these nanomaterials is also included in this chapter.

- **Chapter 2** includes detailed information on a variety of methods of material preparation that has been employed by different researchers to prepare a choice of ferrite nanoparticles. The detailed procedure involved in combustion synthesis route used to prepare rare earth doped manganese zinc ferrite nanoparticles for current investigations, with chemical composition $Mn_{0.6}Zn_{0.4}Fe_{2-x}Nd_xO_4$ and $Mn_{0.65}Zn_{0.35}Fe_{2-x}Nd_xO_4$ (x=0.04, 0.05, 0.06, 0.07, 0.08, 0.09 and 0.1) is also described at length in this chapter.
- **Chapter 3**, A brief description of various analytical methods and instruments used for characterization and to investigate morphological, electrical and magnetic properties is included in this chapter. This chapter includes the basic principles and the procedure involved in utilizing these techniques.
- **Chapter 4** This chapter unfolds all the data that has been recorded as prepared $Mn_{0.6}Zn_{0.4}Fe_{2-x}Nd_xO_4$ and $Mn_{0.65}Zn_{0.35}Fe_{2-x}Nd_xO_4$ nanoparticle samples. By and large inclusion of rare-earth ions in the sample did exhibit noticeable influences on almost all the properties that have been recorded. It showcases the effect of rare earth (N^{d+3}) inclusion on structural parameters, magnetic properties and electrical behavior of manganese zinc ferrite nanoparticles. The results obtained from Rietveld refinement of XRD patterns, Fourier transforms infra red spectra of $Mn_{0.6}Zn_{0.4}Fe_{2-x}Nd_xO_4$ and $Mn_{0.65}Zn_{0.35}Fe_{2-x}Nd_xO_4$ nanoparticles, the structural parameters information obtained from XRD data (lattice constant 'a', mass density 'D_M', X- ray density 'D_X',

crystallite size *'t'*) and the cation distribution estimated from XRD form the main contents of this chapter. Particle size obtained from transmission electron microscope (TEM), Magnetic, Mossbaur spectral data and data on electoral properties data is also included in this chapter. The detailed analysis of the entire data recorded on as prepared nanoparticle samples is presented in this chapter

- **Chapter 5** The entire exercise involved in irradiating the nanoparticle samples with gamma irradiation using Co^{60} source by moulding the nano powders into pallets is presented in this chapter.
- **Chapter 6** This chapter includes the entire set of measurements and the results of the investigations carried out on Gamma irradiated nanoparticle $Mn_{0.6}Zn_{0.4}Fe_{2-x}Nd_xO_4$ and $Mn_{0.65}Zn_{0.35}Fe_{2-x}Nd_xO_4$ ferrite samples. It includes the comparison of these results with the results obtained on as prepared ferrite nanopowded samples. The outcome of the comparison of several investigations carried out is also presented in this chapter which should be of extreme interest to researchers in the field. The detailed analysis of the variations in different properties seen in the gamma irradiated samples indeed speaks about the power or the energy available with the gamma radiations to alter the properties of nanoparticles even after their successful synthesis or preparation which may not be possible through any other tool or energy source. A detailed review on the observations made, their correlation with rare earth doping and radiation exposure is presented in this chapter.
- **Chapter 7:** This chapter gives the summary of the whole exercise taken up in the investigations, the results obtained and the overall conclusions explaining the effect of rare earth (Nd^{+3}) and impact of different doses of high energy gamma radiation on

structural, electrical and magnetic properties of manganese zinc ferrite nanoparticles. A mention of future scope in this area of research involving gamma radiations has been also made in this chapter.

References

1. K. Nagaraja Setty, Journal of Chemical and Pharmaceutical Sciences, Volume 10 Issue 1, (2017) 588-590
2. R. A. Andrievski, A. M. Glezer, Scr. Mater. Vol. 44 (2001), p. 1621-1623.
3. R. A. Andrievski, Materials Science Forum:Current Research in Advanced Materials and Processes, Vol. 494, (2005) pp 113-120
4. Fruhstorfer, H.; A. Seitz (1913). "Family: Morphidae". Macrolepidoptera of the world. Germany: Stuttgart: Alfred Kernen. 5: 333–356
5. J. L. Snoek, New developments in Ferromagnetic Materials (Elsevier Pub. Co., New York, 1949).
6. Néel, Annales de Physique (Paris) 3, (1948)137.
7. R. N. Bhowmik, N. Naresh, International journal engineering science technology, 2, 8 (2010) 40.
8. I. Chicinas, Journal of Optoelectronics And Advanced Material, 8, 2(2006)439.
9. K. J. Standley. Oxide Magnetic Materials, 2nd edi. (1972).
10. P. P. Hankare, R.P. Patil, U.B. Sankpal, S.D. Jadhav, I.S. Mulla, K.M. Jadhav, B.K. Chougule, Journal of Magnetism and Magnetic Materials, 321 (2009) 3270.
11. M.A.Elkestawy, S. Abdel Kader, Physica B:condensed matter physics, 405 (2010) 619-624.

12. S. Soliman, A. Elfalaky, Gerhard H. Fecher, Claudia Felser, Physicsl Review B, 83, (2011)085205.

13. G. Sathishkumar, C. Venkataraju, K. Sivakumar, Material Science and Applications, 1,(2010)19-24.

14. P. P. Naik, R. B. Tangsali, S. S. Meena, Pramod Bhatt, B. Sonaye, S. Sugur, Radiation Physics and Chemistry 102 (2014) 147–152.

15. L. G. Van Uitert, Journal of Chemistry and Physics, 24, (1956)306.

16. N. Millot, S. L. Gallet, D. Aymes, F. Bernard, F. Grin, Journal of European Ceramic Society, 27 (2007) 921.

17. T. A. S. Ferreira, J. C. Waerenborgh, R. Nunes, F. M. Costaa.
Solid State Science, 5 (2003) 383.

14. D. Q. Tang, D. J. Zang, H Ai. Chemistry Letters, 35, 11 (2006) 1238.

15. M. K. Shobana, V. Rajendran, M. Jeyasubramanian, N. S. Kumar. Material Letters, 612 (2007) 2616–2619

16. S. Nasir and M. Anis-ur-Rehman, Physica Scripta, 84 (2011) 025603.

17. J. Grabis, I. Zalite, Material Science Forum, 555 (2007) 267.

18. RB Tangsali, SH Keluskar, GK Naik, JS Budkuley, International Journal of Nanoscience 3 (04n05), 589-597.

19. P. P. Naik, RB Tangsali, B Sonaye, S Sugur, Journal of Nano Research 24, 194-202.

20. P. P Naik, RB Tangsali, B Sonaye, S Sugur, AIP Publishing, 1512 (2012) 354-355.

21. B. Xue, R. Liu, Z. D. Xu, Y. F. Zheng Chemistry Letters 37,10 (2008) 1058.

22. Jae-Gwang Lee, Jae Yun Park and Chul Sung Kim, Journal of Material Science, 33 (1998) 3965 Ð 3968.

23. M. R. Anantharaman, S. Jagatheesan, K. A. Malini, S. Sindhu, A. Narayanasamy, C. N. Chinnasamy, S. Reijne, K. Seshan, R. H. H. Smits, H. H. Brongersma, Journal of Magnetism and Magnetic Materials, 189 (1998) 83Ð88.

24. S. Ghatak, M. Sinha, A.K. Meikap, S.K. Pradhan, Physica E: low dimentional systems and nanostructures, 40 (2008) 2686-2693.

25. W. H. Bragg, Philosophical Magazine, 30 (1915) 305.

26. J. Smit, F. K. Lotgering, P. P. Van Staple, Journal of Physical Society Japan, 17B (1962) 158.

27. E. J. W. Verwey, and E.L. Heilman, Chem. Phys.15 (1947), 174.

28. J. Smit, F. K. Lotgering, P. P. Van Staple, J. Phys. Soc. Japan 17B (1962) 158.

29. P. I. Slik, Ferrites for Non-Microwave Applications 2 (1980) 200.

30. G. Winkler “Crystallography, chemistry and technology of ferrites”; in: Magnetic properties of Materials, ed. J Smit, New York, McGraw- Hill, 1971.

31. Ping Hua, Hai-boYang, De-anPan, HuaWang, Jian-junTian, Shen-gen Zhang, Xin-feng Wang, Alex A. Volinsky, Journal of Magnetism and Magnetic Materials, 322(2010)173–177.

32. J. L. Snoek, New developments in Ferromagnetic Materials (Elsevier Pub. Co., New York, 1949).

33. Néel, Annales de Physique (Paris) 3, (1948)137.

34. R. G. Kulkarni, Asian J. Phy. 6 (1997) 204

33. M. I. Alam, Asian J. Phy. 6 (1997) 212

34. V. Voronkon J. Phy. IV France 7 (1997) 35
35. D. Bahadur, J. Giri, B. Nayak, T. Sriharsha, P. Pradhan, N. Prasad, R. C. Barick,R. D. Ambashta Pramana 65 (2005) 66
36. R. Rangnathan, A. Ray, Pramana 58 (2002) 995
37. M. Sugimoto, J. Am Ceram. Soc. 82 (1999) 269
38. Kyung Young Kim, Jongkyu Lee, Wangsup Kim and Hwan Choi, J. Korean Inst. Tel. Ele 28 (A) (1991) 880
39. S. Nishigaki, S.Yano, H. Kato, T. Nano – Mura. J. Am-Cerm. Soc. 71 (1) (1988) C-11-0-17.
40. N. T. Lan, T. D. Hien, N. P. Duong, D. V. Truong, J. Korean Phys. Soc., 52 (2008) 1522-1525.
41. S.H. Keluskar, R.B. Tangsali, G.K. Naik, J.S. Budkuley, Journal of Magnetism and Magnetic Materials, 305 (2006) 296-303.
42. K. Janghorban, H. Shokrollahi, Journal of Magnetism and Magnetic Materials, 308 (2007) 238-242.
43. P. Mathur, A. Thakur, M. Singh, J. Phy. Chem. Solids, 69 (2008) 187-192.
44. Y. Xuan, Q. Li, G. Yang, Journal of Magnetism and Magnetic Materials, 320 (2008) 1615-1621.
45. L. Nalbandian, A. Delimitis, V.T. Zaspalis, E.A. Deliyanni, D.N. Bakoyannakis, E.N. Peleka, Microporous and Mesoporous Mater., 114 (2008) 465-473.
46. N. Kikukawa, M. Takemori, Y. Nagano, M. Sugasawa, S. Kobayashi, Journal of Magnetism and Magnetic Materials, 284 (2004) 206-214.

47. B. Jeyadevan, K. Tohji, K. Nakatsuka, A. Narayanasamy, Journal of Magnetism and Magnetic Materials, 217 (2000) 99-105.

48. D. Makovec, A. Kosak, M. Drofenic, Nanotechnology 15 (2004) 160

49. M.M. Hessien, M.M. Rashad, K. El-Barawy, I.A. Ibrah, Journal of Magnetism and Magnetic Materials, 320 (2008) 1615-1621.

50. P. Hu, H. Yang, D. Pan, H. Wang, J. Tian, S. Zhang, X. Wang, A.A.Volinsky, Journal of Magnetism and Magnetic Materials, 322 (2010) 173-177

51. K. Praveena, K. Sadhana, S. Bharadwaj, S. R. Murthy, Journal of Magnetism and Magnetic Materials, 321 (2009) 2433-2437

52. R.J. Joseyphus, A. Narayanasamy, K. Shinoda, B. Jeyadevan, K. Tohji, J. Phys. Chem. Solids, 67 (2006) 1510-1517

53. E. Auzans, D. Zins, R. Massart, J. Mater. Sci. 34 (1999)1253.

54. M. Rozman, M. Drofenic, J. Am. Ceram. Soc. 78 (1995) 2249.

55. A. Thakur, M. Singh, Ceram. Int. 29 (2003) 505.

56. Xian- Ming Liu, Shao-Yun Fu, J. Magnetism and Magnetic materials, 308 (2007) 61-64.

57. Shunli Hao, Xin Wang, Yu Wei, Yongming Wang and Chunjing Liu, Vol. 25, issue 6, Supplement 1 (2006) 466-470.

58. F. Li, J. J. Liu, D. G. Evans, X. Daun, Chem. Mater, 16 (2004) 1597.

59. J. Leu, F. Li, D. G. Evans, X. Daun, Chem. Commen. 4 (2003) 242.

60. W. Meng, F. Li, D.G. Evans, X. Duan, Mater. Chem. Phys. 86 (2004)1.

61. S. Yamamoto, S. Horie, N. Tanamachi, H. Kurisu, M. Matsuura, Journal of Magnetism and Magnetic Materials, 335 (2001) 218-222.

62. C. Venkataraju, G.Sathishkumar, K.Sivakumar, Journal of Magnetism and Magnetic Materials, 322 (2010) 230-233.
63. S. Dasgupta, J. Das, J. Eckert, I. Mannaa, J. Magn. Magn. Mater., 306 (2006) 9-15.
64. M.A. Ahmed, N. Okasha, M.M. El-Sayed, Ceram. Int., 33 (2007) 49-58.
65. E. Ateia, M.A. Ahmed, A.K. El-Aziz, Journal of Magnetism and Magnetic Materials, 311 (2007) 545-554.
66. N. Rezlescu, E. Rezlescu, Solid State Commun. 88 (2), (1993)139.
67. L. Zhao, Y. Cui, H. Yang, L. Yu, W. Jin, and S. Feng, Mat. Lett. 60 (2006) 104.
68. A. C. F. M. Costa, M. R. Morelli, and R. H. G. A. Kiminami, J. Mat. Sci. 39, (2004) 1773.
69. L. Zhao, H. Yang, X. Zhao, L. Yu, Y. Cui, and S. Feng, Mat. Lett. 60 (2006)1.
70. M. H. Mahmoud, A. A. Sattar, Journal of Magnetism and Magnetic Materials, 277, 101 (2004).
71. N.Z. Darwish, O.M.Hemeda, M.I.Abd-Elati, Appl. Radiat. Isot. 45 (1994)4.
72. M. Hemeda, M. El-Saadawy, Journal of Magnetism and Magnetic Materials, 256 (2003) 63.
73. I.M. Hamada, Journal of Magnetism and Magnetic Materials, 271 (2004) 318.
74. Dalal, Mohammed Hemeda, J. Appl. Sci. 2 (5) (2005) 989.
75. E. Ateia, Egypt. J. Solids, 29 (2) (2006) 317.
76. M. A. Ahmed, E. Ateia, G. Abdelatif, F.M. Salem, Mater Chem. Phys. 81 (2003) 63.

77. M.A. Ahmed, A. I. Khalil , S. Solyman, J. Mater. Sci. 42 (2007) 4098.445.

78. Okasha N., J. Alloys Compd., 490 (2010) 307

79. Karim Asif, E. Shirsath Sagar, S. J. Shukla, K. M. Jadhav, Nucl. Instr. And Meth.in Phys. Res. B (2010) Accepted Manuscript.

80. Ibrahim Sharifi, H. Shokrollahi, S. Amiri, Journal of Magnetism and Magnetic Materials 324 (2012) 903–915

81. M. Mahmoudi, S. Sant, B. Wang, S. Laurent, T. Sen, Advanced Drug Delivery Reviews 63 (2010) 24–46.

83. H. Mohseni, H. Shokrollahi, Ibrahim Sharifi, Kh. Gheisari, Journal of Magnetism and Magnetic Materials 324 (2012) 3741–3747.

84. Magnetic nanoparticles, R. H. Kodama, Journal of Magnetism and Magnetic Materials 200 (1999) 359-372

85. G. Vaidyanathan, R. Arulmurugan, S. D. Likhite, M. R. Anantharaman, Milind Vaidya, S. Sendhilnathan, N. D. Senthilram, Indian Journal of Engineering & Materials Sciences Vol. 11 (2004), pp. 289-294

86. E. Ranjith kumar, R. Jayaprakash, M.S. Seehra, T. Prakash, Sanjay Kumar, Journal of Physics and Chemistry of Solids 74 (2013) 943–949

87. Pranav P. Naik, R.B. Tangsali, S.S. Meena, S.M. Yusuf, Materials Chemistry and Physics 191 (2017) 215-224.

88. V. Jagadeesha Angadi, A.V. Anupama, Harish K. Choudhary, R. Kumar, H.M. Somashekarappa, M. Mallappa, B. Rudraswamy, B. Sahoo, Journal of Solid State Chemistry 246 (2017) 119–124

89. E. Ateia, M.A. Ahmed, A.K. El-Aziz, Journal of Magnetism and Magnetic Materials 311 (2007) 545–554

90. Y. K. Dasan, B. H. Guan, M. H. Zahari, L. K. Chuan, Plos One, DOI:10.1371/journal.pone.0170075 January 12, 2017

91. S. Solyman, Ceramic International, 32 (2006) 755

92. R.H. Kadam, Kirti Desai, Vishnu S. Shinde, Mohd. Hashim, Sagar E. Shirsath, Journal of Alloys and Compounds 657 (2016) 487-494

93. M. F. Huq, D. K. Saha, R. Ahmed, Z. H. Mahmood, Journal of Scientific Research, 5 (2), (2013) 215-233.

94. A. Mahesh Kumar, M. Chaitanya Varma, G.S.V.R.K. Choudary, P. Prameela, K.H. Rao, Journal of Magnetism and Magnetic Materials 324 (2012) 68–71

95. S. Mahalakshmi, K. SrinivasaManja, S. Nithiyanantham, Journal of Superconductivity and Novel Magnetism, September 2014, Volume 27, Issue 9, pp 2083–2088

96. M.A. Khan, M.U. Islam, M. Ishaque, I.Z. Rahman , Ceramics International 37(7), (2011)2519.

97. E. Rezlescu, N. Rezlescu, P.D. Popa, L. Rezlescu, C. Pasnicu, Physica Status Solidi A, 162(2), (1997) 673.

98. M.A. Ahmed, N. Okasha, M.M. El-Sayed, Ceramics International 33 (1), (2007)49.

99. A. D’souza, Deepak Kumar, M. Chatim, V. Naik, Pranav P. Naik, R. B Tangsali, Advanced Science Letters, Volume 22, Number 4, April 2016, pp.773-779(7)

100. P.P. Naik, R.B. Tangsali, B. Sonaye, S. Sugur Journal of Magnetism and Magnetic Materials, 385(2015)377–385.

101. P.P. Naik, R.B. Tangsali, R. B ; B. Sonaye, S. Sugur, Advanced Science Letters, Volume 22, Number 4, April 2016, pp. 752-758(7)

102. Pranav P. Naik, R.B. Tangsali, B. Sonaye, S. Sugur, Journal of Nanotechnology and Advanced Material, 3, No. 1, 1-7 (2015)

103. L. Ben Tahar, L.S. Smiri, M. Artus, A. L. Joudrier, F. Herbst, M.J. Vaulay, S. Ammar, F. Fievet, Material Research Bulletin, 42 (2007) 1888-1896.

104. G.L. Sun, J.B. Li, J.J. Sun, X.-Z. Yang, Journal of Magnetism and Magnetic Materials, 281 (2004) 173.

105. Xu Feng, Zhou Xiangchun, Li Liangchao, Liu Hui, Jiang Jing, Journal of Rare Earths 25 (Jun. 2007) 232

106. Naveen Kumar Saxena, Nitendar Kumar, P.K.S. Pourush, Journal of Magnetism and Magnetic Materials 322 (2010) 2641–2646

107. Naveen Kumar Saxena, Nitendar Kumar, P.K.S. Pourush, Nature and Science 7(2009) 11-14

CHAPTER 2

METHODS OF MATERIALS PREPARATION

2.1 Introduction

In the current era scientific research has been directed toward development of nanomaterials with improved properties that would provide efficient performance. As performance of a nanomaterial is sensitive to method of preparation, numerous methods have been developed and are being successfully employed [1]. Thus selection of an appropriate sample preparation method carries immense importance in nano research [2]. A considerable control over certain properties of nanomaterials can be achieved by following this simple procedure.

2.2 Synthesis of magnetic ferrite nanomaterials

As mentioned in Chapter I Mn-Zn ferrite nanoparticles of are potential candidates for applications in several important and technology sensitive areas [3-12]. Although several reports on various methods of property alterations of manganese zinc ferrite nanoparticles are available [13-16]. These can be used effectively after synthesizing monophasic nano-samples. Numerous methods of materials preparation like co-precipitation method, sol-gel method, hydrothermal process, Chimie-Douce method, precursor method, combustion method, plasma synthesis, reverse micelle technique, water CTAB, micro-emulsion method, spray pyroliysis method [17-28] etc. are being used on large scale to prepare several types of nanoparticles.

2.2.1 Co precipitation method

In Co-precipitation method, the required metal cations, taken in form of nitrates, are co-precipitated as hydroxides, carbonates, oxalates or citrates from a common medium. In actual practice, one takes oxides or carbonates of the relevant metals, digests them with an acid and then the precipitating reagent is added to the solution. The precipitate obtained after drying is heated to the required temperature in appropriate atmosphere to produce the final product. The decomposition temperatures of the precipitates are generally lower than the temperatures employed in the ceramic method. The pros of this method are that it is simple whereas the cons are, in-spite of being simple control of stoichiometry it times becomes an difficult issue if there is no formation of precipitate.

One of the drawbacks of the co-precipitation method is the difficulty of controlling the particle size and morphology [29].

2.2.2 Hydrothermal process

This method is an sample effective preparation technique used for material synthesis. The method is based on the fact that many oxides are soluble in an alkali solution. The method has been most successfully applied to prepare ferrites. The advantage in the hydrothermal method is that it permits the re-crystallization of the powder. It is also possible to monitor the grain size and shapes. However this method is not a rapid and quick one.

Hydrothermal synthesis can be defined as a method of synthesis of single crystals that depends on the solubility of minerals in hot water under high pressure. The crystal growth is done in a setup comprising of an autoclave which is basically a steel pressure vessel, in which the chemicals are mixed along with water. A gradient of temperature is maintained at the two opposite terminals of the crystal growth chamber in order to dissolve chemicals at hot terminal and seed is made to attain additional growth at cooler terminal. A possible merit of this technique over other variety of crystal growth setup is that it possesses the ability to generate crystalline phases that are unstable at the melting point. Also, the samples with high vapour pressure in the neighborhood of their melting points can also be prepared using hydrothermal method. The method is effectively employed for the growth of large crystals of high quality by managing and maintaining required composition. The only drawback this technique is the requirement of expensive auto-claves, and the complaxities involved in observing the crystal growth [30, 31].

2.2.3 Sol gel process

Sol-gel method is a well known technique employed in preparation of inorganic oxides. It is wet chemical method and a multi step process involving both chemical and physical process such as hydrolysis, polymerization, gelation, drying, dehydration and densification. The name “Sol-gel” is given to the process because of the distinctive viscosity increase that occurs at particular point in the sequence of the steps. A sudden increase in viscosity is the common feature of the sol gel processing, indicating the onset of gel formation. In the sol-gel process, synthesis of inorganic oxides is achieved from inorganic or organo-metallic precursors (generally metal alkoxides). The important features of the sol-gel method are better homogeneity compared to the traditional ceramic method, high purity, lower processing temperature, more uniform phase distribution in multi component systems, better size and morphological control [32] and possibility of preparing new crystalline and non crystalline materials.

In this procedure the solution (‘sol’) gradually transforms into a gel-like diphasic system comprising of both solid and liquid phase. In some cases large fraction of liquid may need to be removed for the formation of gel-like system. Removal of remaining liquid involves drying process resulting in significant amount of shrinkage and densification. The extent of porosity of the material is determined by the rate at which solvent is removed. The ultimate poly-condensation and enhancement in structural and mechanical properties is achieved by sintering of dried mass.

2.2.4 Ceramic method

This is an important and frequently employed technique for synthesis of mixed metals oxides and other solid materials. This technique involves very high temperatures, which are normally achieved by resistance heating. This alters the quality of the product material thus synthesized. The procedure involves grinding of oxides, carbonates, oxalates or other compounds containing the relevant metals in appropriate proportions; followed by heating of the mixture at a desired temperature, generally after palletizing the material. Several mixed metals sulphides, oxides, phosphides materials have been prepared by this method. The containers made up of Platinum, silica and alumina are preferred for the preparation of oxide materials. Graphite containers are employed for the synthesis of sulphides and other chalcogenides. This method has numerous drawbacks. The methods of monitoring the progress of reaction are very complex. The technique is more appropriate for synthesizing bulk materials and oxide materials. Sometimes it becomes difficult to obtain the compositionally homogeneous of the products prepared by ceramic techniques even if the reaction proceeds almost to completion [33,34].

2.2.5 Electrochemical method

Electrochemical methods have been used effectively for the preparation of many materials. Metal borides, carbides, silicides, oxides and sulphides are the materials most commonly prepared in this manner. Vanadate spinels with formula MV_2O_4 as well as tungsten bronzes, A_xWO_3, have been synthesized by electrochemical method. Tungsten bronzes are obtained at the cathode when current is passed through two inert electrodes immersed in a molten solution of alkali metal tungstate, A_2WO_4 and WO_3, Oxygen is liberated at the anode [10]. Oxides containing metals in high oxidation states are conveniently prepared electrochemically. Superconducting $La_2CuO_{(4+\delta)}$ has been prepared by electro chemical oxidation [35,36].

2.2.6 Spray pyrolysis method

In this technique, smaller liquid droplets of chemical solution or precursor mixture are transformed into solid material through conventional heating. This technique is comprised of following steps : (i) Developing smaller droplets of chemical solution containing raw material or precursor solution, (ii) removal of solvent through conventional heating, (iii) condensation of solute, (iv) decomposition of solute followed by reaction, and (v) and high temperature treatment of solid particles [37].

2.2.7 Precursor method

This technique involves synthesis of an easily degradable compound of metals and mixed metals, that produces the required oxides on thermal tretment. One can generate homogeneous, ultra fine particles, highly pure oxide materials from precursors. The synthesis of ferrites using water soluble salts of the desired metals fall under wet chemical technique category. These methods are known to produce ferrite powders having high level of homogeneity, smaller particle size, larger surface area and negligible porosity [38].

In the current times, extraordinary focus has been positioned on obtaining ferrite as a through unconventional approaches, especially chemical methods [39-41] There are several techniques that can be employed to generate the materials comprising of nano-particles [42-46], however their utilities on industrial scale is dependent on their cost and purity of initial raw materials.

2.2.8 Vapour phase method

This method of chemical transport via the vapour phase was introduced by Schafer in 1971. This technique is employed for the synthesis of novel materials, for the growth of single crystals and also for the purification of a material of research interest. The technique is utilized for synthesizing several compounds where in the gas phase is used as a conveying agent and has its impact on reaction rates. Gases react more rapidly than solids as their mobilities are enhanced. Also the gaseous phase is habitually important in usual solid state reactions under isothermal circumstances, where it may play a role of rapid way of conveying matter from one crystal to another [37]

2.2.9 Chimie-Douce method

This method is an extension of precursor method. It is observed that reactions precursor method takes place at much lower temperatures compared to the normal solid state reaction. The process is carried out at temperatures less then 500°C the phases thus formed are thermodynamically metastable. Often new phases are formed having unusual structures and interesting properties. The stable structures are obtained by calcinations at higher temperature. French have coined the term chimie-douce [37] for this method of preparation.

It involves steps such as intercalation where in ions are inserted in existing structures which results in reduction of cations in the host material using electrochemical method. The reverse of intercalation, can be also performed using electrochemical methods. Intercalation is followed by dehydration or removal of hydroxide group is achieved using conventional heating methods keeping temperature below 500^{o}C.

Crystallite sizes of the powder specimen can be obtained on calcinations at various temperatures. It is observed that the size increases with calcination temperature. As the calcinations temperature affects the particle size, all parameters like Curie temperature, permeability, saturation magnetization dielectric properties, resistivity etc. are also affected accordingly.

2.2.10 Plasma synthesis method

This is one of the effective methods employed to yields nanomaterials [47]. Highly crystalline nanomaterials can be synthesized using 50KW-3MHZ rf induction plasma torch. High energy ball milled elemental powders, <10 micrometers in size and in the desired stoichiometric ratio are used as metal species in the plasma. Argon gas is used as plasma gas and plasma stream gas consists of mixture of argon and hydrogen gas. All precursor powders are injected through plasma jet stream by argon, a carrier gas. Once the induction plasma is generated, air under high pressure is also sent in the reactor as an oxidizer [48-51]. This method of preparation is highly tedious and involves complicated systems.

2.2.11 Reverse micelle method

Reverse micelle technique is yet another method suitable for preparation of nanomaterial. Unlike other methods this method can be also used to prepare manganese–zinc ferrite nanoparticles [52, 53]. Wet chemical synthesis performed in Reverse micelle, in which volumes of water are encased by surfactant molecules in an excess volume of oil, provides the high control over size and morphology. During synthesis, surfactant molecules keep particles separated and restrict particle growth this keeps control on size and shape of particles. The fundamental principle for the technique is the use of a surfactant to steady varying aqueous droplet sizes in a medium containing hydrocarbons. Metal salt precursors contained in the aqueous portion are transformed by a reactant from the hydrocarbon phase. Both the structure of the surfactant and the size are able to produce materials having a wide range of grain sizes**.** It has been observed that precipitation of metals is influenced by the pH and the electrochemical potential of the solution; therefore, the initial ratio of metal precursors is modified to account for the reduction of metals in the precipitate and subsequently in the fired samples.

In this method the micelle size can be controlled by the molar ratio of water to AOT, which is chosen to yield a fine particle size in nanometer. The volume of aqueous solution and desired particle sizes are used to determine the amount of the precursor solution to be used. The ammonia solution is then added to the metal–salt solution under constant stirring. The reaction is allowed to proceed for about 2 hrs, until particle flocculation is induced by adding excess methanol. The particles are then collected using centrifugation and washed using methanol to remove excess surfactant, followed by a methanol-water solution to remove any additional unreacted ions. After final centrifugation, the material is dried overnight under a dynamic vacuum, and subsequently fired at 525 °C for 5 hours under inert atmosphere to obtain the required product.

2.3 Synthesis of Rare earth doped manganese zinc ferrite nanoparticles using combustion synthesis

This is one of the simplest method which is cost effective and quick method for material preparation. As per previous reports [53-58], combustion method has been employed successfully in preparing monophasic Mn-Zn Ferrite nanoparticles with narrow particle size distribution and having better structural, electrical and magnetic properties. In current investigations two series of rare earth (Nd^{+3}) doped manganese zinc ferrite nanocrystalline material with the chemical formulae $Mn_{0.6}Zn_{0.4}Fe_{2-x}Nd_xO_4$ and $Mn_{0.65}Zn_{0.35}Fe_{2-x}Nd_xO_4$ with (x= 0.04, 0.05, 0.06, 0.07, 0.08, 0.09, 0.1) were prepared using auto Combustion method.

This process involves several simple steps. Elemental salts of AR grade along with a fuel and complexing agent are dissolved in distilled water to obtain clear solution free from any residues. This solution is subjected to conventional heating with starring for volume reduction. The reduction of water content turns the solution in to a vicious paste which can be further dried to obtain a dry mass. This dry mass, as it dries up fully triggers the auto combustion process. The final product is obtained at the end of combustion process. The method is known to yield a high quality product with narrow particle size distribution.

In the present work nanocrystalline manganese zinc ferrite material with chemical composition $Mn_{0.6}Zn_{0.4}Fe_{2-x}Nd_xO_4$ & $Mn_{0.65}Zn_{0.35}Fe_{2-x}Nd_xO_4$ (x=0.04, 0.05, 0.06, 0.07, 0.08, 0.09 and 0.1) were prepared using combustion route. The various steps involved in the preparation procedure as mentioned above are presented in figure 2.3.1

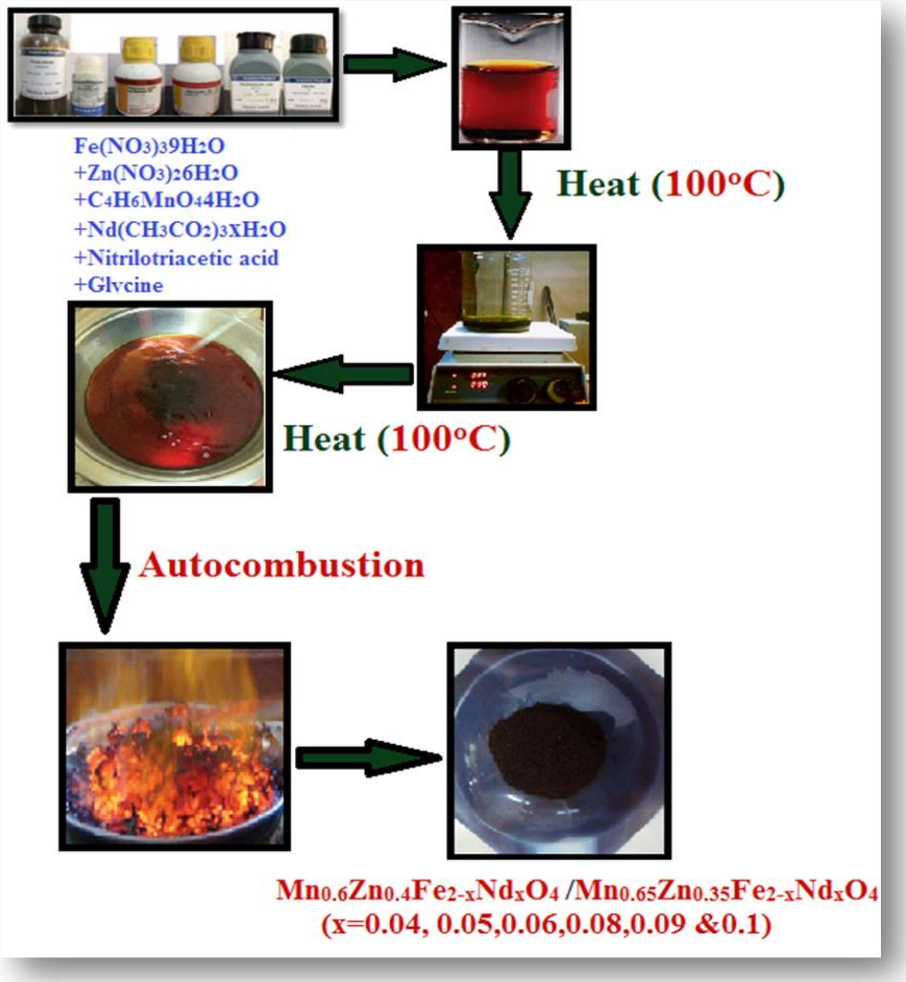

Figure 2.3.1 Steps involved in preparation of rare earth doped manganese zinc ferrite nanoparticles using combustion method

Metal salts $Fe(NO_3)_3 9H_2O$, $Zn(NO_3)_2 6H_2O$, $C_4H_6MnO_4 4H_2O$ and $Nd(CH_3CO_2)_3 xH_2O$ were taken in Stoichiometric quantity along with Nitrilotriacetic acid as complexing agent and Glycine as fuel. The raw materials were dissolved in 400ml double distilled water at 80^{o}C to get a clear solution. The solution was subjected to volume reduction by conventional heating at about 100^{o}C till the auto-combustion is triggered. The entire combustion process can be represented by a Gaussian profile with base width lasting for a maximum of 3 minutes and optimum combustion conditions lasting for less than 30 seconds. The residual powders obtained from the combustion process are actual samples, which were subjected to various characterization techniques without any further annealing [59, 60].

References

1. S.V.N.T. Kuchibhatla, A.S. Karakoti, D. Bera, S. Seal, One dimensional nanostructured materials. Prog. Mater. Sci. 52(5), (2007) 699–913
2. N. Kaur, M. Kaur, Processing and Application of Ceramics, 8 (3), (2014) 137–143
3. Smitha Thankachan, Manju Kurian, Divya S Nair, Sheena Xavier, E M Mohammed, Volume 3, Issue 4, (2014)529-537.
4. F. Muthafar, Al-Hilli, Sean Li, Kassim S. Kassim , Material Chemistry and Physics 128, (2011)127-132.
5. M. A. Ahmed, E. Ateia, S.I. El-Dek, Rare earth doping effect on the structural and electrical properties of Mg-Ti ferrite, Materials letters 57, (2003)4256-4266.
6. Ibrahim Sharifi, H. Shokrollahi, S. Amiri, Journal of Magnetism and Magnetic Materials 324 (2012) 903–915
7. M. Mahmoudi, S. Sant, B. Wang, S. Laurent, T. Sen, Advanced Drug Delivery Reviews 63 (2010) 24–46.

8. H. Mohseni, H. Shokrollahi, Ibrahim Sharifi, Kh. Gheisari, Journal of Magnetism and Magnetic Materials 324 (2012) 3741–3747.
9. R. H. Kodama, Journal of Magnetism and Magnetic Materials 200 (1999) 359-372
10. Alam Abedini, Abdul Razak Daud, Muhammad Azmi Abdul Hamid, Norinsan Kamil Othman, Plose One , Volume 9, Issue 3, (2014)1-8.
11. V. T. Zaspalis, V. Tsakaloudi, G. Kogias, Mn Zn-ferrites: EPJ Web of Conferences, 75, (2014)04004
12. Ibrahim Sharifi, H. Shokrollahi, S. Amiri, Journal of Magnetism and Magnetic Materials 324, (2012)903–915.
13. D.M. Hemeda, American Journal of Applied Sciences 2 (5)(2005)989-992,
14. P. P. Naik, R. B. Tangsali, S. S. Meena, Pramod Bhatt, B. Sonaye, S. Sugur, Radiation Physics and Chemistry, 102 (2014) 147–152.
15. I. M. Hamada, Journal of Magnetism and Magnetic Materials 271 (2004) 318–32.
16. N. Z. Darwish, O. M. Hemeda, M. I. Abd El-Ati, Applied Radiation and Isotopes, vol. 45, no. 4, (1994) pp. 445–448
17. M. Rozman and M. Drofenik , J. Am. Ceram. Soc. 78 (1995) 2449.
18. S. Komarneni, E. Fregeau, E. Breval and R. Roy, J. Am.Ceram. Soc., 71(1988) C26.
19. A. Goldman and A. M. Laing., J. Phys. Coll. 4 (1977) C1 297.
20. A. Attaie, M. R. Piramoon, I. R. Harris, C. B. Ponton, J. Mater. Sci.30(1995)5600.
21. M. Seki, T. Sato and S. Usui, J. Appl. Phys. 63 (1988) 1424.
22. A. Thakur and M. Singh, Ceram. Int. 29 (2003) 505

23. C.F. Zhang, X.C. Zhong, H.Y. Yu, Z.W. Liu, D.C. Zeng, Physica B: Condensed Matter 404 (2009) 2327–2331.
24. A.S. Teja, P.-Y. Koh, Progress in Crystal Growth and Characterization of Materials, 55, (2009) 22–45
25. L. Nalbandian, A. Delimitis, V.T. Zaspalis, E.A. Deliyanni, D.N. Bakoyannakis, E.N. Peleka, Microporous and Mesoporous Materials 114 (2008) 465–473.
26. P.P. Hankare, R.P. Patil, U.B. Sankpal, S.D. Jadhav, K.M. Garadkar, S.N. Achary, Journal of Alloys and Compounds 509 (2011) 276–280.
27. D.S. Mathew, R.-S. Juang, Chemical Engineering Journal 129 (2007) 51–65.
28. A. Kale, S. Gubbala, R. Misra, Journal of Magnetism and Magnetic Materials 277 (2004) 350–358.
29. M. P. Pileni, J. Phys., Chem. 97 **(**1993) 6961.
30. A. B. Gadkari, T. J. Shinde, P. N. Vasambekar, Materials Characterization 60, (2011)1328-1333.
31. Mohammad AkhyarFarrukh, Boon-Tech Heng, Rohana Adnan, Truk. J. Chem. 34(2010)537-550.
32. G. Schikorr, Z. Allg. Chem., 212 (1938) 33.
33. J. Azadmanjiri, J. Non-Cryst. Solids, Volume 353, Issues 44–46, 15 November 2007, Pages 4170–4173
34. G. Vaidyanathan , R. Arulmurugan , S. D. Likhite , M. R. Anantharaman , Milind Vaidya , S. Sendhilnathan, N. D. Senthilram, Indian J. Eng. Mater. Sci.Vol. 11, (2004) pp. 289-294
35. Guozhong Cao, Imperial College Press, (2004).

36. J. C. Grenier, A. Wattiaux, N. Lagueyte, J. C. Park, E. Marquestaut, J. Etoumeau, M. Pouchard, Physica C, 173 (1991) 139.
37. A. R. West, Solid state chemistry and its applications, John Wiley and sons (1984).
38. K. C. Patil, S. Sudar Manoharan and D.Gajapath, 'Handbook of Ceramics and Composites' vol.1 (eds. Nicholas P.Cheremisinoff, Marcel Dekker, INC, New York) p.469.
39. P. C. Fannin, S. W Charles. and J. L. Dormann, J. Magn. Magn. Mater. 201 (1999) 98
40. T. Pannaparayil, S. Komarneni , R. Marande and M. Zadarko, J. Appl. Phys. 67, (1990)5509.
41. Z. Yue, J. Zhou, L. Li, H. Zhang and Z. Gui, J. Magn. Magn.Mater. 208 (2000) 55.
42. B. Martinez, A. Roig, E. Molins and C. Monty, J. Appl. Phys. 79 **(**1996) 2580.
43. F.del Monte, M. P. Morales, D. Levy, A. Fernandez, M. Ocana, A. Roig, E. Molins, K. O'Grady and C. J. Serna, Langmuir, 13 **(**1997) 3627.
44. C. Cannas, D. Gatteschi, A. Musinu, G. Piccalunga and C. Sangregorio, J. Phys. Chem., B 102**(**1998) 7721.
45. J. S. Jiang, L. Gao, X. L.Yang, J. K. Guo and H. L. Shen, J. Mater. Sci. Lett., 18 (1999) 1781.
46. C. Caizer, M. D. Stefanescu, C. Muntean and I. Hrianca 2000 , 3rd Int. Edition of Rom. Conf. on Advanced Materials (Bucharest, Romania, October 23–25) Contribution p 85.

47. C. Savii, M. Popovici, M. Enache, I. Hrianca, A. Zanfir, R. Turicin, C. Caizer, Int. Conf. on Chemical Sciences for Sustainable.Development (Halkidiki, Greece, June 6–9) Contribution, (2000) 276.
48. Z. Tugut, Ph. D. Thesis CMU 2000.
49. M. I. Boulos, J. High Temp. Chem. Processes 1 (1992) 401.
50. S. Son et al., J. Appl. Phys. 91 (10) (2002) 7589.
51. S. Yamamoto, N. Tanamachi, H. Kurisu, M. Matsuura and K. Ishida, 21 Aa I-6 digest 8th Int. Conf. on ferrites Kyoto Japan.
52. P. Poddar, J. L. Wilson, H. Srikanth , S. A. Morrison and E. E. Carpenter, Nanotechnology (IOP publishing) 15 (2004) S570–S574.
53. S. A. Morrison, C. L. Cahill, E. E. Carpenter, S. Calvin, and V. G. Harris, Journal of applied physics 93 (10) 2003.
54. P. P. Naik, R. B. Tangsali, S. S. Meena, Pramod Bhatt, B. Sonaye, S. Sugur, Journal of Nano research, vol 24(2013), 194-202
55. P. P. Naik, R. B. Tangsali, B. Sonaye, and S. Sugur, AIP Conf. Proc. 1512, (2013)354
56. P.P. Naik, R.B. Tangsali, B. Sonaye, S. Sugur Journal of Magnetism and Magnetic Materials, 385(2015)377–385.
57. P.P. Naik, R.B. Tangsali, R. B ; B. Sonaye, S. Sugur, Advanced Science Letters, Volume 22, Number 4, April 2016, pp. 752-758(7)
58. Pranav P. Naik, R.B. Tangsali, B. Sonaye, S. Sugur, Journal of Nanotechnology and Advanced Material, 3, No. 1, 1-7 (2015)

59. A. D’souza, Deepak Kumar, M. Chatim, V. Naik, Pranav P. Naik, R. B Tangsali, Advanced Science Letters, Volume 22, Number 4, April 2016, pp.773-779(7)

60. Pranav P. Naik, R.B. Tangsali, S.S. Meena, S.M. Yusuf, Materials Chemistry and Physics 191 (2017) 215-224.

CHAPTER 3

CHARACTERIZATION AND PROPERTY MEASUREMENT TECHNIQUES

3.1 Introduction

Characterization of the samples prepared is an most essential and crucial step involved in any research oriented work. It plays an important role in ascertaining the formation of materials that have been prepared for establishing the required correlation between several properties and the control parameters proposed in the work. Modern day technology and constant advancement in the instrumentation allows a detailed and critical analysis of the materials and extract significant information about the structural, morphological nature of the material. This information which forms the main foundation of the work, actually helps one to identify the formation of the required materials that have been prepared. The subsequent task on confirming the formation samples, is the measurement of the materials properties which includes several other complicated instruments.

This chapter carries information on the equipment and procedures of different experimental techniques employed for the characterization, measuring electrical and magnetic properties of as prepared and γ irradiated rare earth doped manganese zinc ferrite nano-particles with chemical composition $Mn_{0.6}Zn_{0.4}Fe_{2-x}Nd_xO_4$ and $Mn_{0.65}Zn_{0.35}Fe_{2-x}Nd_xO_4$ with x=0.04,0.05,0.06,0.07,0.08,0.09,0.1.

3.2 X-Ray powder diffraction

The use of X-ray methods in the field of materials analysis is now entering its seventh decade. While the broad definition of X-ray methods covers many techniques based on the scatter, emission and absorption properties of X-radiation.

When a sample of material is bombarded with energetic radiation (X-rays, γ-rays, electrons, protons, etc.) vacancies may arise from the removal of inner orbital electrons. One of the processes by which the atom regains stability is by transference of electrons from outer to inner electron shells. Each of these transitions is accompanied by the emission of an X-ray photon having energy equal to the energy difference between the two states. A beam of monochromatic radiation may also be scattered when X-ray photons collide with atomic electrons. Where the scattered wavelengths interfere with one another diffraction pattern of X-rays occurs [1]. All the materials in nature are made up of numerous atoms. Every substance present the nature has some amount of order of periodicity in the arrangement of these atoms. It is the scattering from these periodic arrays that leads to the diffraction effect, and there is a simple relationship (Bragg's law) between the scattering angle, the wavelength of the radiation and the spacing between the planes of atoms. Since the distances between the atomic planes are dependent on the size and distribution of atoms i.e. the structure of the material, XRD can be used for qualitative and quantitative phase identification [2-5].

When an X-ray beam encounters the regular 3-D arrangement of atoms in a crystal a diffraction pattern is obtained due to the planes satisfying Bragg's equation (eqn. 3.2.1) These planes are termed as Bragg's planes (Figure 3.2.1) as they satisfy Bragg's law.

$$n\lambda = 2d\mathrm{Sin}\theta \qquad 3.2.1a$$

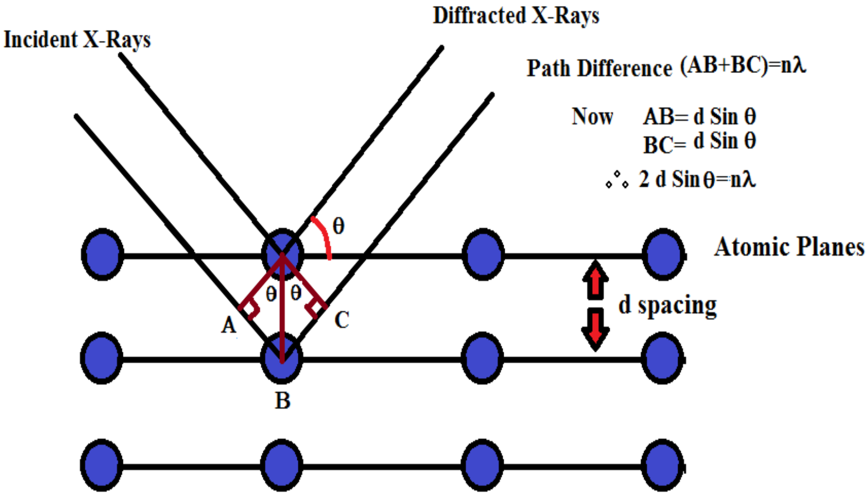

Figure 3.2.1 Diffraction of X-rays by atomic planes

By doing multiple x-ray diffractions at different crystal orientations, crystal structure and the size of the unit cell of the crystal can be determined. The most frequently used basic measurement geometry in X- ray diffraction instrument is the Bragg- Brentano geometry and is depicted in figure 3.2.2. In this arrangement the sample should exhibit a plane or flat surface. The angle of both incident and diffracted X-rays is θ with respect to specimen surface [6,7].

The diffraction pattern is observed by varying the incident angle of the incoming ray by θ and scattering angle by 2θ. The rotations are performed by highly precise goniometer which is the central part of diffratometer.

The focusing condition in the Bragg–Brentano geometry is obeyed when the x-ray source and detector are positioned on the goniometer circle where it intersects the focusing circle. True focusing would indeed occur only for a sample that is bent to the radius of the focusing circle R_{FC}. Typically a scintillation detector is placed behind the receiving slit and this converts the diffracted X-ray photons into voltage pulses and diffraction pattern is obtained on display unit [8,10].

In general there are seven crystal structures and are listed in table 3.2.1a along with the Interplanar spacings d_{hkl} for different crystal systems and their dependency on Miller indices *hkl*. Parameters *a*, *b* and *c* give the lengths of the crystallographic unit cell, while α, β and γ specify the angles between them [11,12].

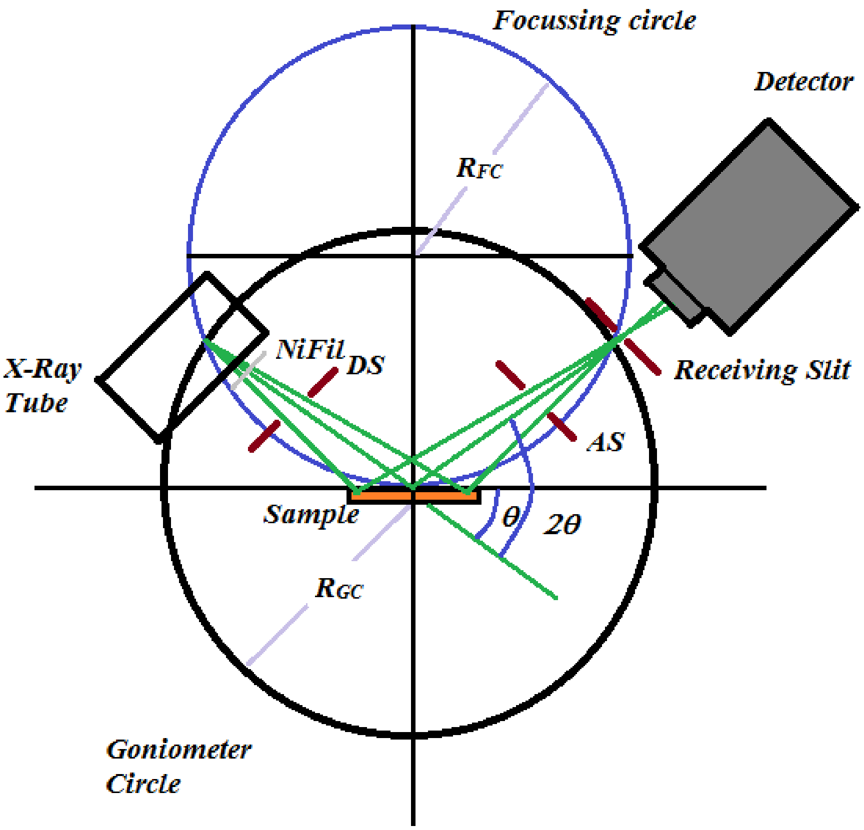

Figure 3.2.2 Schematic representation of θ/2θ diffraction in Bragg-Brentano geometry

Table 3.2.1a Different crystal systems, constraints and their dependence on Miller indices *hkl*, Parameters *a*, *b*, *c*, α , β and γ .

Crystal System	Constraints	$\frac{1}{d_{hkl}} =$
Cubic	$a = b = c$ $\alpha = \beta = \gamma = 90^o$	$\frac{h^2 + k^2 + l^2}{a^2}$
Tetragonal	$a = b \neq c$ $\alpha = \beta = \gamma = 90^o$	$\frac{h^2 + k^2}{a^2} + \frac{l^2}{c^2}$
Orthorhombic	$a \neq b \neq c$ $\alpha = \beta = \gamma = 90^o$	$\frac{h^2}{a^2} + \frac{k^2}{b^2} + \frac{l^2}{c^2}$
Hexagonal	$a = b \neq c$ $\alpha = \beta = 90^o$ $\gamma = 120^o$	$\left(\frac{4}{3}\right)\left(\frac{h^2 + k^2 + hk}{a^2}\right) + \left(\frac{l^2}{c^2}\right)$
Trigonal/ Rombohedral	$a = b = c$ $\alpha = \beta = \gamma \neq 90^o$	$\frac{(h^2 + k^2 + l^2)Sin^2\alpha + 2(hk + hl + kl)(Cos^2\alpha - Cos\alpha)}{a^2(1 - 3Cos^2\alpha + 2Cos^3\alpha)}$
Monoclinic	$a \neq b \neq c$ $\alpha = \gamma = 90°$ $\beta \neq 90°$	$\frac{h^2}{a^2Sin^2\beta} + \frac{k^2}{b^2} + \frac{l^2}{c^2Sin^2\beta} + \frac{2hlCos\beta}{acSin^2\beta}$
Triclinic	$a \neq b \neq c$ $\alpha \neq \beta \neq \gamma$	–

One can also determine the crystallite size from X-ray diffraction pattern using Debye-Scherrer equation given as

$$\mathrm{D} = \frac{0.9\lambda}{\beta \mathrm{Cos}\theta} \qquad 3.2.1b$$

Where λ= Wavelength of incident X-rays

β= Full width at half maximum of Bragg's peaks

θ= Bragg angle

The crystallite strain can be determined using following equation

$$\varepsilon = \frac{\beta}{4\,\mathrm{Tan}\,\theta} \qquad 3.2.1c$$

Where ε= crystallite strain

β= Full width at half maximum of Bragg's peaks

θ= Bragg angle

Rietveld method employed to identify and refine crystal structure. If a test structure of a material is known, from the theoretical model, the crystal structure of the material under investigation may be refined. The method is based on several steps such as generation of trial structure, calculation of a powder diffraction profile and comparison of the same with measured profile. The trial structure is altered by varying different parameters, such as atomic positions, thermal parameters, site occupancies, peak shape parameters, etc. The above mentioned parameters are varied till the best fit is obtained [13-17].

Material preparation for Powder X-ray diffraction

Approximately 0.5g of finely ground sample powders were used for obtaining X-ray diffraction patterns for as prepared as well as γ irradiated rare earth doped manganes zinc ferrite nanopawders with composition $Mn_{0.6}Zn_{0.4}Fe_{2-x}Nd_xO_4$ and $Mn_{0.65}Zn_{0.35}Fe_{2-x}Nd_xO_4$ nanosamples (x=0.04, 0.05, 0.06, 0.07, 0.08, 0.09 & 0.1)

Figure 3.2.3(a & b) shows the Rigaku X-Ray diffractometer and the goniometer with Bragg Brentano geometry.

Figure 3.2.3 a) Rigaku X-Ray diffractometer, Department of Physics, Goa University, b) goniometer with Bragg Brentano geometry.

Investigations for phase confirmation were done using Rigaku X-Ray diffractometer (Bragg Brentano geometry, Cu-kα, λ=1.5418Å) over the 2θ range of 20^o to 80^o in steps of 0.02^o and at scan rate of 2^o/min. Rietveld refinement of XRD data obtained on these samples was done using FullProf suit software.

3.3 Fourier transform infrared spectroscopy

Figure 3.3.1 Shimadzu FTIR 8900 assembly, Department of Physics, Goa University

Infrared spectroscopy is a technique where in the absorption takes place in the wavelength range 1 to 100 μm. The energy of infrared light is no longer sufficient to induce transitions of valence electrons. Instead, infrared radiation excites vibrational and rotational motions in molecules. Except for the differences in the energy transfer from the radiation to the molecule, the principles of IR spectroscopy are the same as those of VIS/UV spectroscopy or other spectroscopic techniques. The absorption of infrared light is again characterized by the Bouger- Lambert-Beer Law which states that absorbance of a material sample is directly proportional to the thickness of the sample and the concentrations of the attenuating species in the material sample. However, infrared spectra are usually presented by a plot of the percentage of transmission vs the wave number in cm^{-1} (as opposed to a plot of absorbance vs. the wavelength in nm in UV/VIS spectroscopy). A typical IR spectrum is therefore recorded from about 5,000 cm^{-1}(upper limit) to about 100 cm^{-1}(lower limit) [17-19].

Infrared spectroscopy is a technique frequently and widely employed in the field of research and industrial purposes as one the most simple and dependable technique for measurement, quality check and control. It is of great importance in terms of its applications in forensic investigations that are related to both criminal and civil cases, facilitating the identification of polymer deprivation. It is perhaps the most widely used method of applied spectroscopy.

IR spectra of solids are usually complex with a large number of peaks, each corresponding to a particular Vibrational transition. A complete assignment of all the peaks, to specific Vibrational modes is possible with solids. The IR spectra of a particular solid are usually quite different since the technique is governed by different selection rules. The number of peaks that are observed with either technique tends to be considerably less than the total number of Vibrational modes and different modes may be active in the technique. For instance, in order for a particular mode to be IR active the associated dipole moment must vary during the Vibrational cycle. Consequently, Centro symmetric Vibrational modes are IR inactive [20-22].

Stretching absorption usually produces stronger peaks than bonding. Symmetrical vibration does not cause absorption of IR radiation. One of the major factors influencing the IR absorption frequency of a bond is the identity of the two atoms involved. To be more precise, it is the masses of the two atoms which are important. The greater the mass of the attached atoms, lower is the IR frequency at which the bond will absorb.

An FT-IR Spectrometer is an instrument which acquires broadband near infra red (NIR) to far infra red (FIR) spectra. This technique is more advantageous as it deals with infra red region, provides better spectral resolution even with weak signals and acquires spectra quickly with high S/N ratio and greater accuracy [23,24].

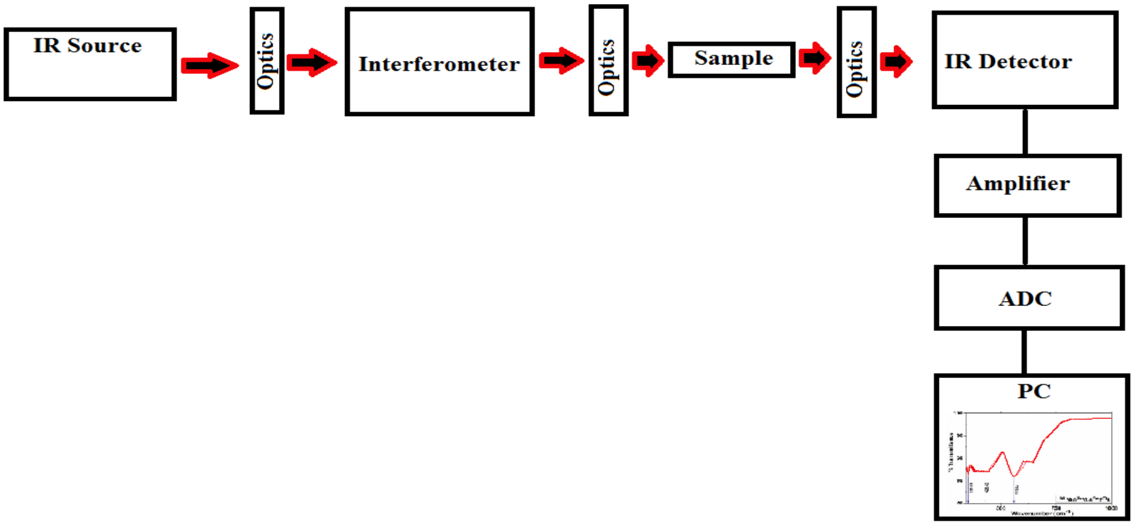

Figure 3.3.2 Schematic diagram of basic components of an FTIR system

In FTIR spectroscopy, basic idea is to use the interference of two beams in an interferometer and the fact that each wavelength produces its own and characteristic interference pattern if the optical path difference (OPD) of the two interfering beams is changed. The schematic diagram of basic components of an FTIR system is shown in figure 3.3.2. The radiation emitted by the source passes through an interferometer. The radiation from the interferometer is either transmitted or reflected by the sample to be analysed and is finally focused on the detector. The analogue detector signal is amplified, converted to digital, and the data are then transferred to a computer for Fourier transformation [25-27].

Material preparation for scanning electron microscope

In order to record FTIR spectra of rare earth doped manganese zinc ferrite nanoparticle samples, 100mg of KBr was weighed and pressed in to pallet with thickness of 1mm and radius 6mm. A background spectrum was recorded on this pallet. Further 2mg of each nano-samples was weighed and mixed with 100mg of KBr. These mixtures were pressed into pallets of similar dimensions and FTIR spectra were obtained for $Mn_{0.6}Zn_{0.4}Fe_{2-x}Nd_xO_4$ and $Mn_{0.65}Zn_{0.35}Fe_{2-x}Nd_xO_4$ nanosamples (x=0.04, 0.05, 0.06, 0.07, 0.08, 0.09 & 0.1) nanosamples.

3.4 Scanning electron microscopy (SEM)

Scanning electron microscope (SEM) is an instrument used for observing the surface of the specimen. When the speciman surface is exposed to fine beam of energetic electrons, secondary electrons are emitted from the surface of the speciman under observation. It provides two dimentional view of specimans topography. Figure 3.4.1 shows Carl Zeiss EVO18 scanning electron microscpe assembly.

The SEM instrument is made up of two main components, the electronic platform and the electron column. The electronic platform provides control buttons and switches for adjusting the parameters of the instrument such as filament current, accelerating voltage, focus, magnification, brightness and contrast in order to obtain best results [28].

Figure 3.4.2 shows a schematic layout of basic construction of scanning electron microscope which shows various essential parts of SEM. It consists of optical setup to generate probing electron, a material mounting stage for placing specimen, secondary electron detector, a display unit such as monitor and an equipped system to carryout various operations. The optical system comprises of electron gun, condenser lens and objective lens to produce electron probe. Scanning coil scans the electron probe and other components. The optical system and the space around the specimen are kept under high vacuum.

Figure 3.4.1 Carl Zeiss EVO18 scanning electron microscope, Instrumentation centre, Goa University

Electron gun: Electron gun produces an electron beam through thermionic emission. The tungsten filament (cathode) used for this purpose is very fine tungsten wire (1mm) which is heated up to 2800K. These thermo-electrons are gathered to form an electron beam flowing towards anode due to application of positive potential (1kV to 30kV). The hole made in the centre of anode allows the beam to travel towards the specimen trough condenser lens, scanning coils and objective lens as shown in figure 3.4.2.

Condenser lens: the main objective of placing condenser lens beneath electron gun is to adjust the diameter of electron beam. A fine beam of electron is required to extract the information from the specimen. This is achieved by placing a combination of condenser lens and objective lens below electron gun. Condenser lens is responsible for increasing or decreasing the diameter and in turn controls the strength of electron beam.

Objective lens: Objective lens is meant for focusing and determines the diameter of final beam striking the specimen. The quality of the final image obtained depends upon the performance of objective lens

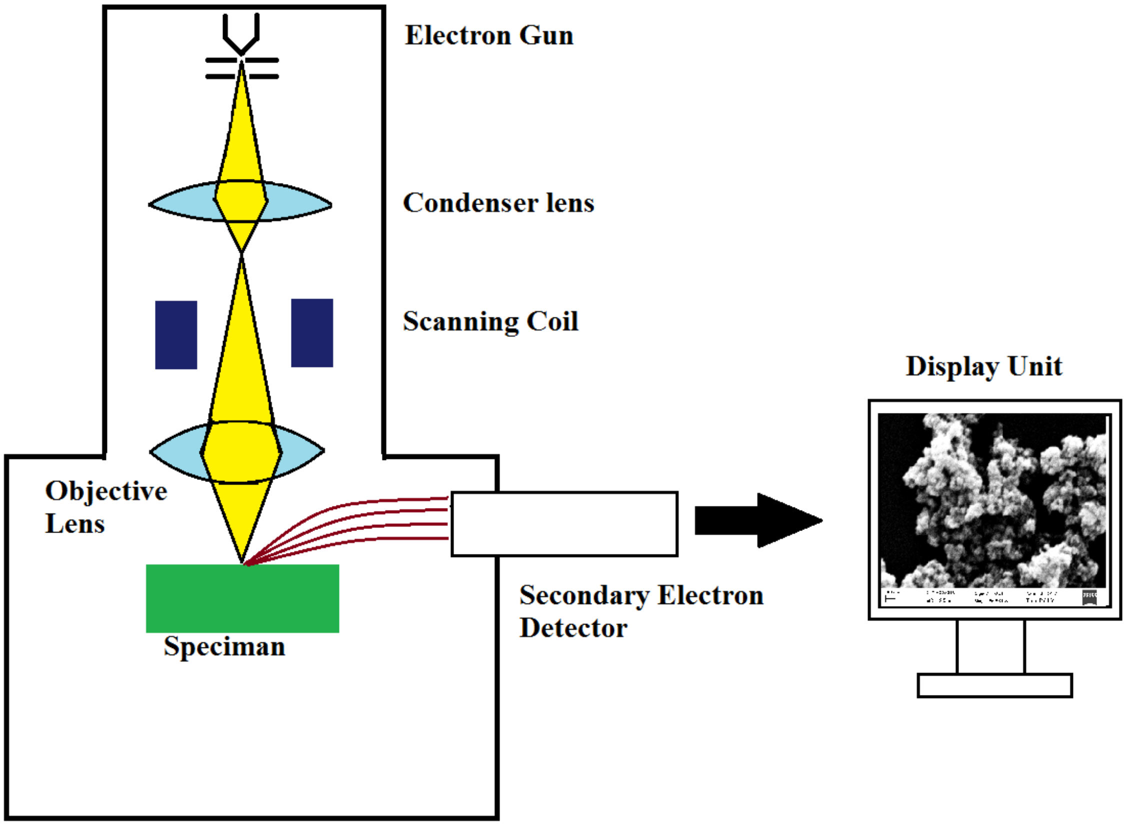

Figure 3.4.2 Basic construction of scanning electron microscope

Specimen stage: Since the specimen is observed at high magnification in an electron microscope, a specimen stage is required to provide a stable support and move smoothly. It can make movements along X, Y and Z direction. It also performs tilting and rotation action.

Secondary electron detector: Secondary electron detector is an assembly employed to detect secondary electron emitted by the specimen surface. It consists of a scintillator coated on the tip of the detector and a high voltage of about 10kV is applied to it. The secondary electrons emitted by the specimen are attracted by this voltage and hit the scintillator producing scintillations. These light signals are then transferred to photo multiplier tube through light guide and then converted into electrical signals to obtain the final image. In addition to secondary electron detector, the SEM assembly can also be equipped with other detectors such Auger electron detector, back scattered electron detector [29-32].

Material preparation for scanning electron microscope

Scanning electrons micrographs of $Mn_{0.6}Zn_{0.4}Fe_{2-x}Nd_xO_4$ and $Mn_{0.65}Zn_{0.35}Fe_{2-x}Nd_xO_4$ nanoparticles were obtained using Carl Zeiss EVO18 scanning electron microscope assembly. A weighed quantity of samples (5mg) was dispersed in 50ml of acetone and the solution was sonicated for one hour. A drop of this sonicated solution was taken on thin glass cover-slips. These cover slips were then exposed to gold sputtering process for 90 seconds for improving the surface conductivity as shown in figure 3.4.3. These gold sputtered cover-slips were mounted on specimen stage for obtaining SEM images.

Figure 3.4.3 Process of gold sputtering using sputtering unit, Instrumentation centre, Goa University

3.5 Transmission electron microscopy (TEM)

Transmission electron microscopy (TEM) is a very powerful technique developed to obtain magnification to a much higher level than the conventional optical microscopes for obtaining detail information of a specimen under observation. In TEM a beam of electrons is made to pass through a very thin specimen. The beam interacts with the specimen during its passage through it. When highly energetic electrons are accelerated up to high energy levels (few hundreds keV) and are incident on a specimen under observation, they scatter or backscatter elastically or in-elastically, or produce many interactions resulting in different signals such as X-rays, Auger electrons or light. Some of these signals form an essential part of transmission electron microscopy (TEM).

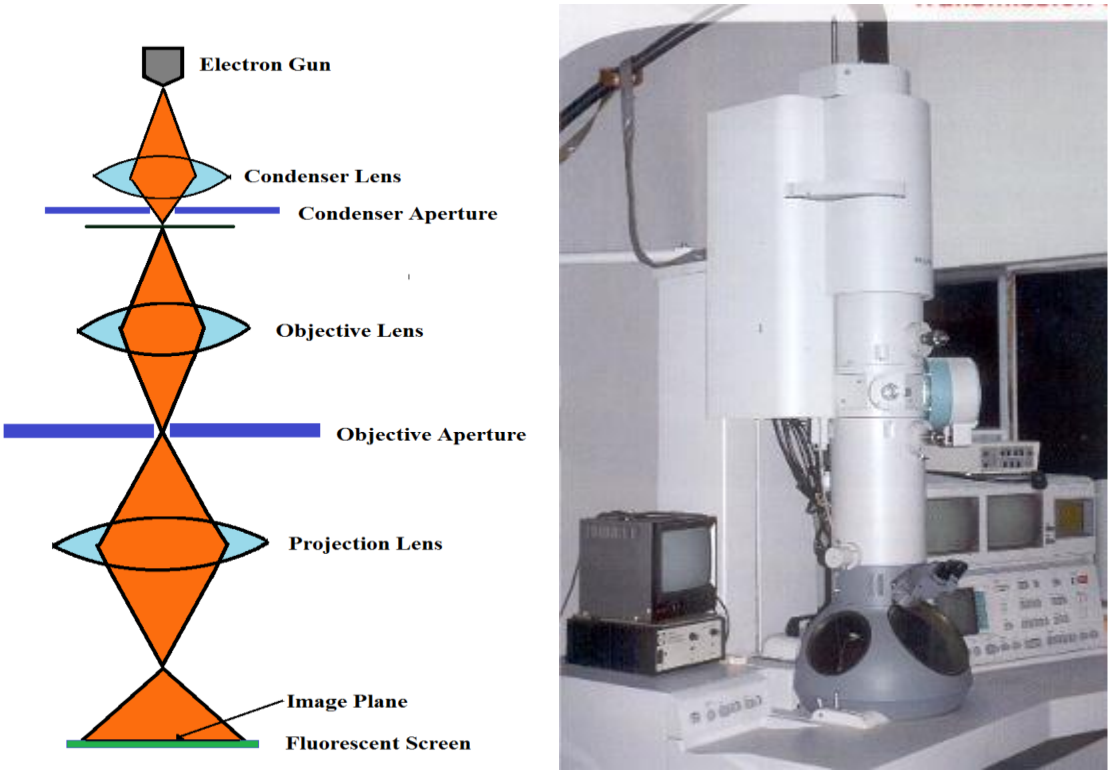

Figure 3.5.1 a) Basic construction of scanning electron microscope, b) PHILIPS CM200 transmission electron microscope at IIT Bombay, Mumbai-India

The final image is produced from the interaction of the electrons transmitted through the material. The magnified and focused image is obtained onto an imaging device, such as a fluorescent screen, layer of photographic film, or can detected by a sensor such as a CCD camera.

TEM forms a crucial material analysis method in a field of scientific research. It also used application in cancer research, virology, materials science as well as pollution, nanotechnology, and semiconductor research [33-38].

TEM works like a slide projector. A projector is designed to shine a beam of light which is allowed pass through the slide. The prints painted on the slide are transparent to only certain parts and the transmitted beam reproduces the patterns on the slide, forming an magnified image on the screen.

Functioning of TEM is very much similar to that of a projector except that the probing tool is a beam of electrons which passes through through the specimen (like the slide). In case of transmission electron microscope the electron beam transmission is highly dependent on the properties of material under investigation such as the density, composition of the material etc. For instance it will be easier for a beam of electrons to pass through a porous material while dense material will present less transparency to the electron beam. This particular property enables a researcher to examine a specimen with a non-uniform density using this technique. The transmitted part is projected onto a phosphor screen for the user to see.

Transmission electron microscope consists of following parts which play a major role in image formation.

Electron gun: It is usually a V-shaped filament made of LaB_6 or W (tungsten) that is wreathed with Wehnelt electrode (Wehnelt Cap). It is kept at negative potential so as to emit electrons from a small area of the filament like a point source that emits monochromatic electrons. A very high positive electrical potential is applied to the anode to attract a stream of electrons emitted by the fillament. The electrons are accelerated by the positive potential down the column, and because of the negative potential of cap, all electrons are repelled toward the optic axis. A gathering of electrons takes place in the region that lies between the Filament tip and Cap, and is termed as a space charge. The electrons that are at the bottom of the space charge (nearest to the anode) can leave the gun region through the small (<1 mm) hole in the Wehnelt Cap and then move down the column to be later used in imaging.

Condenser lens: Condenser lens is used to focus the stream of the electron from the electron gun to a small, thin, coherent beam. The first condenser lens determines the "spot size"; the general size range of the final spot that strikes the sample.

Condenser aperture: It is a thin metal disk or strip with a small circular hole at the centre. It is used to control the electron beams. It also acts like a filter for unwanted scattered electrons before image formation

Objective lens: It focuses the transmitted electron from the sample into an image.

Objective aperture: It is meant to enhance the contrast of the image by blocking out high angle diffracted electrons

Projection lens: The projection lens is used to expand the beam onto the phosphor screen.

Screen: Imaging systems in a transmission electron microscope consists of a thin phosphor screen (10-100 micro meters), normally zinc sulphide, for direct observation by the operator.

Material preparation for transmission electron microscope

Approximately 2-3 mg of ultrafine $Mn_{0.6}Zn_{0.4}Fe_{2-x}Nd_xO_4$ and $Mn_{0.65}Zn_{0.35}Fe_{2-x}Nd_xO_4$ nanoparticle samples were dispersed methanol and ultra-sonicated for one hour. Samples were dispersed on a copper grid after ultra-sonication for obtaining TEM images.

3.6 Vibrating sample magnetometer (VSM)

The operation of vibrating sample magnetometer (VSM) operation is primarily based on on Faraday's Law of Induction, according to which a varying magnetic field will give rise to an electric field which can be measured and the information about the changing magnetic field can be obtained.

A VSM is used to measure the magnetic behavior of magnetic materials. For recording magnetic behavior, sample to be studied is placed in constant magnetic field which magnetizes the sample by aligning the magnetic domains, or the individual magnetic spins, with the field. The extent of magnetization is directly proportional to the magnitude of applied constant field. The magnetic stray field created by magnetic dipole moment is sensed by moving the sample up and down. This motion changes the magnetic stray field as a function of time. This change can be sensed by a set of pick-up coils.

Vibrating Sample Magnetometer (VSM) systems are used to investigate the magnetic properties of materials as a function of magnetic field, temperature, and time. They are ideally suited for research and development, production testing, quality and process control. The alternating magnetic field will generate an electric field in the pick-up coils in accordance with the Faraday's Laws of induction. And the current produced will be proportional to the magnetization of the sample. Greater the magnetization, greater is the induced current [39-41].

The Quantum Design Versa Lab’s 3Tesla Vibrating Sample Magnetometer (VSM) is a fast and sensitive DC magnetometer.

Figure 3.6.1 Quantum Design’s Versa Lab 3 Tesla Vibrating sample magnetometer (VSM), Department of Chemistry, Goa University

The basic measurement involves oscillation of sample in the vicinity of pickup coils and synchronous detection of induced voltage. With a compact gradiometer pickup coil configuration, comparatively large amplitudes of oscillation (1.3 mm peak) and 40 Hz frequency enables the system to resolve magnetization changes of the order 10^{-6} emu at a data acquisition rate of 1 Hz.

The VSM consists primarily of a VSM linear motor transport (head) for vibrating the sample, a coil set pluck for detection, electronics for driving the linear motor transport and detecting the response from the pickup coils, and a copy of the MultiVu software application for automation and control.

The MultiVu software is equipped with advanced features incorporated in data acquisition, temperature and magnetic field control and is capable of sensing low levels of emu generated from extremely small quantity of material. The ambient temperature of the sample environment in instrumental set up could be lowered up to a minimum of 50K and can be raised up to 400 K. It is a cryogen free instrument uses cryo-cooler to achieve cryogenic temperatures.

The magnetic field in Versa Lab is generated by a superconducting niobium-titanium (NbTi) solenoid mounted in the cryostat vacuum space. The standard magnet generate magnetic field of 3T at 20A of current. Versa Lab magnet is cooled by solid conduction. Copper straps connect the magnet to the cryocooler second stage for cooling. The magnitude of VSM precision in a magnetic measurement depends on the stability achieved in created magnetic fields. An integrated environmental magnet shield incorporated VSM ensured magnetic noise isolation [42].

Material preparation for Vibrating sample magnetometer (VSM)

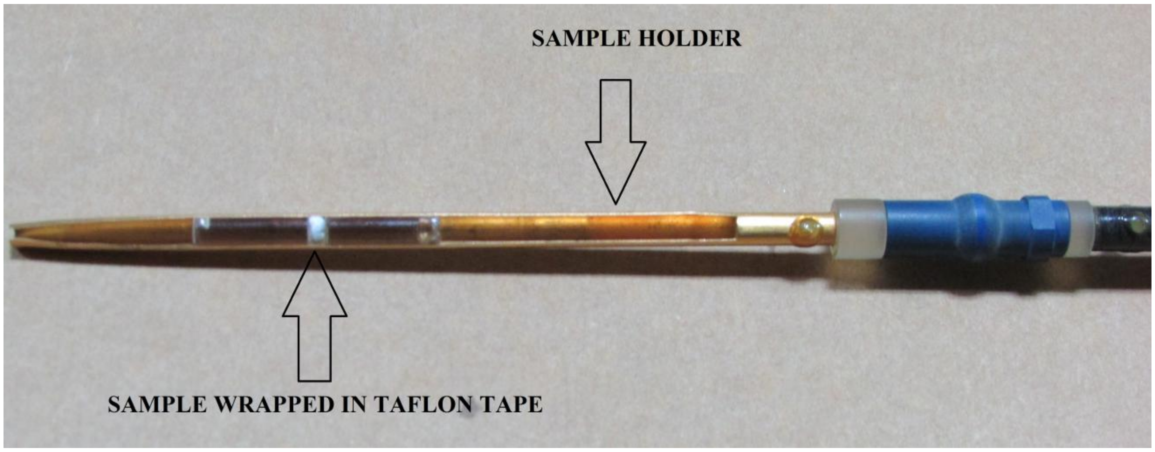

Figure 3.6.2 VSM sample holder and the sample wrapped in Teflon

In order to investigate magnetic properties of as prepared as well as γ irradiated rare earth doped manganese zinc ferrite nano-powders with composition $Mn_{0.6}Zn_{0.4}Fe_{2-x}Nd_xO_4$ and $Mn_{0.65}Zn_{0.35}Fe_{2-x}Nd_xO_4$ nano-samples (x=0.04, 0.05, 0.06, 0.07, 0.08, 0.09 & 0.1) , 5mg of sample was wrapped in Teflon tape and was mounted on sample holder as shown in figure 3.6.2. Magnetization of all samples as a function of applied magnetic field up to 3T was recorded for as prepared as well as gamma irradiated samples at room temperature. Variation in magnetization as a function of temperature was also recorded at constant field of 750Oe over the temperature range of 50K to 395K.

3.7 Mössbauer spectroscopy

Mössbauer spectroscopy is a unique technique that can provide information in several areas of science that involves the like of Physics, Chemistry, Biology and Metallurgy. It is competent of availing very accurate information about the structural, chemical, magnetic and time-dependent behavior of a material. The major credit of success of this technique can be given to the discovery of recoilless emission and resonant absorption of gamma ray by nucleus which is now referred to as the 'Mössbauer Effect', named after its discoverer Rudolph Mössbauer, who first observed the effect in 1957 and received the Nobel Prize in Physics in 1961 for his work [43].

Nuclei in atoms undergo transitions between various energy levels, along with emission or absorption of a gamma ray. These energy levels are greatly infuenced by their surrounding electronic and magnetic environment, which can alter or split these energy levels. These deviations in the energy levels can disclose information about the local environment of an atom within a system under investigation and can be observed using resonance-fluorescence. There are two major difficulties in acquiring this information: one is that the 'hyperfine' interactions between the nucleus and its environment are extremely negligible, and secondly the recoil of the nucleus as the gamma-ray is emitted or absorbed avoids resonance.

In a given material under investigation if the absorbing nuclei and the emiting nuclei are in similar environment that are cubic in symmetry then the changeover energies are also similar and this condition produces a single line absorption spectrum as shown in Figure 3.7.1.

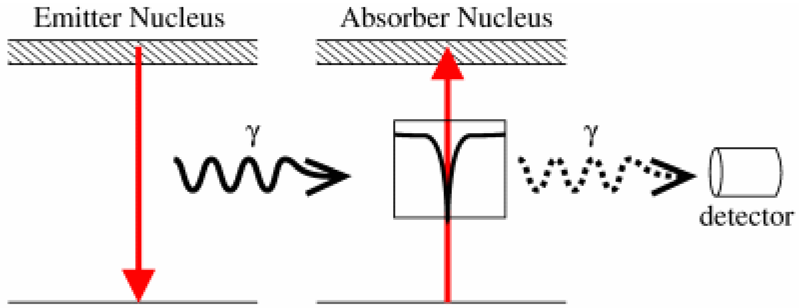

Figure 3.7.1 Simple Mössbauer spectrum from identical source and absorber

One can probe the minute hyperfine interactions between an atom's nucleus and its surrounding as it is possible to obtain resonant emission and absorption. The resolution now that recoil and doppler broadening have been eliminated is the natural linewidth of the excited nuclear state. This effect is dependent on average lifetime of an excited state of the nucleus after which it undergoes decay and result in emission of gamma ray. ^{57}Fe is the frequently used Mössbauer isotope and the linewidth is of the order 10^{-9}eV. For a gamma-ray energy of 14.4keV Mössbauer gives a resolution of 1 in 10^{12}, This level of high accuracy is very important to sense the hyperfine interactions occurring inside the nucleus.

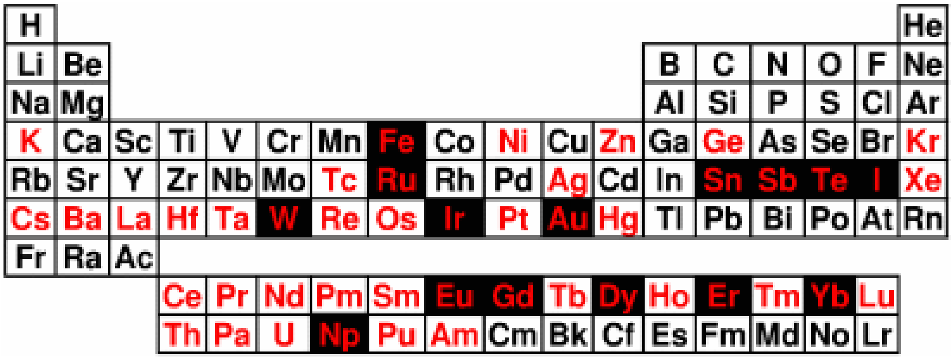

Figure 3.7.2 Elements of the periodic table which have known Mössbauer isotopes (shown in red font).

As resonance occurs only when the transition energy of the emitting and absorbing nucleus match exactly, the effect is isotope specific. The relative number of recoil-free events (and hence the strength of the signal) is strongly dependent upon the gamma-ray energy and so the Mössbauer effect is only detected in isotopes with very low lying excited states. The resolution produced in this technique is decided by the lifetime of the excited state. These factors restrict the count of isotopes that can be utilized for Mössbauer spectroscopy. The ^{57}Fe is the best option available which has very low energy and log lived excited state that satisfies the requirements. The isotopes in which the Mössbauer effect has been detected is shown in Figure 3. 7. 2.

As the environment of the nuclei in a system to be studied will almost certainly be different to the source, the hyperfine interactions between the nucleus and the environment will change the energy of the nuclear transition. To detect this it is necessary to change the energy of probing gamma-rays. The energy changes caused by the hyperfine interactions are very small, of the order of billionths of an electron volt. Such miniscule variations of the original gamma-ray are quite easy to achieve by the use of the Doppler effect. This is gained frequently via oscillation of a source which is radioactive in nature and obtaining the in quantized velocity steps. .

There are three ways in which energy levels of absorbing nuclei can be modified; (i) the Isomer Shift (IS), (ii) Quadrupole Splitting (QS) and (iii) Magnetic Hyperfine Splitting.

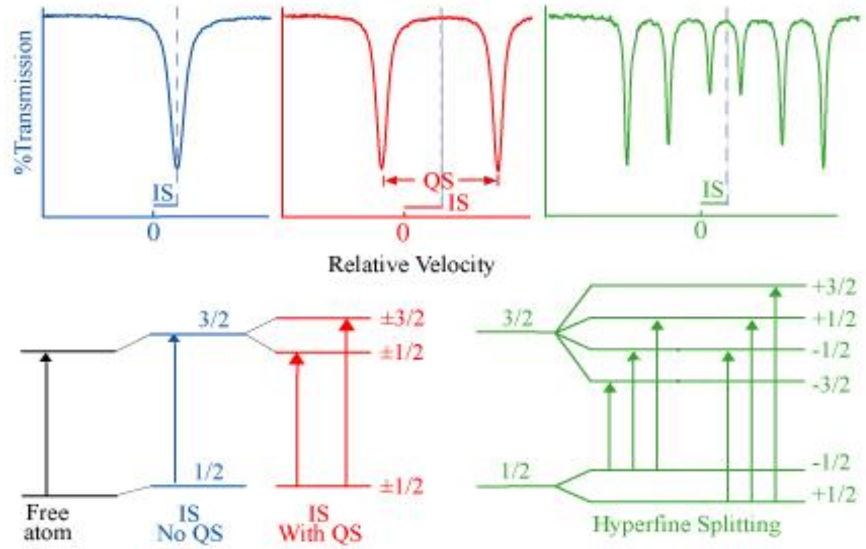

Figure 3.7.3 Isomer shift (a), Quadrupole splitting (b) and Hyperfine splitting(c)

Isomer Shift

The isomer shift is generated due the finite volume of electron charge density due to s-electrons and the nucleus. Such interaction produces a monopole interaction, changing the energy levels of nucleus. Variation in the s-electron environment of the source and the same of an absorber results in a shift in the resonance energy as shown in Figure 3.7.3(a). As a result the entire spectrum positively or negatively depending upon the s-electron density, and sets the centroid of the spectrum.

Quadrupole Splitting

Nuclei in states with an angular momentum quantum number I>1/2 have a non-spherical charge distribution. This produces a nuclear quadrupole moment. In the presence of an asymmetrical electric field (produced by an asymmetric electronic charge distribution or ligand arrangement) this splits the nuclear energy levels as shown in Figure 3.7.3. The magnitude of quadrrupole splitting, Delta, is dependent on nuclear quadrupole moment, Q, and the principle component of the EFG, V_{zz}, by the relation

$$\Delta = \frac{eQV_{ZZ}}{2} \qquad 3.7.1$$

Hyperfine Magnetic Splitting

Nuclear spin moment experiences a dipolar interaction In the presence of a magnetic field which is known as Zeeman splitting. There are numerous sources of magnetic fields that can be interacting with the nucleus. The total effective magnetic field at the nucleus, B_{eff} is given by:

$$B_{eff} = (B_{contact} + B_{orbital} + B_{dipolar}) + B_{applied} \qquad 3.7.2$$

The initial three terms are due to the partially filled electron shells of the atom. The spin on those electrons polarising the spin density at the nucleus give rise to $B_{contact}$, $B_{orbital}$ is generated due to the orbital moment in the electrons, and the dipolar field due to the spin of those electrons give rise to $B_{dipolar}$ is [44-49].

Experimental setup

The basic elements of a Mössbauer spectrometer are a source, sample, detector, and a drive to move the source or absorber.

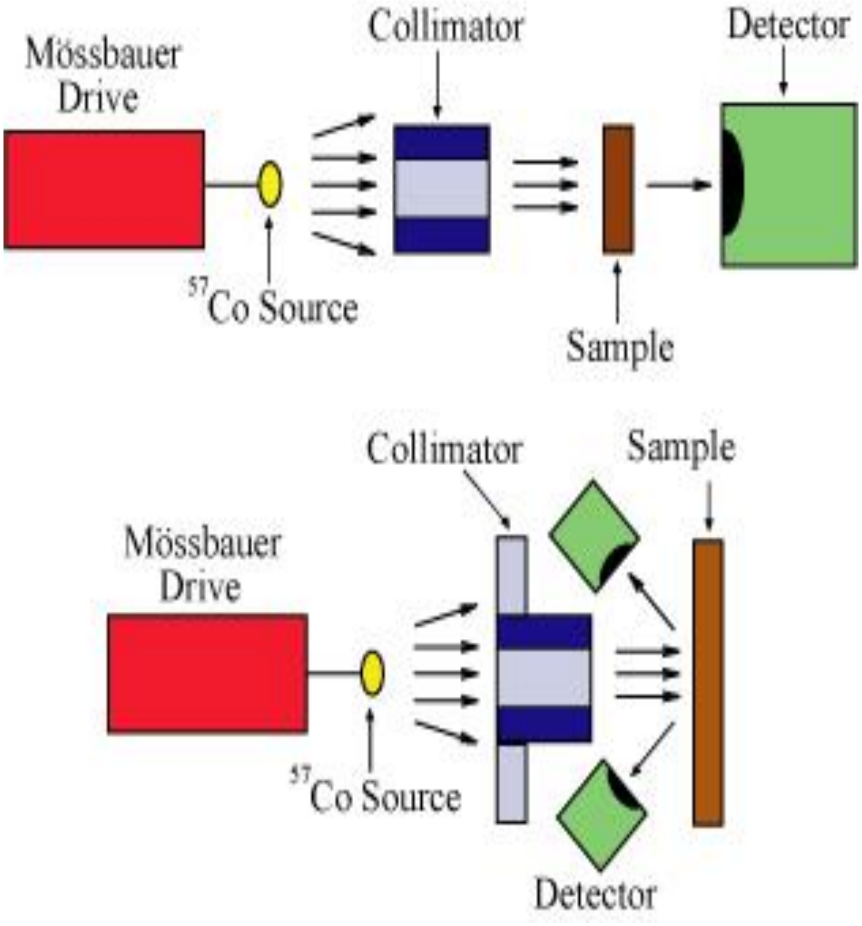

Figure 3.7.4 Geometry of the experimental set up with transmission and backscatter modes.

Under normal scenario this is achieved by moving the source to and fro in the direction of the sample, by changing the velocity linearly as a function of time. For simplicity, "mm/sec" is the conventional "energy" unit in Mössbauer spectroscopy. One can also keep the source stationary and move the sample in an oscillatory manner to and fro as is done with synchrotron Mössbauer. The postion of the detector with reference to source and the sample defines the geometrical confugration of the experiment; most commonly, either transmission or backscatter modes as shown in figure 3.7.4. The decay of ^{57}Co to ^{57}Fe, emission of γ-ray and all probable interactions with the absorber are shown in figure 3.7.5.

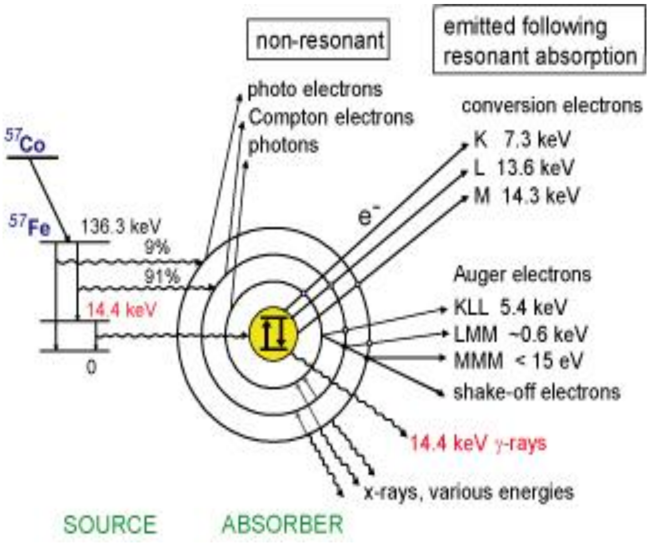

Figure 3.7.5 The decay of ^{57}Co to ^{57}Fe, emission of γ-ray and all probable interactions with the absorber

For the present study Mössbauer spectra have been obtained using a spectrometer operated in constant acceleration mode in transmission geometry. The source employed is ^{57}Co in Rh matrix of strength ≈50mCi. The calibration of the velocity scale is done using iron metal foil. The outer line width of calibration spectra was 0.29 mm/s. Actual photograph of the Mössbauer spectrometer is shown in Figures 3.7.6.

Figure 3.7.6 Photograph of the room temperature Mössbauer spectrometer at SSPD, BARC

Sample preparation for Mössbauer measurements

Nearly 35 mg sample in powder form has been used for the Mössbauer spectroscopy measurements and same has been spread over 15 mm diameter capsule (sample holder, male-female) of Perspex material. Thickness of the bottom layer of both male and female Perspex capsules is~ 0.5 mm.

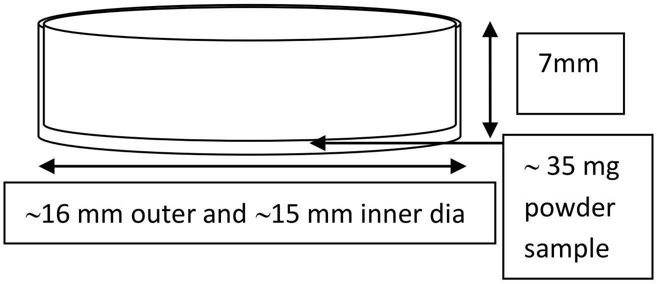

Figure 3.7.7 Sample preparation for Mössbauer measurements.

3.8 DC Resistivity

For sensor applications it is necessary that the material should have semiconductor like resistivity profile with high resistivity variation over large range of temperature [50]. The electrical resistivity of ferrites is very sensitive to their composition and microstructure, and to their preparative conditions [51]. The conduction mechanism is different from that in conventional semiconductors. In ferrites conductivity is greatly affected by mobility of charge carriers which in turn depends upon the temperature. In the case of ferrite material electrons are localized to magnetic cations that are caged close packed oxygen anions. Hence localized electron model can be applied to this system. These differences between conventional semiconductors and ferrite materials also gave rise to electron hopping model in order to understand the conduction mechanism in these materials [52,53]
Resistivity in ferrites varies over a wide range of $10^{-3}\Omega$cm to $10^{10}\Omega$cm [54]. This variation is mainly dependent on the distribution of different cations on tetrahedral (A) site and octahedral (B) site and also on the hopping mechanism. Lower values of resistivity depict the dominance of divalent cations at octahedral site and carrier hoping between two sites where as the higher values of resitivity can be attributed to greater occupancy of trivalent cations at octahedral site.

According to the hopping model, charge carriers are not free to move through the crystal lattice but instead they jump from one cationic site to another. Due to the presence of lattice vibrations the probability of electron transfer is high as the ions come close enough to facilitate electron transfer. Thus in this case the conduction is triggered due to lattice vibrations. The conduction mechanism shows a temperature dependence of carrier mobility and is characterized by activation energy.

The conduction mechanism due to carrier hopping in the case of ferrite can be shown as follows [55]

$$Fe^{+2} + Fe^{+3} \Leftrightarrow Fe^{+3} + Fe^{+2} + \Delta E$$

$$Fe^{+2} + M^{+3} \Leftrightarrow M^{+2} + Fe^{+3} + \Delta E$$

Where ΔE is the activation energy required for the charge carrier to hop from M^{2+} to Fe^{3+} and vice versa. The valance states of two cations get interchanged during this hopping process and these electrons conduct under the action of applied electric field [56].

Thus the transport of charge carriers is achieved by hopping process through interaction with phonons. On the basis of this the temperature dependence of resistivity of ferrites is given by the relation [57].

$$\rho = \rho_o e^{\left(\frac{-\Delta E}{kT}\right)} \qquad 3.8.1a$$

Where ρ_o = Temperature dependent constant

ΔE = activation energy

K = Boltzmann constant

T = Temperature in K

Material preparation for DC Resistivity of ferrite

Nanopowders of $Mn_{0.6}Zn_{0.4}Fe_{2-x}Nd_xO_4$ and $Mn_{0.65}Zn_{0.35}Fe_{2-x}Nd_xO_4$ with x=0.04, 0.05, 0.06, 0.07, 0.08, 0.09 and 0.1 were pressed into pallets of thickness ranging between 3mm to 2.5mm and the diameter of 12mm. The pallets were silver painted on both sides for establishing good ohmic contacts with the electrodes. Variation of current was recorded for these samples over the range of 300K to 773K using two probe resistivity setup shown in figure 3.8.1 and Figure 3.8.2 shows a block diagram of two probe resistivity setup. The resistivity ‘ρ’ for the samples at different temperature was calculated using following equation

$$\rho = \left(\frac{\mathrm{VA}}{\mathrm{It}}\right) \qquad 3.8.1b$$

Where V = applied voltage across the sample

A = area of the sample pallet

I = Current

t = thickness of the pallet

Figure 3.8.1 Two probe D.C. Resistivity setup with data acquisition system, Department of Physics, Goa University

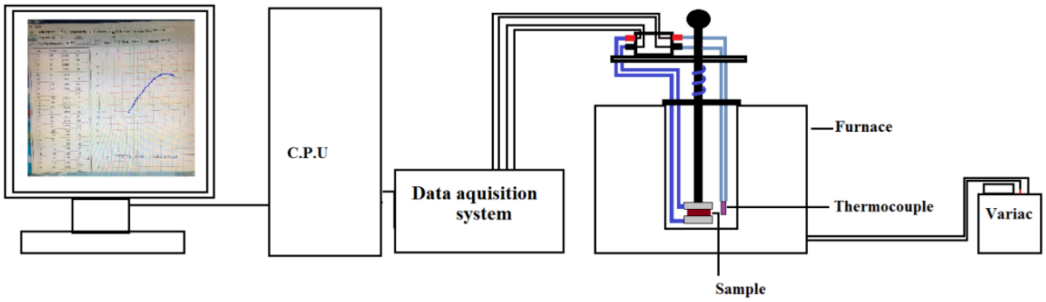

Figure 3.8.2 Block diagram of two probe D.C. Resistivity setup with data acquisition system

3.9 Dielectric Measurements

Dielectrics are the materials with insulating nature and exhibit an important property of electrical polarization, by virtue of which they modify the dielectric variation of the vacuum. A dielectric material gets polarized when it is introduced into an electric. Figure 3.9.1a shows a dielectric material in the absence of an electric field while figure 3.9.1b shows a dielectric material polarized in the presence of electric field. This phenomenon is known as dielectric polaraztaion. Mossotti [58, 59] and Clausius [60] successfully correlated microscopic structure of the material with specific inductive capacity, a macroscopic characteristic of the insulator introduced by Faraday [61] which is now popularly termed as dielectric constant. Following Faraday in considering the dielectrics to be composed of conducting spheres in a non-conducting medium, Clausius and Mossotti succeeded in deriving a relation between the real part of the dielectric constant ε_r and the volume fraction occupied by the conducting particles in the dielectric.

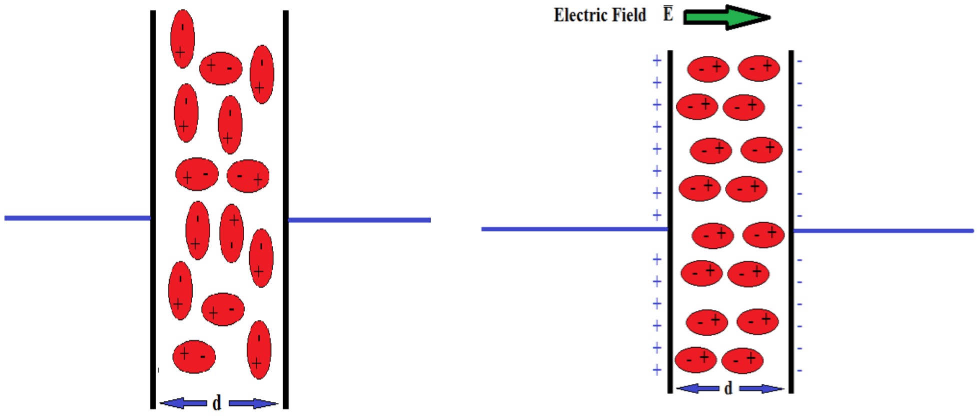

(a) (b)

Figure 3.9.1 a) Dielectric material in the absence of electric field, b) Dielectric in the presence of electric field.

It was first brought into notice by Michael Faraday that if a capacitor of value C_0 under vacuum is filled with a dielectric material, its charge storage capacity (capacitance) increases to a value of C. The ratio χ' of the increase of capacitance is given by

$$\chi = \frac{C - C_o}{C_o} = \frac{\Delta C}{C_o} \qquad 3.9.1a$$

χ' is called the electrical susceptibility of the dielectric. The most often used terminology is the dielectric permittivity or dielectric constant instead of susceptibility, which is defined as the ratio of the capacitance C of the capacitor filled with a dielectric to the value C_o of the same capacitor under vacuum.

$$\varepsilon_r = \frac{C}{C_o} \qquad 3.9.1b$$

Hence the dielectric constant or permittivity of a material is a dimensionless quantity which is a measure of the extent to which the electric charge distribution in the material can be distorted or polarized by the application of an electric field.

Ferrites are known as excellent dielectric materials at lower frequencies. In the case of highly crystalline materials the dielectric constant is strongly dependent on operational frequencies. Ferrites with relatively high dielectric constants can be utilized effectively in designing efficient microwave devices such as isolators, circulators, etc. The dielectric behavior of ferrites which is highly dependent on method of preparation, chemical composition and substitution, grain structure or size, sintering temperature and doping element is very essential and the most important property.

Dielectric loss

The permittivity of a dielectric material has real and imaginary mathematical representations denoted by ε_r and ε” respectively. The imaginary part provides the information about energy loss from an AC signal during its passage through the dielectric material. The real part of permittivity is also termed as the dielectric constant and relative permittivity. The permittivity of a dielectric material specifies the relationship between an transmission speed of AC signal and the capacitance of dielectric material. The term “relative” is used in front of permittivity, implies that the value is presented by taking dielectric properties of a vacuum as reference mark. The imaginary part of the dielectric permittivity is a measure extent of field that is lost as heat dissipated during the process of polarization of a material in an applied alternating electric field and hence is termed as dielectric loss and is given by following equation

$$\tan\delta = \frac{\varepsilon''}{\varepsilon'} \qquad 3.9.1c$$

The distinguishing alignment of the dipoles in an electric field results in alteration in frequency of dielectric constant and dielectric loss over a wide range of frequencies. The relative permittivity of material is associated with various physical phenomena that give rise to as well as enhance the polarization of the dielectric material. In the low frequency range the imaginary part of permittivity is strongly suppressed under the influence of ion conductivity. The alterations produced in permittivity are due to several factors such as dipolar relaxation. The absorption peaks obtained in the infrared region and above, are mainly due to atomic and electronic polarizations. In the applications such as microwave devices and radio frequency based instrumentation the dielectric properties of the material highly altered and affected by the positions of ions and the alteration caused by the lattice vibrations. In a crystalline solid, two types of losses can occur at high frequencies and are termed as intrinsic loss and extrinsic loss. The factors such as ionic masses, electric charge/valence state of the ions, spring constant of the bond, lattice imperfections etc. determine the dielectric dispersion in solids. The estimation of dielectric losses close to the lattice vibration frequencies is generally done in terms of the anharmonicity of lattice vibrations. Intrinsic dielectric losses in solid dielectrics generally caused due to low frequency phonons. The intrinsic loss mechanism is highly dependent on the microwave field and phonon interaction caused to the relaxation of the phonon distribution function. The intrinsic limits of the high frequency dielectric losses in crystalline solids are determined by the lattice phonon modes. The interaction between the charged defects and the microwave fields give rise to extrinsic losses.

Material preparation for dielectric property investigations

Figure 3.9.2 Wayne Kerr precision component analyzer 6440B, Department of Physics, Goa University

Nanopowders of $Mn_{0.6}Zn_{0.4}Fe_{2-x}Nd_xO_4$ and $Mn_{0.65}Zn_{0.35}Fe_{2-x}Nd_xO_4$ with x=0.04, 0.05, 0.06, 0.07, 0.08, 0.09 and 0.1 were pressed into pallets of thickness ranging between 3mm to 2.5mm and the diameter of 12mm. The pallets were silver painted on both sides for establishing good ohmic contacts with the electrodes. Capacitance and dielectric loss were measured as a function of frequency over the range of 20Hz to 3MHz. Temperature dependence of capacitance and the dielectric loss was recorded over the temperature range of 300K to 773K at ten different frequencies (20Hz, 100Hz, 500Hz, 1kHz, 10kHz, 100kHz, 500kHz, 1MHz, 2MHz and 3MHz) for these samples using Wayne Kerr precision component analyzer 6440B shown in figure 3.9.2. Dielectric constant was determined using following equation

$$\varepsilon_r = \frac{Cd}{\varepsilon_o A} \qquad 3.9.1.d$$

Where C = Capacitance

d = Thickness of the pallet

ε_o = Absolute permittivity of free space (8.85x10-12 $C^2m^{-2}N^{-1}$)

A = Area of the pallet.

3.10 Permeability

The general definition of permeability in electromagnetic theory goes as the precise quantification of the ability of a material to facilitate the formation of a magnetic field within the material itself. It can be also defined as the degree of magnetization that a specimen acquires in response to an applied magnetic field. Magnetic permeability is typically represented by the (italicized) Greek letter μ. In SI units, permeability is measured Hm^{-1}, or equivalently in $N.A^{-2}$. The permeability constant (μ_0), also known as the magnetic constant or the permeability of free space, is a measure o the amount of resistance encountered when forming a magnetic field in free space or vacuum. The magnetic constant has the exact value ($\mu_0 = 4\pi \times 10^{-7}$ $H{\cdot}m^{-1} \approx 1.27{\times}10^{-6}$ $H{\cdot}m^{-1}$ or $N{\cdot}A^{-2}$).

Relation between self inductance and permeability

The self inductance of a material is defined as property of the material that opposes the change in current flowing through the material. In an electrical circuit, when the emf is induced in the same circuit in which the current is changing this effect is called Self-induction, (L) but it is also called as back-emf because of the polarity which is in the opposite direction to the applied voltage. The basic unit for inductance is Henry, (H) named after Joseph Henry, but it can be also expressed as Webers per Ampere (1 H = 1 Wb/A).

Mathematically the induced emf due to self inductance (L) in a coil is give by following equation

$$V_{\mathrm{Induced}} = -L\left(\frac{di}{dt}\right) \qquad 3.\ 10.1a$$

Hence the inductance of the coil can be given by

$$L = -\frac{V}{\left(\frac{di}{dt}\right)} \qquad 3.10.1b$$

Where V_{induced} is the induced voltage and (di/dt) is the rate at which the current in the coil changes. Magnetic flux associated with a coil is given by

$$\Phi = B.A \qquad 3.10.1c$$

Where Φ is the magnetic flux linked with the coil, B is the flux density and A is the area.

If the inner core of a long solenoid coil with N number of turns per metre length is hollow, “air cored”, then we have

$$B = \mu_o H = \mu_o \frac{NI}{l} \qquad 3.10.1d$$

Therefore the self inductance can be now defined as

$$L = \frac{N\Phi}{I} = \frac{N^2 \mu_o A}{l} \qquad 3.10.1e$$

Where I is the current through the coil and *l* is the length of the coil.

If the coil is wound on magnetic core with relative permeability μ_r then we get

$$L = \frac{N^2 \mu_o \mu_r A}{l} \qquad 3.10.1f$$

Therefore

$$\mu_r = \frac{Ll}{N^2 \mu_o A} \qquad 3.10.1g$$

Ferrite core

If the inner core is made of some ferrimagnetic material such as manganese zinc ferrite which is known for high permeability then the inductance of the coil would greatly increase because for the same amount of current flow the magnetic flux generated would be much stronger. This is because the material concentrates the lines of force more strongly through the softer ferrimagnetic core material [62].

Material preparation for relative permeability measurement of samples

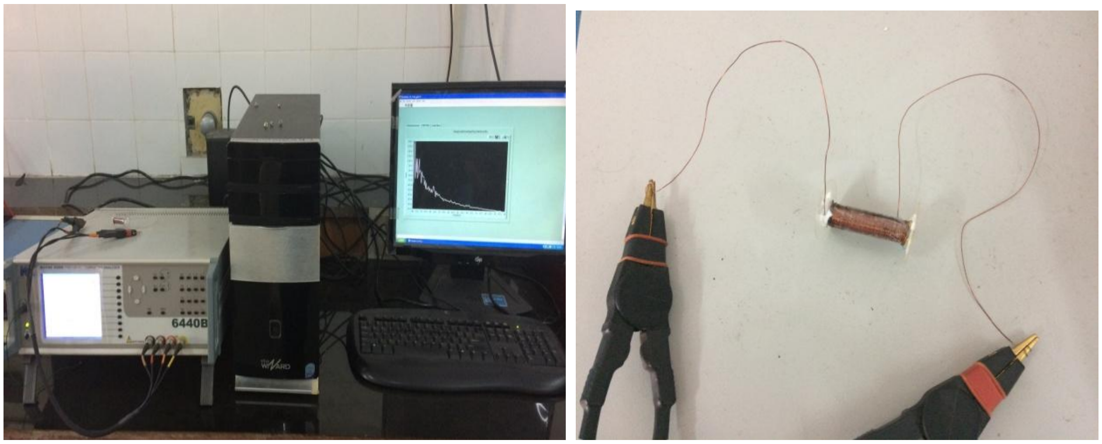

Figure 3.10.1 a) Wayne Kerr precision component analyzer 6440B, Department of Physics, Goa University

b) Wire wound rare earth doped ferrite core for permeability measurement

A copper wire of radius 0.05cm was wound to get 100 turns over a hollow, thin cylinder of plastic with thickness 0.085cm, length 3.61cm and inner radius 0.32 cm. This cylinder was filled completely with 2.25g of samples with composition $Mn_{0.6}Zn_{0.4}Fe_{2-x}Nd_xO_4$ and $Mn_{0.65}Zn_{0.35}Fe_{2-x}Nd_xO_4$ (x = 0.04, 0.05, 0.06, 0.07, 0.08, 0.09 and 0.1) in a compact manner by applying a pressure of 50 kN/m^2 to obtain a solenoid wound on rare earth doped manganese zinc ferrite core. The cylinder was sealed from both the ends and the solenoid was subjected to permeability measurement as shown in figure 3.10.1.

Reference

1. W.C. Roentgen, Ann. Phys. Chem., 64(1898)1–11.
2. G. Von Hevesey, Chemical Analysis by X-rays and its Application, McGraw-Hill, New York, 1932.
3. R. Jenkins, An Introduction to X-ray Spectrometry, Wiley/Heyden, London, Chapter 4, 1974.

4. L.S. Birks, ‘History of X-ray Spectrochemical Analysis’, American Chemical Society Centennial Volume, ACS, Washington DC, 1976.
5. H.G.J. Moseley, Philosophical Magazine, 26, (1912)1024–1034.
6. Brady, B. John, Boardman, J. Shelby, Journal of Geoscience. Education, v. 43 (5) (1995), 471-476.
7. M. Birkholz, C. Genzel, T. Jung, Journal of Applied Physics, **96** (2004) 7202.
8. R. Jenkins, D. J. Haas, F. R. Paolini, Norelco Reporter, 18, (1971)1–16.
9. C.L. Mallory, R.L. Snyder, Advances in X-Ray Analysis, 22, (1979)121–132.
10. B. E. Warren, X-Ray Diffraction, Addison-Wesley, Reading, MA, 1969.
11. B. D. Cullity, Elements of X-Ray Diffraction, Addison-Wesley, Reading, MA, 1967.
12. P. P. Naik, R. B. Tangsali, B. Sonaye, S. Sugur, Journal of Magnetism and Magnetic Materials, 385(2015)377–385.
13. V.D. Mote, Y. Purshotham, B. N. Dole, Journal of Theoretical and Applied Physics, 6-6(2012) 2251–7235.
14. Xiaolin Hong Deng, Qing Li, Xun Peng, Jinping Wang, Chen, Yadong Li, Angewandte Chemie, 117, (2005)2842–2845.
15. C. Venkataraju, G. Sathishkumar, K. Sivakumar, Journal of Magnetism and Magnetic Materials, 322 (2010)230–233.
16. A. R. Bueno, Maria L. Gregori, Maria C. S. Nobrega, Material Chemistry and Physics, 105 (2007)229–233.
17. Ratnamala Chatterjee, AnjaliVerma, Journal of Magnetism and Magnetic Materials,.306(2006) 313–320.

18. B. Stuart, Infrared Spectroscopy: Fundamentals and Applications (Chichester: Wiley) 2004
19. H. Gunzler, H. U. Gremlich, IR Spectroscopy: An Introduction (Weinheim: Wiley) 2002
20. R. J. Bell Introductory Fourier Transform Spectroscopy (New York: Academic) 1972
21. www.bruker.com
22. M. Vollmer, K-P Möllmann, The Physics Teacher, 46 (2008) 114–7
23. J. Kauppinen, J Partanen, Fourier Transforms in Spectroscopy (Berlin: Wiley) 2001
24. W. S. Lau, Infrared Characterization for Microelectronics (Singapore: World Scientific) 1999
25. E. D. Palik, Handbook of Optical Constants of Solids (Boston, MA: Academic) 1985
26. H M Heise, J Fritzsche, H Tkatsch, F Waag, K Karch, K Henze, S Delbeck, J Budde, European Journal of Physics, 34 S139–592013
27. M Vollmer, K-P Möllmann, Infrared Thermal Imaging: Fundamentals, Research and Applications (Weinheim: Wiley) 2010
28. R. F. Egerton, Physical Principles of Electron Microscopy: An Introduction to TEM, SEM, and AEM, Springer: New York, 1986.
29. J. Goldstein, D. Newbury, D. Joy, C. Lyman, C.; Echlin, P.; Lifshin, E.; Sawyer, L.; Michael, J. Scanning Electron Microscopy and X-Ray Microanalysis, 3rd ed., Kluwer: New York, 2003.

30. M.T. Postek, K.S. Howard, A.H. Johnson and K.L. McMichael, Scanning Electron Microscopy: A Student’s Handbook, (Ladd Research Ind., Inc.Williston, VT., 1980).
31. C.E. Lyman, D.E. Newbury, J.I. Goldstein, D.B. Williams, A.D. Romig, J.T. Armstrong, P. Echlin, C.E. Fiori, D.C. Joy, E. Lifshin, Klaus-Ruediger Peters, Scanning Electron Microscopy, X-Ray Microanalysis and Analytical Electron Microscopy: A Laboratory Workbook, (Plenum Press. New York, N.Y., 1990).
32. J.I. Goldstein, H. Yakowitz, D.E. Newbury, E. Lifshin, J.W. Colby, J.W. Colby, J.R. Coleman, Pratical Scanning Electron Microscopy: Electron and Ion Microprobe Analysis, edited by J.I. Goldstein and H. Yakowitz (Pelnum Press. New York, N.Y., 1975)
33. Thomas LaGrange, Introduction: Basics of Transmission Electron Microscopy (TEM), TEM Doctoral Course MS-637, April 25-27th, 2016
34. S. J. B. Reed, Electron Microprobe Analysis Cambridge Univ. Press. Second edition, 1993.
35. S. J. B. Reed, Electron Microprobe Analysis and Scanning Electron Microscopy in Geology by Cambridge Univ. Press. 1996.
36. M. Von Heimendahl, W. Bell, G. Thomas, Journal of Applied Physics 35 (1964)3614.
37. C. Richard Brundle, Charles A. Evans Jr, Shaun Wilson. Encyclopedia of materials characterization, Butterworth-Heinemann publications, 1992.

38. Joachim Mayer, Lucille A. Giannuzzi, Takeo Kamino, Joseph Michael, TEM Sample Preparation and FIB-Induced Damage. Mrs Bulletin, volume 32, May 2007.
39. A. Hubert, R. Schäfer. Magnetic Domains. Springer-Verlag, Berlin Heidelberg, 1998.
40. B. D. Cullity, C. D. Graham, Introduction to Magnetic Materials. John Wiley & Sons, New Jersey, 2009
41. O' Handley, R. C. Modern magnetic materials: principles and applications. John Wiley & Sons, New York, 2000.
42. Quantum Design’s Versa lab 3 Tesla VSM user manual, part no. 1300-001, A0.
43. G Breit, E. Wigner, Physical Review, 49 (1936) 519
44. T E Cranshaw, B W Dale, G O Longworth, C E Johnson, Mössbauer Spectroscopy and its Applications, (Cambridge Univ. Press: Cambridge) 1985
45. R.L. Mössbauer, Zeitschrift Physik, 1958, 151, 124.
46. U. Gonser (ed), Mössbauer Spectroscopy, Topics in Applied Physics, Vol 5, Springer, Berlin-HeidelbergNew York, 1975
47. R. L. Mössbauer, E. Wiedemann, Zeitschrift Physik 159, (1960)33
48. P. Gütlich, E.Bill, A. X. Trautwein, Mössbauer spectroscopy and transition metal chemistry, Springer-Verlag Berlin Heidelberg, 2011.,
49. E. Kankeleit, Review of Scientific Instruments, 35,(1964)194
50. D. Santosh Kumar and K. Chandra Mouli, International Journal of Nanotechnology and Applications, Volume 4, No.1 (2010) 51-59.

51. Sangeeta Thakur and S. C. Katyal M. Singh, Applied Physics Letters, 91, (2007) 262501.
52. A. A. Samokhvalov, A.G. Rustamov, Soviet Physics Solid state, 6, (1964). 749
53. A. A. Samokhvalov, A.G. Rustamov, Soviet Physics Solid state, 7, (1965)961.
54. L. G. Van Uitert, Proc.I.R.E. 44 (1956) 1294.
55. G. H. Jonker, J. Phys. Chem. Solids, 9, (1959), 165.
56. E. J. W. Verwey and J. H. de Boer, Reauil Ches Travaux chimques des Phys. Bas (Czeckh), 55(1936) 531.
57. Pranav P. Naik, R.B. Tangsali, B. Sonaye, S. Sugur, Journal of Nanotechnology and Advanced Material, 3, No. 1, 1-7 (2015)
58. "The NIST reference on fundamental physical constants"Physics.nist.gov. Retrieved 2011-11-08
59. M. Faraday, Phil. Trans 128:1 79 (1837)265
60. O. F. Mossoti, Bibl. univ. modena 6, (1847)193
61. O. F. Mossoti, Mem. di Mathem e.di.fisica in modena, 24(2) (1850)49
62. R. Clausius Vieweg. Braunschweigh Volume 2 (1879)

CHAPTER 4

STRUCTURAL CHARACTERIZATION, MAGNETIC AND ELECTRICAL PROPERTIES OF AS-PREPARED $Mn_{0.6}Zn_{0.4}Fe_{2-x}Nd_xO_4$ & $Mn_{0.65}Zn_{0.35}Fe_{2-x}Nd_xO_4$ NANOPARTICLES

The entire investigations are focused on the properties of Nd^{+3} doped Mn-Zn ferrites nanoparticles basically to study effect of doping on the properties and secondly to investigate the effect of gamma radiation on the properties of these samples, the data collection of several types as described in chapter II, was done in two different sequences. The first set of data was obtained on as prepared ultrafine powdered samples $Mn_{0.6}Zn_{0.4}Fe_{2-x}Nd_xO_4$ and $Mn_{0.65}Zn_{0.35}Fe_{2-x}Nd_xO_4$. X-ray powder diffraction (XRPD) and Fourier transform infrared spectroscopy (FTIR) data was collected and analyzed using appropriate models/software for materials structure determination and to confirm formation of monophasic materials. Surface morphology of as prepared samples was studied using micrographs obtained from scanning electron microscope (SEM) while the particle size estimation was done using XRD data and micrographs obtained from transmission electron microscopy (TEM). These set of data actually confirmed formation of nanoparticle samples of required type. Magnetic behavior which is an fundamental property of these nanomaterials was analyzed using vibrating sample magnetometer as a function of magnetic field (0-3T) and as a function of temperature over a temperature range from 50K to 390K. Relative magnetic permeability μ_r of these nanoparticles was also obtained as a function of frequency using a very simple theory and technique covered in basic Physics. Mössbauer spectroscopy which is yet another tool to know several things about magnetic aspects of the samples was employed to investigate the magnetic environment of Mossbauer active ions present in the material at octahedral site and tetrahedral site. Electrical transport in this type of materials is of utmost importance as it enlightens one about several other factors that are interlinked and remotely control or effect other properties. Electrical transport properties like dc resistivity ‘ρ’, dielectric constant ‘ε’ and dielectric loss ‘tan δ’ were measured as a function of temperature over the range of 300K to 773K. Also constant ‘ε’ and dielectric loss ‘tan δ’, were measured as a function of frequency over the range of 20Hz to 3MHz. The outcome of these measurements obtained after detailed analysis are presented below and are qualitatively discussed in detail.

Structural property exploration

4.1 X- ray diffraction (XRD)

X-ray diffraction patterns obtained on samples with composition $Mn_{0.6}Zn_{0.4}Fe_{2-x}Nd_xO_4$ and $Mn_{0.65}Zn_{0.35}Fe_{2-x}Nd_xO_4$ (x=0.04, 0.05, 0.06, 0.07, 0.08, 0.09 and 0.1) are presented in figure 4.1.1 (a & b).

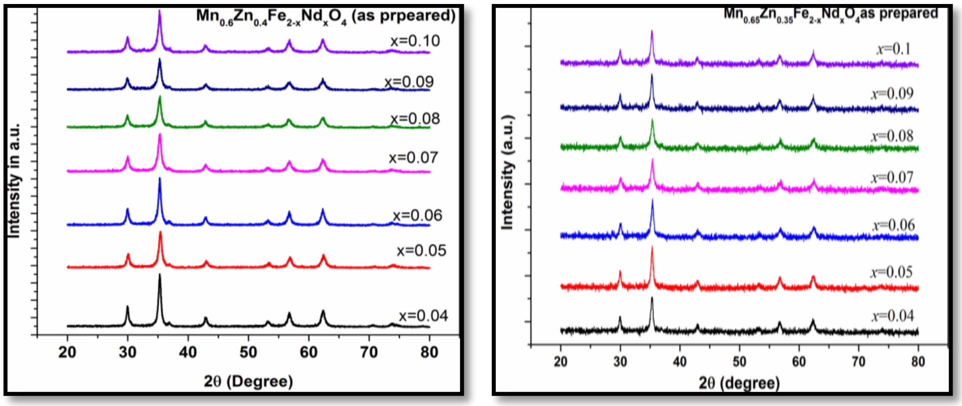

(a) (b)

Figure 4.1.1 X-ray diffraction pattern obtained on (a) $Mn_{0.6}Zn_{0.4}Fe_{2-x}Nd_xO_4$ & (b) $Mn_{0.65}Zn_{0.35}Fe_{2-x}Nd_xO_4$

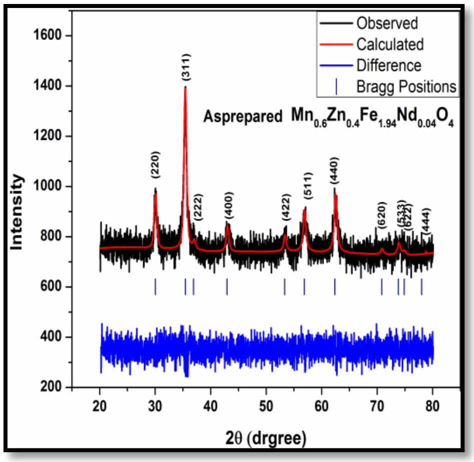
Observed
Calculated
Difference
Bragg Positions
Asprepared Mn0.6Zn0.4Fe1.94Nd0.04O4
(220)
(311)
(222)
(400)
(422)
(511)
(440)
(620)
(533)
(622)
(444)
Intensity
2θ (drgree)

(a)

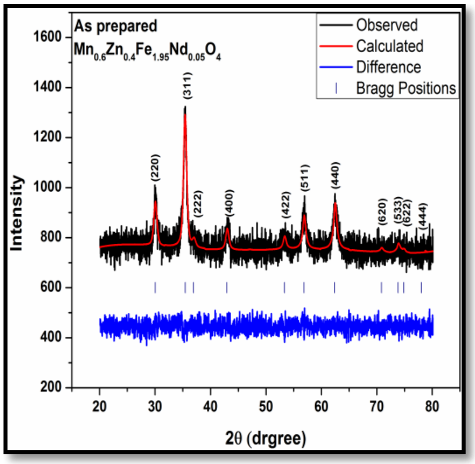
As prepared
Mn0.6Zn0.4Fe1.95Nd0.05O4
Observed
Calculated
Difference
Bragg Positions
(220)
(311)
(222)
(400)
(422)
(511)
(440)
(620)
(533)
(622)
(444)
Intensity
2θ (drgree)

(b)

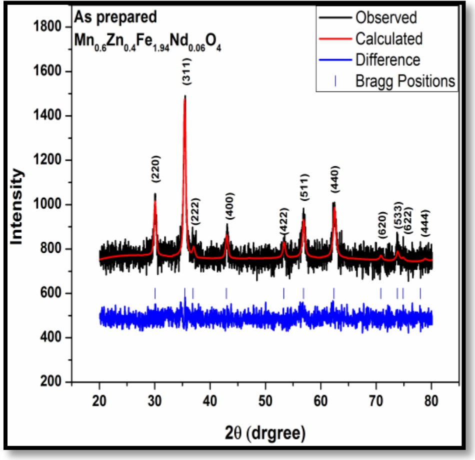
As prepared
Mn0.6Zn0.4Fe1.94Nd0.06O4
Observed
Calculated
Difference
Bragg Positions
(220)
(311)
(222)
(400)
(422)
(511)
(440)
(620)
(533)
(622)
(444)
Intensity
2θ (drgree)

(c)

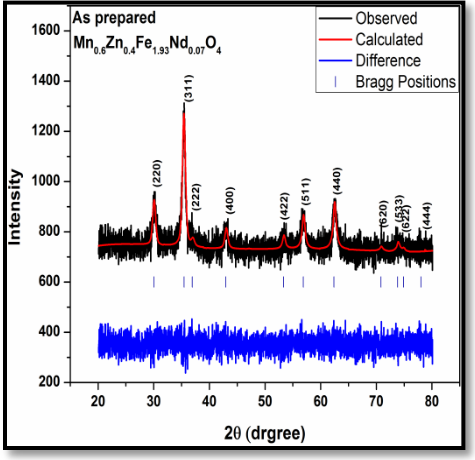
As prepared
Mn0.6Zn0.4Fe1.93Nd0.07O4
Observed
Calculated
Difference
Bragg Positions
(220)
(311)
(222)
(400)
(422)
(511)
(440)
(620)
(533)
(622)
(444)
Intensity
2θ (drgree)

(d)

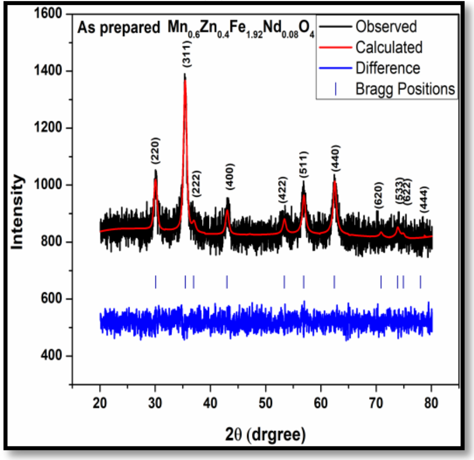
As prepared Mn0.6Zn0.4Fe1.92Nd0.08O4
Observed
Calculated
Difference
Bragg Positions
(220)
(311)
(222)
(400)
(422)
(511)
(440)
(620)
(533)
(622)
(444)
Intensity
2θ (drgree)

(e)

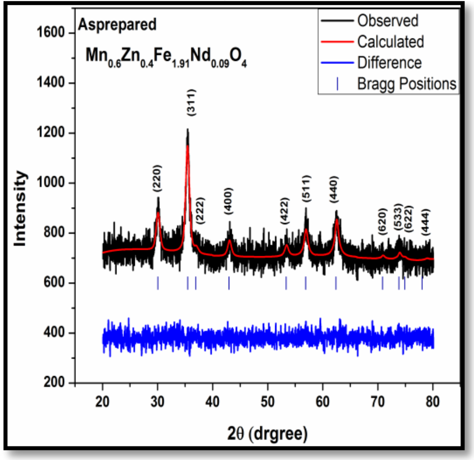
Asprepared
Mn0.6Zn0.4Fe1.91Nd0.09O4
Observed
Calculated
Difference
Bragg Positions
(220)
(311)
(222)
(400)
(422)
(511)
(440)
(620)
(533)
(622)
(444)
Intensity
2θ (drgree)

(f)

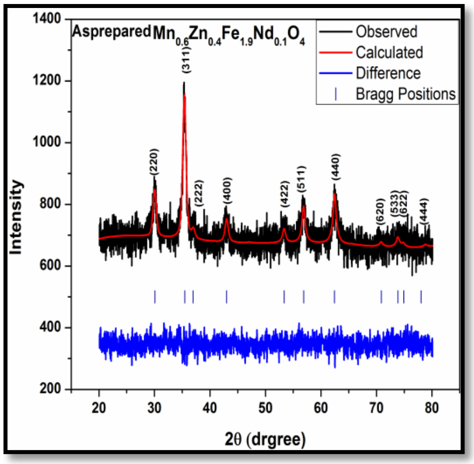

(g)

Figure 4.1.2 Rietveld analysis of XRD patterns for $Mn_{0.6}Zn_{0.4}Fe_{2-x}Nd_xO_4$ nanoarticles

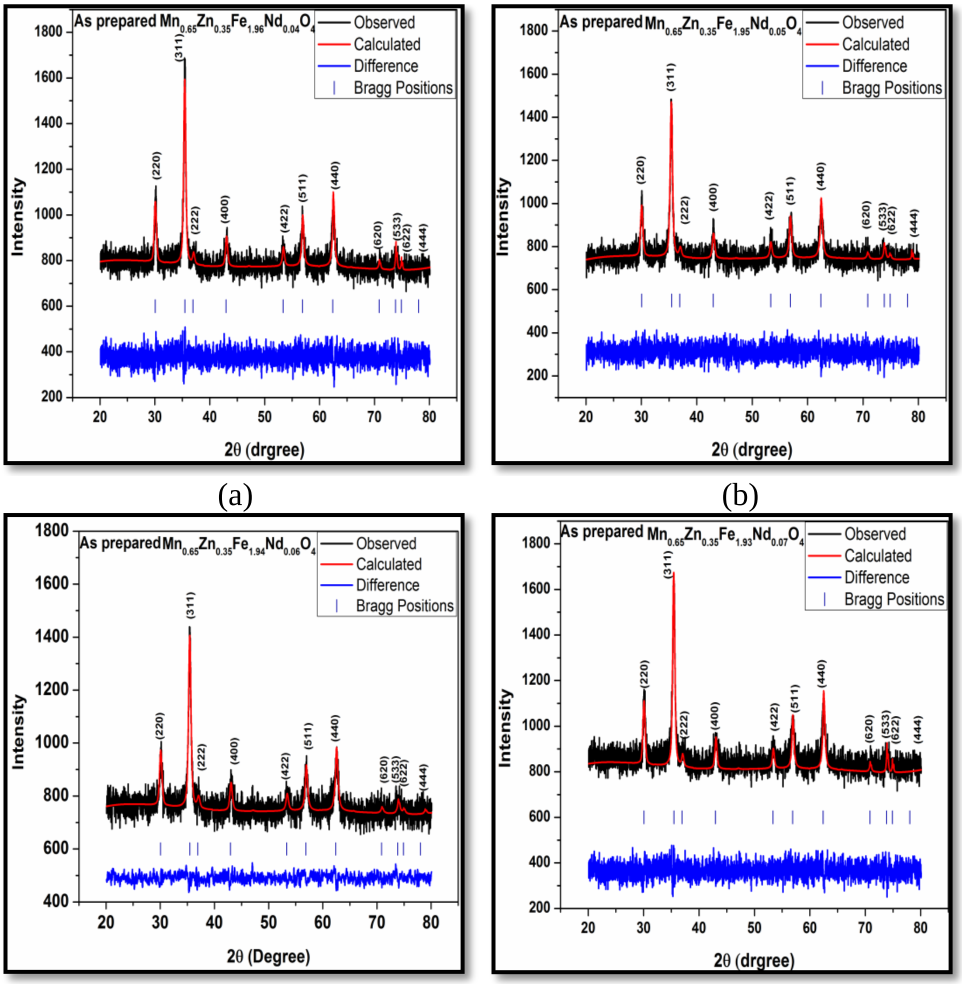

(a)

(b)

(c)

(d)

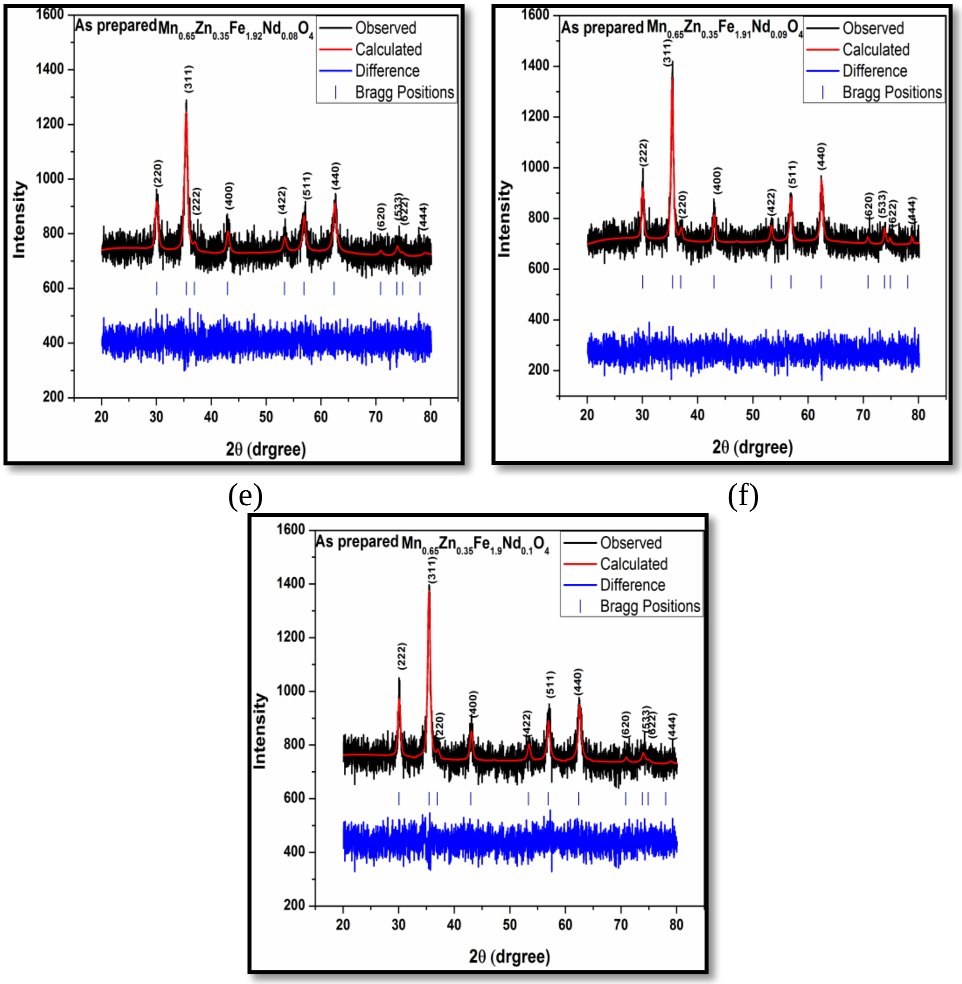

(e) (f)

(g)

Figure 4.1.3 Rietveld analysis of XRD patterns for $Mn_{0.65}Zn_{0.35}Fe_{2-x}Nd_xO_4$ nanoparticles

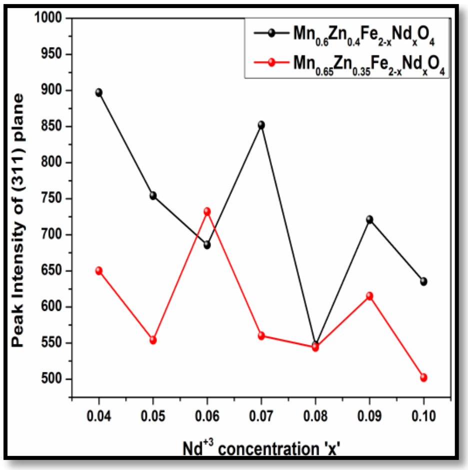

Figure 4.1.4 Variation in peak intensity of (311) plane with Nd^{+3} concentration for $Mn_{0.6}Zn_{0.4}Fe_{2-x}Nd_xO_4$ and $Mn_{0.65}Zn_{0.35}Fe_{2-x}Nd_xO_4$ nanoparticles

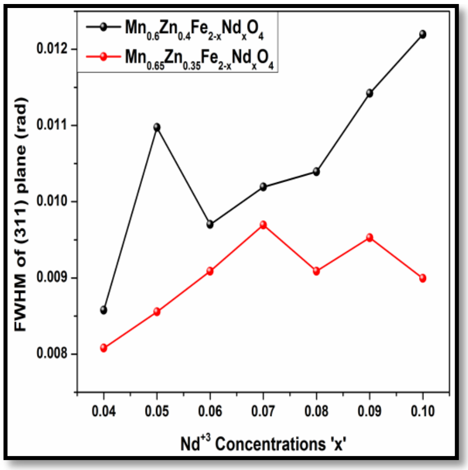

Figure 4.1.5 Variation in FWHM of (311) plane with Nd^{+3} concentration for $Mn_{0.6}Zn_{0.4}Fe_{2-x}Nd_xO_4$ and $Mn_{0.65}Zn_{0.35}Fe_{2-x}Nd_xO_4$ nanoparticles

Variation of peak intensity of (311) plane with Nd^{+3} concentration for $Mn_{0.6}Zn_{0.4}Fe_{2-x}Nd_xO_4$ and $Mn_{0.65}Zn_{0.35}Fe_{2-x}Nd_xO_4$ nanoparticles is shown Figure 4.1.3 where in an uneven yet on an average a decreasing trend was observed indicating reduction in crystalline nature with increasing Nd^{+3}concentrations in the ferrite lattice. Full width at half maximum (FWHM) variation of (311) plane with increasing Nd^{+3} concentrations is presented in Figure 4.1.5. FWHM values for $Mn_{0.6}Zn_{0.35}Fe_{2-x}Nd_xO_4$ nanoparticles showed a non uniform abrupt increase indicating reduction in crystallite sizes. For $Mn_{0.65}Zn_{0.35}Fe_{2-x}Nd_xO_4$ samples FWHM values were observed to increase linearly from x=0.04 to x=0.07 followed by an uneven variation for higher concentrations of Nd^{+3}.

All the samples were found to exhibit pure spinel phase without formation of any secondary phase indicating successful inclusion of rare earth ion (Nd^{+3}) which is evident from the Rietveld refined data presented in figures 4.1.2 and 4.1.3. Refinement of the XRD data was done using Full prof suit software and the refined patterns of composition $Mn_{0.6}Zn_{0.4}Fe_{2-x}Nd_xO_4$ and $Mn_{0.65}Zn_{0.35}Fe_{2-x}Nd_xO_4$ nanosamples are shown in figure 4.1.2 and figure 4.1.3 respectively. The XRD patterns were fitted with space group Fd3m assigning tetrahedral ions at 8a sites while octahedral ions were assigned 16d sites. The values of atomic positions of cations and refinement parameters for as prepared $Mn_{0.6}Zn_{0.4}Fe_{2-x}Nd_xO_4$ and $Mn_{0.65}Zn_{0.35}Fe_{2-x}Nd_xO$ are listed in Table 4.1.1a and table 4.1.1b respectively where R_{WP} is the discrepancy factor, R_{EXP} expected value and χ^2 is the goodness fit factor.

Table 4.1.1a Atomic positions and agreement R_p, R_{exp}, χ^2 obtaitained from Rietveld refinement of XRD patterns of $Mn_{0.6}Zn_{0.4}Fe_{2-x}Nd_xO_4$.

Sample	Atoms	Atomic positions x	 y	 z	R_P	R_{EXP}	χ^2
0.04	Mn/Zn/Fe	0.125	0.125	0.125	17.5	15.01	1.36
	Mn/Fe/Nd	0.500	0.500	0.500			
0.05	Mn/Zn/Fe	0.125	0.125	0.125	19.66	15.09	1.31
	Mn/Fe/Nd	0.500	0.500	0.500			
0.06	Mn/Zn/Fe	0.125	0.125	0.125	18.7	15.37	1.48
	Mn/Fe/Nd	0.500	0.500	0.500			
0.07	Mn/Zn/Fe	0.125	0.125	0.125	22.21	15.41	1.45
	Mn/Fe/Nd	0.500	0.500	0.500			
0.08	Mn/Zn/Fe	0.125	0.125	0.125	21.1	17.11	1.52
	Mn/Fe/Nd	0.500	0.500	0.500			
0.09	Mn/Zn/Fe	0.125	0.125	0.125	21.31	14.35	1.49
	Mn/Fe/Nd	0.500	0.500	0.500			
0.1	Mn/Zn/Fe	0.125	0.125	0.125	22.4	17.87	1.57
	Mn/Fe/Nd	0.500	0.500	0.500			

Table 4.1.1b Atomic positions and agreement R_p, R_{exp} χ^2 obtaitained from Rietveld refinement of XRD patterns of $Mn_{0.65}Zn_{0.35}Fe_{2-x}Nd_xO_4$.

Sample	Atoms	Atomic positions x	 y	 z	R_{exp}	R_{wp}	χ^2
0.04	Mn/Zn/Fe	0.125	0.125	0.125	19.19	14.32	1.34
	Mn/Fe/Nd	0.500	0.500	0.500			

0.05	Mn/Zn/Fe	0.125	0.125	0.125	19.95	14.46	1.38
	Mn/Fe/Nd	0.500	0.500	0.500			
0.06	Mn/Zn/Fe	0.125	0.125	0.125	21.01	14.39	1.46
	Mn/Fe/Nd	0.500	0.500	0.500			
0.07	Mn/Zn/Fe	0.125	0.125	0.125	20.86	15.01	1.39
	Mn/Fe/Nd	0.500	0.500	0.500			
0.08	Mn/Zn/Fe	0.125	0.125	0.125	21.61	15.22	1.42
	Mn/Fe/Nd	0.500	0.500	0.500			
0.09	Mn/Zn/Fe	0.125	0.125	0.125	21.81	15.31	1.43
	Mn/Fe/Nd	0.500	0.500	0.500			
0.1	Mn/Zn/Fe	0.125	0.125	0.125	22.67	15.42	1.47
	Mn/Fe/Nd	0.500	0.500	0.500			

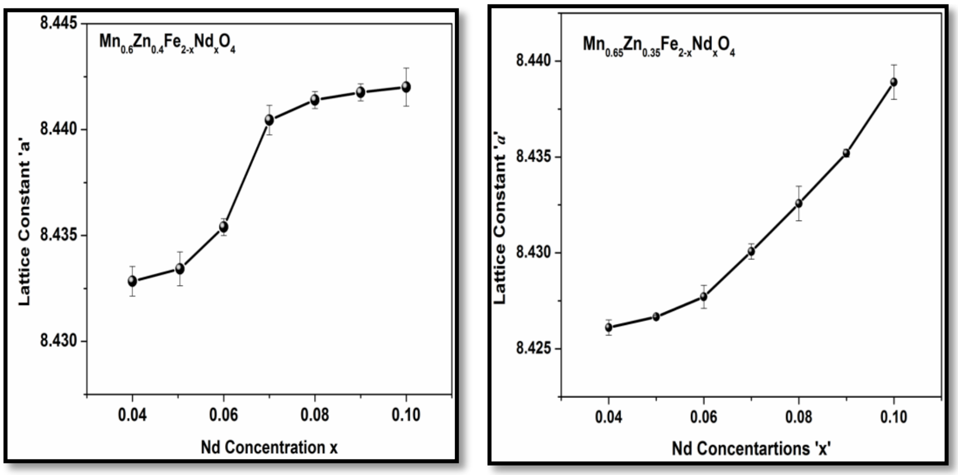

(a) (b)

Figure 4.1.6(a & b) Variation of lattice constant '*a*' with $Nd^{+3}$for $Mn_{0.6}Zn_{0.4}Fe_{2-x}Nd_xO_4$ and $Mn_{0.65}Zn_{0.35}Fe_{2-x}Nd_xO_4$ nanoparticle.

Figure 4.1.6 (a,b) shows the variation of lattice constant '*a*' with increasing Nd^{+3} concentrations for $Mn_{0.6}Zn_{0.4}Fe_{2-x}Nd_xO_4$ and $Mn_{0.65}Zn_{0.35}Fe_{2-x}Nd_xO_4$ nanoparticles. Lattice constant was observed to increase with increasing Nd^{+3} concentrations which can be attributed to the larger ionic radius of Nd^{+3} (1.12Å) which replaces Fe^{+3} (0.64Å) at octahedral site. This replacement causes an expansion of octahedral sub lattice resulting in an overall increase in lattice constant [1]. Lattice constant '*a*' value for the sample with composition $Mn_{0.6}Zn_{0.4}Fe_{1.96}Nd_{0.04}O_4$ was found to be equal to 8.433 Å while '*a*' value for $Mn_{0.65}Zn_{0.35}Fe_{1.96}Nd_{0.04}O_4$ was found to be equal to 8.426 Å. Similar trend was observed in all the samples where in the lattice constant values for $Mn_{0.6}Zn_{0.4}Fe_{2-x}O_4$ samples were observed to have relatively higher values compared to $Mn_{0.65}Zn_{0.35}Fe_{2-x}Nd_xO_4$ samples which can be attributed high specific gravity of Mn ions and weaker electrostatic shielding of nuclear charge by 3d electrons which leads to marginal contraction of Mn^{+2}/Mn^{+3} ions and overall reduction in lattice constant values in the case of samples with higher Mn content [2]. The variation of crystallite size with increasing rare earth ion (Nd^{+3}) concentration is shown in figure 4.1.7 (a,b). It can be clearly seen that in general the crystallite size decreases with increase in Nd^{+3} concentrations. However the actual variations are not smooth and are uneven. For sample $Mn_{0.6}Zn_{0.4}Fe_{2-x}Nd_xO_4$ a major dip and a local rise is seen at x=0.05 and x=0.06 respectively followed by a nearly smooth fall in the crystallite for higher values of x. Whereas for sample $Mn_{0.65}Zn_{0.35}Fe_{2-x}Nd_xO_4$ the crystallite size shows a smooth fall for x=0.04 to x=0.07 followed by uneven bounces in the crystallite size as x increases. Thus if one ignores the local undulations observed both these trends indicate a decrease of crystallite size with increasing Nd^{+3} concentration in the samples. This indicates that inclusion of rare earth ion develops lattice strain that hinders the crystallite growth responsible for drastic reduction of crystallite size in these materials. Moreover presence of Zn^{+2} ions with maximum electrostatic shielding by 3d electrons contribute to additional strain, which result in drastic reduction in samples with composition $Mn_{0.6}Zn_{0.4}Fe_{2-x}Nd_xO_4$ compared to samples with composition $Mn_{0.65}Zn_{0.35}Fe_{2-x}Nd_xO_4$ [4-9].

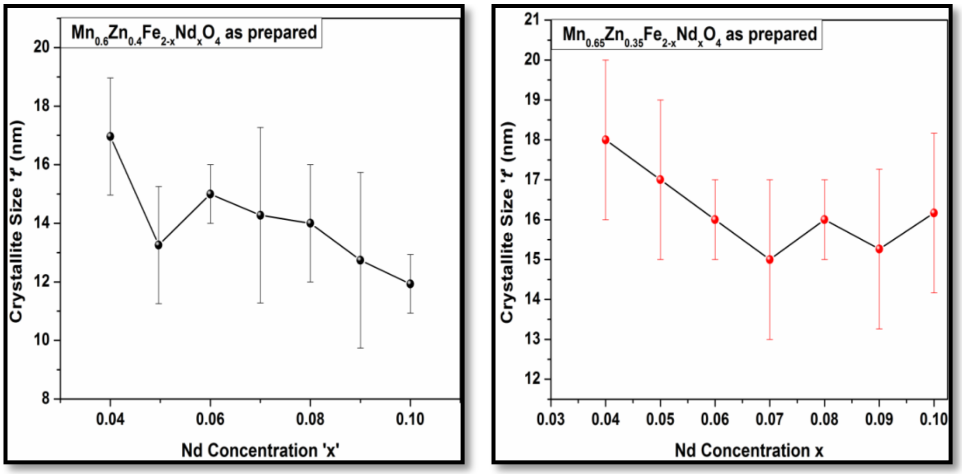

(a) (b)

Figure 4.1.7(a & b) Variation of Crystallite size 't' with Nd^{+3} concentrations for as prepared $Mn_{0.6}Zn_{0.4}Fe_{2-x}Nd_xO_4$ and $Mn_{0.65}Zn_{0.35}Fe_{2-x}Nd_xO_4$ nanoparticle

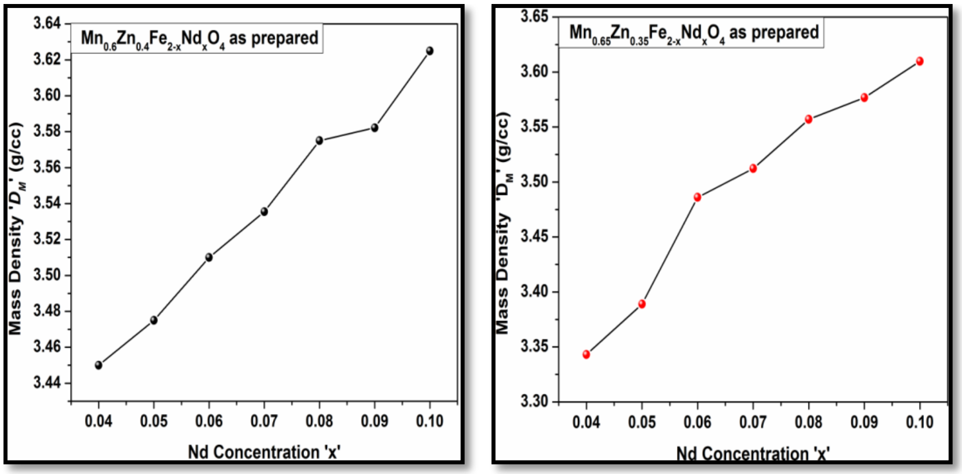

(a) (b)

Figure 4.1.8(a & b) Variation of Mass density with Nd^{+3} concentrations for $Mn_{0.6}Zn_{0.4}Fe_{2-x}Nd_xO_4$ and $Mn_{0.65}Zn_{0.35}Fe_{2-x}Nd_xO_4$ nanoparticle

Mass density for all the samples, as shown in Figure 4.1.8 was found to increase with increasing concentrations of heavier rare earth ion (Nd^{+3}) in the samples. The mass density of the samples with composition $Mn_{0.6}Zn_{0.4}Fe_{2-x}Nd_xO_4$ was seen to be marginally higher than that of the samples with composition $Mn_{0.65}Zn_{0.35}Fe_{2-x}Nd_xO_4$. This can be attributed excess of Zn^{+2} ions which are relatively heavier than Mn^{+2}/Mn^{+3} ions.

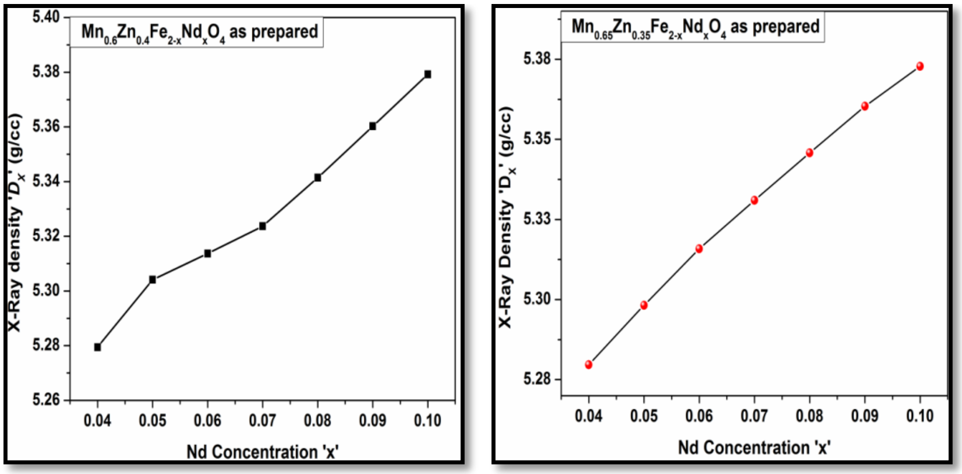

(a) (b)

Figure 4.1.9(a & b) Variation of X-ray density with Nd^{+3} concentration for $Mn_{0.6}Zn_{0.4}Fe_{2-x}Nd_xO_4$ and $Mn_{0.65}Zn_{0.35}Fe_{2-x}Nd_xO_4$ nanoparticle

X-ray density was measured using equation 4.1.1(a) for all rare earth doped samples and was observed to increase with increasing Nd^{+3} concentrations. The variation X-ray density is shown in Figure 4.1.9(a,b).

$$D_X = \frac{8M_X}{N_a a^3} \qquad 4.1.1(a)$$

Where 'N_a' is Avogadro's number (6.02×10^{23} atoms/mole) and M_X is the molecular weight of the sample and 'a' is lattice constant [7-10]. Porosity of $Mn_{0.6}Zn_{0.4}Fe_{2-x}Nd_xO_4$ and $Mn_{0.65}Zn_{0.35}Fe_{2-x}Nd_xO_4$ nanoparticles was calculated using equation 4.1.1(b) and was found to decrease with increasing Nd^{+3} concentrations as shown in Figure 4.1.10.

$$P(\%) = \left[1 - \frac{D_M}{D_X}\right] \times 100 \qquad 4.1.1(b)$$

Where D_M and D_X are the mass densities and X-ray densities of the samples.

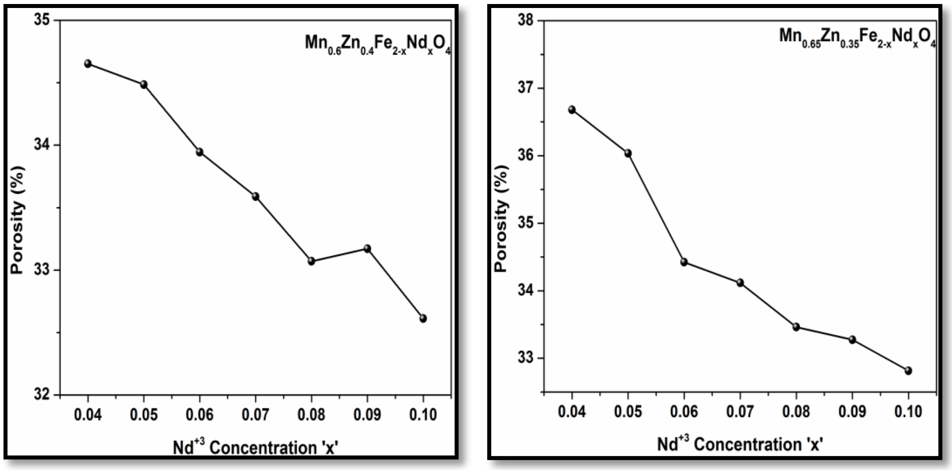

(a) (b)

Figure 4.1.10(a & b) Variation of porosity % with Nd^{+3} concentration for $Mn_{0.6}Zn_{0.4}Fe_{2-x}Nd_xO_4$ and $Mn_{0.65}Zn_{0.35}Fe_{2-x}Nd_xO_4$ nanoparticle

Since different metal ions occupy two different sites in spinel structure, three types of magnetic interactions are possible between the cations through intermediate O^{-2} ions, by super-exchange mechanism namely, A-A interaction, B-B interaction and A-B interaction. The interaction energies are negative and hence induce anti-parallel spin orientation. The magnitude of interaction energy between interacting cations depends upon distances between the cations to the oxygen and the angle between cations distributed over two sites. An angle of 180^o will result in greatest exchange energy. Interaction energy decreases rapidly with increasing distances. Out of these three interactions, A-B interaction is the strongest in magnitude as the bond angles are fairly large and the cation anion bond lengths are smaller. A-A interaction is the weakest interaction as the cation anion distance is large. Out of two possible configurations of B-B interaction only first interaction with bond angel θ_3 is prominent due to smaller values of bond lengths.

The bond lengths between metal ions at tetrahedral site and metal at octahedral site denoted as **b, c, d, e and f** (bond length between cations) were estimated using equations

4.1.2 (a, b, c, d, e) in order to investigate the effect of Nd^{+3} doping on the structural aspects of the nanoparticles prepared as shown in Figure 4.1.11.

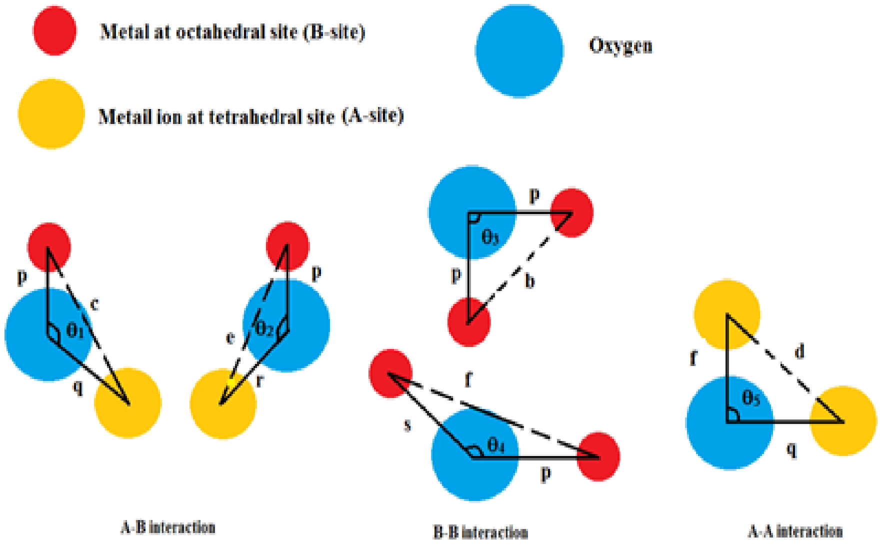

Figure 4.1.11 Ion pair configuration in ferrite with bond lengths and angles

$$b = \sqrt{2}\frac{a}{4} \qquad 4.1.2\ a$$

$$c = \sqrt{11}\frac{a}{8} \qquad 4.1.2\ b$$

$$d = \sqrt{3}\frac{a}{4} \qquad 4.1.2\ c$$

$$e = \sqrt{3}\frac{3a}{8} \qquad 4.1.2\ d$$

$$f = \sqrt{6}\frac{a}{4} \qquad 4.1.2\ e$$

Where ‘*a*’ is the lattice parameter. The calculated values of bond lengths between metal ions at tetrahedral site and metal at octahedral site are listed in table 4.1.2. (a,b)

Table 4.1.2aVariation of bond lengths between cations with Nd^{+3} concentrations for $Mn_{0.6}Zn_{0.4}Fe_{2-x}Nd_xO_4$

Sample $Mn_{0.6}Zn_{0.4}Fe_{2-x}Nd_xO_4$	*b* (Å)	*c* (Å)	*d* (Å)	*e* (Å)	*f* (Å)
x=0.04	2.981(4)	3.496(1)	3.651(5)	5.477(2)	5.164(1)
x=0.05	2.981(6)	3.496(3)	3.651(7)	5.477(6)	5.164(4)
x=0.06	2.982(3)	3.497(1)	3.652(6)	5.478(9)	5.165(6)
x=0.07	2.984(1)	3.499(2)	3.654(8)	5.482(2)	5.168(6)
x=0.08	2.984(4)	3.499(6)	3.655(2)	5.482(8)	5.169(2)
x=0.09	2.984(6)	3.499(7)	3.655(3)	5.483(1)	5.169(5)
x=0.1	2.984(7)	3.499(8)	3.655(4)	5.483(2)	5.169(6)

Table 4.1.2bVariation of bond lengths between cations with Nd^{+3} concentrations for $Mn_{0.65}Zn_{0.35}Fe_{2-x}Nd_xO_4$

Sample $Mn_{0.65}Zn_{0.35}Fe_{2-x}Nd_xO_4$	*b* (Å)	*c* (Å)	*d* (Å)	*e* (Å)	*f* (Å)
x=0.04	2.979(1)	3.493(3)	3.648(6)	5.472(9)	5.159(9)
x=0.05	2.979(2)	3.493(5)	3.648(8)	5.473(3)	5.160(3)
x=0.06	2.979(6)	3.493(9)	3.649(3)	5.473(9)	5.160(9)
x=0.07	2.980(4)	3.494(9)	3.650(3)	5.475(5)	5.162(3)
x=0.08	2.981(4)	3.495(9)	3.651(4)	5.477(1)	5.163(8)
x=0.09	2.982(3)	3.497(1)	3.652(6)	5.478(8)	5.165(5)
x=0.1	2.983(6)	3.498(9)	3.654(2)	5.481(2)	5.167(8)

The bond lengths between metal ions and oxygen at various sites are denoted as **p, q, r** and **s** (bond lengths between cation-anion) were estimated using following equations 4.1.3 (a, b, c, d). Here “u” is the oxygen parameter.

$$p = a\left(\frac{5}{8} - u\right) \qquad 4.1.3a$$

$$q = a\sqrt{3}\left(u - \frac{1}{4}\right) \qquad 4.1.3b$$

$$r = a\sqrt{11}\left(u - \frac{1}{8}\right) \qquad 4.1.3c$$

$$s = a\sqrt{3}\left(\frac{u}{3} + \frac{1}{8}\right) \qquad 4.1.3d$$

Table 4.1.3aVariation of bond lengths between cations and anions with Nd^{+3} concentrations for $Mn_{0.6}Zn_{0.4}Fe_{2-x}Nd_xO_4$

Sample $Mn_{0.6}Zn_{0.4}Fe_{2-x}Nd_xO_4$	p (Å)	q(Å)	r (Å)	s(Å)
x=0.04	2.108(2)	1.825(7)	6.992(1)	3.651(5)
x=0.05	2.108(4)	1.825(8)	6.992(6)	3.651(7)
x=0.06	2.108(9)	1.826(3)	6.994(2)	3.652(6)
x=0.07	2.110(1)	1.827(4)	6.998(4)	3.654(8)
x=0.08	2.110(4)	1.827(6)	6.999(2)	3.655(2)
x=0.09	2.110(4)	1.827(7)	6.999(5)	3.655(4)
x=0.1	2.110(5)	1.827(7)	6.999(7)	3.655(5)

Table 4.1.3bVariation of bond lengths between cations and anions with Nd^{+3} concentrations $Mn_{0.65}Zn_{0.35}Fe_{2-x}Nd_xO_4$

Sample $Mn_{0.65}Zn_{0.35}Fe_{2-x}Nd_xO_4$	p (Å)	q(Å)	r (Å)	s (Å)
x=0.04	2.106(5)	1.824(3)	6.986(5)	3.648(6)
x=0.05	2.106(7)	1.824(4)	6.987(1)	3.6488(5)
x=0.06	2.106(9)	1.824(6)	6.987(9)	3.649(3)
x=0.07	2.107(5)	1.825(2)	6.989(8)	3.650(3)
x=0.08	2.108(1)	1.825(7)	6.991(9)	3.651(4)
x=0.09	2.108(8)	1.826(3)	6.994(1)	3.652(6)
x=0.1	2.109(7)	1.827(5)	6.997(2)	3.654(2)

An increasing parameter was observed in cation cation and cation anion bond lengths with increasing concentration of Nd^{+3} at octahedral site replacing Fe^{+3}. This increase in bond lengths can be attributed to the larger ionic radius of Nd^{+3} ions. The values of anion cation bond lengths for as prepared $Mn_{0.6}Zn_{0.4}Fe_{2-x}Nd_xO_4$ and $Mn_{0.65}Zn_{0.35}Fe_{2-x}Nd_xO_4$ nanoparticle are listed in table 4.1.3 (a,b)

Table 4.1.4aVariation of bond angles between cations with Nd^{+3} concentrations for $Mn_{0.6}Zn_{0.4}Fe_{2-x}Nd_xO_4$

Sample $Mn_{0.6}Zn_{0.4}Fe_{2-x}Nd_xO_4$	θ_1	θ_2	θ_3	θ_4	θ_5
x=0.04	125.264(4)	142.322(1)	89.999(9)	125.264(3)	81.240(5)
x=0.05	125.264(6)	142.322(3)	90.000(5)	125.264(1)	81.240(4)
x=0.06	125.265(3)	142.322(8)	90.001(2)	125.263(9)	81.240(1)
x=0.07	125.265(1)	142.323(3)	90.001(5)	125.263(6)	81.239(9)
x=0.08	125.265(6)	142.323(9)	90.001(7)	125.263(5)	81.239(7)
x=0.09	125.265(7)	142.324(3)	90.002(1)	125.263(7)	81.239(6)
x=0.1	125.265(5)	142.324(7)	90.001(9)	125.263(3)	81.239(5)

Table 4.1.4bVariation of bond angles between cations with Nd^{+3} concentrations for $Mn_{0.65}Zn_{0.35}Fe_{2-x}Nd_xO_4$

Sample $Mn_{0.65}Zn_{0.35}Fe_{2-x}Nd_xO_4$	θ_1	θ_2	θ_3	θ_4	θ_5
x=0.04	125.264(7)	142.322(3)	90.000(9)	125.264(6)	81.240(4)
x=0.05	125.264(9)	142.322(7)	90.001(2)	125.264(2)	81.240(2)
x=0.06	125.265(5)	142.323(1)	90.001(7)	125.263(6)	81.239(8)
x=0.07	125.266(1)	142.323(5)	90.001(6)	125.263(2)	81.239(8)
x=0.08	125.266(4)	142.323(9)	90.001(9)	125.262(8)	81.239(7)
x=0.09	125.266(2)	142.324(8)	90.002(2)	125.262(9)	81.239(3)
x=0.1	125.265(8)	142.325(3)	90.002(1)	125.263(5)	81.239(4)

The various bond angles between cations are denoted as $\boldsymbol{\theta_1}$, $\boldsymbol{\theta_2}$, $\boldsymbol{\theta_3}$, $\boldsymbol{\theta_4}$ and $\boldsymbol{\theta_5}$ and were calculated using following equations 4.1.4 (a, b, c, d, e).

In the present study the bond lengths were found to be marginally higher for $Mn_{0.6}Zn_{0.4}Fe_{2-x}Nd_xO_4$ as compared to that of $Mn_{0.65}Zn_{0.35}Fe_{2-x}Nd_xO_4$ nanoparticles. The values of bond lengths were seen to decrease marginally with increasing Nd^{+3} concentrations at octahedral sites for all samples. However the bond angles $\boldsymbol{\theta_1}$, $\boldsymbol{\theta_2}$ and $\boldsymbol{\theta_3}$ were seen to increase with increasing Nd^{+3} concentrations resulting in enhancement exchange energy and strengthening A-B and B-B interaction [1,11,12]. The cation distribution over the two sites for all as prepared rare earth doped Mn-Zn ferrite nanoparticles is obtained from eq.4.1.5a

$$\mathrm{Mn_{(\beta-\alpha)}Zn_{\beta}Fe_{\alpha}\left[Mn_{\alpha}Fe_{(2-x-\alpha)}Nd_{x}\right]O_4} \qquad 4.1.5a$$

Where α, and β are the concentrations of Fe, Zn in terms of molar fractions at tetrahedral site while x represents concentration of Nd^{+3} at the octahedral site. The term inside the square bracket represents cation concentrations at octahedral sites while the terms outside the bracket represent tetrahedral cation concentrations. From above equation the mean radius of tetrahedral site and octahedral site can be expressed as follows:

$$(\beta-\alpha)\, r_{Mn}+\beta\, r_{Zn}+\alpha\, r_{Fe}=r_{tetra} \qquad 4.1.5b$$

$$\alpha\, r_{Mn}+(2-x-\alpha)r_{\,Fe}+x\, r_{Nd}\ =r_{octa} \qquad 4.1.5c$$

Where $r_{Mn/\ Zn/\ Fe/\ Nd}$ represents ionic radius of corresponding Mn, Zn, Fe and Nd ions respectively. The mean radii of tetrahedral site and octahedral site expressed in terms of the lattice constant 'a' and oxygen parameter 'u' are given the equations 4.1.5d and 4.1.5e. where 'r_o' is oxygen ionic radii

$$r_{trtra}=a\sqrt{3}(u-0.25)-r_o \qquad 4.1.5d$$

$$r_{octa}=a(0.625-u)-r_o \qquad 4.1.5e$$

By substituting the values of '*a*', '*u*' and r_o and comparing the equations 4.1.5 (d and e) with equation 4.1.5(b and c), value of α and β can be determined [13,14]. The cation distribution estimated from above equations for $Mn_{0.6}Zn_{0.4}Fe_{2-x}Nd_xO_4$ and $Mn_{0.65}Zn_{0.35}Fe_{2-x}Nd_xO_4$ nano particles is presented in table 4.1.5a. The distribution of various divalent and trivalent cations on octahedral site and tetrahedral sites plays a vital role in deciding and monitoring the values of various structural, magnetic and electrical properties of the spinel structure. It can be seen from the table 4.1.5a that with Nd^{+3} occupies octahedral (B) site in all the samples. While the Zn^{+2} shows a strong affinity towards tetrahedral environment restricting itself up to A-site. As the Nd^{+3} (1.12Å) concentrations are increased at octahedral site, the fraction of Fe^{+3} ions (0.64Å) occupying tetrahedral is found to increase as shown in Figure 4.1.11.

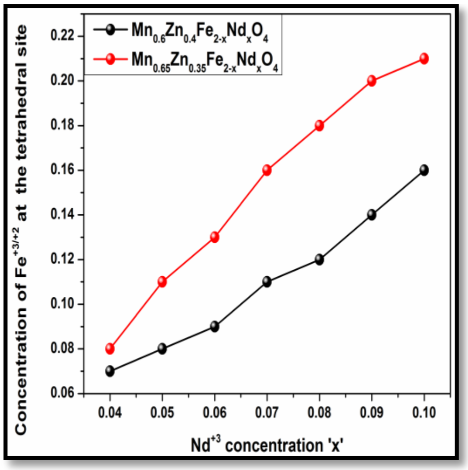

Figure 4.1.12 Variation of $Fe^{+3/+2}$ concentration at tetrahedral site with increasing Nd^{+3} concentration

Table 4.1.5a Variation of cation distribution with Nd^{+3} concentrations of $Mn_{0.6}Zn_{0.4}Fe_{2-x}Nd_xO_4$ and $Mn_{0.65}Zn_{0.35}Fe_{2-x}Nd_xO_4$ nanoparticles

Concentrations of Nd^{+3} (x)	As prepared $Mn_{0.6}Zn_{0.4}Fe_{2-x}Nd_xO_4$ A-site	B-site	As prepared $Mn_{0.65}Zn_{0.4}Fe_{2-x}Nd_xO_4$ A-site	B-site
0.04	$Mn_{0.53}Zn_{0.4}$	$Mn_{0.07}Fe_{1.89}$	$Mn_{0.56}Zn_{0.35}$	$Mn_{0.09}Fe_{1.88}$

	$Fe_{0.07}$	$Nd_{0.04}$	$Fe_{0.08}$	$Nd_{0.04}$
0.05	$Mn_{0.52}Zn_{0.4}Fe_{0.08}$	$Mn_{0.08}Fe_{1.87}Nd_{0.04}$	$Mn_{0.54}Zn_{0.35}Fe_{0.11}$	$Mn_{0.11}Fe_{1.84}Nd_{0.05}$
0.06	$Mn_{0.51}Zn_{0.4}Fe_{0.09}$	$Mn_{0.09}Fe_{1.85}Nd_{0.06}$	$Mn_{0.52}Zn_{0.35}Fe_{0.13}$	$Mn_{0.13}Fe_{1.81}Nd_{0.06}$
0.07	$Mn_{0.49}Zn_{0.4}Fe_{0.11}$	$Mn_{0.11}Fe_{1.82}Nd_{0.07}$	$Mn_{0.49}Zn_{0.35}Fe_{0.16}$	$Mn_{0.16}Fe_{1.77}Nd_{0.07}$
0.08	$Mn_{0.48}Zn_{0.4}Fe_{0.12}$	$Mn_{0.12}Fe_{1.80}Nd_{0.08}$	$Mn_{0.47}Zn_{0.35}Fe_{0.18}$	$Mn_{0.18}Fe_{1.74}Nd_{0.08}$
0.09	$Mn_{0.46}Zn_{0.4}Fe_{0.14}$	$Mn_{0.14}Fe_{1.77}Nd_{0.09}$	$Mn_{0.45}Zn_{0.35}Fe_{0.20}$	$Mn_{0.20}Fe_{1.71}Nd_{0.09}$
0.1	$Mn_{0.44}Zn_{0.4}Fe_{0.16}$	$Mn_{0.16}Fe_{1.74}Nd_{0.1}$	$Mn_{0.44}Zn_{0.35}Fe_{0.21}$	$Mn_{0.21}Fe_{1.69}Nd_{0.1}$

This migration of Fe^{+3} ions at tetrahedral site is compensated by migration of relatively larger Mn^{+2}(0.81Å). This cationic arrangement results in an increase in structural parameter, the lattice constant that induces lattice strain which inhibits the growth of crystallites of larger dimensions resulting in reduction in crystallite size as shown in Figure 4.1.5 (a,b). Increase in mass density of all the rare earth doped samples is essentially a consequence of this effect as smaller crystallites can effetely reduce the porosity of material.

4.2 Fourier Transform infra red (FTIR) spectroscopy

Fourier transform infra red spectra of as prepared $Mn_{0.6}Zn_{0.4}Fe_{2-x}Nd_xO_4$ & $Mn_{0.65}Zn_{0.35}Fe_{2-x}Nd_xO_4$ obtained on Simadzu FTIR 8900 assembly are shown in Figure 4.2.1 (a&b).

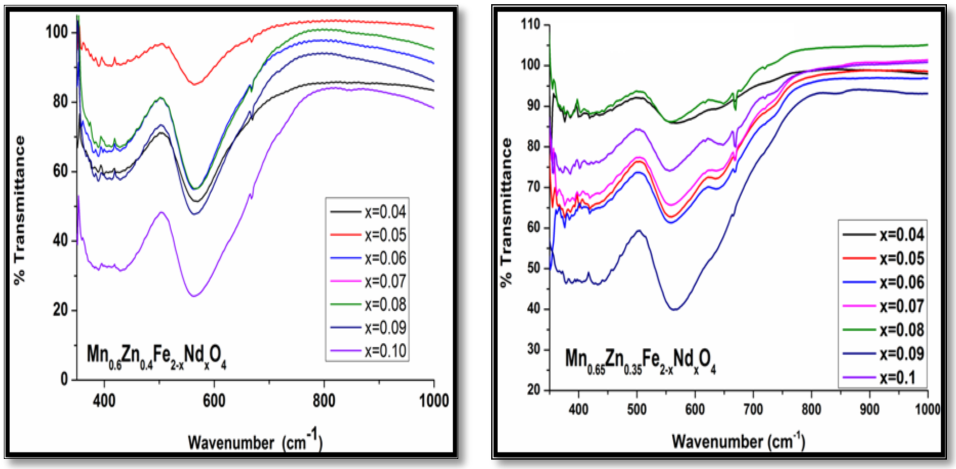

(a) (b)

Figure 4.2.1 (a & b) Fourier Transform Infra Red spectra of $Mn_{0.6}Zn_{0.4}Fe_{2-x}Nd_xO_4$ & $Mn_{0.65}Zn_{0.35}Fe_{2-x}Nd_xO_4$

The broad absorption band in the range from 559cm^{-1} to 565cm^{-1} is assigned to M_T --O bond stretching vibration whereas the absorption peak in the range 370cm^{-1} to 450cm^{-1} is due to stretching vibration of metal at M_O--O bond and a band in the range of 343cm^{-1} to 352cm^{-1} is due to M_T --O--M_O banding vibrations. Where O is oxygen, the metal in octahedral site is denoted as M_O while M_T represents metal ion at the tetrahedral site. Presence of three types of vibrational bonds in the material that are examined with the absorption band frequencies coinciding with that of spinel ferrite material. The multiple bands observed within the range 350cm^{-1} to 450 cm^{-1} represent the existence of different cations such as Nd^{+3}, Fe $^{+3}$, and Mn^{+3} at octahedral site. The bands observed at around 375cm^{-1}, 400cm^{-1} and 430cm^{-1} represent Fe^{+3}-O^{-2}, Mn^{+3}-O^{-2} and Nd^{+3}-O^{-2} stretching vibrations respectively [16-20]. It has been observed that substitution of Nd^{3+} with Fe^{3+} at octahedral site causes shifts of band (Fe^{3+}–O^{2-}) which is of the type M_T --O bond, towards higher frequency side. This also suggests the occupancy of Nd^{3+} at B-sites [15,21].

4.3 Scanning electron microscopy (SEM)

Scanning electron micrographs of as prepared nanoparticles of $Mn_{0.6}Zn_{0.4}Fe_{2-x}Nd_xO_4$ & $Mn_{0.65}Zn_{0.35}Fe_{2-x}Nd_xO_4$ are shown in Figure 4.3.1 and Figure 4.3.2 respectively.

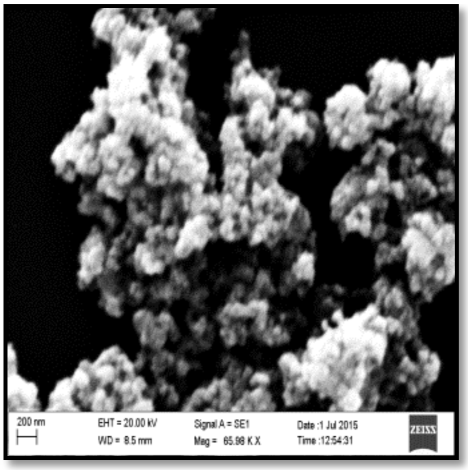

x=0.04

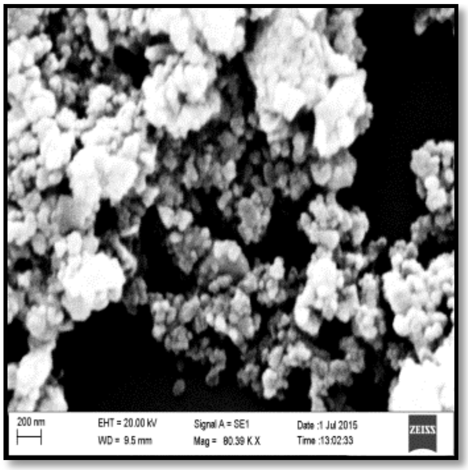

x=0.05

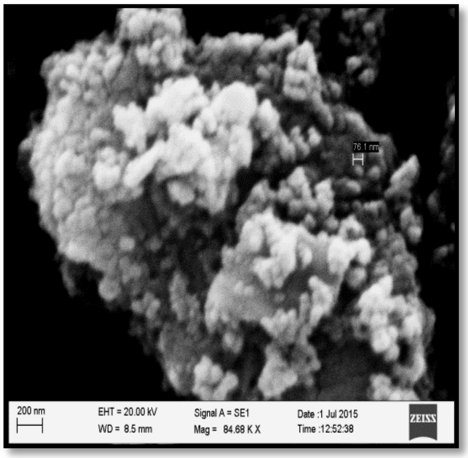

x=0.06

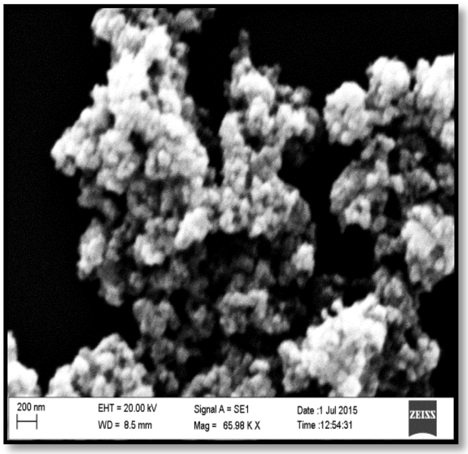

x=0.07

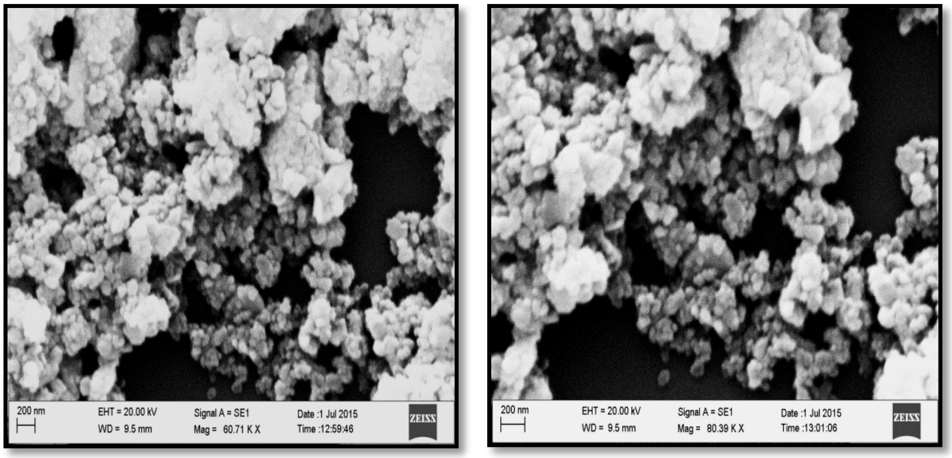

x=0.08 x=0.09

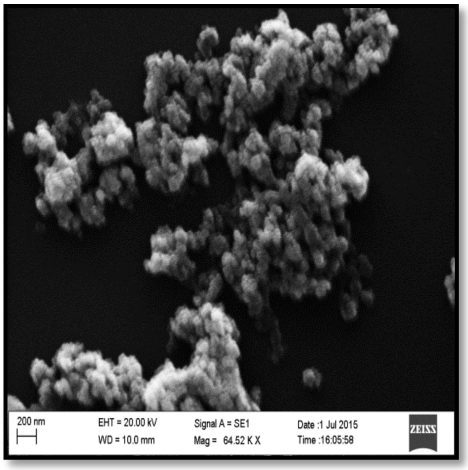

x=0.1

Figure 4.3.1 Scanning electron micrographs of $Mn_{0.6}Zn_{0.4}Fe_{2-x}Nd_xO_4$

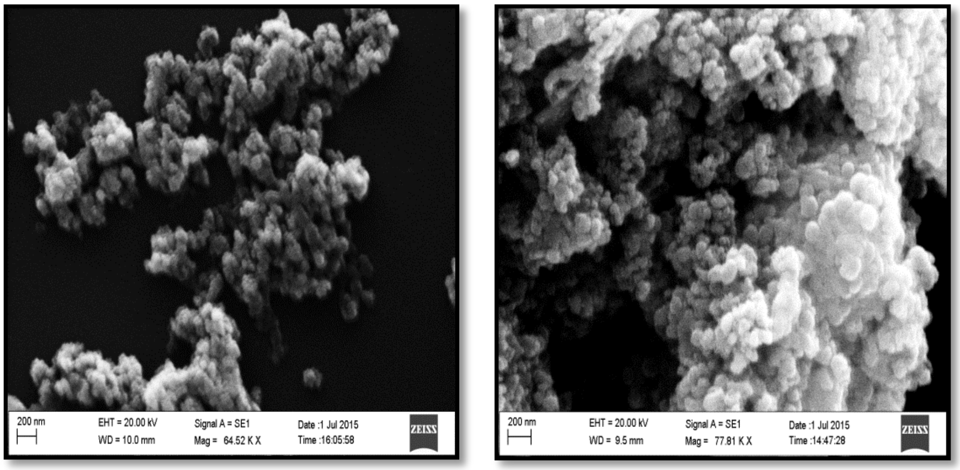

x=0.04 x=0.05

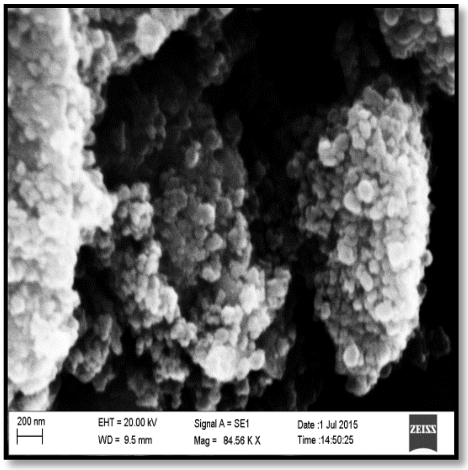

x=0.06

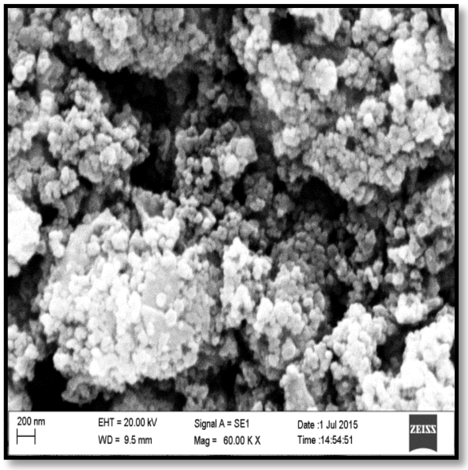

x=0.07

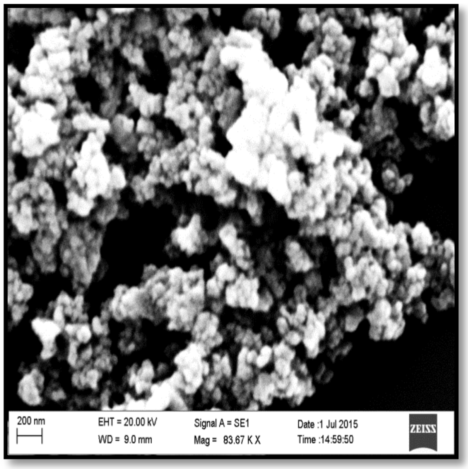

x=0.08

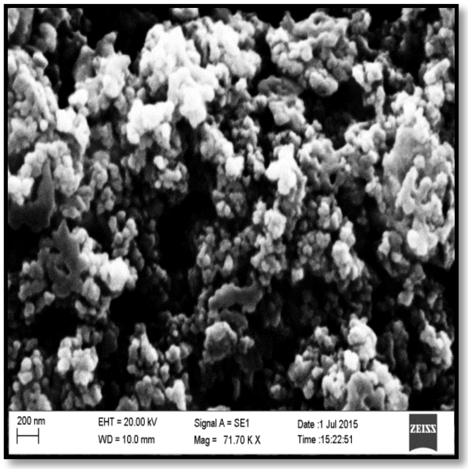

x=0.09

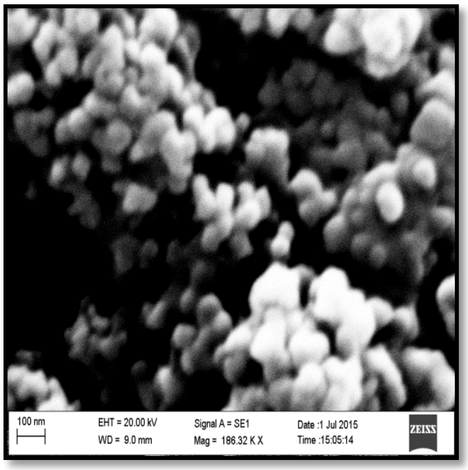

x=0.1

Figure 4.3.2 Scanning electron micrographs of $Mn_{0.65}Zn_{0.35}Fe_{2-x}Nd_xO_4$

It can be seen from all the micrographs that due to highly magnetic nature of the nanoparticles large agglomerates are formed containing numerous particles. However the presence of clusters with clear grain boundaries in nano range is clearly visible in all micrographs. The extent of agglomeration is also observed to increase due to enhancement in magnetic character due to Nd^{+3} inclusions at octahedral site, presence of surface charges and other weak surface interactions such van der Waals forces [2, 22]. The nanograins of as prepared samples were observed have spherical geometry which can be clearly seen in all the micrographs.

4.4 Transmission electron microscopy (TEM)

Figure 4.4.1 (a, b, c &d) and Figure 4.4.2 (a, b, c & d) show transmission electron micrographs and the particle size distribution histograms obtained for as prepared $Mn_{0.6}Zn_{0.4}Fe_{2-x}Nd_xO_4$ and $Mn_{0.65}Zn_{0.35}Fe_{2-x}Nd_xO_4$ with x=0.04, 0.06, 0.08 and 0.1.

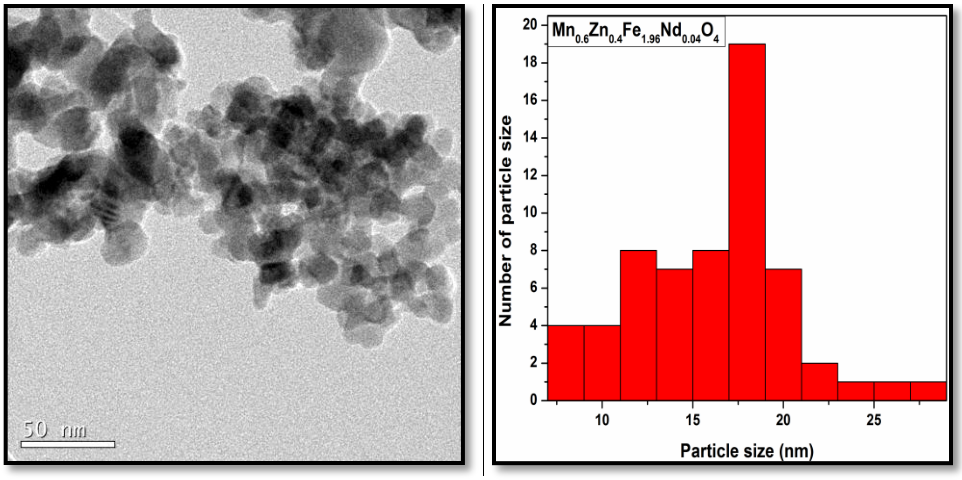

(a)

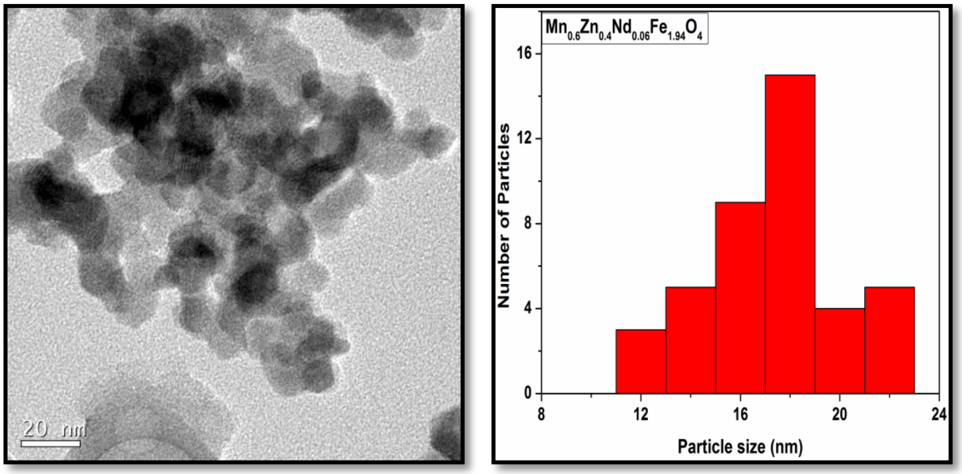

(b)

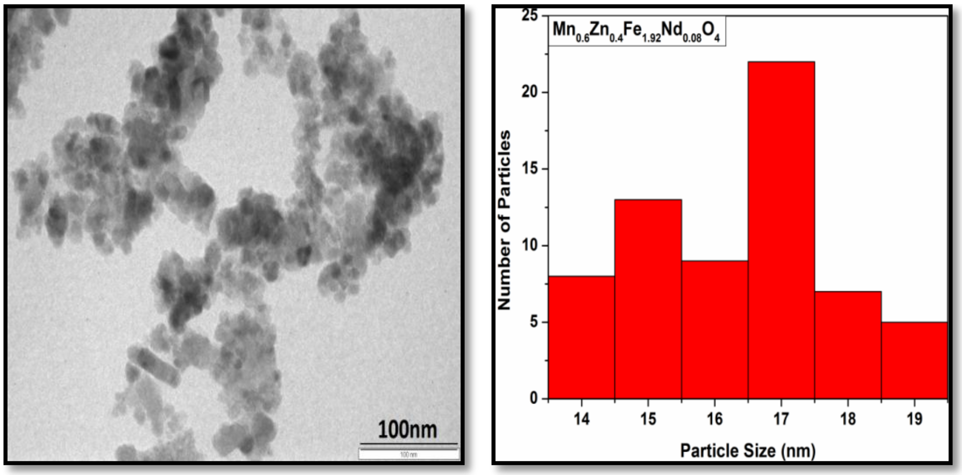

(c)

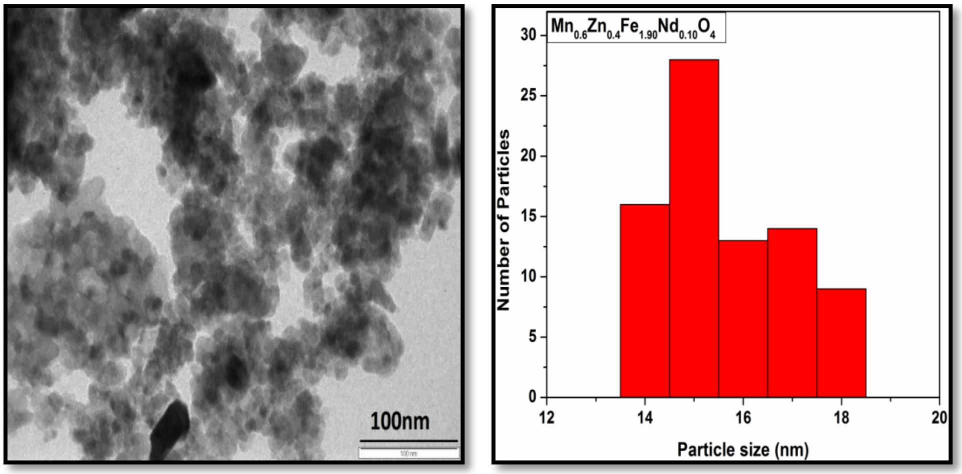

(d)

Figure 4.4.1 (a,b,c & d) Transmission electron micrographs and the particle size distribution histograms of $Mn_{0.6}Zn_{0.4}Fe_{2-x}Nd_xO_4$(x=0.04,0.06,0.08,0.1)

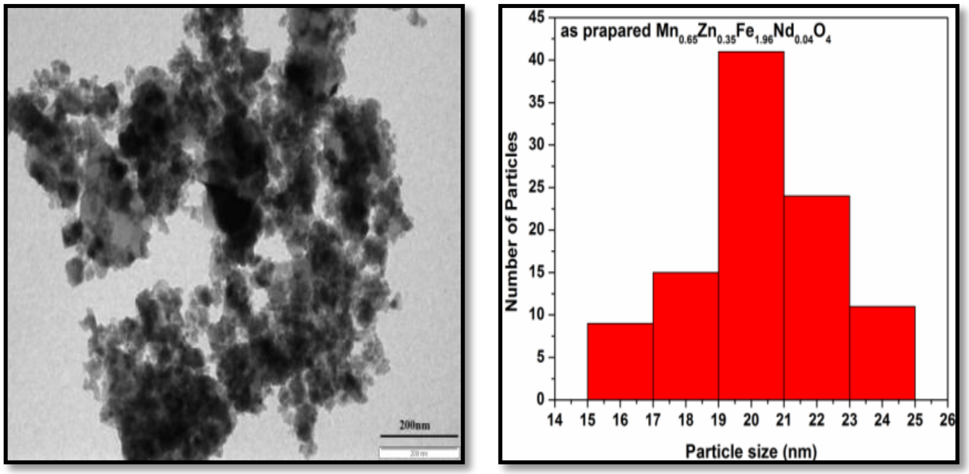
200nm
200 nm
as prapared $Mn_{0.65}Zn_{0.35}Fe_{1.96}Nd_{0.04}O_4$
Number of Particles
0
5
10
15
20
25
30
35
40
45
14
15
16
17
18
19
20
21
22
23
24
25
26
Particle size (nm)

(a)

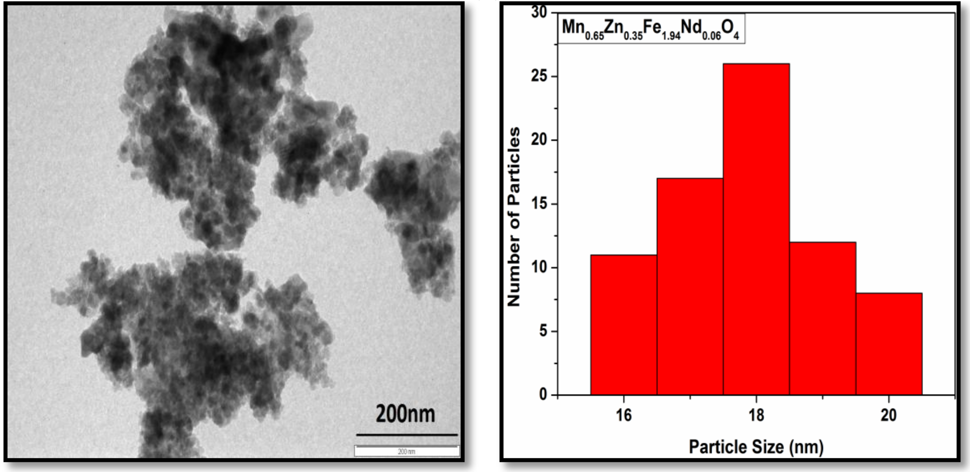
200nm
200 nm
$Mn_{0.65}Zn_{0.35}Fe_{1.94}Nd_{0.06}O_4$
Number of Particles
0
5
10
15
20
25
30
16
18
20
Particle Size (nm)

(b)

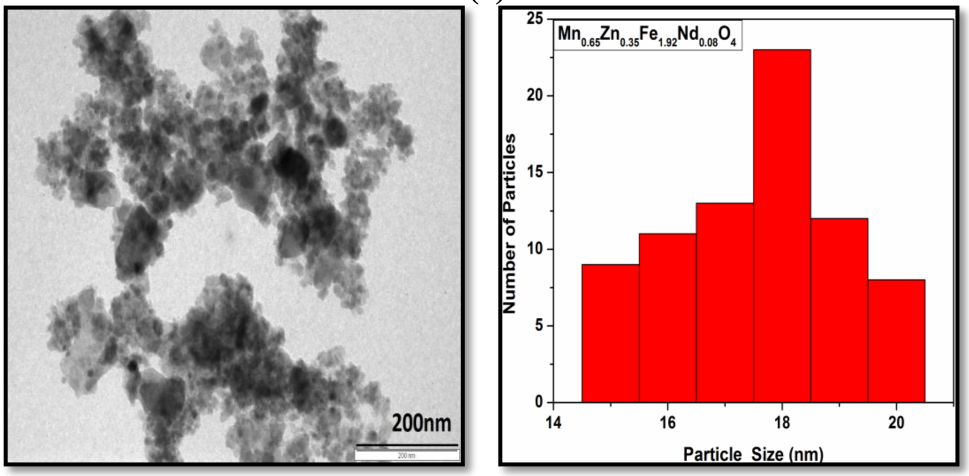
200nm
200 nm
$Mn_{0.65}Zn_{0.35}Fe_{1.92}Nd_{0.08}O_4$
Number of Particles
0
5
10
15
20
25
14
16
18
20
Particle Size (nm)

(c)

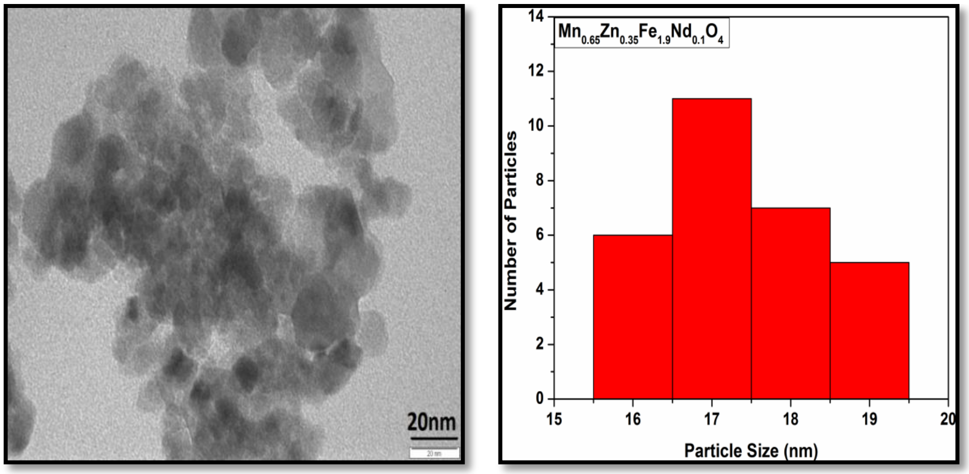

(d)

Figure 4.4.2 (a,b,c & d) Transmission electron micrographs and the particle size distribution histograms of $Mn_{0.65}Zn_{0.35}Fe_{2-x}Nd_xO_4$(x=0.04,0.06,0.08,0.1)

Table 4.4.1 Variation of particle size with Nd^{+3} concentrations for $Mn_{0.6}Zn_{0.4}Fe_{2-x}Nd_xO_4$ & $Mn_{0.65}Zn_{0.35}Fe_{2-x}Nd_xO_4$

Nd^{+3} Concentration 'x'	$Mn_{0.6}Zn_{0.4}Fe_{2-x}Nd_xO_4$ Particle Size (nm)	$Mn_{0.65}Zn_{0.35}Fe_{2-x}Nd_xO_4$ Particle Size (nm)
0.04	18±3	20±4
0.06	18±3	18±2
0.08	17±4	18±3
0.1	15±3	17±2

Since rare earth ion Nd^{+3} occupies octahedral site that produces significant strain in the lattice as well as on the grain boundaries due to its larger ionic radii, causes hindrance in the grain growth which results in particle size reduction. This reduction in particle size with increasing Nd^{+3} concentrations can be seen from table 4.4.1. Formation of large agglomerates evidently visible in transmission electron micrographs is a clear indication of strong magnetic nature of the doped nanoparticle samples [24,25].

Magnetic property exploration

4.5 Vibrating sample magnetometer (VSM)

Magnetic hysterisis loops obtained for $Mn_{0.6}Zn_{0.4}Fe_{2-x}Nd_xO_4$ and $Mn_{0.65}Zn_{0.35}Fe_{2-x}Nd_xO_4$ nanoparticles on Quantum design's Versa lab 3Tesla vibrating sample magnetometer (VSM) are shown in Figure 4.5.1 (a & b). The inserts in the Figure 4.5.1 (a & b) are the enlarged section of the central portion of hysteresis loops which show low values of remnant magnetization (M_R) and coercive field (H_C) exhibited by the Nd^{+3} doped Mn-Zn ferrite samples. Figure 4.5.2 shows the variation of saturation magnetization with Nd^{+3} concentrations.

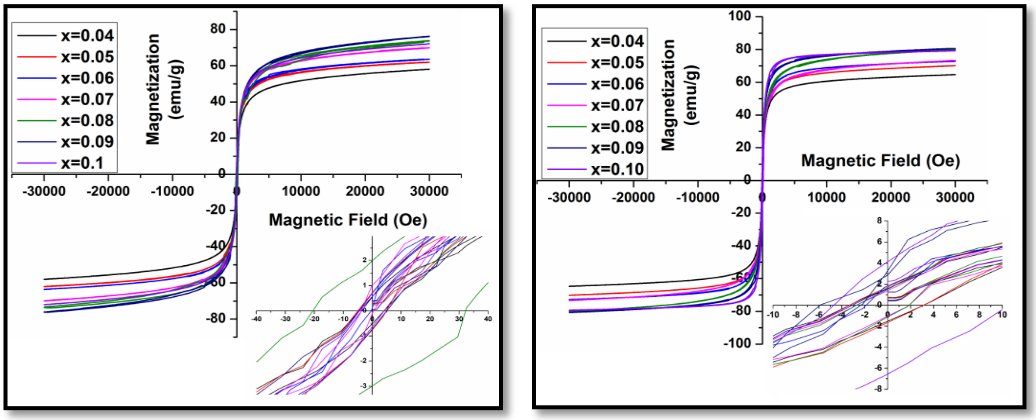

(a) (b)

Figure 4.5.1 (a&b) Hysterisis loops for $Mn_{0.6}Zn_{0.4}Fe_{2-x}Nd_xO_4$ and $Mn_{0.65}Zn_{0.35}Fe_{2-x}Nd_xO_4$ nanoparticles

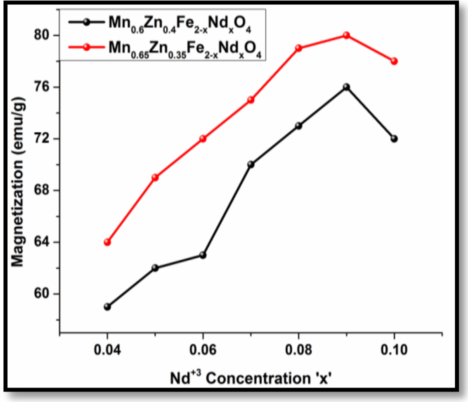

Figure 4.5.2 Variation of saturation magnetization (M_S) for $Mn_{0.6}Zn_{0.4}Fe_{2-x}Nd_xO_4$ and $Mn_{0.65}Zn_{0.35}Fe_{2-x}Nd_xO_4$ nanoparticles

Shape of the hysteresis is partially defined by domain states. One can classify the magnetic character of nanoparticles into superparamagnetic (SPM), single domain (SD), pseudo-single domain (PSD) and multi domain (MD) with the help of parameters like remnant magnetization, coercivity and the squareness value which is defined as the ratio of M_R and M_S. High coercivity values indicate the presence of single domain structure while coercivity reduces for multi domain structure. As the grain size decreases to a critical limit, the grain is unable to accommodate domain wall and the structure thus obtained is said to exhibit single domain. Multi domain is a structure large enough to accommodate multiple domain walls. For such grains M_R/M_S ratio is found to be less than 0.1. Pseudo-single domain exhibits high remnance and low coercivity. If the particle size is reduced further within the SD range another critical limit is reached at which coercivity and remanence goes to zero and the grain is termed as superparamagnetic grain. For such grains squareness values are very much less than 0.01.

Table 4.5.1 Squareness ratio (M_R/M_S) for $Mn_{0.6}Zn_{0.4}Fe_{2-x}Nd_xO_4$ and $Mn_{0.65}Zn_{0.35}Fe_{2-x}Nd_xO_4$

Nd^{+3} concentrations ‘x’	M_R/M_S Ratio for $Mn_{0.6}Zn_{0.4}Fe_{2-x}Nd_xO_4$	M_R/M_S Ratio for $Mn_{0.65}Zn_{0.35}Fe_{2-x}Nd_xO_4$
0.04	0.007	0.030
0.05	0.010	0.024
0.06	0.009	0.019
0.07	0.014	0.032
0.08	0.025	0.020
0.09	0.008	0.027
0.1	0.008	0.055

Squareness ratios calculated for $Mn_{0.6}Zn_{0.4}Fe_{2-x}Nd_xO_4$ and $Mn_{0.65}Zn_{0.35}Fe_{2-x}Nd_xO_4$ nanoparticles are listed in Table 4.5.1. Squareness values of all the samples with composition $Mn_{0.6}Zn_{0.4}Fe_{2-x}Nd_xO_4$ were observed to be less than 0.01 indicating the presence of superparamagnetic grains except for the samples with x = 0.07 and x = 0.08 depicting the presence of multidomain structured nano grains in these samples. Squareness ratio for the samples with composition $Mn_{0.65}Zn_{0.35}Fe_{2-x}Nd_xO_4$ was observed to be greater than superparamagnetic limit but much less than MD limit indicating a mixed behavior of MD and nearly SPM nature.

The magnetic behavior of manganese zinc ferrite is mainly governed by type of cations occupying tetrahedral and octahedral site. Generally Zn^{+2} ions show a strong affinity towards tetrahedral site [26] while Mn^{+2} occupy both tetrahedral and octahedral sites [27,28]. Fe being predominantly in +3 state is reported to occupy primarily octahedral site and partially tetrahedral site [29]. The net magnetic moment of ferrite unit cell is generally expressed as

$$M = |M_B - M_A| \qquad 4.5.1$$

Where M_B is the magnetic moment of octahedral site and M_A is the magnetic moment of tetrahedral site in Bohr magneton (μB). With an increase in Nd^{+3} concentration, the net magntic moment and hence saturation magnetization (MS) of rare earth doped samples is observed to increase and attain maximum value for x=0.09 beyond which the magnetization begins to decrease. The increase in magnetic moment and hence the saturation magnetization M_S is attributed to redistribution of cations at two sites triggered due to Nd^{+3} ion incorporated at octahedral site. This increase is also due to the decrease in canting Yafet-Kittel angle (θ_{YK}) between moments in B-sites. Inclusion of Nd^{+3}

(moment =3.5 μB) replacing Fe^{+3} (moment=5.6 μB) decreases B-B interaction resulting in a decrease in Yafet-Kittel angle Such a decrease in (θ_{YK}) improves the parallelism between the magnetic moments at the B site and leads to increase M_S accordance with the following equation.

$$M = |M_B Cos\theta_{YK} - M_A| \qquad 4.5.2$$

For x > 0.09 the decrease in θ_{YK} could be neglected hence the magnetization is observed to decrease as explained by equation 4.5.1 [30-33]

The magnetic moment per formula unit in Bohr magneton (μ_B) is calculated by using the following relation [34] and is shown in Figure 4.5.3(a & b)

$$\eta_B = \frac{M_X M_S}{5585} \qquad 4.5.3$$

Where M_X is the molecular weight of a particular ferrite composition and M_S is saturation magnetization (emu/g).

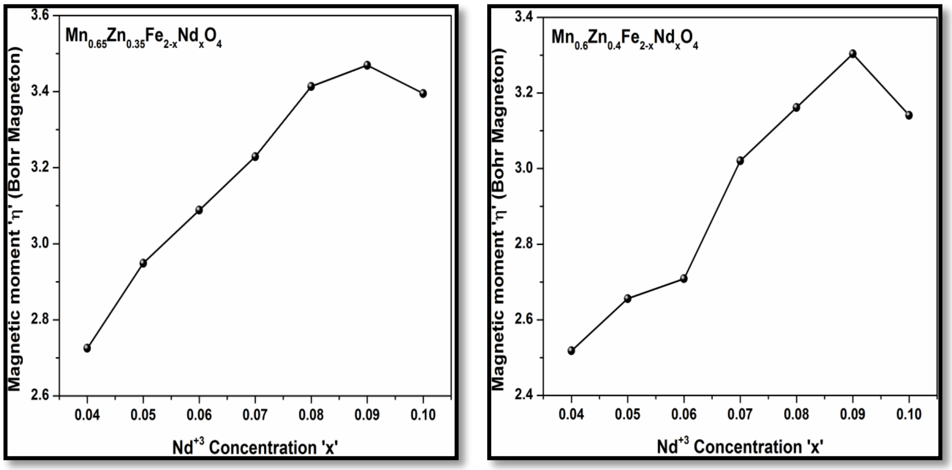

Figure 4.5.3(a & b) Variation of Magnetic moment 'η' for $Mn_{0.6}Zn_{0.4}Fe_{2-x}Nd_xO_4$ and $Mn_{0.65}Zn_{0.35}Fe_{2-x}Nd_xO_4$ nanoparticle.

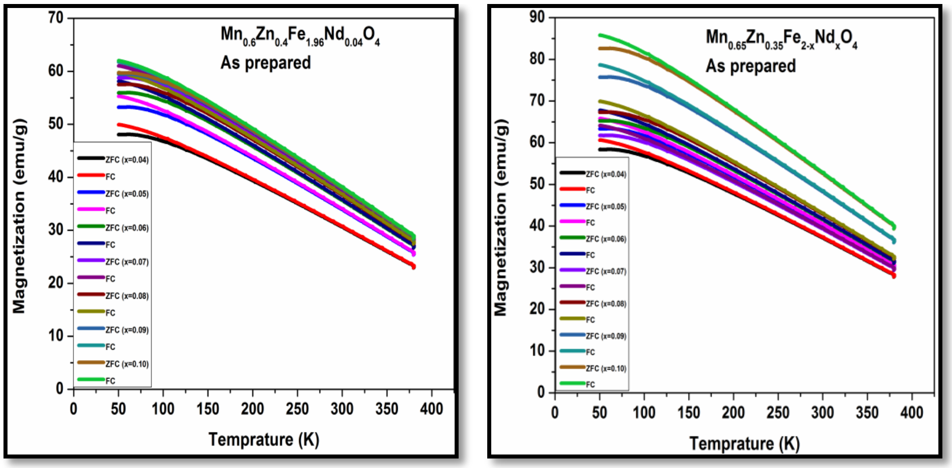

(a) (b)

Figure 4.5.4 (a & b) Field cooled (FC) and zero field cooled (ZFC) curves for $Mn_{0.6}Zn_{0.4}Fe_{2-x}Nd_xO_4$ and $Mn_{0.65}Zn_{0.35}Fe_{2-x}Nd_xO_4$ nanoparticles

Variation of magnetization as a function of temperature was also determined for as prepared $Mn_{0.6}Zn_{0.4}Fe_{2-x}Nd_xO_4$ and $Mn_{0.65}Zn_{0.35}Fe_{2-x}Nd_xO_4$ nanoparticles over the temperature range of 50K to 385K at constant applied field of 750Oe and the field cooled (FC) and zero field cooled (ZFC) curves thus obtained for all as prepared samples are shown in Figure 4.5.4 (a &b).

In zero field cooled (ZFC) measurement, the sample is cooled down to 50 K from room temperature in the absence of external magnetic field. The nanoparticles get cooled with their moments in random directions. An external magnetic field corresponding to the initial magnetization is applied and moment of the sample is measured by increasing the temperature. In field cooled (FC) measurement, the sample is cooled in the presence of an applied field and the moment at different temperature is recorded. In the beginning of ZFC measurement, the moments are aligned in random directions.

The anisotropy energy acts as an energy barrier, given by

$$E_{\mathrm{anis}} = \mathrm{KV} \tag{4.6.1}$$

Where K is anisotropy constant and V is the particle volume. This energy maintains the spins alignment along easy axis. As the temperature increases more and more spins align along easy axis resulting in increase in net magnetic moment and hence magnetization increases. At particular temperature when the thermal energy given by equation 4.6.2 equals anisotropy energy the moment becomes maximum. This temperature is called blocking temperature T_B.. Beyond this temperature thermal energy becomes more than anisotropy energy breaking the alignment of the spins and the moment decreases with increasing temperature.

$$\mathrm{E}_{\mathrm{Thermal}} = \mathrm{k}_B\mathrm{T} \qquad 4.6.2$$

Where k_B is the Boltzmann constant. In the presence of external magnetic field the particles have Zeeman energy given by equation 4.6.3

$$\mathrm{E}_{\mathrm{Zeeman}} = \mathrm{mH} \qquad 4.6.3$$

This energy tries to align the moment in the field direction causing an increase in the susceptibility. Hence the moment of FC curve is higher than that of ZFC curve. However, with increasing temperature thermal energy component dominates anisotropy energy and Zeeman energy terms resulting in reduction of moment and hence the magnetization of the material.

When the particle size distribution in the material is not uniform, T_B varies as a function of particle size distribution. The spins of smallest of the particles freeze at lower temperature at which the moment of ZFC curve is maximum. This temperature is denoted as T_{MAX}. Spins of biggest particles free as higher temperature. This temperature is dented as T_{DIFF} which is also a bifurcation point of FC and ZFC curves and called is the irreversibility temperature, T_{IRR}. This is the highest blocking temperature corresponding to largest particles in the material [35-37]. T_{MAX} and T_{DIFF} define the distribution of blocking temperature T_B. The values of T_{MAX} and T_{DIFF} obtained from FC and ZFC curves for as prepared $Mn_{0.6}Zn_{0.4}Fe_{2-x}Nd_xO_4$ and $Mn_{0.65}Zn_{0.35}Fe_{2-x}Nd_xO_4$ nanoparticles are listed in Table 4.5.2

Table 4.5.2 variation of T_{MAX} and T_{DIFF} obtained for as prepared $Mn_{0.6}Zn_{0.4}Fe_{2-x}Nd_xO_4$ and $Mn_{0.65}Zn_{0.35}Fe_{2-x}Nd_xO_4$ nanoparticles

Nd^{+3} concentration 'x'	$Mn_{0.6}Zn_{0.4}Fe_{2-x}Nd_xO_4$		$Mn_{0.65}Zn_{0.35}Fe_{2-x}Nd_xO_4$	
	T_{MAX} (K)	T_{DIFF} (K)	T_{MAX} (K)	T_{DIFF} (K)
0.04	70	118	71	121
0.05	70	116	70	120
0.06	69	117	70	119
0.07	70	115	69	117
0.08	68	117	68	118
0.09	69	116	69	117
0.1	67	116	68	118

The narrow distribution of blocking temperature (T_B) indicates uniform distribution of particles size. The ZFC curves show broad maxima indicating the superparamagnetic behavior for all samples. For temperature below T_B the moment of ZFC curve remains almost constant while the FC curve was observed to follow a slow increasing trend which can be attributed to inter-particle interaction which enhances the anisotropy, making moments pinned to one another and the thermal energy is too small to overcome the energy barriers. At $T > T_B$ both curves follow decrease of moment obeying Curie-Weiss law.

4.6 Mössbauer spectroscopy

Figure 4.6.1 and Figure 4.6.2 show Mössbauer spectra of $Mn_{0.6}Zn_{0.4}Fe_{2-x}Nd_xO_4$ and $Mn_{0.65}Zn_{0.35}Fe_{2-x}Nd_xO_4$ nanoparticles recorded at room temperature in the velocity of ±11.5 mm/s using conventional Mössbauer spectrometer. Mössbauer spectra for Nd^{+3} doped samples are fitted with three sextets and a superparamagnetic doublet. The presence of these sextets can be attributed to superexchange interaction between the magnetic ions at A– and B–sub-lattices.

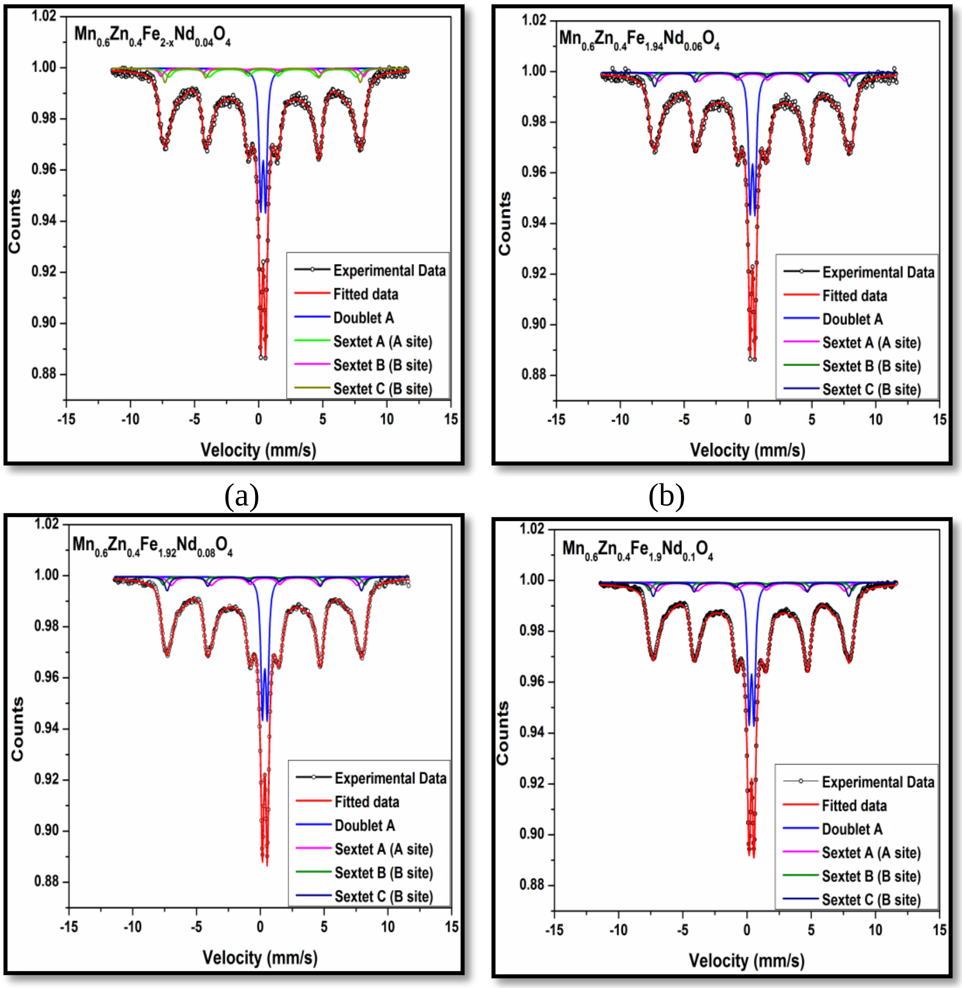

(a) (b)

(a) (b)

Figure 4.6.1 Mossbauer spectra for as prepared $Mn_{0.6}Zn_{0.4}Fe_{2-x}Nd_xO_4$ nanoparticles

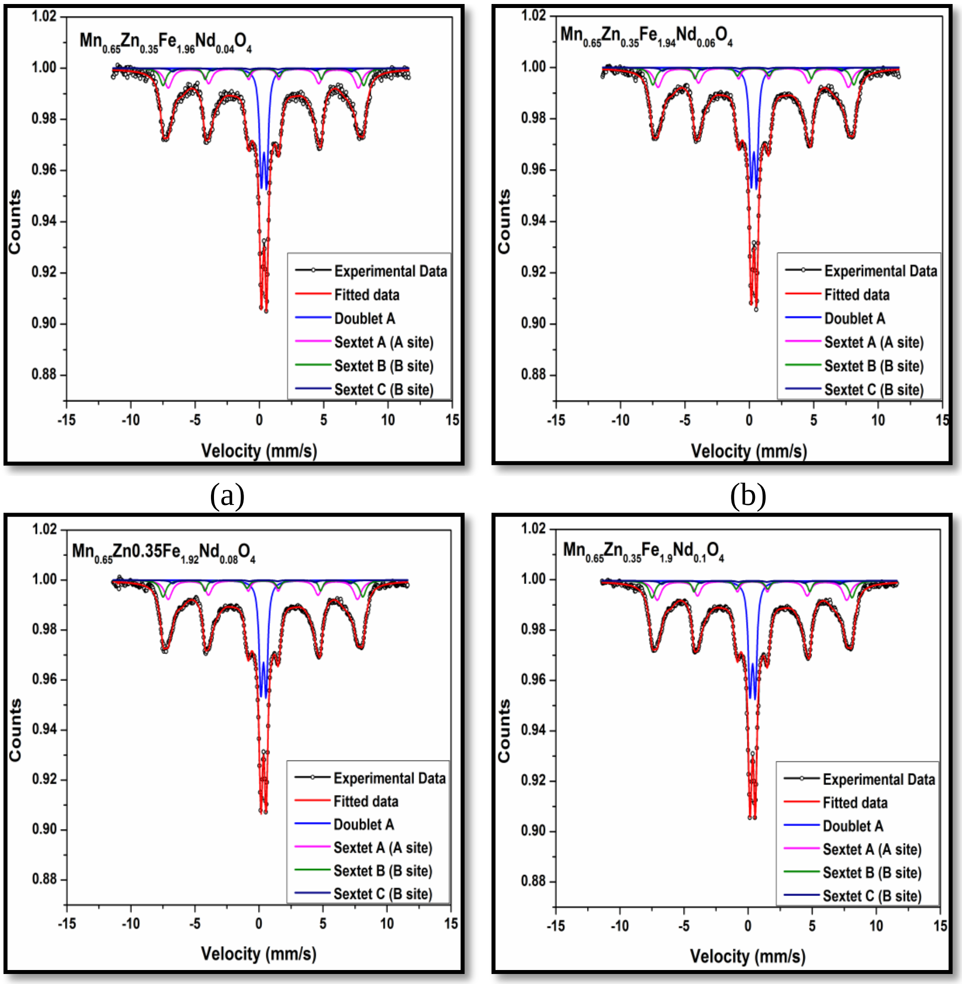

(a) (b)

(c) (d)

Figure 4.6.2 Mossbauer spectra for as prepared $Mn_{0.65}Zn_{0.35}Fe_{2-x}Nd_xO_4$ nanoparticles

Table 4.6.1a Calculated values of isomer shift (IS), quadrupole splitting (QS) and hyperfine magnetic field for $Mn_{0.6}Zn_{0.4}Fe_{2-x}Nd_xO_4$.

Sample	Iron site spectra	Isomer shift (IS) mm/s	Qudrupole splitting (QS) mm/s	Hyperfine field (Tesla)	Relative area (%)
X=0.04	Doublet (S. P.)	0.349±0.002	0.470±0.004	-	35.13
	Sextet A (Octa)	0.398±0.012	0.036±0.008	46.72±0.12	16.84
	Sextet B (Octa)	0.323±0.021	0.046±0.011	42.78±0.31	16.35
	Sextet C (Tetra)	0.293±0.021	0.020±0.003	35.07±0.91	31.68
X=0.06	Doublet (S. P.)	0.342±0.032	0.448±0.012	-	37.33
	Sextet A (Octa)	0.368±0.042	0.038±0.013	46.98±1.27	16.81
	Sextet B (Octa)	0.333±0.052	0.048±0.006	43.11±1.64	16.66

	Sextet C (Tetra)	0.298±0.029	0.038±0.009	28.33±2.13	29.20
X=0.08	Doublet (S. P.)	0.348±0.048	0.435±0.018	-	39.61
	Sextet A (Octa)	0.349±0.067	0.043±0.032	47.54±0.88	16.75
	Sextet B (Octa)	0.369±0.066	0.045±0.011	43.66±1.34	16.81
	Sextet C (Tetra)	0.294±0.018	0.047±0.027	20.21±0.98	26.83
X=0.1	Doublet (S. P.)	0.348±0.048	0.416±0.071	-	41.33
	Sextet A (Octa)	0.337±0.067	0.068±0.017	47.89±0.17	16.69
	Sextet B (Octa)	0.369±0.066	0.047±0.021	43.81±1.23	17.11
	Sextet C (Tetra)	0.289±0.018	0.046±0.033	19.61±1.45	24.87

Table 4.6.2a Calculated values of isomer shift (IS), quadrupole splitting (QS) and hyperfine magnetic field for $Mn_{0.65}Zn_{0.25}Fe_{2-x}Nd_xO_4$.

Sample	Iron site spectra	Isomer shift (IS) mm/s	Qudrupole splitting (QS) mm/s	Hyperfine field (Tesla)	Relative area (%)
X=0.04	Doublet (S. P.)	0.333±0.021	0.390±0.012	-	37.21
	Sextet A (Octa)	0.389±0.022	0.019±0.011	46.36±0.11	21.03
	Sextet B (Octa)	0.396±0.031	0.054±0.021	43.68±0.26	15.93
	Sextet C (Tetra)	0.289±0.009	0.031±0.007	34.33±0.73	25.83
X=0.06	Doublet (S. P.)	0.348±0.027	0.441±0.024	-	37.85
	Sextet A (Octa)	0.355±0.051	0.069±0.009	47.05±1.36	20.71
	Sextet B (Octa)	0.327±0.052	0.043±0.011	42.88±0.76	17.12
	Sextet C (Tetra)	0.288±0.036	0.075±0.027	29.66±1.03	24.32
X=0.08	Doublet (S. P.)	0.357±0.037	0.463±0.011	-	39.21
	Sextet A (Octa)	0.359±0.067	0.068±0.013	48.88±1.12	21.10
	Sextet B (Octa)	0.355±0.066	0.048±0.022	42.18±0.55	16.65
	Sextet C (Tetra)	0.301±0.013	0.033±0.004	22.36±0.73	23.04
X=0.1	Doublet (S. P.)	0.348±0.048	0.399±0.001	-	41.30
	Sextet A (Octa)	0.316±0.058	0.052±0.033	46.38±0.22	20.45
	Sextet B (Octa)	0.379±0.056	0.049±0.009	43.53±0.88	16.22
	Sextet C (Tetra)	0.289±0.018	0.056±0.038	20.63±1.22	22.13

The presence of Mössbauer active ion in three different environments is confirmed from three sextets along with the paramagnetic doublet in the Mössbauer spectra of rare earth (Nd) doped samples which also confirm the ferrimagnetic nature of the samples.

The broad doublet present in all spectra indicates the existence of super paramagnetic nature in all rare earth doped samples. The increase in relative area of super paramagnetic doublet with increasing Nd^{+3} concentrations indicates the enhancement in super paramagnetic behavior. Out of remaining three sub-spectra, one corresponds to the tetrahedral site Fe ion and rest two to the octahedral site Fe ion. The isomer shift (IS), quadrupole splitting (QS) and hyperfine field (H_{hf}) calculated from the fitting of spectra of Nd^{+3} doped samples were calculated.

The non-zero volume of the nucleus and the electron charge density due to s-electrons within the vicinity of the nucleus gives rise to isomer shift which leads to a monopole interaction, altering the nuclear energy levels. Any variation in the s-electron environment between the absorber and source thus produces a shift in the resonance energy of the transition. This causes the spectra to shift either in the positive direction or negative direction based upon the s-electron density, and fixes the centroid of the spectrum. Isomer shift for octahedral (B) sites is more than that of the tetrahedral (A) sites due to larger bond length between Fe^{3+}-O in cubic spinel ferrites as compared to that for tetrahedral sites [38]. As a result over lapping of orbitals of Fe^{3+} ions is smaller at octahedral (B) sites and thus, a larger IS is produced indicating a higher s- electron density at B site [39]. The IS is a physical parameter for determining the valence state of Mössbauer active atom. It is reported that the IS values for Fe^{3+} lie in the range 0.1–0.5 mm/s [40]. By comparing the values in Table 4.6.1 and Table 4.6.2 of the samples with reported values we can conclude the presence of iron in Fe^{3+} state at octahedral and tetrahedral site.

Non-zero quadrupole splitting occurs due to chemical disorder in the material, results in an electric field gradient (EFG) of varying magnitude, directions, sign and symmetry. It is observed that paramagnetic doublet appears in all spectra within the sextet due to the interaction of electric field gradient (EFG) with the quadruple moment of ^{57}Fe nucleus and reduction in magnetic interaction between Fe^{+3} ions due to inclusion of Nd^{+3} ions and non magnetic Zn^{+2} ions [41-43].

Generally in ferrites B-site hyperfine field is greater than that of A-site and the similar trend was observed in Nd^{+3} doped samples. The hyperfine field at B site is observed to increase due to inclusion of Nd^{+3} at octahedral site where as the hyperfine field at A-site was found to decrease due to lower occupancy of iron and presence on non magnetic Zn^{+2} ion. The hyperfine magnetic field and area of sextet corresponding to tetrahedral site is seen to decrease with increasing Nd^{+3} concentration at octahedral site due to reduction in Yaffet Kittel angle . For composition $x = 0.04$, large amount Fe^{+3} ions occupy tetrahedral site, and hence the area of sextet for tetrahedral site was found to be maximum. This is also confirmed from VSM results wherein $x=0.04$ shows the lowest value of saturation magnetization (M_S) [44]. Increase in relative area of paramagnetic doublet at the expense of relative area of magnetic sextets indicates the enhanced superparamagnetic behavior due to dominance of Nd^{+3} at octahedral site. Thus the Mossbauer data confirms the presence of Fe^{+3} at both octahedral and tetrahedral sites and enhancement of Nd^{+3} at octahedral site is responsible for the enhancement of superparamagnetic behavior in the samples.

4.7 Relative permeability

Relative permeability 'μ_r' is an important magnetic parameter, which decides the suitability of a ferrite material for high frequency application. Figure 4.7.1(a,b) shows the variation of relative permeability 'μ_r' with frequency for as prepared $Mn_{0.6}Zn_{0.4}Fe_{2-x}Nd_xO_4$ and $Mn_{0.65}Zn_{0.35}Fe_{2-x}Nd_xO_4$ nanoparticles over the frequency range of 20Hz to 3MHz.

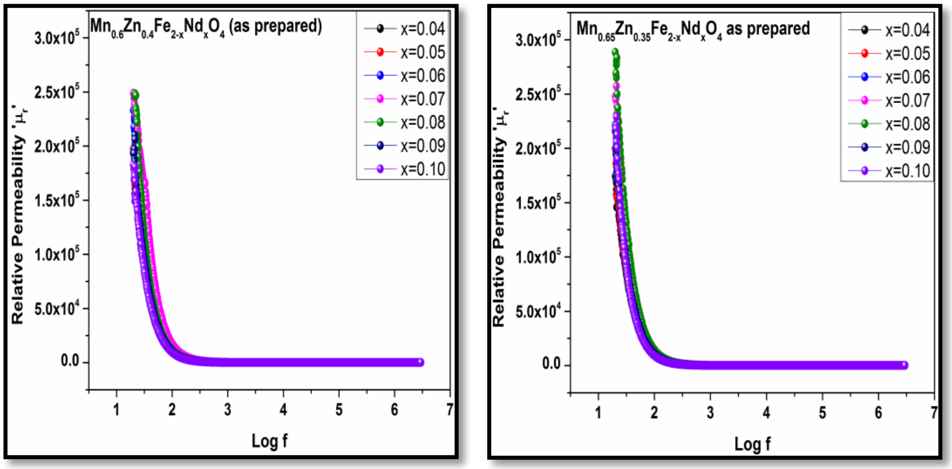

(a) (b)

Figure 4.7.1 (a, b) Variation of relative permeability 'μ_r' of $Mn_{0.6}Zn_{0.4}Fe_{2-x}Nd_xO_4$ and $Mn_{0.65}Zn_{0.35}Fe_{2-x}Nd_xO_4$ nanoparticles

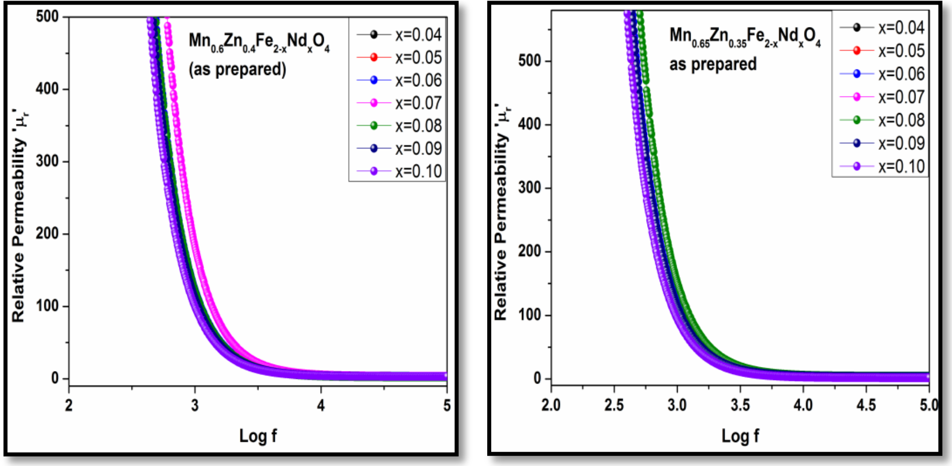

(a) (b)

Figure 4.7.2 (a, b) Variation of relative permeability 'μ_r' of $Mn_{0.6}Zn_{0.4}Fe_{2-x}Nd_xO_4$ and $Mn_{0.65}Zn_{0.35}Fe_{2-x}Nd_xO_4$ nanoparticles in frequency range of 100Hz to 100kHz

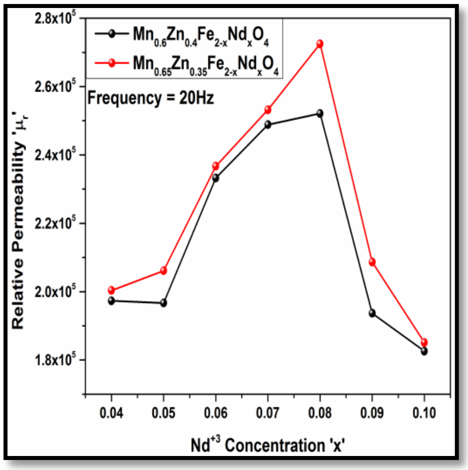

Figure 4.7.3 Variation of relative permeability 'μ_r' of $Mn_{0.6}Zn_{0.4}Fe_{2-x}Nd_xO_4$ and $Mn_{0.65}Zn_{0.35}Fe_{2-x}Nd_xO_4$ nanoparticles at 20Hz

Relative permeability 'μ_r' is an important magnetic parameter, which decides the suitability of a ferrite material for high frequency application. Figure 4.7.1(a,b) shows the variation of relative permeability 'μ_r' with frequency for as prepared $Mn_{0.6}Zn_{0.4}Fe_{2-x}Nd_xO_4$ and $Mn_{0.65}Zn_{0.35}Fe_{2-x}Nd_xO_4$ nanoparticles over the frequency range of 20Hz to 3MHz. Variation of relative permeability 'μ_r' with Nd^{+3} concentration at 20Hz for as prepared $Mn_{0.6}Zn_{0.4}Fe_{2-x}Nd_xO_4$ and $Mn_{0.65}Zn_{0.35}Fe_{2-x}Nd_xO_4$ nanoparticles is presented in Figure 4.7.3. At lower frequencies permeability of the material was observed to increase from $2x10^5$ for Nd^{+3} concentrations x=0.04 to a maximum of $2.4x10^5$ for x=0.08 for as prepared $Mn_{0.6}Zn_{0.4}Fe_{2-x}Nd_xO_4$ samples. The enlarged section of permeability curves over the frequency range of 100 Hz to 100kHz are shown in the Figure 4.7.2 (a, b) which clearly indicate that permeability values for all the samples are of the order of 10^2 up to 1000Hz and decreases further to a very low nonzero value for higher frequencies. For higher concentrations of Nd^{+3}, permeability is observed to decrease and attain minimum value of $1.81x10^5$ for x=0.1. Similarly for as prepared $Mn_{0.65}Zn_{0.35}Fe_{2-x}Nd_xO_4$ nanosamples, permeability values is observed to increase from $2.1x10^5$ for x=0.04 to a maximum of $2.76x10^5$ for x=0.08 followed by a decrease up to $1.82x10^5$ for x=0.1. The increasing trend Permeability values from x=0.04 to x=0.08 for $Mn_{0.6}Zn_{0.3}Fe_{2-x}Nd_xO_4$ and $Mn_{0.65}Zn_{0.35}Fe_{2-x}Nd_xO_4$ nanosamples indicate better magnetic ordering of domains, reduced distortions in the crystals and lower defects. Reduction in permeability with higher concentrations of Nd^{+3} can be attributed to the lattice defects and strain introduced in the lattice disturbing the magnetic ordering and formation of pinning centers hamper domain wall motion. Permeability was observed to decrease rapidly with increasing frequency for all the nanosamples as the materials are composed of single domain nanoparticle which posses lower stability towards higher frequencies being superparamagnetic in nature.

Electrical transport property exploration

4.8 D. C. Resistivity

Figure 4.8.1 (a & b) shows variation of DC resistivity (ρ) as a function of temperature for as prepared $Mn_{0.6}Zn_{0.4}Fe_{2-x}Nd_xO_4$ and $Mn_{0.65}Zn_{0.35}Fe_{2-x}Nd_xO_4$ nanoparticles. Room temperature variation of resistivity values with Nd^{+3}concentration is shown in Figure 4.8.2 (a, b). The overall room temperature resistivity of all the samples is very high and is of the order of 10^9 Ohm-cm. This is due to a couple of reasons. Firstly the samples are composed of nanoparticles of very small crystallite sizes ranging from 13nm to 18nm. This actually amounts to a huge increase in the grain boundary available in the sample. The charge carrier tunneling through grain boundary has a large contribution to in enhancing the resistivity of the sample. Secondly since the samples are Nd^{+3} doped the samples are deficient of Fe^{+3} ions which are actually the generators of charge carriers. Thus the deficiency of charge carriers is another factor responsible for enhancement of resistivity of the samples. Thus one can effectively say that inclusion of Nd^{+3} at octahedral site also inhibits the electron hopping mechanism responsible for conduction process as it increases the lattice constant of the sample. All the resistivity curves showed two regions the first one in the temperature range of 300K to 440K and the second in 441K to 773K range. In the first region the resistivity profile shows a small decrement in the resistivity as we move from 300K to 441K that can be seen in Figure 4.8.1 (a & b). The thermal energy available in this region ranges from 0.03 to 0.04 eV. This energy is not sufficient for the generation of free charges and can only be utilized in increasing the velocity of available free charges in the lattice and also for the release of trapped charges.

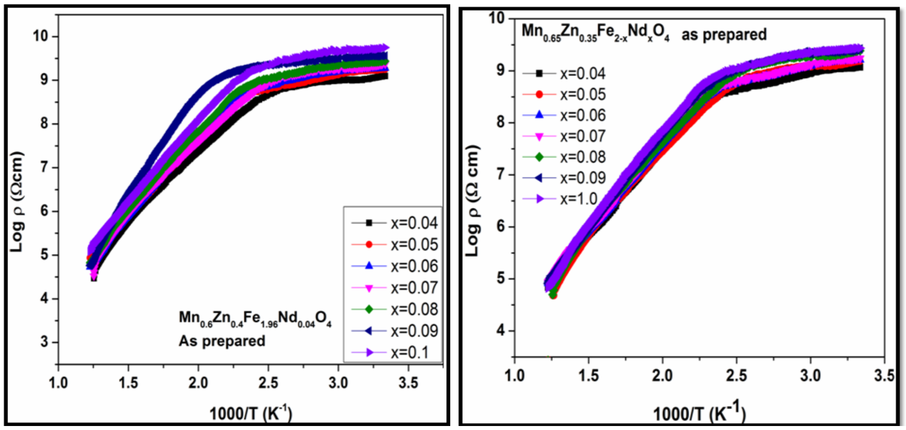

(a) (b)

Figure 4.8.1 (a & b) Variation of D.C. resistivity of $Mn_{0.6}Zn_{0.4}Fe_{2-x}Nd_xO_4$ and $Mn_{0.65}Zn_{0.35}Fe_{2-x}Nd_xO_4$ nanoparticles

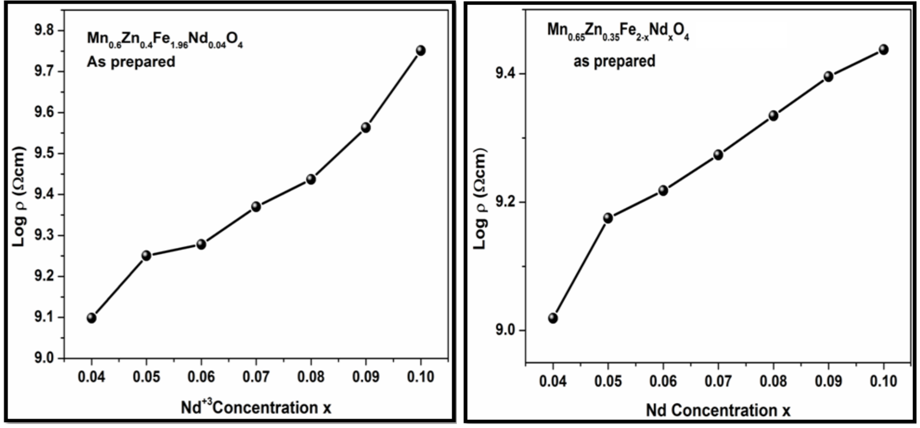

(a) (b)

Figure 4.8.2 (a & b) Variation of room temperature D.C. resistivity of $Mn_{0.6}Zn_{0.4}Fe_{2-x}Nd_xO_4$ and $Mn_{0.65}Zn_{0.35}Fe_{2-x}Nd_xO_4$ nanoparticles

The slope of all the plots in this region is very small. Normally a broad peak in resistivity is expected in this region that is due to activation of phonon vibrations which results in scattering of charge carriers. However such behavior is not observed in the resistivity profiles of all the samples. This can be due to enhancement observed in the lattice constant and damping of phonon vibrations due to introduction of Nd^{+3} ions at octahedral site. Nd^{+3} ions being large and heavy ion requires a larger amount of energy to produce phonon vibrations sufficient to scatter charge carriers which are now reduced in number as Fe^{+3} ions have been replaced by Nd^{+3} ions. Therefore the thermal energy is easily gained by the charge carriers which increase their kinetic energy to some extent. This is indicated in the resistivity profile by a slower fall of resistivity in initial stages before the thermal energy equals the activation energy of the sample. Partially the high value of resistivity in this region may be also attributed to poor charge mobility as notified earlier. In the second region (beyond 441K) all the plots obey Arrhenius relation, depicting semiconductor like behavior [45]. It may be seen from the plots that the resistivity drops very sharply from its higher value from 10^9 to 10^4 within a temperature band of 441K to 773K. This phenomenon is similar to the ones observed in semiconductors and in most of the nanoparticle ferrite materials. However a direct comparison of these values of resistivity obtained for Nd^{+3} doped samples with the resistivity trends obtained for undoped Manganese Zinc ferrite nanoparticle samples reported in previous reports [46, 47] suggest that the Nd^{+3} doping has an essential feature of eliminating eddy current losses as far as applications are concerned. Gradual increase in activation energy E_a as Nd^{+3} concentration increases in the samples can be attributed to the increasing Nd^{+3} concentrations at octahedral site (B site) which reduces Fe^{+3}occupancy marginally.

Larger ionic radii of Nd^{+3} ions in addition to reducing the electron hopping rate by increasing the lattice constant is also responsible for increasing the separation between Fe^{+2} and Fe^{+3} ions. This increase adversely affects the hopping rate of charge carriers between Fe^{+2}/Fe^{+3} Fe^{+2}/Mn^{+3} and Mn^{+2}/Mn^{+3} ions. Activation energy for $Mn_{0.6}Zn_{0.4}Fe_{2-x}Nd_xO_4$ and $Mn_{0.65}Zn_{0.35}Fe_{2-x}Nd_xO_4$ as calculated from resistivity plots is tabulated in table 4.8.1. It may be seen that the activation energy for $Mn_{0.6}Zn_{0.4}Fe_{2-x}Nd_xO_4$ samples is higher compared to the values obtained for $Mn_{0.65}Zn_{0.35}Fe_{2-x}Nd_xO_4$ samples which is due to higher manganese content in the later series.

Table 4.8.1 Activation energy (Ea) obtained from resistivity plots of $Mn_{0.6}Zn_{0.4}Fe_{2-x}Nd_xO_4$ and $Mn_{0.65}Zn_{0.35}Fe_{2-x}Nd_xO_4$

Concentrations of Nd^{+3} 'x'	Activation energy (eV) $Mn_{0.6}Zn_{0.4}Fe_{2-x}Nd_xO_4$	Activation energy (eV) $Mn_{0.65}Zn_{0.35}Fe_{2-x}Nd_xO_4$
0.04	0.20	0.18
0.05	0.20	0.19
0.06	0.21	0.21
0.07	0.20	0.21
0.08	0.22	0.22
0.09	0.22	0.21
0.1	0.24	0.23

At higher temperature region large amount of energy is available for liberation of trapped charge carriers and accordingly large numbers of secondary electrons move in the conduction band and help the conduction process thereby lowering the resistivity of the material. Reduction in resistivity can be also attributed to alteration of Fe^{+2}/ Fe^{+3} ions ratio and presence of Fe^{+3} in high spin state with larger ionic radius on both the sites resulting in lower separation between the ions irrespective of enhancement in the lattice constant caused by Nd^{+3} inclusion in the sample [48]. It can be also attributed to increase in drift mobility of thermally activated charge carriers at higher temperatures [48,49]. The variation of drift mobility 'μ_d' for all the samples was determined using equation 4.8.1 and is shown in Figure 4.8.3 (a & b)

$$\boldsymbol{\mu_d} = \frac{1}{ne\rho} \qquad 4.8.1$$

Where ρ is electrical resistivity, e is the electron charge and n is the charge carrier concentration which is calculated from following equation 4.8.2.

$$n = \frac{N_a X_M C_{Fe/Mn}}{M} \qquad 4.8.2$$

Where N_a is the Avogadro's number, X_M is the bulk density; M is the molar mass of the samples, $C_{Fe/Mn}$ is the number of Fe and Mn atoms in the chemical formula of the samples [50].

Drift mobility was found to exhibit very low values for all the samples in the lower temperature region of 300K to 440K as the thermal energy available in this temperature region is extremely low. However it rises very slowly with increasing temperature moving towards a transitional phase at about 440K wherein there is a dramatic rise in the drift mobility. Eventually this slow rising mobility up to 440K appears in the resistivity plots as a slow fall of resistivity values up to 440K. Beyond this temperature of 440K the drift mobility of the charge carriers that is seen to increase sharply in the temperature region of 441K to 773K also shows it resemblance in the resistivity curves, as a rapid fall in the resistivity.

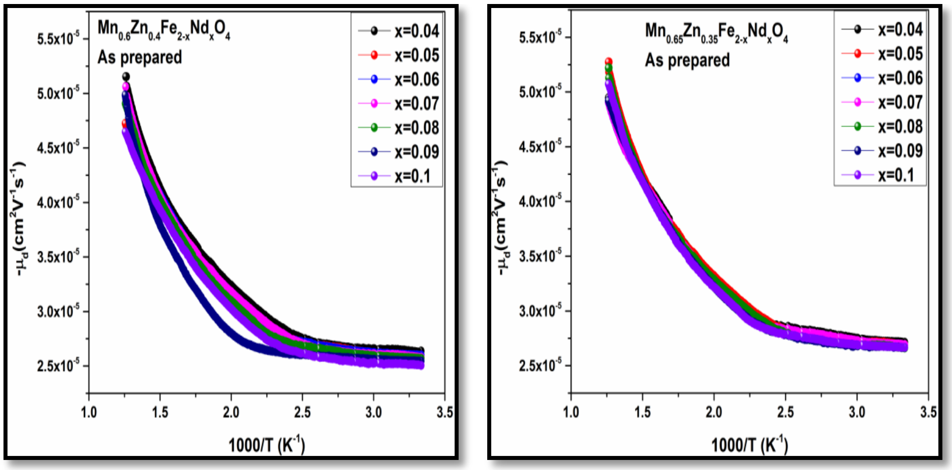

(a) (b)

Figure 4.8.3 (a & b) Variation of drift mobility of charge carriers with temperature $Mn_{0.6}Zn_{0.4}Fe_{2-x}Nd_xO_4$ and $Mn_{0.65}Zn_{0.35}Fe_{2-x}Nd_xO_4$ nanoparticles

This can be due to two reasons, firstly as the energy supplied is more than activation energy that increases with rising temperature, more charge carries are pumped in to the conduction band, and secondly the excess energy is supplied to these charge carriers as kinetic energy. Thus the charge carrier motion is more rapid in this region which brings down the resistivity drastically from an order to 10^9 to 10^4. This whole phenomenon can be actually has a resemblance to a second order phase transition.

4.9 Dielectric constant variation with frequency

Variation of dielectric constant 'ε' as a function of frequency with increasing Nd^{+3} concentrations for $Mn_{0.6}Zn_{0.4}Fe_{2-x}Nd_xO_4$ and $Mn_{0.65}Zn_{0.35}Fe_{2-x}Nd_xO_4$ nanoparticles is shown in Figure 4.9.1(a,b). Rare earth doped samples were observed to exhibit higher dielectric values as compared to the values reported for undoped Mn-Zn ferrite nanoparticles [46,47]. At lower frequencies the values of dielectric constant are seen to be higher for all the samples belonging to $Mn_{0.65}Zn_{0.35}Fe_{2-x}Nd_xO_4$ series as compared to the values obtained for $Mn_{0.6}Zn_{0.4}Fe_{2-x}Nd_xO_4$ nanosamples. This enhancement can be attributed to the higher $Mn^{+2/+3}$ content present in $Mn_{0.65}Zn_{0.35}Fe_{2-x}Nd_xO_4$ nanosamples. It can be clearly seen from figure 4.9.1(a,b) that with increasing Nd^{+3} dielectric constant is decreasing for all the samples.

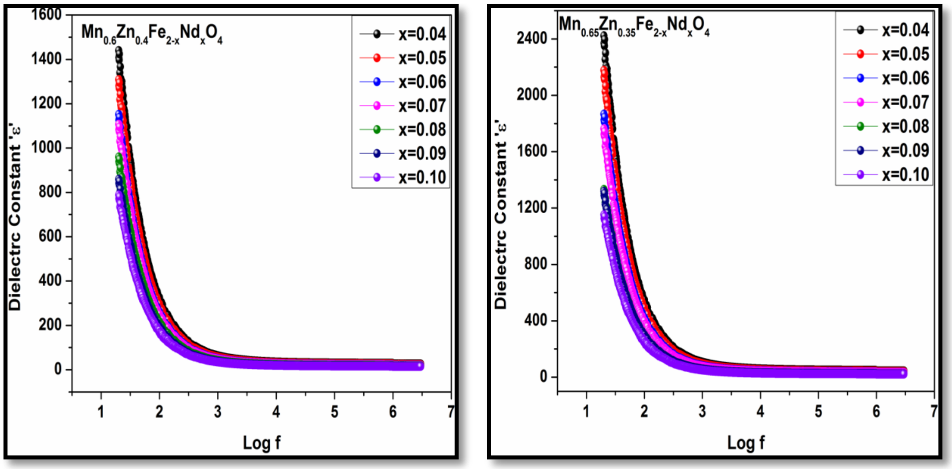

(a) (b)

Figure 4.9.1 (a & b) Variation of Dielectric constant 'ε' with frequency of $Mn_{0.6}Zn_{0.4}Fe_{2-x}Nd_xO_4$ and $Mn_{0.65}Zn_{0.35}Fe_{2-x}Nd_xO_4$ nanoparticles

Dielectric properties of a ferrite material are predominantly dependents on electronic exchange Fe^{+3} and Fe^{+2} ions. Inclusion of Nd^{+3} ions at octahedral site increases the lattice constant and also reduces ferric and ferrous ion concentration at octahedral site. Both these factors inhibit electron hopping between Fe^{+3} and Fe^{+2} ions responsible for lowering the conductivity and dielectric constant. The dielectric constant values are seen to drastically fall down to a lower value with increase in frequency and maintain a uniform value which remains immune for further frequency variations in the higher frequency region. This behavior may be explained using space charge polarization phenomenon according to which, a good dielectric material consists of highly conducting grains fenced by non conducting grain boundaries [51, 52]. On application of electric field, space charge is accumulated at the grain boundaries and potential drop occurs at these grain boundaries. The effect of grain boundaries is predominantly observed at lower frequencies [53, 54]. When the frequency is increased beyond a certain value the electronic transfer between Fe^{+2} and Fe^{+3} ions fails to follow the variation of electric field resulting in low and constant dielectric values [55-57].

4.10 Dielectric loss variation with frequency

The plots of loss tangents versus frequency for different Nd^{+3} concentrations are shown in Figure 4.10.1(a,b). The samples with composition $Mn_{0.6}Zn_{0.4}Fe_{2-x}Nd_xO_4$ are found to exhibit higher loss values in comparison with the nanosamples with composition $Mn_{0.65}Zn_{0.35}Fe_{2-x}Nd_xO_4$.

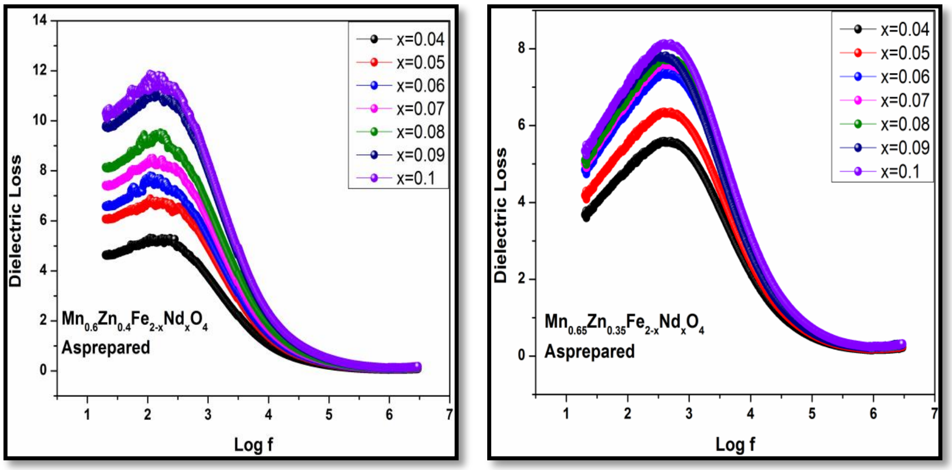

(a) (b)

Figure 4.10.1 (a & b) Variation of Dielectric loss with frequency of $Mn_{0.6}Zn_{0.4}Fe_{2-x}Nd_xO_4$ and $Mn_{0.65}Zn_{0.35}Fe_{2-x}Nd_xO_4$ nanoparticles

It can be seen that for as prepared nanoparticle samples dielectric loss increases with increasing Nd^{+3} concentrations in the low frequency region and maintains a uniform value at high frequencies for all Nd^{+3} concentrations. At lower frequencies the loss tangent is seen to show broad peaks in the vicinity of 100Hz. The increase in the loss tangent with increasing Nd^{+3} concentrations at low frequencies could be due to hindrance in electronic exchange between ferric and ferrous ions due to larger ionic radii of Nd^{+3} as visualized in resistivity and dielectric constant profiles.

The peaking behavior observed around 100Hz is a consequence of the resonance effect between electron hopping frequency and applied field frequency (exact match of electron hoping between Fe^{+2} and Fe^{+3} ions and applied field frequency). Secondly fine particle nature that results in increased surface area along with inclusion of rare earth ions increases the amount of energy required for electronic exchange resulting in high loss. At higher frequencies the electronic exchange cannot follow the applied frequency and hence loss is found to decrease [58].

4.11 Dielectric constant variation with Temperature

Variation of dielectric constant as a function of temperature at various frequencies for $Mn_{0.6}Zn_{0.4}Fe_{2-x}Nd_xO_4$ and $Mn_{0.65}Zn_{0.35}Fe_{2-x}Nd_xO_4$ nanoparticles is shown in Figure 4.11.1 and Figure 4.11.2 respectively. Variation of dielectric constant at 20Hz as with temperature $Mn_{0.6}Zn_{0.4}Fe_{2-x}Nd_xO_4$ and $Mn_{0.65}Zn_{0.35}Fe_{2-x}Nd_xO_4$ nanoparticles is shown in Figure 4.11.3. All the samples are observed to exhibit low dielectric constant over the temperature range of 30^oC to 160^oC as in this region the mobility of the charge carriers is very low and the materials exhibit high resistivity. Beyond this temperature dielectric constant shows a gradual increase due to enhancement in charge carrier hopping rate. This temperature also coincides with the transition temperature in resistivity plots beyond which resistivity of the samples is seen to decrease sharply. At higher temperature large amount of thermal energy is available which results in increase in electronic hopping rate. Liberation of trapped charges also enhances the rate of electronic charge transfer which facilitates polarization process [47].

The dielectric constant is found to decrease with increasing Nd^{+3} concentration as shown in Figures 4.11.1, Figure 4.11.2 and in Figure 4.11.3. This reduction can be attributed to the larger ionic radii of Nd^{+3} ions. Inclusion of larger ion in the lattice increases the distance between Fe^{+2} /Fe^{+3}, Mn^{+2} /Mn^{+3} and Fe^{+2}/Mn^{+3} ions which hampers the electronic charge transfer amongst these ions.

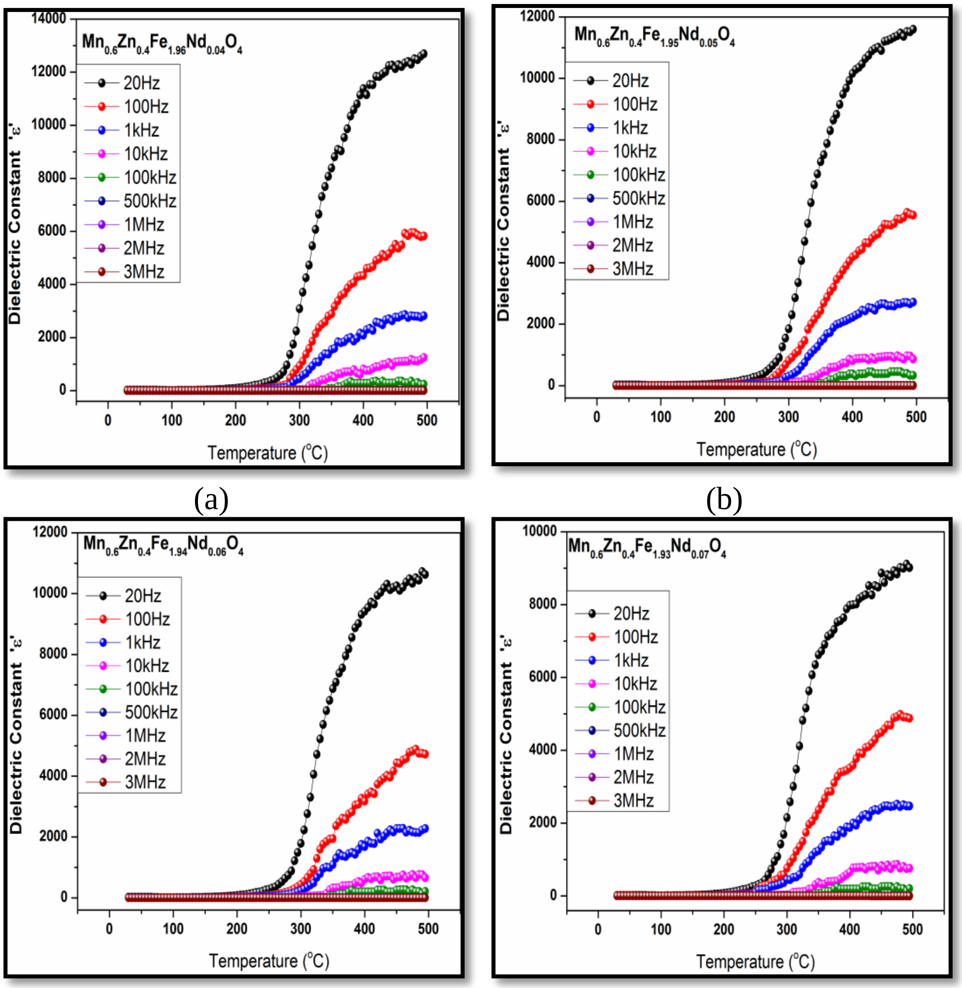

(a)

(b)

(c)

(d)

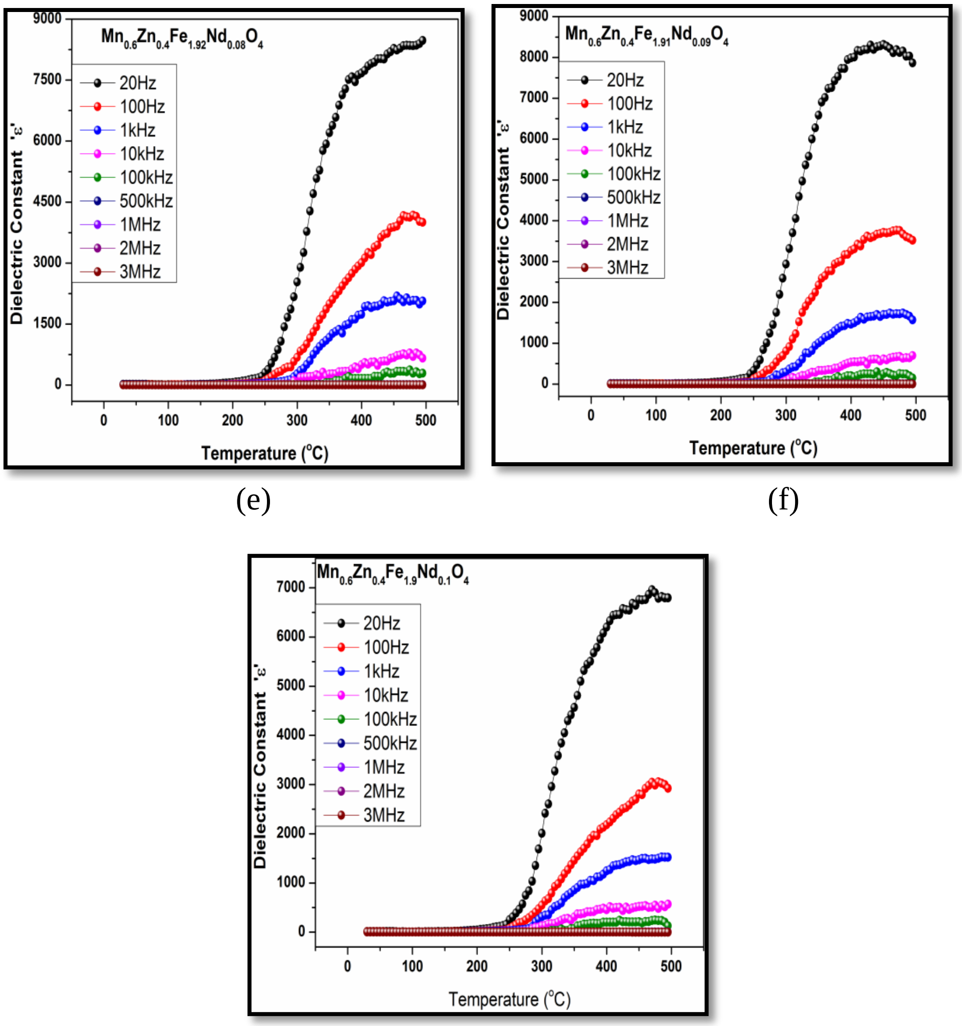

(e) (f)

(g)

Figure 4.11.1 (a, b, c d, e, f, g) Variation of Dielectric constant with temperature of $Mn_{0.6}Zn_{0.4}Fe_{2-x}Nd_xO_4$ nanoparticles

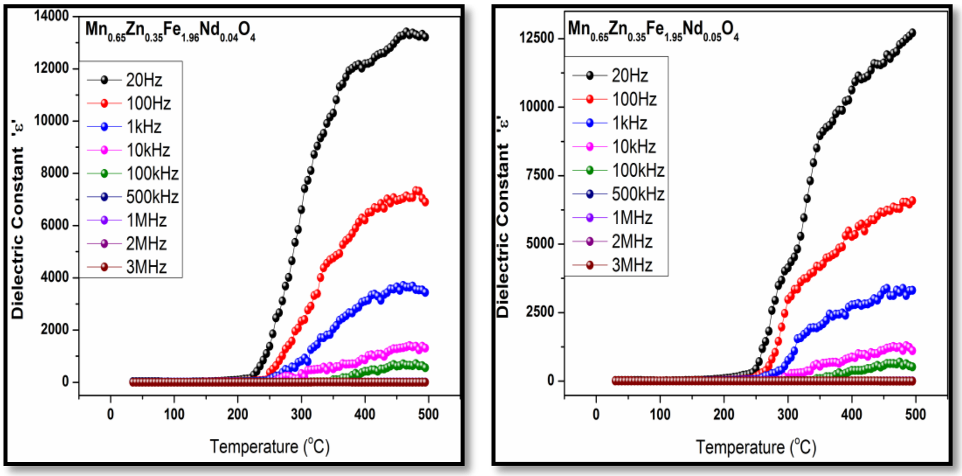

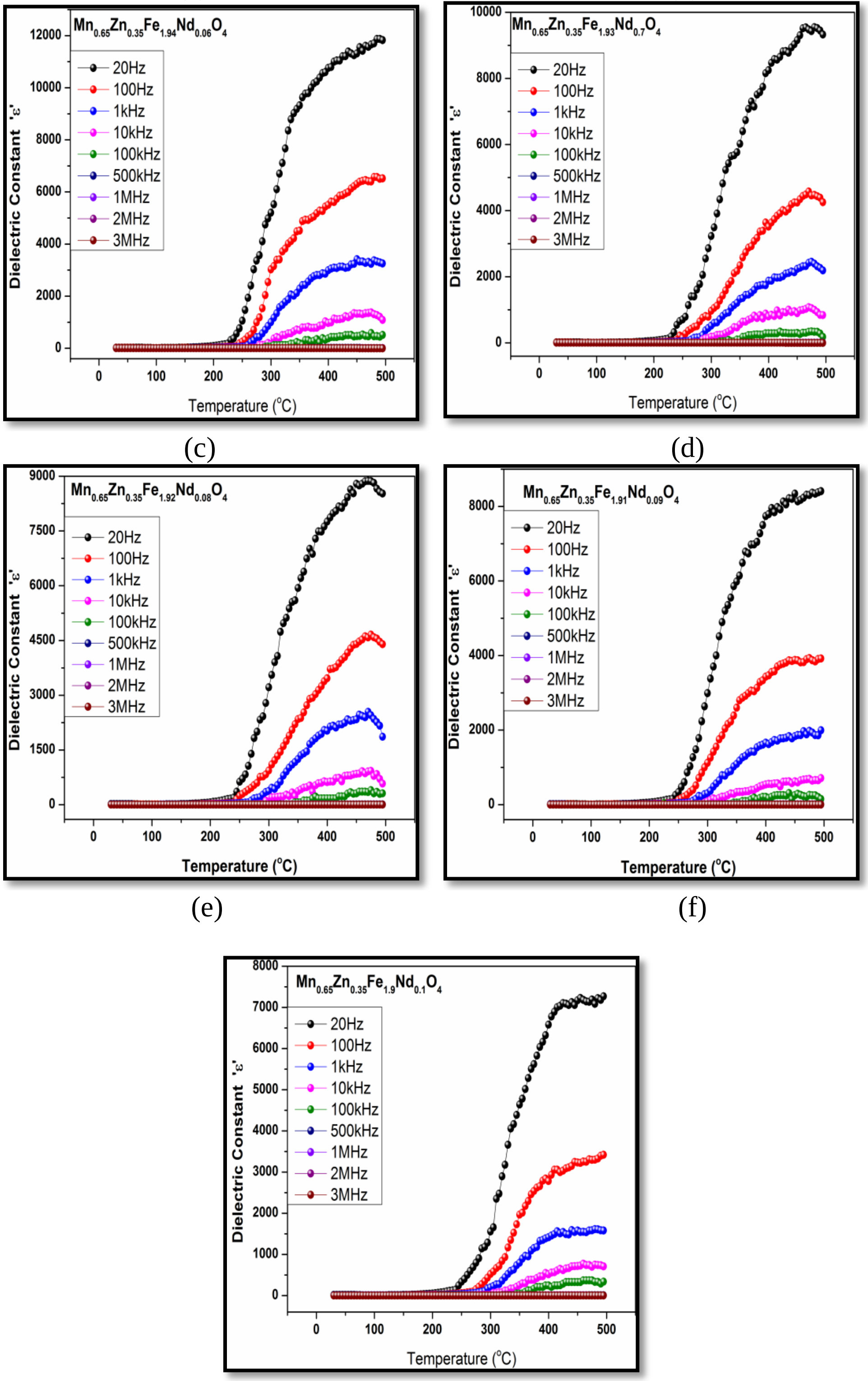

(a) (b)

(c) (d)

(e) (f)

(g)

Figure 4.11.2 (a, b,c d, e, f, g) Variation of Dielectric constant with temperature of $Mn_{0.65}Zn_{0.35}Fe_{2-x}Nd_xO_4$ nanoparticles

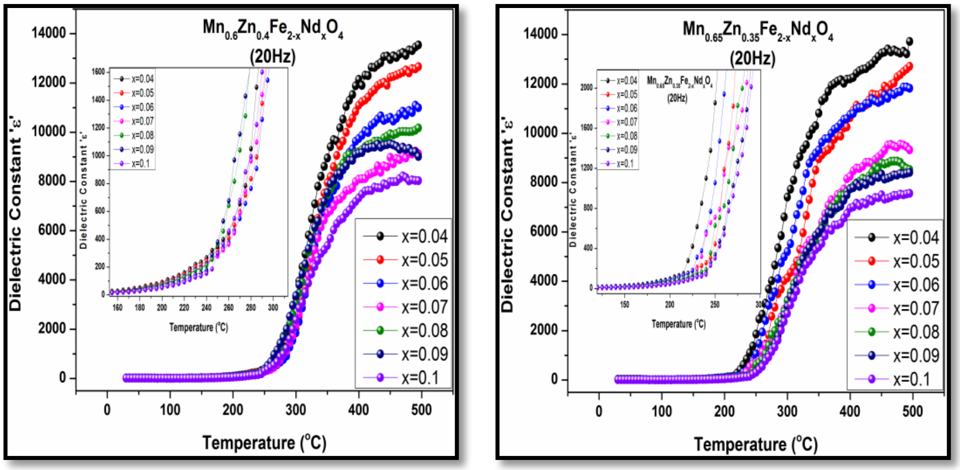

(a) (b)

Figure 4.11.3 Variation of Dielectric constant with temperature at 20Hz for $Mn_{0.6}Zn_{0.4}Fe_{2-x}Nd_xO_4$ and $Mn_{0.65}Zn_{0.35}Fe_{2-x}Nd_xO_4$ nanoparticles

At higher frequencies the dielectric constant is seen to decrease as the electronic charge transfer between Fe^{+2} and Fe^{+3} is unable to follow applied field. This causes the reduction in polarization which in turn reduces the dielectric constant.

Samples with composition $Mn_{0.65}Zn_{0.35}Fe_{2-x}Nd_xO_4$ are observed to exhibit higher dielectric constant values then the $Mn_{0.6}Zn_{0.4}Fe_{2-x}Nd_xO_4$ nanoparticles. This can be attributed to higher Mn^{+2} and Mn^{+3} responsible for additional electronic charge transfer.

4.12 Dielectric loss variation with temperature

Figure 4.12.1 and Figure 4.12.2 show the variation of dielectric loss with temperature for different frequencies for $Mn_{0.6}Zn_{0.4}Fe_{2-x}Nd_xO_4$ and $Mn_{0.65}Zn_{0.35}Fe_{2-x}Nd_xO_4$ nanoparticles with x=0.04, 0.05, 0.06, 0.07, 0.08, 0.09 and 0.1.

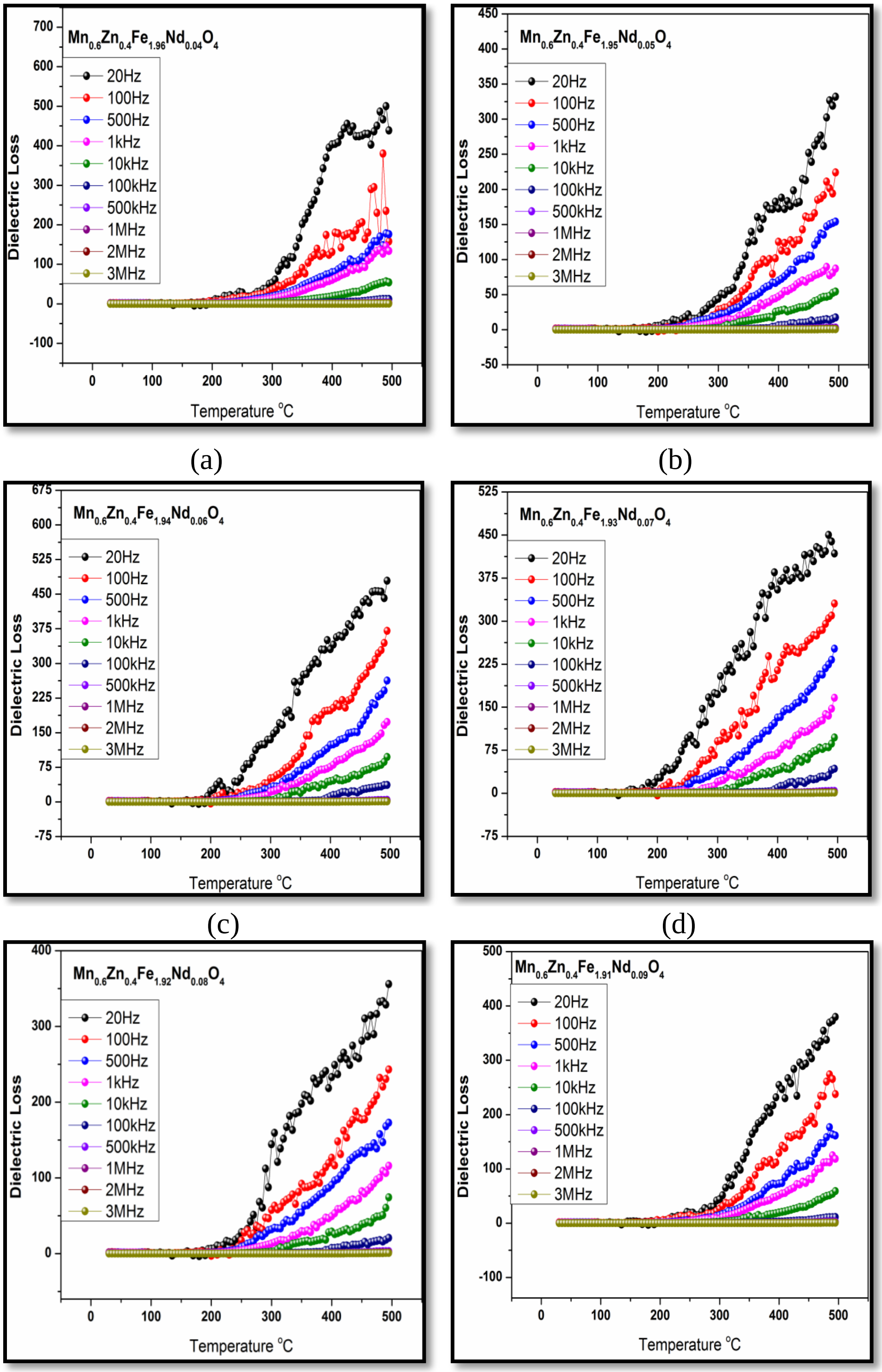
$Mn_{0.6}Zn_{0.4}Fe_{1.96}Nd_{0.04}O_4$
$Mn_{0.6}Zn_{0.4}Fe_{1.95}Nd_{0.05}O_4$
$Mn_{0.6}Zn_{0.4}Fe_{1.94}Nd_{0.06}O_4$
$Mn_{0.6}Zn_{0.4}Fe_{1.93}Nd_{0.07}O_4$
$Mn_{0.6}Zn_{0.4}Fe_{1.92}Nd_{0.08}O_4$
$Mn_{0.6}Zn_{0.4}Fe_{1.91}Nd_{0.09}O_4$
20Hz
100Hz
500Hz
1kHz
10kHz
100kHz
500kHz
1MHz
2MHz
3MHz
Dielectric Loss
Temperature °C
0
100
200
300
400
500
700
600
-100
450
350
250
150
50
-50
675
525
375
225
75
-75

(a)

(b)

(c)

(d)

(e)

(f)

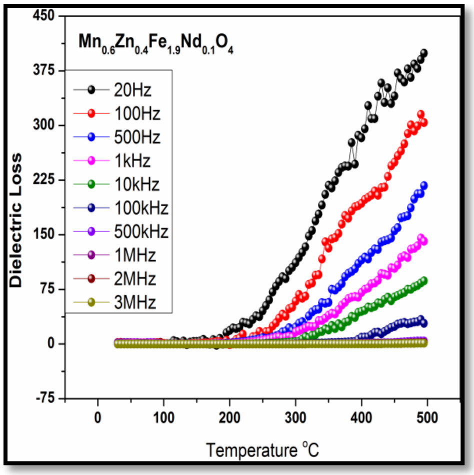

(g)

Figure 4.12.1 (a, b,c d, e, f) Variation of Dielectric loss with temperature of $Mn_{0.6}Zn_{0.4}Fe_{2-x}Nd_xO_4$ nanoparticles

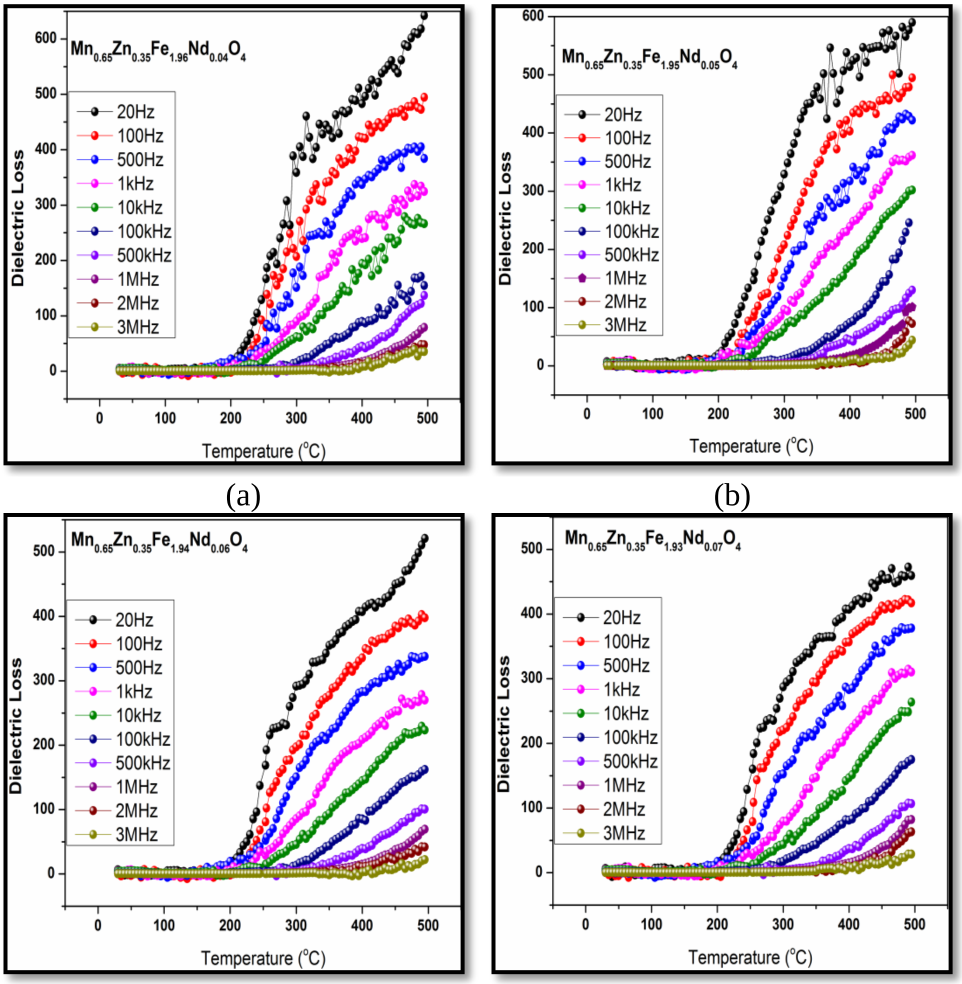

(a)

(b)

(c)

(d)

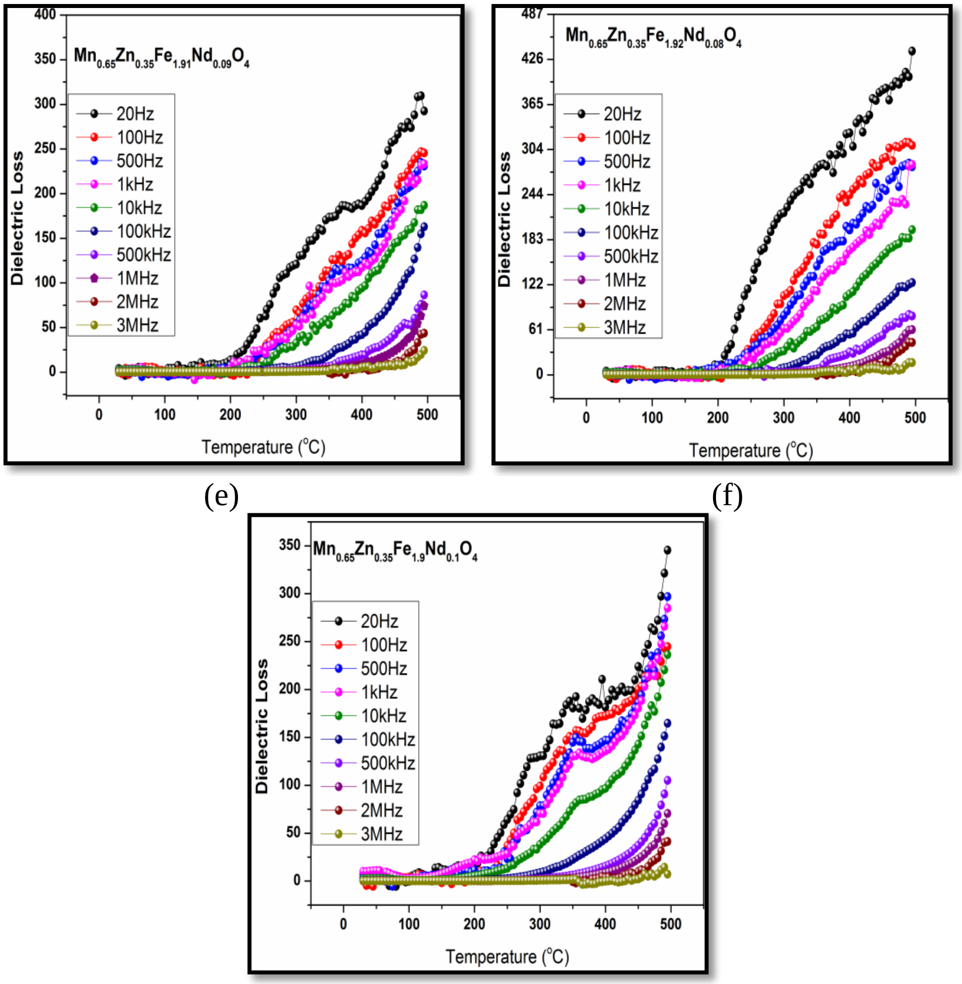

(e) (f)

(g)

Figure 4.11.2 (a, b,c d, e, f) Variation of Dielectric loss with temperature of $Mn_{0.6}Zn_{0.4}Fe_{2-x}Nd_xO_4$ nanoparticles

It can be clearly seen that all the samples exhibit low loss in the region of low temperature (30°C to 160°C) and is found to increase rapidly with increasing temperature.

4.13 Summary

Nanocrystalline rare earth doped manganese zinc ferrite materials with composition $Mn_{0.6}Zn_{0.4}Fe_{2-x}Nd_xO_4$ and $Mn_{0.65}Zn_{0.35}Fe_{2-x}Nd_xO_4$ (x=0.04, 0.05, 0.06, 0.07, 0.08, 0.09 and 0.1) were synthesized successfully using combustion method of material preparation. From the analysis of XRD data, all the samples were seen to exhibit cubic spinel phase identified with Fd3m space group. Lattice parameters for both the series of nanosamples were observed to increase with increasing Nd^{+3} concentrations at octahedral sites in the spinel lattice. This increase is attributed to the larger ionic radii of Nd^{+3} ions. Structural parameters like mass density and X-ray density were found to increase with increasing Nd^{+3} concentrations in the samples. Crystallite size estimated for all the samples from Scherrer's equation with strain correction showed a decrease from 17nm to 12nm for $Mn_{0.6}Zn_{0.4}Fe_{2-x}Nd_xO_4$ and from 18nm to 15nm for $Mn_{0.65}Zn_{0.35}Fe_{2-x}Nd_xO_4$ due to increase in lattice strain as a result of inclusion of rare earth ion in the lattice. Cation distribution estimated from XRD data show transfer of Fe^{+3} from octahedral site to tetrahedral site compensated by the transfer of Mn^{+3} from tetrahedral site to octahedral site with increasing Nd^{+3} concentrations. From TEM micrographs and particle size distribution histogram showed a very narrow particle size distribution ranging from 15nm to 18nm and 20nm to 17nm for $Mn_{0.6}Zn_{0.4}Fe_{2-x}Nd_xO_4$ and $Mn_{0.65}Zn_{0.35}Fe_{2-x}Nd_xO_4$ respectively. Large agglomerates of nanoparticles were seen in SEM images for all the samples indicating a strong magnetic behavior, high surface charges and also due to other weak surface interaction such as the Van der Waals forces. Hysteresis loops obtained on VSM showed an increase in saturation magnetization with increasing Nd^{+3} for x=0.04 to x=0.09 and decrease further for x=0.1. All samples exhibit negligible hysteresis loss. Samples with composition $Mn_{0.6}Zn_{0.4}Fe_{2-x}Nd_xO_4$ were seen to exhibit a mixed character of multi domain and nearly superparamagnetic structure while the samples with composition $Mn_{0.65}Zn_{0.35}Fe_{2-x}Nd_xO_4$ were observed to be superparamagnetic in nature.

Samples were seen to exhibit very resistivity of the order 10^9 Ω cm due to large number of non conducting grain boundaries and low mobility of charge carriers at low temperatures. DC resistivity was observed to increase further with increasing Nd^{+3} concentrations at octahedral site as it is responsible for increase in lattice constant and reduction of Fe^{+3} content. At higher temperature resistivity was seen to decrease sharply depicting semiconductor behavior.

Dielectric constant as a function of frequency was observed to decrease with increasing frequency and attain constant value. It was also observed to decrease with increasing Nd^{+3} concentrations while the dielectric loss was observed to increase with Nd^{+3} concentrations. Dielectric constant as a function of temperature was also observed to exhibit low values up to $160^{o}C$ beyond which it is seen to increase with increasing temperature. Dielectric constant was found to decrease with increasing Nd^{+3} concentrations. Rare earth doped manganese zinc ferrite nanosamples exhibit low loss in the temperature range of $30^{o}C$ to $160^{o}C$ beyond which the loss increases rapidly with increasing temperature.

References

1. Pranav P. Naik, R.B. Tangsali, S.S. Meena, S.M. Yusuf, Materials Chemistry and Physics 191 (2017) 215-224
2. Bashar Issa, Ihab M. Obaidat, Borhan A. Albiss, Yousef Haik, International Journal of Molecular Sciences, 14, (2013) 21266-21305
3. Manisha Dhiman, Santosh Bhukal, Bhupendra Chudasama, Sonal Singhal, Journal of Sol-Gel Science and Technology, 81 (2017) 831–843
4. B. Antic, A. Kremenovic, A.S. Nikolic, M. Stoiljkovic, Journal of Physical Chemistry B, 108 (2004) 12646-12651.

5. A. Kremenovic, B. Antic, V. Spasojevic, M. Vucinic-Vasic, Z. Jaglicic, J. Pirnat, Z. Trontelj, Journal of Physics: Condensed Matter 17 (2005) 4285-4299.
6. Z. Cvejic, B. Antic, A. Kremenovic, S. Rakic, G.F. Goya, H.R. Rechenberg, C. Jovalekic, V. Spasojevic, Journal of Alloys and Compdounds, 472 (2009) 571-575.
7. C. Venkataraju, Applied Physics Research1 (No. 1) (2009) 41-45.
8. M.M. Haque, M. Huq, M.A. Hakim, Indian J. Phys. 78A (3) (2004) 397-400.
9. Emad M.M. Ewais, Mahmoud M. Hessien, Abdel-Hady A. El-Geassy, Journal of Australian Ceramic Society, 44 (1) (2008) 57-62.
10. K. Rama Krishna, K. Vijaya Kumar, Dachepalli Ravinder, Advances in Materials Physics and Chemistry 2, (2012) 185-191.
11. Z. Karimi, Y. Mohammadifar, H. Shokrollahi, Sh. Khameneh Asl, Gh. Yousefi, L. Karimi, Journal of magnetism and magnetic materials, 361 (2014) 150.
12. Zein K. Heiba, Mohamed Bakr Mohamed, L. Arda, N. Dogan, Journal of magnetism and magnetic materials, 391 (2015) 195-202.
13. A.A. Sattar, H.M. El-Sayed, K.M. El-Shokrofy, and M.M. El-Tabey, Journal of Materials Engineering and Performance, 14, 99-103(2005)
14. P. P. Naik, R. B. Tangsali, B. Sonaye, S. Sugur, Journal of Magnetism and Magnetic Materials, 385,377–385(2015)
15. S.M. Patange, S.E. Shirsath, G.S. Jangam, K.S. Lohar, S.S. Jadhav, K.M. Jadhav, Journal of Applied Physics, 109 (2011) 053909.
16. M. A. Amer, T. Meaz, S. Attalah, F. Fakhry, Journal of Magnetism and Magnetic Materials 401(2016)150–158

17. M. A. Amer, T. M. Meaz, M. El-Kestawy, A. I. Ghoneim, Journal of Magnetism and Magnetic Materials, 405(2016)137–144

18. M. A. Amer, Journal of Magnetism and Magnetic Materials 426 (2017) 771–778

19. M. A. Amer, A. Matsuda, G. Kawamura, R. El-Shater, T. Meaz, F. Fakhry, Journal of Magnetism and Magnetic Materials 439 (2017) 373–383

20. E. H. El-Ghazzawy, M. A. Amer, Journal of Alloys and Compounds 690 (2017) 293-303

21. L. Ben Tahar, L.S. Smiri, M. Artus, A.-L. Joudrier, F. Herbst, M.J. Vaulay, S. Ammar, F. Fie´vet, Materials Research Bulletin 42(2007) 1888–1896

22. K. Manju, T. Smitha, D. S. Nair, E. K Aswathy, B. Aswathy, T Arathy, Binu, K. T. Krishna, Journal of Advanced Ceramics, 2015, 4(3): 199–205

23. Y.G. Zhang, Magnetic Materials, Chengdu, Pekin, 1988 (Chapter 1).

24. .R. Naik, A.V. Salker, Journal of Material Chemistry, 22(2012) 2740.

25. L. Zhao, H. Yang, X. Zhao, L. Yu, Y. Cui, S. Feng, Material Letters 60 (2006)1-6.

26. AA Sattar, HM El-Sayed, KM El-Shokrofy, MM El-Tabey, Journal of Applied Science, 5(1)(2005)162−8.

27. Chikazumi S, Charap S. Physics of magnetism. New York, London, Sydney: John Wiley and Sons, Inc.; 1964.

28. Y.G. Zhang, Magnetic Materials, 1988. Chengdu, Pekin (Chapter 1).

29. F.X. Cheng, J.T. Jia, Z.G. Xu, B. Zhou, C.S. Liao, L.Y. Chen, H.B. Zhao, Journal of Applied Physics, 86(1999) 2727-2732.

30. Fuxiang Cheng, Chunsheng Liao, Junfeng Kuang, Zhigang Xu, Chunhua Yan, Liangyao Chen, Haibin Zhao, Zhu Liu, Journal of Applied Physics 85 (1999) 2782.
31. A. Baykal, A.Z. Elmal, M. Sertkol, H. S€ozeri, Journal of Superconductivity and Novel Magnetism, 28 (2015) 3405-3410.
32. A. Baykal, F. Genç, A.Z. Elmal, S. G€okçe, M. Sertkol, H. S€ozeri, Journal of Inorganic and Organometallic Polymers and Materials 26 (2016) 134-141.
33. Y. Bao, A. B. Pakhomov, and Kannan M. Krishnan, Journal of Applied Physics **99**(2006),08H107
34. A.A. Kadam, S.S. Shinde, S.P. Yadav, P.S. Patil, K.Y. Rajpure, Journal of Magnetism and Magnetic materials, 329 (2013) 59-64.
35. Jose. M. Vargas et al, Nanotechnology 16 (2005)S285-90
36. Xu ZC. Journal of Applied Physics, 93(2003)4746-9.
37. F. Patil, M Lenglet. Solid State Communications, 86(1993) 67−71.
38. D.C. Dobson, J.W. Linnet, M.M. Rahman, Journal of Physics and Chemistry of Solids, 31 (12) (1970) 2727-2733.
39. S.S. Shinde, Sher Singh Meena, S.M. Yusuf, K.Y. Rajpure, Journal of Physical Chemistry C, 115 (2011) 3731-3736.
40. K. Vasundhara, S.N. Achary, S.K. Deshpande, P.D. Babu, S.S. Meena, A.K. Tyagi, Journal of Applied Physics, 113 (2013) 194101.
41. P.P. Naik, R.B. Tangsali, S.S. Meena, Pramod Bhatt, B. Sonaye, S. Sugur, Radiation Physics and Chemistry, 102 (2014)147e152.

42. S.R. Naik, A.V. Salker, S.M. Yusuf, S.S. Meena, Journao of Alloys and Compounds, 566 (2013) 54e61.
43. Shalendra Kumar, A.M.M. Farea, Khalid Mujasam Batoo, Chan Gyu Lee, B.H. Koo, Ali Yousef, Alimuddin, Physica B 403 (2008) 3604-3607.
44. D.E. Dickson, F.J. Berry, M€ossbauer Spectroscopy, Cambridge University Press, London, 1986, p. 22.
45. Ishtiaq Ahmad and Muhammad Tahir Farid, World Applied Sciences Journal, 19(4) (2012), 464.
46. P. P. Naik, R. B. Tangsali, B. Sonaye, S. Sugur, Journal of Nano Research Vol. 24 (2013) pp 194-202
47. Pranav P. Naik, R. B. Tangsali, B. Sonaye and S. Sugur, Journal of Nanotechnology and Advanced Materials, 3, No. 1, (2015) 1-7
48. Lanje, N.Y., D.K. Kulkarni, Journal of Magnetism and Magnetic Materials,234, (2001) 114.
49. Manisha, V. Rane, D. Bahadur, A.K Nigam and C.M. Srivastava, Journal of Magnetism and Magnetic Materials, 192, (1999) 288-296.
50. M. T. Farid, I. Ahmad, S. Aman, M. Kanwal, G. Murtaza, I. Ali, I. Ahmad, M. Iishfaq, Digest Journal of Nanomaterials and Biostructures, Vol. 10, No. 1, January - March 2015, p. 265 – 275
51. M. Asif Iqbal, M.U. Islam, Irshad Ali, Muhammad Azhar khan, Imran Sadiq and Ihsan Ali, Journal of Alloys and Compounds 586, (2014)404.
52. Chandra Babu, B, Naresh. V. Jayaprakash. B, S. Buddhudu , Ferro Electrics letter, 38, (2011) 124.

53. N. Rezlescu, E. Rezlescu, Physics Status Solidi A. 23, (1974)575.
54. I.H. Gul, A. Maqsood, M. Naeem, M. Naeem Ashiq, Journal of alloys and compounds, 507, (2010)201.
55. K.W. Wagner, Dissipation of energy under AC, American Physics 40, (1973)317.
56. Muhammad Tahir Farid, Ishtiaq Ahmad, Salma Aman, Journal of Chemical Society of Pakistan, 35, (2013)793.
57. B. Baruwati, K. M. Reddy, V. Sunkara, R. K. Manorama, O. Singh, J. Prakash, Applied Physics Letters 14, (2004) 85.
58. R. S. Devan, B. K. Chougule, Journal of Applied Physics 101, (2007)014109.

CHAPTER 5

EXPOSURE OF $Mn_{0.6}Zn_{0.4}Fe_{2-x}Nd_xO_4$ AND $Mn_{0.65}Zn_{0.35}Fe_{2-x}Nd_xO_4$ FERRITE NANOPARTICLES TO GAMMA (γ) RADIATION

5.1 Introduction

Gamma rays were discovered after the discovery of X-rays. In 1896, French scientist Henri Becquerel observed that uranium minerals could expose a photographic plate through another material. Becquerel presumed that uranium emitted some invisible light similar to X-rays, which were recently discovered by W. C. Roentgen. He called it **"**metallic phosphorescence**".** Gamma rays were observed to be reflected from crystal surfaces, proving that they must be electromagnetic radiation, but with higher frequency and hence energy (higher frequency and shorter wavelengths).

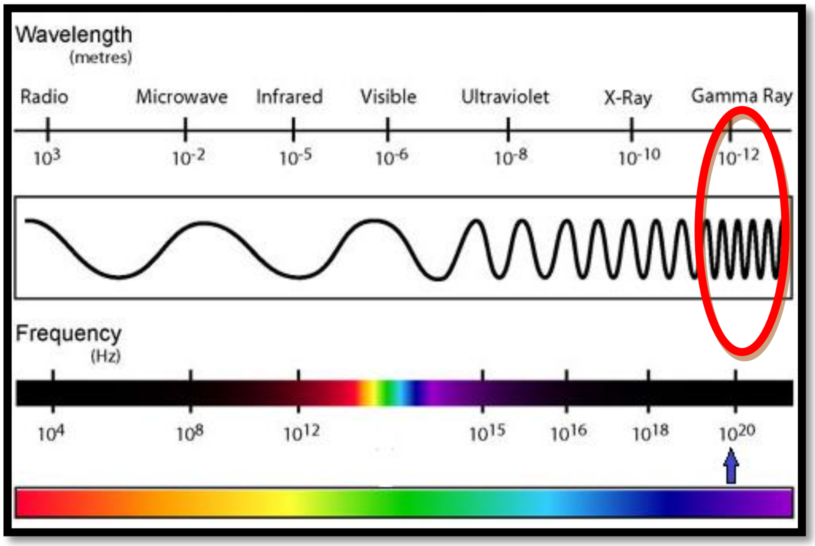

Figure 5.1.1 Electromagnetic spectra

Gamma rays refer to electromagnetic radiation (no rest mass, no charge) of very high energies. Gamma rays are high-energy radiation with very short wavelengths and thus very high frequency as shown in Figure 5.1.1.

Since the gamma rays are high-energy photons, they posses immense penetrating strength due to very short wavelength (10^{-12}m) and are biologically hazardous. Gamma rays are emitted by unstable nuclei during their transition from a high energy state to a lower state and the process is known as gamma decay. In most practical laboratory sources, the excited nuclear states are created in the decay of a parent radionuclide, therefore a gamma decay typically accompanies other forms of decay, such as alpha or beta decay. Radiations and gamma rays are the part of our natural world that has been here since the birth of our planet. Natural sources of gamma rays on Earth are the naturally occurring radio-nuclides.

5.2 Interaction of Gamma radiations with matter

The interaction of radiation with substances is an extremely important from the viewpoint of theory and practice. This interaction may be considered from various aspects. When radiation passes through a material, its properties may change as these high energy radiations can bring about several changes like creation of defects in the structure, excitations and ionizations in atoms which can help to alter the material properties [2-11]. Gamma ray photon possesses much higher energies then the energy required to dislocate K- shell and L-shell electrons from the atom. Moreover gamma ray sources such as Co^{60} emit gamma radiation of energy higher than 1MeV which are capable of producing electron positron pairs near nucleus which later combine and provide recoil energy to the nucleus. So gamma rays of energy higher than 1MeV can even dislocate an atom from its site in a material. However the resultant modifications would depend on total dose absorbed in the material. Thus high energy gamma radiation can bring about wide ranging changes in the properties of nanoparticles and these changes can be of permanent nature. In the recent years, a broad development of nuclear engineering, use of radioactive isotopes, accelerators of elementary particles put forward much attention to study the radiation effect on materials used in electronic devices and control systems.

5.3 Cobalt 60 (^{60}Co) as gamma source

It is a well known synthetic radioactive isotope of cobalt. Cobalt 60 has a half-life of 5.2714 years and is used in numerous applications. It is artificially synthesized in nuclear reactors. Deliberate industrial production depends on neutron activation of bulk samples of the mono-isotopic and mono-nuclidic cobalt isotope [12]. Mass production is also done as a by-product of a normal nuclear power plant operation and may be detected externally when leaks occur. In the latter case (in the absence of added cobalt)the incidentally produced ^{60}Co is largely the result of multiple stages of neutron activation of iron isotopes in the reactor's steel structures[13] via the creation of ^{59}Co precursor. The simplest case of the latter would result from the activation of ^{58}Fe.

^{60}Co decays by beta decay to the stable isotope nickel-60 (^{60}Ni). The activated nickel nucleus emits two gamma rays with energies of 1.17 and 1.33 MeV, hence the overall nuclear equation of the reaction is as follows

$$ {}^{59}_{27}\mathrm{Co} + \mathrm{n} \rightarrow {}^{60}_{27}\mathrm{Co} \rightarrow {}^{60}_{28}\mathrm{Ni} + \mathrm{e}^{-} + \nu_{\mathrm{e}} + \gamma \text{ rays} \qquad 5.3.1\mathrm{a} $$

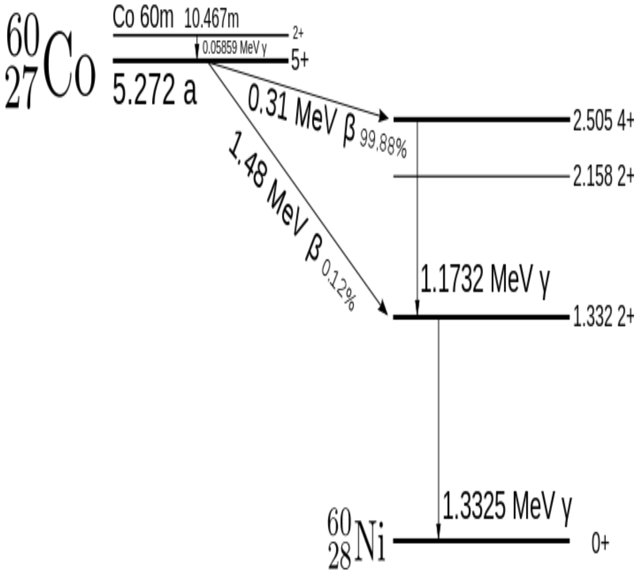

Figure 5.3.1 Decay scheme of ^{60}Co into ^{60}Ni and emission of γ photon

The main β-decay transitions are shown in figure 5.3.1. Energy transfers between the three levels generate six different gamma-ray frequencies [14]. In the diagram the two important ones are marked. Internal conversion energies are well below the main energy levels. Co60m is a nuclear isomer of ^{60}Co with a half-life of 10.467 minutes. It decays through a transition emitting 58.6 keV gamma rays to 60Co, or with a low probability (0.22%) by β-decay into ^{60}Ni [15]

Being an high intensity emitter of gamma rays is the biggest advantage of 60Co along with a relatively long half-life, compared to other gamma ray sources of similar intensity. The energy of β-decay process energy is low hence can be easily shielded; but the gamma-ray emission lines have very high energies of around 1.3 MeV, and are highly penetrating. The main uses for 60Co are:

- Sterilization of medical equipment [16].

- Radiation source for medical radiotherapy [17]. Cobalt therapy, using beams of gamma rays from ^{60}Co tele-therapy machines to treat cancer, has been widely used since the 1950s.
- Radiation source for industrial radiography [17].
- Radiation source for leveling devices and thickness gauges [17].
- Radiation source for pest insect sterilization [18].
- As a radiation source for food irradiation and blood irradiation [16].

5.4 Procedure of irradiating $Mn_{0.6}Zn_{0.4}Fe_{2-x}Nd_xO_4$ and $Mn_{0.65}Zn_{0.35}Fe_{2-x}Nd_xO_4$ nanoparticles using ^{60}Co gamma (γ) ray source.

Structurally characterized nanoparticles of $Mn_{0.6}Zn_{0.4}Fe_{2-x}Nd_xO_4$ and $Mn_{0.65}Zn_{0.35}Fe_{2-x}Nd_xO_4$ with x= 0.04, 0.05, 0.06, 0.07, 0.08, 0.09, 0.1 investigated for various properties as described in chapter IV were radiated with gamma radiation obtained from ^{60}Co gamma (γ) ray source for different time durations. The powdered samples were pressed into palates of thickness 2.5mm and radius 5mm using hydraulic press with a pressure 50KN/mt^2 that was maintained for a period of five minutes. The arrangement as shown in the schematic diagram in figure 5.2.1 was adopted for the purpose. All the pallets to be irradiated were placed at a distance of 60cm from the source in the centre of the radiation field area. A central region of 5cm x 5cm of the radiation field area was used for the purpose.

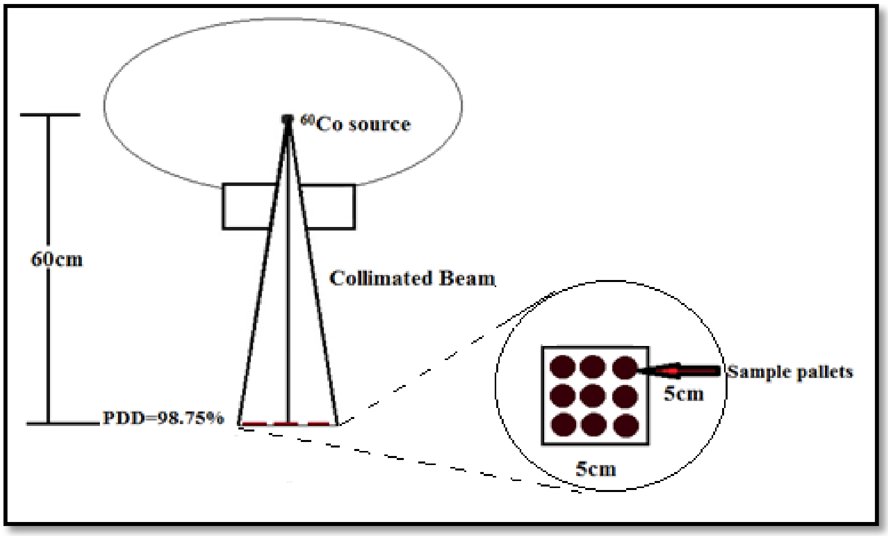

Figure 5.4.1 Schematic diagram of gamma irradiation process using ^{60}Co source.

Figure 5.4.2 Theratron 780C Cobalt 60 unit used for gamma irradiation.

Figure 5.4.2 is the photograph of the actual setup used for the purpose. Samples were irradiated for three different time durations in order to obtain three magnitudes of gamma radiation dose (500Gy, 750Gy and 1000Gy). The detailed calculation of dose time for different doses has been discussed further in this chapter.

5.5 Dose calculation for gamma irradiation process

Source dose rate (I): 83.603 R/min

Percentage depth dose (PDD): 98.75%

Field area: 5cm x 5cm

Effective dose rate (I_1) at distance (d_1=80cm) is given by following equation

$$I_1 = \frac{PDD \times I}{100} \qquad \text{eq. 5.2.1a}$$

Effective dose rate (I_2) at distance (d_2=60cm) can be determined as follows

$$I_2 = I_1 \times \left(\frac{d_1}{d_2}\right)^2 \qquad \text{eq. 5.2.1b}$$

Time of irradiation (T) for dose D can be calculated using following equation

$$T = \frac{D}{I_2} \qquad \text{eq. 5.2.1c}$$

Table 5.5.1 Gamma irradiation dose parameters and radiation time.

Gamma Radiation Dose D (Gy)	Distance from the source d_2 (cm)	Dose Area (cm^2)	Irradiation Time T(min)
500	60	25	341
750	60	25	511
1000	60	25	682

Table 5.5.1. gives the values of various parameters selected and the radiation times obtained using various equations listed above[19-22]. All the pellets (three sets of each sample) were irradiated for durations as mentioned in the above table. The γ irradiated pellets were grounded for duration of 5 hours to obtain fine powders which were

subjected to various characterization techniques and electrical and magnetic property investigations. The detail outcome of these investigations is described in the next chapter.

References

1. http://www.butane.chem.uiuc.edu
2. Pranav P. Naik, R. B. Tangsali, B. Sonaye, S. Sugur, Advanced Science Letters, Volume 22, (2016)pp752-758
3. Pranav P. Naik, R. B. Tangsali, B. Sonaye and S. Sugur, J. Nano. Adv. Mat. 3, No. 1, (2015)1-7
4. Pranav P. Naik, R. B. Tangsali, B. Sonaye, S. Sugur, Journal of Magnetism and Magnetic Materials 385(2015)377–385
5. P. P. Naik, R. B. Tangsali, S. S. Meena, Pramod Bhatt, B. Sonaye, S. Sugur, Radiation Physics and Chemistry, September 2014, Pages 147–152
6. P. P. Naik, R. B. Tangsali, S. S. Meena, Pramod Bhatt, B. Sonaye, S. Sugur, Journal of Nano research, vol 24(2013), 194-202
7. P. P. Naik, R. B. Tangsali, B. Sonaye, and S. Sugur, AIP Conf. Proc. 1512, (2013) 354.
8. H.E. Hassan, T. Sharshar, M.M. Hssien and O.M. Hemeda, Nuclear Instrumentation Methods B, 304(2013)72-79.
9. D.M. Hemeda, American Journal of Applied Sciences 2 (5), (2005)989-992.
10. O.M. Hemeda, Phase Transition, 51, (1994) 87
11. I. M. Hamada, Journal of Magnetism and Magnetic Materials, 271,(2004)318–325.

12. National Institute of Standards and Technology. "Radionuclide Half-Life Measurements". Retrieved 2011-11-07.
13. Korea Atomic Energy Research Institute. "Nuclide Table". Retrieved 2009-03-14.
14. Malkoske, G. R. Cobalt-60 production in CANDU power reactors
15. http://www.epa.gov/radiation/radionuclides/cobalt.html#wheredoes Radiation Protection: Cobalt
16. "Table of Isotopes decay data". Retrieved April 16, 2012.
17. "Table of Isotopes decay data". Retrieved April 16, 2012.
18. Gamma Irradiators For Radiation Processing (PDF). IAEA. 2005.
19. "Cobalt Radiation Protection US EPA". EPA. Retrieved April 16, 2012.
20. Chandra, Ramesh. Introductory Physics of Nuclear Medicine. 4th ed. Philadelphia: Lea & Febiger, 1992.
21. Early, Paul J. and Sodee, D. Bruce. Principles and Practices of Nuclear Medicine. 2nd ed. St. Louis: Mosby, 1995.
22. Saha, Gopal B. Fundamentals of Nuclear Pharmacy. 4th ed. New York: Springer, 199

CHAPTER 6

STRUCTURAL CHARACTERIZATION, MAGNETIC AND ELECTRICAL PROPERTIES OF GAMMA IRADIATED $Mn_{0.6}Zn_{0.4}Fe_{2-x}Nd_xO_4$ & $Mn_{0.65}Zn_{0.35}Fe_{2-x}Nd_xO_4$ NANOPARTICLES

6.1 Introduction

Interaction of high energy gamma (γ) radiation with ferrite nano materials is known to produce several changes in various properties of ferrite material by means of generation of strain, creation of defects in the structure, excitations and ionizations in atoms etc [1]. As per the reports the alterations produced in these ferrite nano materials are proportional to the magnitude of the radiation dose absorbed by the materials [2-4]. Researchers have studied the effect of gamma radiation on structural, magnetic and electrical properties of manganese zinc ferrite nanoparticles and have reported notable variations in all the aspects of these nanomaterials [5-7]. It is still more interesting to investigate the influence of high energy gamma radiations of rare earth doped manganese zinc ferrite nanoparticles as the materials studied earlier are different from the ones that are currently prepared as their method of materials preparation and their properties differ. As discussed in chapter 4, inclusion of rare earth (Nd^{+3}) ion in the Mn-Zn ferrite lattice was seen to produce significant variations in various properties that were proportional to the concentration of Nd^{+3} ions. Gamma irradiated samples as discussed in chapter 5 were characterized again for determination of structural modifications and further investigated systematically to study the modifications produced in magnetic and electrical properties due to high energy gamma radiation exposure. This chapter gives the results and the detailed discussion on these investigations.

Structural property exploration

6.2 X-Ray diffraction (XRD)

The X-ray diffraction patterns obtained for the γ irradiated $Mn_{0.6}Zn_{0.4}Fe_{2-x}Nd_xO_4$ & $Mn_{0.65}Zn_{0.35}Fe_{2-x}Nd_xO_4$ with x= 0.04, 0.05, 0.06, 0.07, 0.08, 0.09 and 0.1 are given in Figure 6.2.1 and Figure 6.2.2. Figure 6.2.3 to Figure 6.2.10 show the rietveld analysis of γ irradiated $Mn_{0.6}Zn_{0.4}Fe_{2-x}Nd_xO_4$ and $Mn_{0.65}Zn_{0.35}Fe_{2-x}Nd_xO_4$ nanoparticles. The XRD patterns were fitted with space group Fd3m assigning tetrahedral ions at 8a sites while octahedral ions were assigned 16d sites. The immediate observation is that the samples retain the original spinel structure even after γ irradiation without formation of any secondary phase. An observation made carefully indicates a substantial decrease in diffraction peak intensities marred by their broadening. This observation indicates a lowering of crystalline nature in the samples thereby bringing in a small or minor amorphous character in the samples. This amorphous character was found to increase with increasing γ radiation dose. Similar partial transformation towards amorphous nature of the material has been reported by several investigators [8].

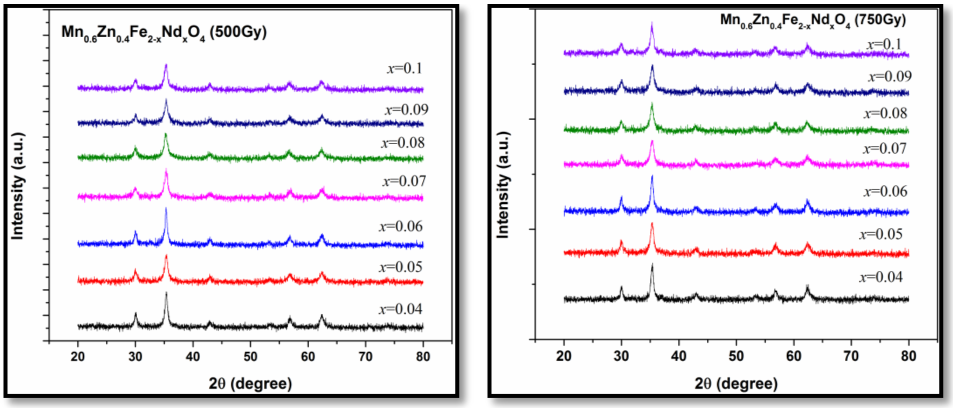

(a) (b)

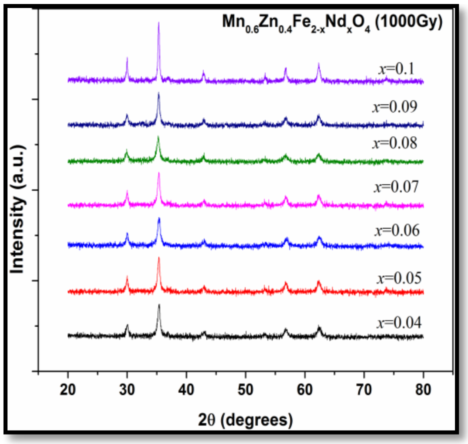

(c)

Figure 6.2.1 X- ray diffraction pattern obtained on γ irradiated $Mn_{0.6}Zn_{0.4}Fe_{2-x}Nd_xO_4$ nanoparticles

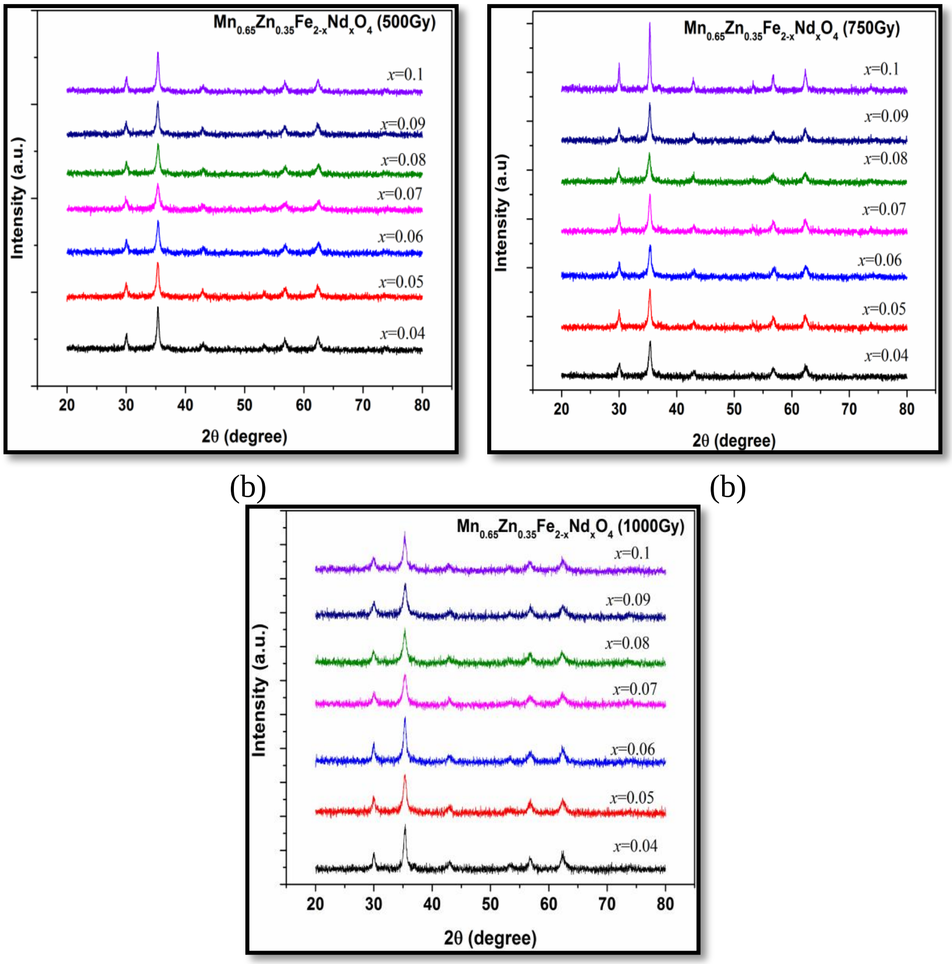

(b) (b)

(c)

Figure 6.2.2 X- ray diffraction pattern obtained on γ irradiated $Mn_{0.65}Zn_{0.35}Fe_{2-x}Nd_xO_4$ nanoparticles

The values of atomic positions of cations and refinement parameters for γ irradiated $Mn_{0.6}Zn_{0.4}Fe_{2-x}Nd_xO_4$ and $Mn_{0.65}Zn_{0.35}Fe_{2-x}Nd_xO_4$ have been obtained for all the samples by rietveld refinements and are listed in Table 6.2.1 (a,b,c) and Table 6.2.2 (a,b,c) respectively where R_{WP} is the discrepancy factor, R_{EXP} expected value and χ^2 is the goodness fit factor.

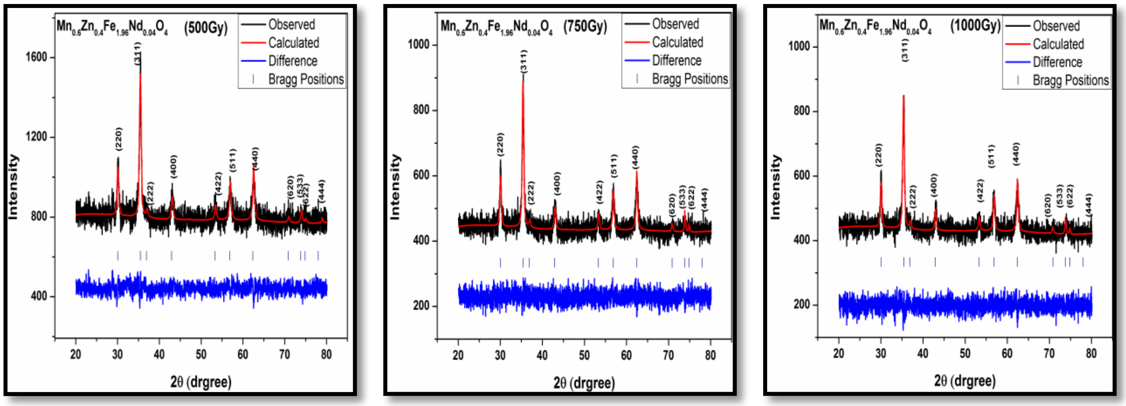

(a) (b) (c)

Figure 6.2.3 Rietveld refinement of γ irradiated $Mn_{0.6}Zn_{0.4}Fe_{1.96}Nd_{0.04}O_4$ nanoparticles

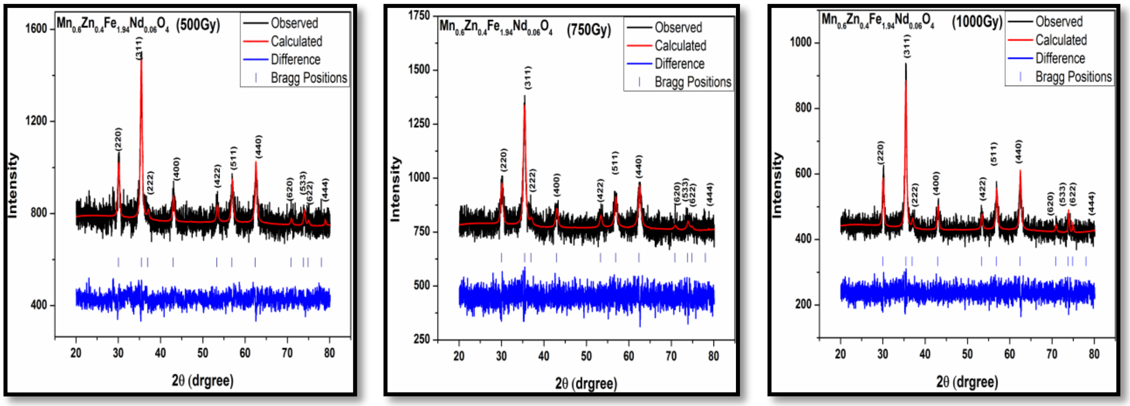

(a) (b) (c)

Figure 6.2.4 Rietveld refinement of γ irradiated $Mn_{0.6}Zn_{0.4}Fe_{1.94}Nd_{0.06}O_4$ nanoparticles

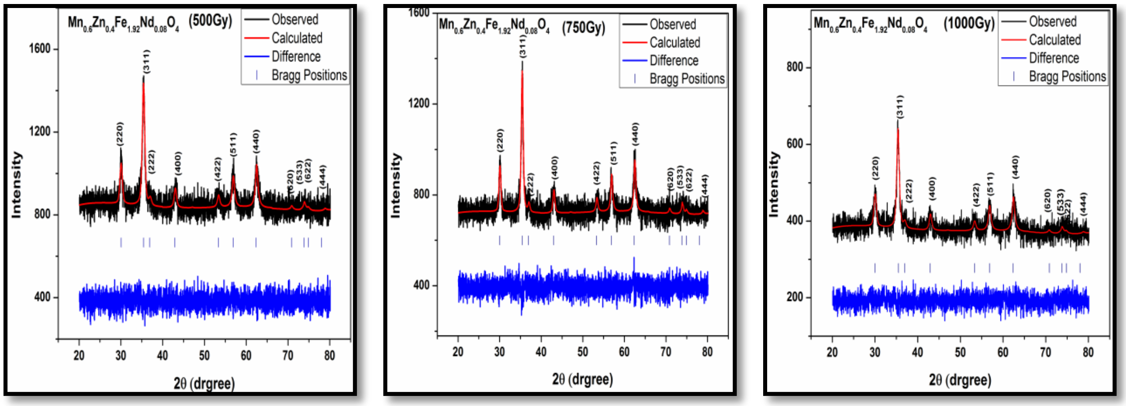

(a) (b) (c)

Figure 6.2.5 Rietveld refinement of γ irradiated $Mn_{0.6}Zn_{0.4}Fe_{1.92}Nd_{0.08}O_4$ nanoparticles

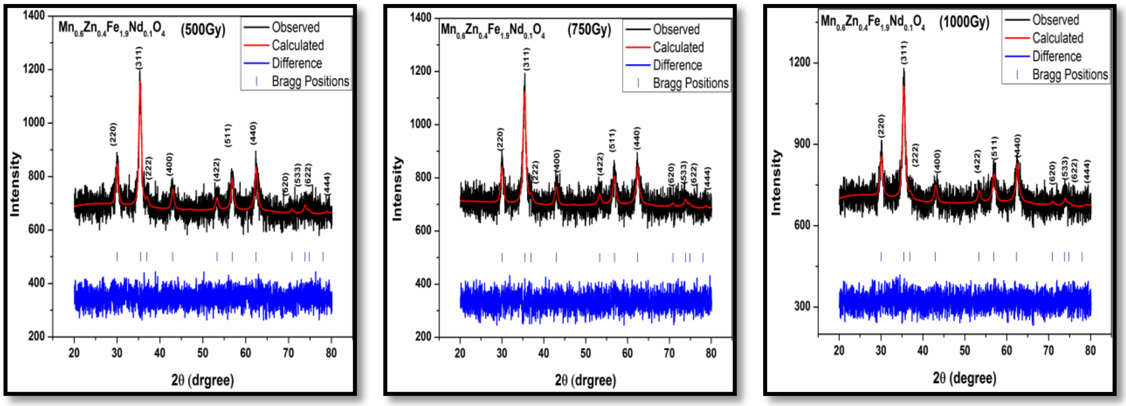

(a) (b) (c)

Figure 6.2.6 Rietveld refinement of γ irradiated $Mn_{0.6}Zn_{0.4}Fe_{1.9}Nd_{0.1}O_4$ nanoparticles

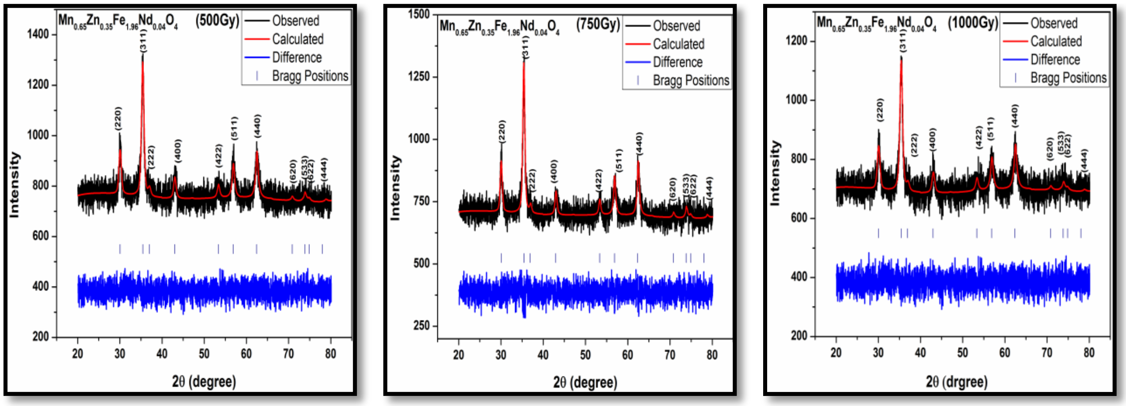

(a) (b) (c)

Figure 6.2.7 Rietveld refinement of γ irradiated $Mn_{0.65}Zn_{0.35}Fe_{1.96}Nd_{0.04}O_4$ nanoparticles

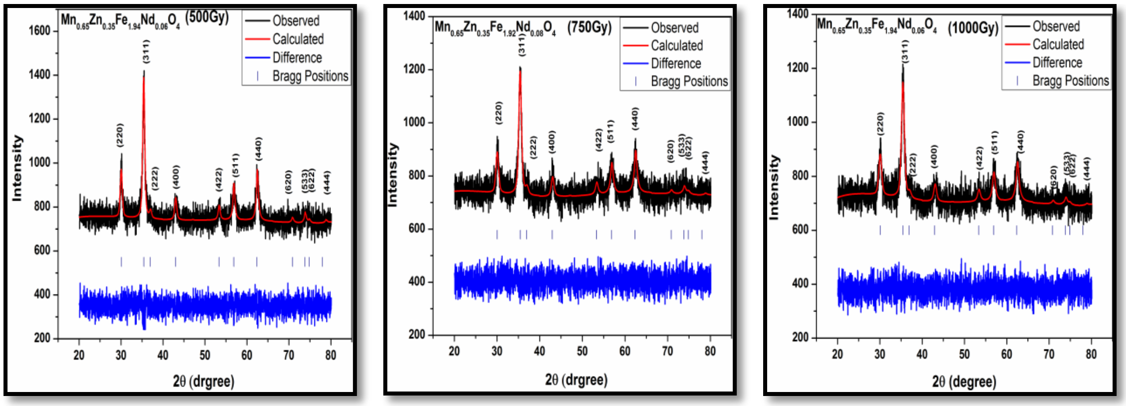

(a) (b) (c)

Figure 6.2.8 Rietveld refinement of γ irradiated $Mn_{0.65}Zn_{0.35}Fe_{1.94}Nd_{0.06}O_4$ nanoparticles

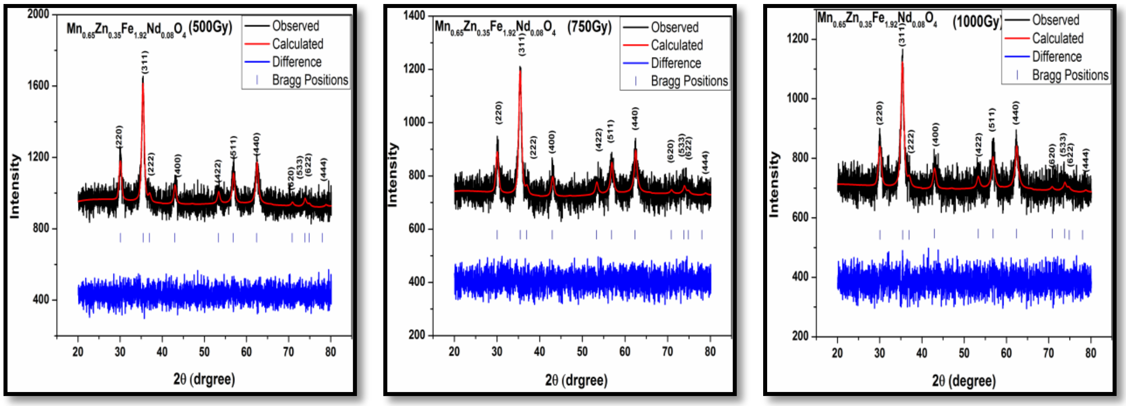

(a) (b) (c)

Figure 6.2.9 Rietveld refinement of γ irradiated $Mn_{0.6}Zn_{0.4}Fe_{1.92}Nd_{0.08}O_4$ nanoparticles

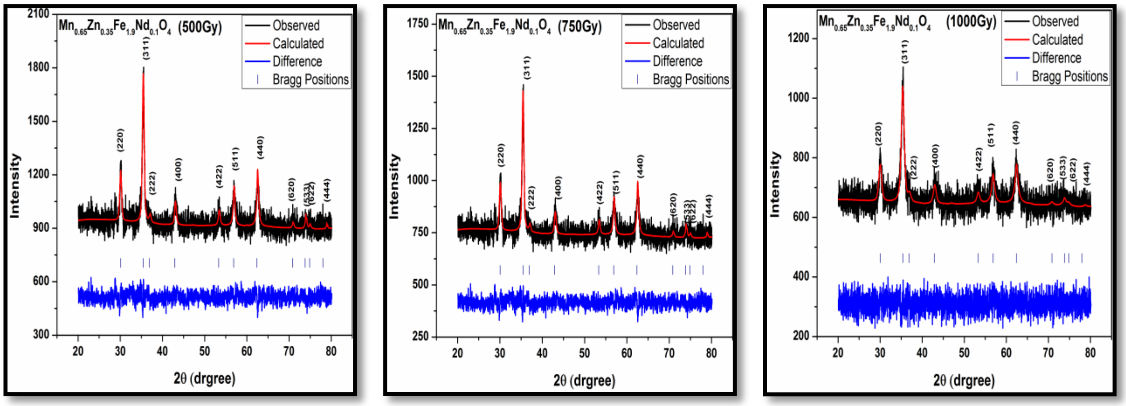

(a) (b) (c)

Figure 6.2.10 Rietveld refinement of γ irradiated $Mn_{0.65}Zn_{0.35}Fe_{1.9}Nd_{0.1}O_4$ nanoparticles

Table 6.2.1a Atomic positions and agreement R_p, R_{exp}, χ^2 obtaitained from Rietveld refinement of XRD patterns of $Mn_{0.6}Zn_{0.4}Fe_{2-x}Nd_xO_4$ nanoparticles irradiated with γ radiation dose of 500Gy.

Sample	Atoms	Atomic positions			R_P	R_{EXP}	χ^2
		x	y	z			
0.04	Mn/Zn/Fe	0.125	0.125	0.125	18.3	14.52	1.26
	Mn/Fe/Nd	0.500	0.500	0.500			
0.05	Mn/Zn/Fe	0.125	0.125	0.125	18.11	14.03	1.29
	Mn/Fe/Nd	0.500	0.500	0.500			
0.06	Mn/Zn/Fe	0.125	0.125	0.125	18.35	13.49	1.36
	Mn/Fe/Nd	0.500	0.500	0.500			
0.07	Mn/Zn/Fe	0.125	0.125	0.125	19.36	12.82	1.51
	Mn/Fe/Nd	0.500	0.500	0.500			
0.08	Mn/Zn/Fe	0.125	0.125	0.125	20.34	15.18	1.34
	Mn/Fe/Nd	0.500	0.500	0.500			
0.09	Mn/Zn/Fe	0.125	0.125	0.125	19.32	12.46	1.55
	Mn/Fe/Nd	0.500	0.500	0.500			
0.1	Mn/Zn/Fe	0.125	0.125	0.125	21.26	14.66	1.45
	Mn/Fe/Nd	0.500	0.500	0.500			

Table 6.2.1b Atomic positions and agreement R_p, R_{exp}, χ^2 obtaitained from Rietveld refinement of XRD patterns of $Mn_{0.6}Zn_{0.4}Fe_{2-x}Nd_xO_4$ nanoparticles irradiated with γ radiation dose of 750Gy.

Sample	Atoms	Atomic positions			R_P	R_{EXP}	χ^2
		x	y	z			
0.04	Mn/Zn/Fe	0.125	0.125	0.125	16.31	12.64	1.29
	Mn/Fe/Nd	0.500	0.500	0.500			
0.05	Mn/Zn/Fe	0.125	0.125	0.125	19.34	13.84	1.34
	Mn/Fe/Nd	0.500	0.500	0.500			
0.06	Mn/Zn/Fe	0.125	0.125	0.125	19.37	13.64	1.42
	Mn/Fe/Nd	0.500	0.500	0.500			
0.07	Mn/Zn/Fe	0.125	0.125	0.125	20.38	14.66	1.39

	Mn/Fe/Nd	0.500	0.500	0.500			
0.08	Mn/Zn/Fe	0.125	0.125	0.125	21.12	14.17	1.49
	Mn/Fe/Nd	0.500	0.500	0.500			
0.09	Mn/Zn/Fe	0.125	0.125	0.125	22.09	14.53	1.52
	Mn/Fe/Nd	0.500	0.500	0.500			
0.1	Mn/Zn/Fe	0.125	0.125	0.125	21.29	14.38	1.48
	Mn/Fe/Nd	0.500	0.500	0.500			

Table 6.2.1c Atomic positions and agreement R_p, R_{exp}, χ^2 obtaitained from Rietveld refinement of XRD patterns of $Mn_{0.6}Zn_{0.4}Fe_{2-x}Nd_xO_4$ nanoparticles irradiated with γ radiation dose of 1000Gy.

Sample	Atoms	Atomic positions			R_P	R_{EXP}	χ^2
		x	y	z			
0.04	Mn/Zn/Fe	0.125	0.125	0.125	18.35	12.92	1.42
	Mn/Fe/Nd	0.500	0.500	0.500			
0.05	Mn/Zn/Fe	0.125	0.125	0.125	19.55	14.16	1.38
	Mn/Fe/Nd	0.500	0.500	0.500			
0.06	Mn/Zn/Fe	0.125	0.125	0.125	20.31	15.21	1.55
	Mn/Fe/Nd	0.500	0.500	0.500			
0.07	Mn/Zn/Fe	0.125	0.125	0.125	19.36	12.47	1.45
	Mn/Fe/Nd	0.500	0.500	0.500			
0.08	Mn/Zn/Fe	0.125	0.125	0.125	20.24	13.05	1.56
	Mn/Fe/Nd	0.500	0.500	0.500			
0.09	Mn/Zn/Fe	0.125	0.125	0.125	20.55	12.61	1.63
	Mn/Fe/Nd	0.500	0.500	0.500			
0.1	Mn/Zn/Fe	0.125	0.125	0.125	21.34	12.70	1.68
	Mn/Fe/Nd	0.500	0.500	0.500			

Table 6.2.2a Atomic positions and agreement R_p, R_{exp} χ^2 obtaitained from Rietveld refinement of XRD patterns of $Mn_{0.65}Zn_{0.35}Fe_{2-x}Nd_xO_4$ nanoparticles irradiated with γ radiation dose of 500Gy.

Sample	Atoms	Atomic positions x	 y	 z	R_{exp}	R_{wp}	χ^2
0.04	Mn/Zn/Fe	0.125	0.125	0.125	19.38	13.65	1.42
	Mn/Fe/Nd	0.500	0.500	0.500			
0.05	Mn/Zn/Fe	0.125	0.125	0.125	20.21	13.84	1.46
	Mn/Fe/Nd	0.500	0.500	0.500			
0.06	Mn/Zn/Fe	0.125	0.125	0.125	22.04	14.59	1.51
	Mn/Fe/Nd	0.500	0.500	0.500			
0.07	Mn/Zn/Fe	0.125	0.125	0.125	21.36	18.23	1.37
	Mn/Fe/Nd	0.500	0.500	0.500			
0.08	Mn/Zn/Fe	0.125	0.125	0.125	22.35	15.20	1.47
	Mn/Fe/Nd	0.500	0.500	0.500			
0.09	Mn/Zn/Fe	0.125	0.125	0.125	22.36	14.71	1.43
	Mn/Fe/Nd	0.500	0.500	0.500			
0.1	Mn/Zn/Fe	0.125	0.125	0.125	23.25	14.90	1.56
	Mn/Fe/Nd	0.500	0.500	0.500			

Table 6.2.2b Atomic positions and agreement R_p, R_{exp} χ^2 obtaitained from Rietveld refinement of XRD patterns of $Mn_{0.65}Zn_{0.35}Fe_{2-x}Nd_xO_4$ nanoparticles irradiated with γ radiation dose of 750Gy.

Sample	Atoms	Atomic positions x	 y	 z	R_{exp}	R_{wp}	χ^2
0.04	Mn/Zn/Fe	0.125	0.125	0.125	18.21	13.59	1.34
	Mn/Fe/Nd	0.500	0.500	0.500			
0.05	Mn/Zn/Fe	0.125	0.125	0.125	18.95	13.73	1.38
	Mn/Fe/Nd	0.500	0.500	0.500			
0.06	Mn/Zn/Fe	0.125	0.125	0.125	20.11	14.16	1.42
	Mn/Fe/Nd	0.500	0.500	0.500			
0.07	Mn/Zn/Fe	0.125	0.125	0.125	21.35	14.62	1.46
	Mn/Fe/Nd	0.500	0.500	0.500			

0.08	Mn/Zn/Fe	0.125	0.125	0.125	21.47	14.60	1.53
	Mn/Fe/Nd	0.500	0.500	0.500			
0.09	Mn/Zn/Fe	0.125	0.125	0.125	22.31	14.97	1.49
	Mn/Fe/Nd	0.500	0.500	0.500			
0.1	Mn/Zn/Fe	0.125	0.125	0.125	22.37	15.01	1.49
	Mn/Fe/Nd	0.500	0.500	0.500			

Table 6.2.2c Atomic positions and agreement R_p, R_{exp} χ^2 obtaitained from Rietveld refinement of XRD patterns of $Mn_{0.65}Zn_{0.35}Fe_{2-x}Nd_xO_4$ nanoparticles irradiated with γ radiation dose of 1000Gy.

Sample	Atoms	Atomic positions			R_{exp}	R_{wp}	χ^2
		x	y	z			
0.04	Mn/Zn/Fe	0.125	0.125	0.125	19.38	13.64	1.42
	Mn/Fe/Nd	0.500	0.500	0.500			
0.05	Mn/Zn/Fe	0.125	0.125	0.125	19.55	13.29	1.47
	Mn/Fe/Nd	0.500	0.500	0.500			
0.06	Mn/Zn/Fe	0.125	0.125	0.125	20.01	13.89	1.44
	Mn/Fe/Nd	0.500	0.500	0.500			
0.07	Mn/Zn/Fe	0.125	0.125	0.125	21.22	13.96	1.52
	Mn/Fe/Nd	0.500	0.500	0.500			
0.08	Mn/Zn/Fe	0.125	0.125	0.125	22.38	14.25	1.57
	Mn/Fe/Nd	0.500	0.500	0.500			
0.09	Mn/Zn/Fe	0.125	0.125	0.125	22.36	14.33	1.56
	Mn/Fe/Nd	0.500	0.500	0.500			
0.1	Mn/Zn/Fe	0.125	0.125	0.125	21.37	14.53	1.47
	Mn/Fe/Nd	0.500	0.500	0.500			

A comparison of lattice constant as a function of Nd^{+3} concentrations for all the un-radiated and irradiated samples is shown in figure 6.2.11 (a & b). The plots are self explanatory. Ignoring out minor variations it may be seen that all the plots of radiated samples follow the corresponding trends of non-radiated $Mn_{0.6}Zn_{0.4}Fe_{2-x}Nd_xO_4$ and

$Mn_{0.65}Zn_{0.35}Fe_{2-x}Nd_xO_4$ nanoparticle samples respectively. Although the trends are similar there is an systematic vertical enhancement of the lattice constant with increasing Gamma radiation dose for a given Nd^{+3} concentration in the sample.

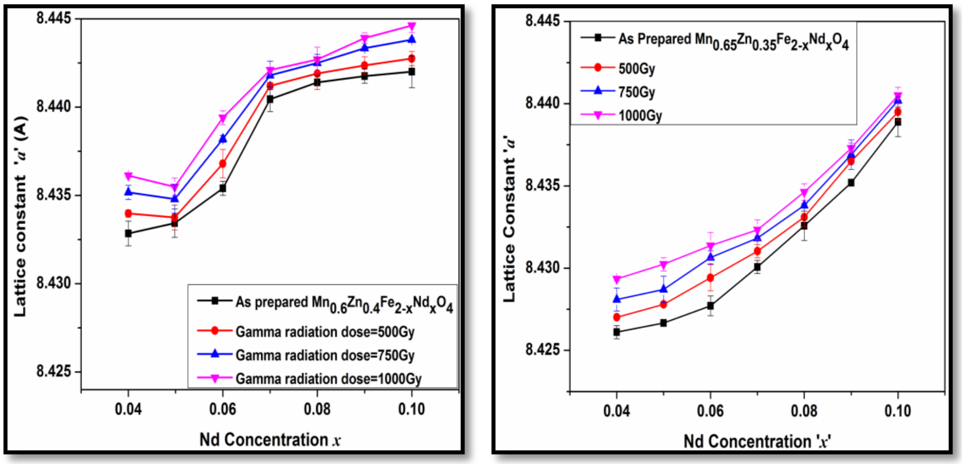

(a) (b)

Figure 6.2.11(a & b) Variation of lattice constant '*a*' with Nd^{+3} for as prepared and Gamma (γ) irradiated $Mn_{0.6}Zn_{0.4}Fe_{2-x}Nd_xO_4$ and $Mn_{0.65}Zn_{0.35}Fe_{2-x}Nd_xO_4$ nanoparticle.

For the samples with composition $Mn_{0.6}Zn_{0.4}Fe_{2-x}Nd_xO_4$, sample with x=0.04 showed a maximum increase of 3.3% in the lattice constant while the lowest variation of about 1.4% was observed for x=0.08. For $Mn_{0.65}Zn_{0.35}Fe_{2-x}Nd_xO_4$, sample with x=0.05 showed a maximum variation in '*a*' value of about 2.4% and minimum of 0.9% was seen for x=0.1. These enhancements in lattice constants coupled with the observations made in the XRD diffraction patterns which are the outcomes of radiating the samples with gamma radiation are long lasting irreversible effects as these are rather damaging effects that have occurred to the crystallinity of the material. It's long lasting nature has been verified by making repeated measurements after long intervals of time the maximum being six months. This increase in '*a*' value can be attributed to lattice distortions caused by increase in concentration of Fe^{+3} in high spin state which has a larger ionic radii (0.78Å) compared to (0.69 Å) the radius of Fe^{+3} in low spin state that is normally found at both the tetrahedral and the octahedral sites [9]. Figure 6.2.12 shows the variation of peak intensity of (311) plane with of the radiated samples with increasing Nd^{+3} concentrations. The peak intensities are seen to decrease with increasing gamma radiation dose indicating reduction in crystallinity with increase in amorphous content in the samples. Variation of full width at half maximum (FWHM) of peaks corresponding to (311) plane are represented in Figure 6.2.13. Increase in FWHM values with increasing gamma radiation dose is a indication of decrease in crystallite size. Thus the average crystallite size of the samples keeps decreasing with increasing gamma radiation dose. The variation of crystallite size with increase in gamma radiation dose is shown in Fig 6.2.14 (a & b).

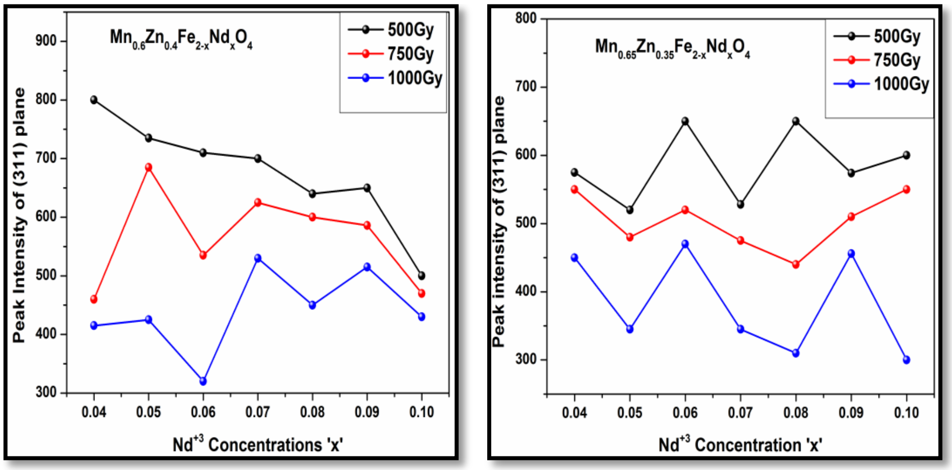

(a) (b)

Figure 6.2.12(a & b) Variation of peak intensity of (311) plane with Nd^{+3} for as prepared and Gamma (γ) irradiated $Mn_{0.6}Zn_{0.4}Fe_{2-x}Nd_xO_4$ and $Mn_{0.65}Zn_{0.35}Fe_{2-x}Nd_xO_4$ nanoparticle

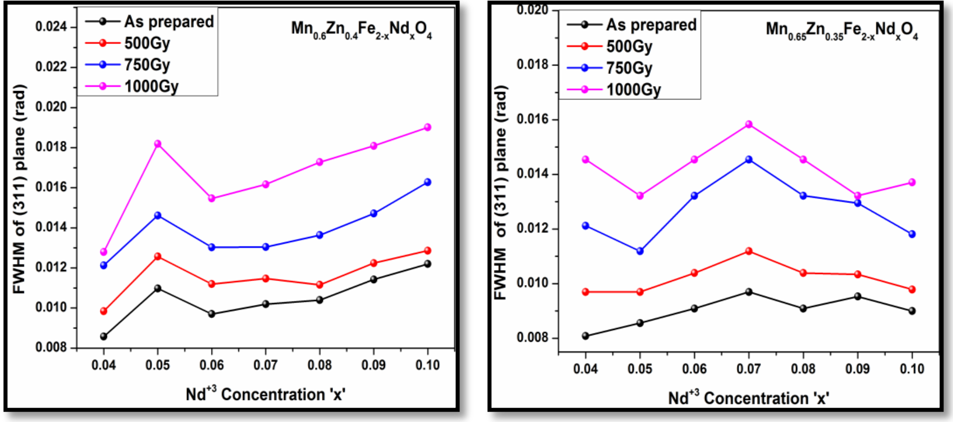

(a) (b)

Figure 6.2.13(a & b) Variation of FWHM of (311) peak with $Nd^{+3}$for as prepared and Gamma (γ) irradiated $Mn_{0.6}Zn_{0.4}Fe_{2-x}Nd_xO_4$ and $Mn_{0.65}Zn_{0.35}Fe_{2-x}Nd_xO_4$ nanoparticle

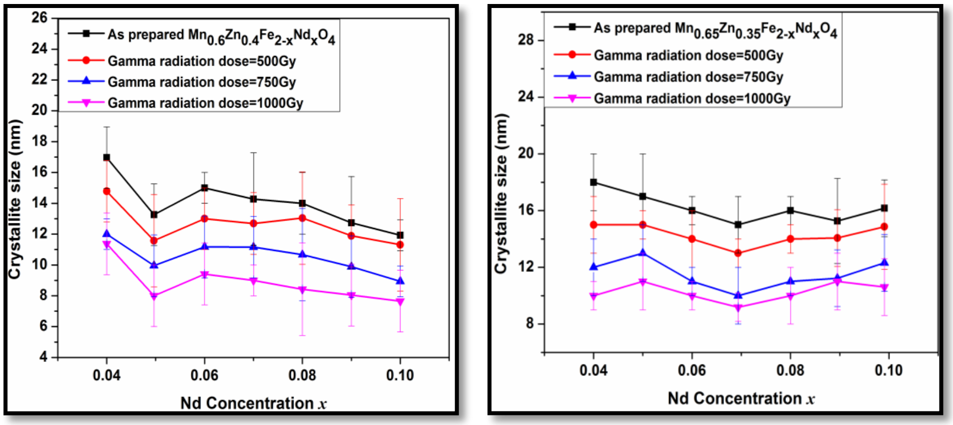

(a) (b)

Figure 6.2.14(a & b) Variation of crystallite size'*t*' with Nd^{+3}for as prepared and Gamma (γ) irradiated $Mn_{0.6}Zn_{0.4}Fe_{2-x}Nd_xO_4$ and $Mn_{0.65}Zn_{0.35}Fe_{2-x}Nd_xO_4$ nanoparticle.

Samples with x=0.05 and x=0.01 showed a maximum decrement of 6 nm and minimum of 4 nm respectively for $Mn_{0.6}Zn_{0.4}Fe_{2-x}Nd_xO_4$ while for the samples with composition $Mn_{0.65}Zn_{0.35}Fe_{2-x}Nd_xO_4$, a maximum decrement of 6 nm was seen for x=0.04 and minimum reduction of around 3nm was observed for x=0.09.

This decrease in crystallite size can be attributed to strain developed in the lattice due transition of Fe^{+3} in high spin state (which has a larger radius) on both the tetrahedral and the octahedral sites [9]. In the high spin state electrons occupy each of the five d orbitals of transition metal ion before any pairing occurs in accord with Hund's rule as the energy difference separation between e_g orbitals and t_{2g} orbitals is small enough and it is easier for an electron to occupy higher energy orbitals than to pair up with another electron into the same low-energy orbital, because of the repulsion resulting from matching two electrons in the same orbital. This kind of electronic arrangement results in an increase in ionic radius.

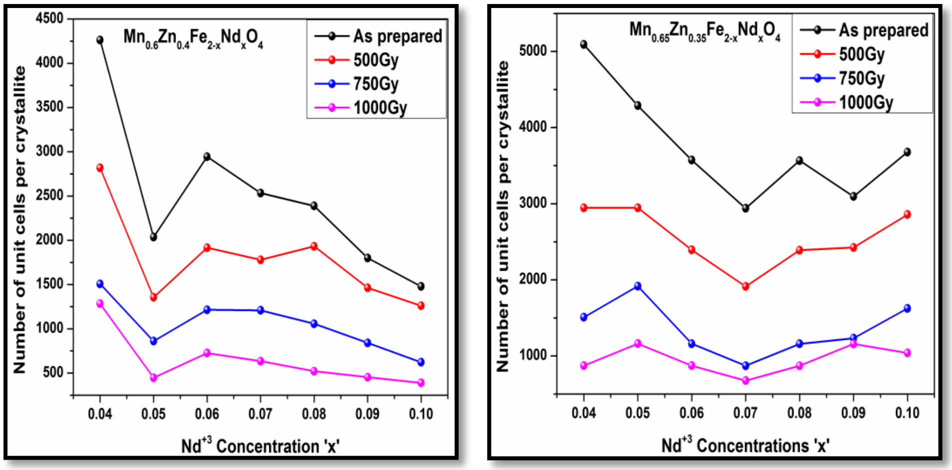

(a) (b)

Figure 6.2.15(a & b) Variation of number of unit cells per crystallite with Nd^{+3}for as prepared and Gamma (γ) irradiated Mn$_{0.6}$Zn$_{0.4}$Fe$_{2-x}$Nd$_x$O$_4$ and Mn$_{0.65}$Zn$_{0.35}$Fe$_{2-x}$Nd$_x$O$_4$ nanoparticle.

By considering the crystallites as spherical (hypothetical assumption) an estimate of number of unit cells per crystallite for as prepared and gamma radiated samples was made as the lattice size *"a"* is known and is represented in Figure 6.2.15. Enhancement of lattice constant with increasing gamma radiation indicates that there is a proportionate increment in the cell volume. Increase in cell volume and decrease in crystallite size taken together should show a decreasing trend of number of unit cells in the hypothetical crystallite. This is evident from the plots shown in fig. 6.2.15. Reduction in peak intensities (Fig. 6.2.12), increment in FWHM (Fig. 6.2.13), decrease in crystallite sizes (Fig.6.2.14) indicate that the porosity in the samples should increase with increasing dose of gamma radiation. Such a behavior is actually observed in the radiated samples and is evident from the plots shown in Fig. 6.2.16. The figure shows that percentage porosity in the samples decreases with increasing Nd^{+3} concentration but the same increases with increasing gamma radiation dose.

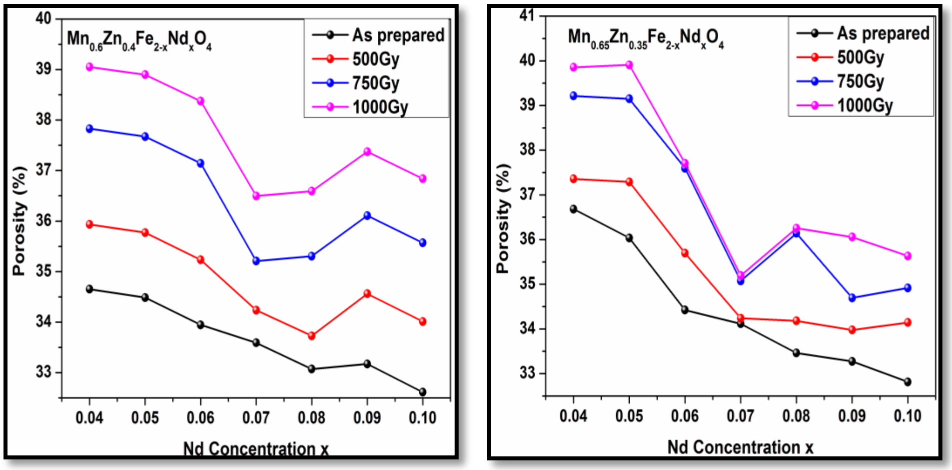

(a) (b)

Figure 6.2.16(a & b) Variation of X-ray Density with $Nd^{+3}$for as prepared and Gamma (γ) irradiated $Mn_{0.6}Zn_{0.4}Fe_{2-x}Nd_xO_4$ and $Mn_{0.65}Zn_{0.35}Fe_{2-x}Nd_xO_4$ nanoparticle.

Increasing porosity in the samples will result in decrease in both mass density and X-ray density. Variation of mass density and X-ray density of all the samples is presented in Fig.6.2.17 and 18. It may be seen that the results actually tally with the deductions arrived at that is the both the densities show that the samples are becoming less denser with increasing radiation dose.

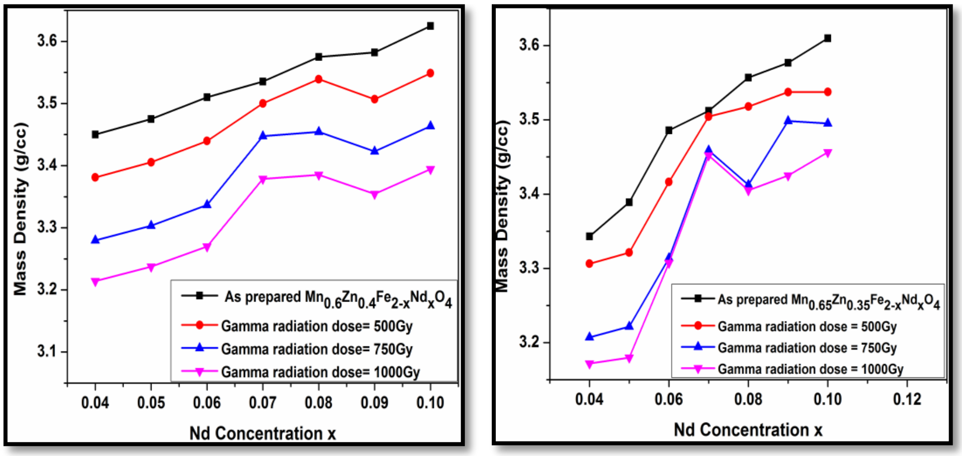

(a) (b)

Figure 6.2.17(a & b) Variation of Mass Density with $Nd^{+3}$for as prepared and Gamma (γ) irradiated $Mn_{0.6}Zn_{0.4}Fe_{2-x}Nd_xO_4$ and $Mn_{0.65}Zn_{0.35}Fe_{2-x}Nd_xO_4$ nanoparticle.

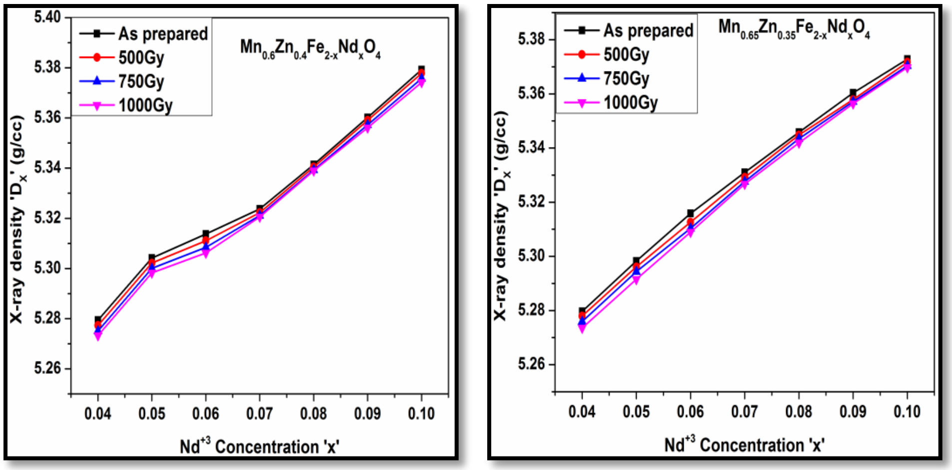

(a) (b)

Figure 6.2.18(a & b) Variation of X-ray Density with $Nd^{+3}$for as prepared and Gamma (γ) irradiated $Mn_{0.6}Zn_{0.4}Fe_{2-x}Nd_xO_4$ and $Mn_{0.65}Zn_{0.35}Fe_{2-x}Nd_xO_4$ nanoparticle.

Thus the above set of analysis and results indicate that the amorphous content in the samples increases with increase in gamma radiation dose. This phenomenon can be presented in the form of the following model.

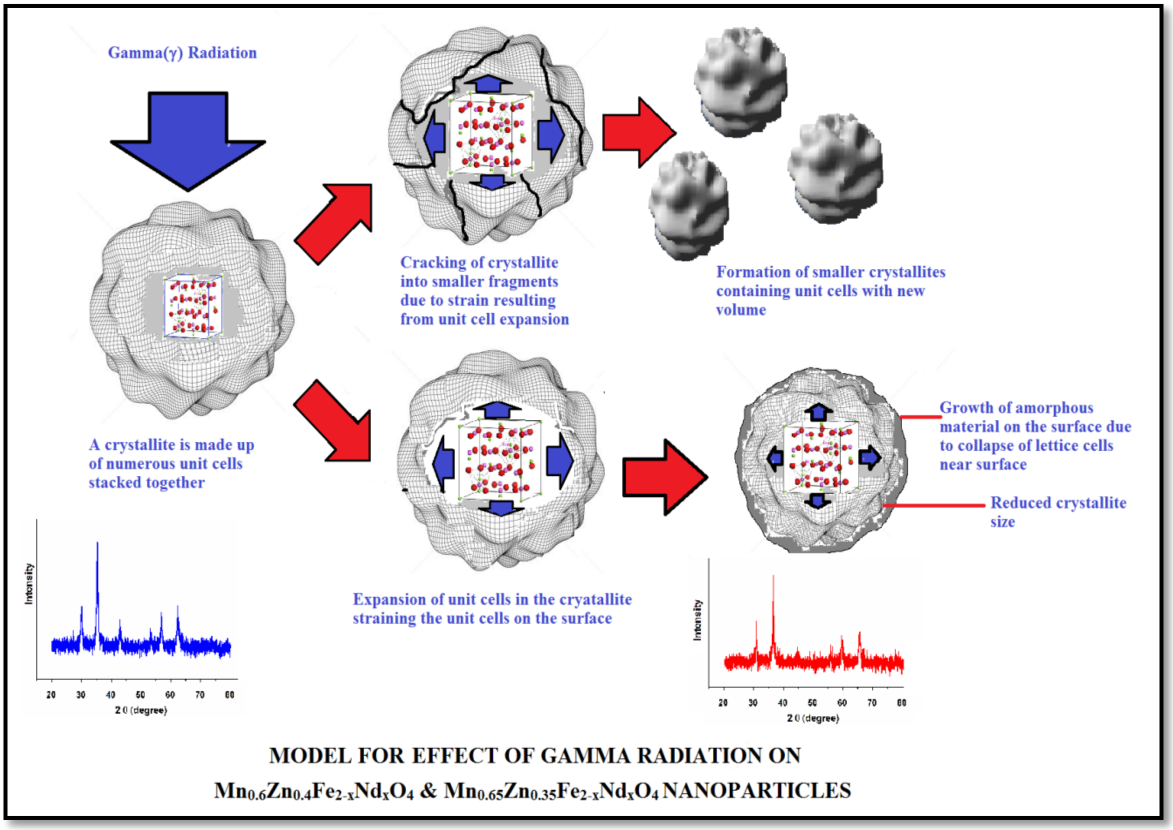

Figure 6.2.19 Hypothetical model for reduction of crystallite size

The pictorial representation of the model is depicted in Figure 6.2.19. It may be seen that when a $Mn_{0.6}Zn_{0.4}Fe_{2-x}Nd_xO_4$ or a $Mn_{0.65}Zn_{0.35}Fe_{2-x}Nd_xO_4$ nanoparticle is exposed to gamma radiation with wavelength 0.0106Å and 0.009Å with energy 1.17 MeV and 1.31MeV it imparts this energy within the particle as a result of which Fe^{+3} goes from low spin state to high spin state that has about 13% larger ionic radius. This radiation forced increase in the Fe^{+3} ion radius induces a large amount of strain in the lattice there by increasing the lattice size. The transition of Fe^{+3} low spin state to high spin state can also have impounding effect on the various bond lengths, other properties of the sample like magnetic and electrical properties of these materials that have been addressed in the later part of this chapter. This increment in the lattice constant increases the unit cell volume. This increase simultaneously occurs in all the unit cells located in the crystallite thereby developing large amount of pressure within the crystallite. The increased pressure within the crystallite can produce two types of effects. Firstly the pressure can break the larger crystallite in to smaller crystallites thereby increasing the surface area and the porosity to some extent. Secondly the pressure can push the unit cells near the surface in to a disordered structure which can result in increase of the amorphous component. Applying same analogy to all the crystallites in the samples would show drastic decrement in average crystallite size, sample density, X-ray density, with appropriate increase amorphous content and sample porosity. This particular character would increase with increase in radiation dose as increase in the dose means long exposure times. With the type of results obtained that are depicted in various graphs and plots given and discussed in the preceding part of this section the possibility of fitting/applying this model to the gamma radiated nanoparticles under study seems to be more appropriate. Thus the observed facts support this model and its application.

Variation in the bond lengths of the various bonds in the material is another important parameter that needs to be considered in gamma irradiated samples. The bond lengths between metal ions at tetrahedral site and metal at octahedral site denoted as **b, c, d, e** and **f** (bond length between cations) have been estimated for γ irradiated $Mn_{0.6}Zn_{0.4}Fe_{2-x}Nd_xO_4$ and $Mn_{0.65}Zn_{0.35}Fe_{2-x}Nd_xO_4$ nanosamples and are listed Tables 6.2.3a to 6.2.4c

Table 6.2.3a Variation of bond lengths between cations with Nd^{+3} concentration for $Mn_{0.6}Zn_{0.4}Fe_{2-x}Nd_xO_4$ irradiated with 500Gy

Sample $Mn_{0.6}Zn_{0.4}Fe_{2-x}Nd_xO_4$	*b* (Å)	*c* (Å)	*d* (Å)	*e* (Å)	*f* (Å)
x=0.04	2.981(8)	3.496(5)	3.652(1)	5.478(1)	5.164(7)
x=0.05	2.981(8)	3.496(4)	3.651(9)	5.477(8)	5.164(5)
x=0.06	2.982(9)	3.497(7)	3.653(2)	5.479(8)	5.166(4)
x=0.07	2.984(4)	3.499(5)	3.655(1)	5.482(7)	5.169(1)
x=0.08	2.984(7)	3.499(8)	3.655(4)	5.483(1)	5.169(5)
x=0.09	2.984(8)	3.500(1)	3.655(6)	5.483(4)	5.169(8)
x=0.1	2.984(9)	3.500(2)	3.655(8)	5.483(7)	5.170(1)

Table 6.2.3b Variation of bond lengths between cations with Nd^{+3} concentration for $Mn_{0.6}Zn_{0.4}Fe_{2-x}Nd_xO_4$ irradiated with 750Gy

Sample $Mn_{0.6}Zn_{0.4}Fe_{2-x}Nd_xO_4$	*b* (Å)	*c* (Å)	*d* (Å)	*e* (Å)	*f* (Å)
x=0.04	2.982(2)	3.497(1)	3.652(5)	5.478(8)	5.165(4)
x=0.05	2.982(1)	3.496(8)	3.652(3)	5.478(5)	5.165(2)
x=0.06	2.983(3)	3.498(2)	3.653(8)	5.480(7)	5.167(3)
x=0.07	2.984(6)	3.499(9)	3.655(4)	5.483(1)	5.169(5)
x=0.08	2.984(8)	3.500(1)	3.655(7)	5.483(5)	5.169(9)
x=0.09	2.985(1)	3.500(4)	3.656(1)	5.484(1)	5.170(4)

x=0.1	2.985(3)	3.500(6)	3.656(3)	5.484(4)	5.170(7)

Table 6.2.3c Variation of bond lengths between cations with Nd^{+3} concentration for $Mn_{0.6}Zn_{0.4}Fe_{2-x}Nd_xO_4$ irradiated with 1000Gy

Sample $Mn_{0.6}Zn_{0.4}Fe_{2-x}Nd_xO_4$	*b* (Å)	*c* (Å)	*d* (Å)	*e* (Å)	*f* (Å)
x=0.04	2.982(6)	3.497(4)	3.652(9)	5.479(4)	5.166(1)
x=0.05	2.982(3)	3.497(1)	3.652(6)	5.479(1)	5.165(6)
x=0.06	2.983(7)	3.498(7)	3.654(3)	5.481(5)	5.168(5)
x=0.07	2.984(7)	3.499(9)	3.655(5)	5.483(3)	5.169(7)
x=0.08	2.984(9)	3.500(1)	3.655(7)	5.483(6)	5.170(1)
x=0.09	2.985(3)	3.500(6)	3.656(3)	5.484(5)	5.170(8)
x=0.1	2.985(6)	3.500(9)	3.656(6)	5.484(9)	5.171(2)

Table 6.2.4a Variation of bond lengths between cations with Nd^{+3} concentration for $Mn_{0.65}Zn_{0.35}Fe_{2-x}Nd_xO_4$ irradiated with 500Gy

Sample $Mn_{0.65}Zn_{0.35}Fe_{2-x}Nd_xO_4$	*b* (Å)	*c* (Å)	*d* (Å)	*e* (Å)	*f* (Å)
x=0.04	2.979(3)	3.493(6)	3.649(1)	5.473(5)	5.160(4)
x=0.05	2.979(6)	3.493(9)	3.649(3)	5.474(2)	5.160(9)
x=0.06	2.980(2)	3.494(6)	3.650(1)	5.475(1)	5.161(9)
x=0.07	2.980(8)	3.495(3)	3.650(7)	5.476(1)	5.162(9)
x=0.08	2.981(5)	3.496(1)	3.651(6)	5.477(4)	5.164(2)
x=0.09	2.982(7)	3.497(5)	3.653(1)	5.479(6)	5.166(3)
x=0.1	2.983(8)	3.498(8)	3.654(4)	5.481(6)	5.168(2)

Table 6.2.4b Variation of bond lengths between cations with Nd^{+3} concentration for $Mn_{0.65}Zn_{0.35}Fe_{2-x}Nd_xO_4$ irradiated with 750Gy

Sample $Mn_{0.65}Zn_{0.35}Fe_{2-x}Nd_xO_4$	*b* (Å)	*c* (Å)	*d* (Å)	*e* (Å)	*f* (Å)
x=0.04	2.979(7)	3.494(1)	3.649(5)	5.474(2)	5.161(1)
x=0.05	2.979(9)	3.494(3)	3.649(7)	5.474(6)	5.161(5)
x=0.06	2.980(6)	3.495(1)	3.650(5)	5.475(8)	5.162(6)
x=0.07	2.981(1)	3.495(6)	3.651(1)	5.476(6)	5.163(4)
x=0.08	2.981(8)	3.496(4)	3.651(9)	5.477(9)	5.164(6)
x=0.09	2.982(8)	3.497(7)	3.653(2)	5.479(9)	5.166(5)
x=0.1	2.984(1)	3.499(1)	3.654(7)	5.482(1)	5.168(5)

Table 6.2.4c Variation of bond lengths between cations with Nd^{+3} concentration for $Mn_{0.65}Zn_{0.35}Fe_{2-x}Nd_xO_4$ irradiated with 1000Gy

Sample $Mn_{0.65}Zn_{0.35}Fe_{2-x}Nd_xO_4$	*b* (Å)	*c* (Å)	*d* (Å)	*e* (Å)	*f* (Å)
x=0.04	2.980(2)	3.494(6)	3.650(1)	5.475(1)	5.161(9)
x=0.05	2.980(5)	3.494(9)	3.650(4)	5.475(6)	5.162(4)
x=0.06	2.980(9)	3.495(4)	3.650(8)	5.476(3)	5.163(1)
x=0.07	2.981(2)	3.495(8)	3.651(3)	5.476(9)	5.163(7)
x=0.08	2.982(1)	3.496(8)	3.652(3)	5.478(4)	5.165(1)
x=0.09	2.983(1)	3.497(9)	3.653(4)	5.480(1)	5.166(7)
x=0.1	2.984(1)	3.499(2)	3.654(8)	5.482(2)	5.168(7)

Bond length values for all the samples were observed to increase with increasing γ irradiation dose as estimated in the model. This increase in the bond lengths can be attributed to increase in the concentration of Fe^{+3} in high spin state with larger ionic radius (0.78Å) at both the octahedral and the tetrahedral site. Similar trend is observed in the bond lengths between cations and anions at both tetrahedral site and octahedral site with increasing radiation dose. The bond lengths elevated from XRD-data are listed in Table 6.2.5a to table 6.2.6c [8]. The observed increase in all the bond lengths of the gamma irradiated samples further supports the analogy proposed in the model that is depicted in Fig.6.2.19

Table 6.2.5aVariation of bond lengths between cations and anions with Nd^{+3} concentrations for $Mn_{0.6}Zn_{0.4}Fe_{2-x}Nd_xO_4$ irradiated with 500Gy

Sample $Mn_{0.6}Zn_{0.4}Fe_{2-x}Nd_xO_4$	*p* (Å)	*q*(Å)	*r* (Å)	*s*(Å)
x=0.04	2.108(4)	1.826(1)	6.993(1)	3.652(1)
x=0.05	2.108(4)	1.825(9)	6.992(8)	3.651(9)
x=0.06	2.109(2)	1.826(6)	6.995(4)	3.653(2)
x=0.07	2.110(3)	1.827(5)	6.999(1)	3.655(1)
x=0.08	2.110(4)	1.827(7)	6.999(6)	3.655(4)
x=0.09	2.110(6)	1.827(8)	7.000(0)	3.655(6)
x=0.1	2.110(7)	1.827(9)	7.000(3)	3.655(8)

Table 6.2.5b Variation of bond lengths between cations and anions with Nd^{+3} concentrations for $Mn_{0.6}Zn_{0.4}Fe_{2-x}Nd_xO_4$ irradiated with 750Gy

Sample $Mn_{0.6}Zn_{0.4}Fe_{2-x}Nd_xO_4$	*p* (Å)	*q*(Å)	*r* (Å)	*s*(Å)
x=0.04	2.108(7)	1.826(2)	6.994(1)	3.652(5)
x=0.05	2.108(6)	1.826(5)	6.993(7)	3.652(3)
x=0.06	2.109(5)	1.826(9)	6.996(5)	3.653(8)
x=0.07	2.110(5)	1.827(7)	6.999(5)	3.655(4)
x=0.08	2.110(6)	1.827(8)	7.000(1)	3.655(7)
x=0.09	2.110(8)	1.828(1)	7.000(8)	3.656(1)
x=0.1	2.1109(5)	1.828(1)	7.001(2)	3.656(3)

Table 6.2.5c Variation of bond lengths between cations and anions with Nd^{+3} concentrations for $Mn_{0.6}Zn_{0.4}Fe_{2-x}Nd_xO_4$ irradiated with 1000Gy

Sample $Mn_{0.6}Zn_{0.4}Fe_{2-x}Nd_xO_4$	*p* (Å)	*q*(Å)	*r* (Å)	*s*(Å)
x=0.04	2.109(1)	1.826(4)	6.994(8)	3.652(9)
x=0.05	2.109(8)	1.826(3)	6.994(3)	3.652(6)
x=0.06	2.109(9)	1.827(2)	6.997(6)	3.654(4)
x=0.07	2.110(5)	1.827(8)	6.999(8)	3.655(5)
x=0.08	2.110(7)	1.827(9)	7.000(3)	3.655(8)
x=0.09	2.110(9)	1.828(2)	7.001(3)	3.656(3)
x=0.1	2.111(1)	1.828(3)	7.001(9)	3.656(6)

Table 6.2.6aVariation of bond lengths between cations and anions with Nd^{+3} concentrations for $Mn_{0.65}Zn_{0.35}Fe_{2-x}Nd_xO_4$ irradiated with 500Gy

Sample $Mn_{0.65}Zn_{0.35}Fe_{2-x}Nd_xO_4$	*p* (Å)	*q*(Å)	*r* (Å)	*s*(Å)
x=0.04	2.106(7)	1.824(5)	6.987(3)	3.649(1)
x=0.05	2.106(9)	1.824(6)	6.987(9)	3.649(3)
x=0.06	2.107(3)	1.825(1)	6.989(3)	3.650(4)
x=0.07	2.107(7)	1.825(3)	6.990(6)	3.650(7)
x=0.08	2.108(2)	1.825(8)	6.992(3)	3.651(6)
x=0.09	2.109(1)	1.826(5)	6.995(2)	3.653(1)
x=0.1	2.109(8)	1.827(2)	6.997(6)	3.654(4)

Table 6.2.6b Variation of bond lengths between cations and anions with Nd^{+3} concentrations for $Mn_{0.65}Zn_{0.35}Fe_{2-x}Nd_xO_4$ irradiated with 750Gy

Sample $Mn_{0.65}Zn_{0.35}Fe_{2-x}Nd_xO_4$	*p* (Å)	*q*(Å)	*r* (Å)	*s*(Å)
x=0.04	2.107(1)	1.824(7)	6.988(2)	3.649(4)
x=0.05	2.107(2)	1.824(8)	6.988(7)	3.649(7)
x=0.06	2.107(6)	1.825(2)	6.990(3)	3.650(5)

x=0.07	2.107(9)	1.825(5)	6.991(3)	3.651(1)
x=0.08	2.108(5)	1.825(9)	6.992(9)	3.651(9)
x=0.09	2.109(2)	1.826(6)	6.995(5)	3.653(2)
x=0.1	2.110(1)	1.827(3)	6.998(2)	3.654(7)

Table 6.2.6c Variation of bond lengths between cations and anions with Nd^{+3} concentrations for $Mn_{0.65}Zn_{0.35}Fe_{2-x}Nd_xO_4$ irradiated with 1000Gy

Sample $Mn_{0.65}Zn_{0.35}Fe_{2-x}Nd_xO_4$	*p* (Å)	*q*(Å)	*r* (Å)	*s*(Å)
x=0.04	2.107(3)	1.825(1)	6.989(3)	3.650(1)
x=0.05	2.107(5)	1.825(2)	6.989(9)	3.650(5)
x=0.06	2.107(8)	1.825(4)	6.990(9)	3.650(8)
x=0.07	2.108(1)	1.825(6)	6.991(7)	3.651(3)
x=0.08	2.108(6)	1.826(2)	6.993(6)	3.652(3)
x=0.09	2.109(3)	1.826(7)	6.995(8)	3.653(4)
x=0.1	2.110(1)	1.827(4)	6.998(5)	3.654(8)

Table 6.2.7aVariation of bond angles between cations with Nd^{+3} concentrations for $Mn_{0.6}Zn_{0.4}Fe_{2-x}Nd_xO_4$ irradiated with 500Gy

Sample $Mn_{0.6}Zn_{0.4}Fe_{2-x}Nd_xO_4$	θ_1	θ_2	θ_3	θ_4	θ_5
x=0.04	125.264(5)	142.322(3)	90.000(2)	125.264(5)	81.240(2)
x=0.05	125.264(9)	142.322(5)	90.000(7)	125.264(8)	81.240(1)
x=0.06	125.265(5)	142.323(1)	90.001(3)	125.263(9)	81.239(9)
x=0.07	125.265(7)	142.323(5)	90.001(8)	125.263(7)	81.239(7)
x=0.08	125.265(9)	142.323(9)	90.001(9)	125.263(4)	81.239(5)
x=0.09	125.265(8)	142.324(5)	90.002(4)	125.263(5)	81.239(4)
x=0.1	125.265(8)	142.324(9)	90.002(6)	125.263(1)	81.239(3)

Table 6.2.7bVariation of bond angles between cations with Nd^{+3} concentrations for $Mn_{0.6}Zn_{0.4}Fe_{2-x}Nd_xO_4$ irradiated with 750Gy

Sample $Mn_{0.6}Zn_{0.4}Fe_{2-x}Nd_xO_4$	θ_1	θ_2	θ_3	θ_4	θ_5
x=0.04	125.264(7)	142.322(3)	90.000(8)	125.264(4)	81.240(1)
x=0.05	125.264(9)	142.322(7)	90.000(9)	125.264(1)	81.239(8)
x=0.06	125.265(2)	142.322(9)	90.001(3)	125.263(7)	81.239(5)
x=0.07	125.265(7)	142.323(4)	90.001(9)	125.263(5)	81.239(3)
x=0.08	125.265(9)	142.323(8)	90.002(3)	125.263(3)	81.239(1)
x=0.09	125.266(3)	142.324(7)	90.002(7)	125.263(1)	81.239(1)
x=0.1	125.266(7)	142.324(9)	90.002(9)	125.262(9)	81.238(9)

Table 6.2.7cVariation of bond angles between cations with Nd^{+3} concentrations for $Mn_{0.6}Zn_{0.4}Fe_{2-x}Nd_xO_4$ irradiated with 1000Gy

Sample $Mn_{0.6}Zn_{0.4}Fe_{2-x}Nd_xO_4$	θ_1	θ_2	θ_3	θ_4	θ_5
x=0.04	125.264(9)	142.322(6)	90.001(2)	125.264(2)	81.239(8)
x=0.05	125.265(1)	142.322(9)	90.001(6)	125.263(9)	81.239(6)
x=0.06	125.265(5)	142.323(5)	90.002(0)	125.263(4)	81.239(2)
x=0.07	125.265(8)	142.324(1)	90.002(3)	125.263(1)	81.238(9)
x=0.08	125.266(1)	142.324(5)	90.002(5)	125.262(8)	81.238(6)
x=0.09	125.266(3)	142.324(9)	90.002(8)	125.262(6)	81.238(5)
x=0.1	125.266(5)	142.325(7)	90.003(1)	125.262(7)	81.238(3)

Table 6.2.8a Variation of bond angles between cations with Nd^{+3} concentrations for $Mn_{0.65}Zn_{0.35}Fe_{2-x}Nd_xO_4$ irradiated with 500Gy

Sample $Mn_{0.65}Zn_{0.35}Fe_{2-x}Nd_xO_4$	θ_1	θ_2	θ_3	θ_4	θ_5
x=0.04	125.264(8)	142.322(5)	90.001(3)	125.264(5)	81.240(2)
x=0.05	125.265(2)	142.322(9)	90.001(6)	125.264(1)	81.239(8)
x=0.06	125.266(4)	142.323(3)	90.001(9)	125.263(7)	81.239(6)

x=0.07	125.266(7)	142.323(6)	90.002(2)	125.263(5)	81.239(4)
x=0.08	125.266(9)	142.324(3)	90.002(5)	125.263(3)	81.239(1)
x=0.09	125.267(1)	142.324(7)	90.002(8)	125.263(1)	81.238(9)
x=0.1	125.267(3)	142.325(1)	90.003(0)	125.262(8)	81.238(6)

Table 6.2.8b Variation of bond angles between cations with Nd^{+3} concentrations for $Mn_{0.65}Zn_{0.35}Fe_{2-x}Nd_xO_4$ irradiated with 750Gy

Sample $Mn_{0.65}Zn_{0.35}Fe_{2-x}Nd_xO_4$	θ_1	θ_2	θ_3	θ_4	θ_5
x=0.04	125.265(7)	142.322(8)	90.001(5)	125.264(2)	81.239(9)
x=0.05	125.265(9)	142.323(1)	90.001(8)	125.263(9)	81.239(7)
x=0.06	125.266(3)	142.323(4)	90.002(2)	125.263(5)	81.239(5)
x=0.07	125.266(8)	142.323(7)	90.002(5)	125.263(3)	81.239(2)
x=0.08	125.267(2)	142.324(5)	90.002(7)	125.263(1)	81.238(9)
x=0.09	125.267(5)	142.324(8)	90.002(9)	125.262(8)	81.238(6)
x=0.1	125.267(8)	142.325(3)	90.003(2)	125.262(6)	81.238(3)

Table 6.2.8c Variation of bond angles between cations with Nd^{+3} concentrations for $Mn_{0.65}Zn_{0.35}Fe_{2-x}Nd_xO_4$ irradiated with 1000Gy

Sample $Mn_{0.65}Zn_{0.35}Fe_{2-x}Nd_xO_4$	θ_1	θ_2	θ_3	θ_4	θ_5
x=0.04	125.265(9)	142.323(2)	90.001(7)	125.263(8)	81.239(7)
x=0.05	125.266(2)	142.323(5)	90.002(0)	125.263(6)	81.239(5)
x=0.06	125.266(6)	142.323(7)	90.002(3)	125.263(4)	81.239(3)
x=0.07	125.266(9)	142.324(1)	90.002(7)	125.263(2)	81.238(8)
x=0.08	125.267(3)	142.324(6)	90.002(7)	125.262(7)	81.238(7)
x=0.09	125.267(7)	142.325(1)	90.003(2)	125.262(6)	81.238(4)
x=0.1	125.267(9)	142.325(6)	90.003(2)	125.262(3)	81.238(1)

The various bond angles between cations denoted as **θ_1, θ_2, θ_3, θ_4** and **θ_5** were calculated for γ irradiated $Mn_{0.6}Zn_{0.4}Fe_{2-x}Nd_xO_4$ and $Mn_{0.65}Zn_{0.35}Fe_{2-x}Nd_xO_4$ nanosamples from XRD- data as calculated and discussed in chapter 4.

The bond angles **θ_1, θ_2** and **θ_3** were found to increase with increasing γ radiation dose resulting in enhancement in exchange energy and strengthening A-B and B-B interaction [1,9,10].

The cation distributions over the two sites for all γ irradiated $Mn_{0.6}Zn_{0.4}Fe_{2-x}Nd_xO_4$ and $Mn_{0.65}Zn_{0.35}Fe_{2-x}Nd_xO_4$ nano-samples are obtained as discussed in chapter 4 and are listed in Tables 6.3.7a to 6.3.8c.

Table 6.3.7a Variation of cation distribution with Nd $^{+3}$ concentrations of $Mn_{0.6}Zn_{0.4}Fe_{2-x}Nd_xO_4$ and $Mn_{0.65}Zn_{0.35}Fe_{2-x}Nd_xO_4$ irradiated with 500Gy

Concentrations of Nd^{+3} (x)	$Mn_{0.6}Zn_{0.4}Fe_{2-x}Nd_xO_4$		$Mn_{0.65}Zn_{0.4}Fe_{2-x}Nd_xO_4$	
	A-site	B-site	A-site	B-site
0.04	$Mn_{0.51}Zn_{0.4}Fe_{0.09}$	$Mn_{0.09}Fe_{1.87}Nd_{0.04}$	$Mn_{0.48}Zn_{0.35}Fe_{0.17}$	$Mn_{0.17}Fe_{1.79}Nd_{0.04}$
0.05	$Mn_{0.50}Zn_{0.4}Fe_{0.10}$	$Mn_{0.10}Fe_{1.85}Nd_{0.05}$	$Mn_{0.47}Zn_{0.35}Fe_{0.18}$	$Mn_{0.18}Fe_{1.77}Nd_{0.05}$
0.06	$Mn_{0.49}Zn_{0.4}Fe_{0.11}$	$Mn_{0.11}Fe_{1.83}Nd_{0.06}$	$Mn_{0.45}Zn_{0.35}Fe_{0.20}$	$Mn_{0.20}Fe_{1.74}Nd_{0.06}$
0.07	$Mn_{0.47}Zn_{0.4}Fe_{0.13}$	$Mn_{0.13}Fe_{1.80}Nd_{0.07}$	$Mn_{0.44}Zn_{0.35}Fe_{0.21}$	$Mn_{0.21}Fe_{1.72}Nd_{0.07}$
0.08	$Mn_{0.46}Zn_{0.4}Fe_{0.14}$	$Mn_{0.14}Fe_{1.78}Nd_{0.08}$	$Mn_{0.43}Zn_{0.35}Fe_{0.23}$	$Mn_{0.22}Fe_{1.70}Nd_{0.08}$
0.09	$Mn_{0.44}Zn_{0.4}Fe_{0.16}$	$Mn_{0.16}Fe_{1.75}Nd_{0.09}$	$Mn_{0.41}Zn_{0.35}Fe_{0.24}$	$Mn_{0.24}Fe_{1.67}Nd_{0.09}$
0.1	$Mn_{0.47}Zn_{0.4}Fe_{0.17}$	$Mn_{0.17}Fe_{1.73}Nd_{0.1}$	$Mn_{0.39}Zn_{0.35}Fe_{0.26}$	$Mn_{0.26}Fe_{1.64}Nd_{0.1}$

Table 6.3.7b Variation of cation distribution with Nd $^{+3}$ concentrations of $Mn_{0.6}Zn_{0.4}Fe_{2-x}Nd_xO_4$ and $Mn_{0.65}Zn_{0.35}Fe_{2-x}Nd_xO_4$ irradiated with 750Gy

Concentrations of Nd^{+3} (x)	$Mn_{0.6}Zn_{0.4}Fe_{2-x}Nd_xO_4$		$Mn_{0.65}Zn_{0.4}Fe_{2-x}Nd_xO_4$	
	A-site	B-site	A-site	B-site
0.04	$Mn_{0.48}Zn_{0.4}Fe_{0.12}$	$Mn_{0.12}Fe_{1.84}Nd_{0.04}$	$Mn_{0.43}Zn_{0.35}Fe_{0.22}$	$Mn_{0.22}Fe_{1.74}Nd_{0.04}$
0.05	$Mn_{0.46}Zn_{0.4}Fe_{0.14}$	$Mn_{0.14}Fe_{1.81}Nd_{0.05}$	$Mn_{0.41}Zn_{0.35}Fe_{0.24}$	$Mn_{0.24}Fe_{1.71}Nd_{0.05}$
0.06	$Mn_{0.45}Zn_{0.4}Fe_{0.15}$	$Mn_{0.15}Fe_{1.79}Nd_{0.06}$	$Mn_{0.40}Zn_{0.35}Fe_{0.25}$	$Mn_{0.25}Fe_{1.69}Nd_{0.06}$
0.07	$Mn_{0.44}Zn_{0.4}Fe_{0.16}$	$Mn_{0.16}Fe_{1.77}Nd_{0.07}$	$Mn_{0.39}Zn_{0.35}Fe_{0.26}$	$Mn_{0.26}Fe_{1.67}Nd_{0.07}$
0.08	$Mn_{0.43}Zn_{0.4}Fe_{0.17}$	$Mn_{0.17}Fe_{1.75}Nd_{0.08}$	$Mn_{0.38}Zn_{0.35}Fe_{0.27}$	$Mn_{0.27}Fe_{1.65}Nd_{0.08}$
0.09	$Mn_{0.42}Zn_{0.4}Fe_{0.18}$	$Mn_{0.18}Fe_{1.73}Nd_{0.09}$	$Mn_{0.36}Zn_{0.35}Fe_{0.29}$	$Mn_{0.29}Fe_{1.62}Nd_{0.09}$
0.1	$Mn_{0.40}Zn_{0.4}Fe_{0.20}$	$Mn_{0.20}Fe_{1.70}Nd_{0.1}$	$Mn_{0.35}Zn_{0.35}Fe_{0.30}$	$Mn_{0.30}Fe_{1.60}Nd_{0.1}$

Table 6.3.7c Variation of cation distribution with Nd $^{+3}$ concentrations of $Mn_{0.6}Zn_{0.4}Fe_{2-x}Nd_xO_4$ and $Mn_{0.65}Zn_{0.35}Fe_{2-x}Nd_xO_4$ irradiated with 1000Gy

Concentrations of Nd^{+3} (x)	$Mn_{0.6}Zn_{0.4}Fe_{2-x}Nd_xO_4$		$Mn_{0.65}Zn_{0.4}Fe_{2-x}Nd_xO_4$	
	A-site	B-site	A-site	B-site
0.04	$Mn_{0.45}Zn_{0.4}Fe_{0.15}$	$Mn_{0.15}Fe_{1.81}Nd_{0.04}$	$Mn_{0.40}Zn_{0.35}Fe_{0.25}$	$Mn_{0.25}Fe_{1.71}Nd_{0.04}$
0.05	$Mn_{0.44}Zn_{0.4}Fe_{0.16}$	$Mn_{0.16}Fe_{1.79}Nd_{0.05}$	$Mn_{0.39}Zn_{0.35}Fe_{0.26}$	$Mn_{0.26}Fe_{1.69}Nd_{0.05}$
0.06	$Mn_{0.43}Zn_{0.35}Fe_{0.17}$	$Mn_{0.17}Fe_{1.77}Nd_{0.06}$	$Mn_{0.38}Zn_{0.35}Fe_{0.27}$	$Mn_{0.27}Fe_{1.67}Nd_{0.06}$
0.07	$Mn_{0.42}Zn_{0.4}Fe_{0.18}$	$Mn_{0.18}Fe_{1.75}Nd_{0.07}$	$Mn_{0.37}Zn_{0.35}Fe_{0.28}$	$Mn_{0.28}Fe_{1.65}Nd_{0.07}$
0.08	$Mn_{0.41}Zn_{0.4}Fe_{0.19}$	$Mn_{0.19}Fe_{1.73}Nd_{0.08}$	$Mn_{0.36}Zn_{0.35}Fe_{0.29}$	$Mn_{0.29}Fe_{1.63}Nd_{0.08}$
0.09	$Mn_{0.40}Zn_{0.4}$	$Mn_{0.20}Fe_{1.71}$	$Mn_{0.35}Zn_{0.35}$	$Mn_{0.30}Fe_{1.61}$

0.1	$Fe_{0.20}$ $Mn_{0.38}Zn_{0.4}$ $Fe_{0.22}$	$Nd_{0.09}$ $Mn_{0.22}Fe_{1.68}$ $Nd_{0.1}$	$Fe_{0.30}$ $Mn_{0.34}Zn_{0.35}$ $Fe_{0.31}$	$Nd_{0.09}$ $Mn_{0.31}Fe_{1.59}$ $Nd_{0.1}$

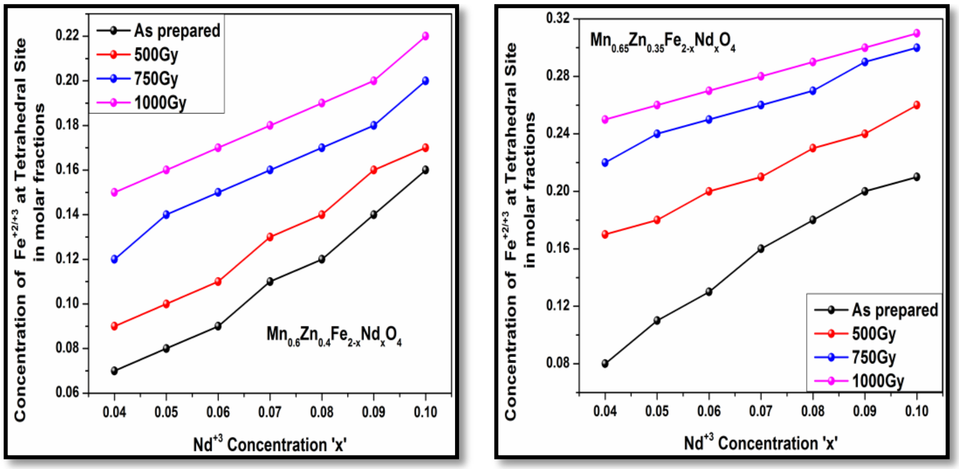

(a) (b)

Figure 6.2.20 Variation of $Fe^{+3/+2}$ concentration at tetrahedral site with increasing Nd^{+3} concentration for different γ radiation doses

It can be clearly seen in Tables 6.3.7a to 6.3.7c that with increasing gamma radiation dose alters the Fe^{+3} content at both octahedral and the tetrahedral site. The transfer of Fe^{+3} from octahedral site to tetrahedral site is enhanced with increasing gamma radiation dose. For $Mn_{0.6}Zn_{0.4}Fe_{2-x}Nd_xO_4$ series, sample with x=0.04 showed a maximum Fe^{+3} transfer of 0.08 units while a minimum transfer of 0.06 units was observed for x=0.1. The corresponding variations of Fe^{+3} transfers to tetrahedral site are presented in Figure 6.2.17(a). A comparison of the two series of samples as far as over all Fe^{+3} transfers to tetrahedral site is concerned the second series that is $Mn_{0.65}Zn_{0.35}Fe_{2-x}Nd_xO_4$ shows a greater transfer then $Mn_{0.6}Zn_{0.4}Fe_{2-x}Nd_xO_4$ series. A remarkable Fe^{+3} transfer of 0.17 units while a minimum of 0.11 units was seen for x=0.1 as shown in Figure 6.2.20(b). Thus exposure to gamma radiation enhances the concentration of larger Fe^{+3} ions in high spin state that are transferred to tetrahedral site. The cation distribution Table 6.3.7 (a,b,c) shows that this heavy Fe^{+3} transfer is compensated by transfer of Mn^{+3} to octahedral site to maintain overall balance [3].

6.3 Fourier transform infrared spectroscopy

Fourier transform infra red spectra of gamma irradiated $Mn_{0.6}Zn_{0.4}Fe_{2-x}Nd_xO_4$ & $Mn_{0.65}Zn_{0.35}Fe_{2-x}Nd_xO_4$ obtained on Simadzu FTIR 8900 assembly are shown in Figure 6.3.1 (a,b & c) and Figure 6.3.2(a, b & c).

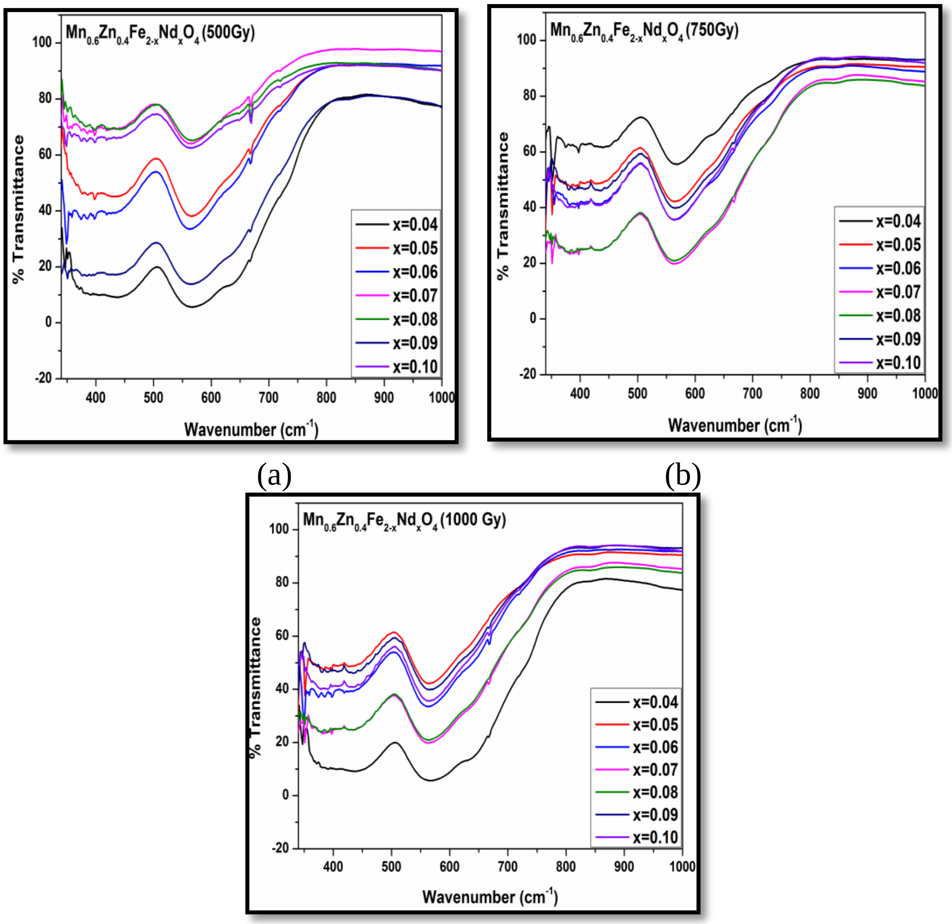

(a) (b)

(c)

Figure 6.3.1 Fourier Transform Infra Red spectra for $Mn_{0.6}Zn_{0.4}Fe_{2-x}Nd_xO_4$ Irradiated with a) 500 Gy b) 750 Gy and c)1000 Gy

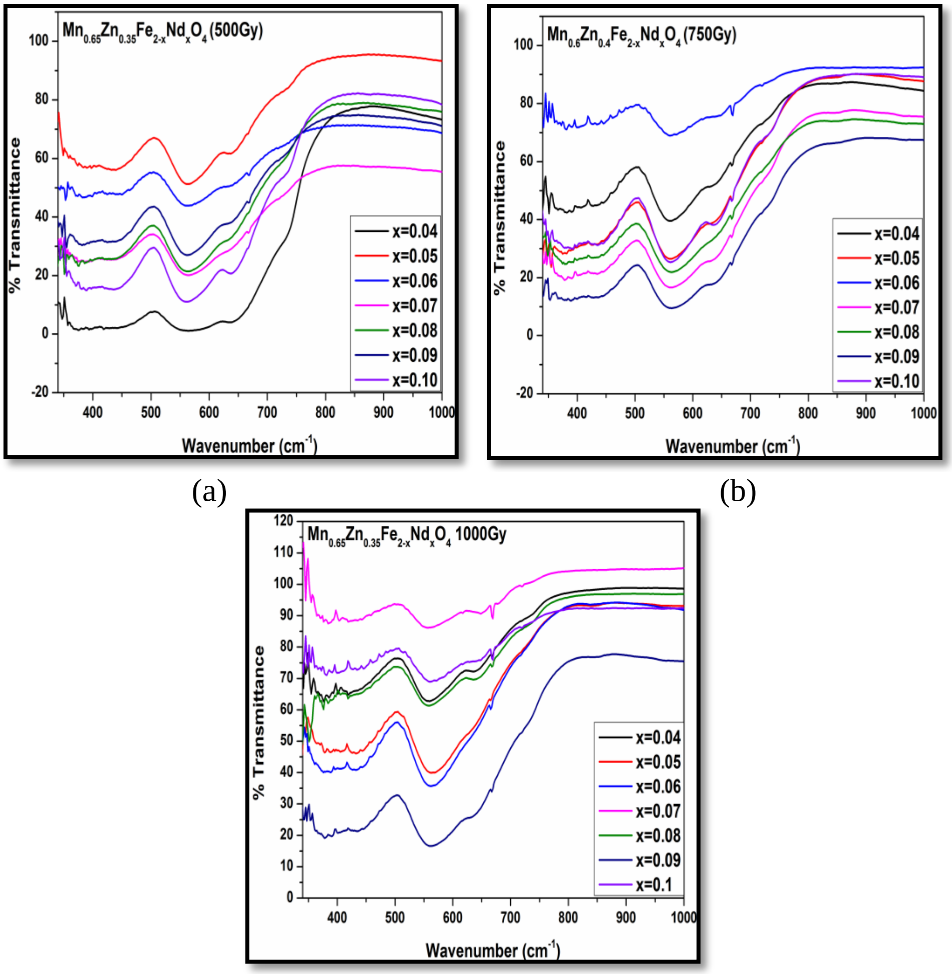

(a) (b)

(c)

Figure 6.3.2 Fourier Transform Infra Red spectra for $Mn_{0.65}Zn_{0.35}Fe_{2-x}Nd_xO_4$ Irradiated with a) 500 Gy b) 750 Gy and c) 1000 Gy

All the spectra comprised of characteristic bands for ferrites in the ranges 559cm^{-1} to 565cm^{-1} representing M_T --O bond stretching vibration, 370cm^{-1} to 450cm^{-1} for M_O--O bond stretching vibration and 343cm^{-1} to 352cm^{-1} representing M_T --O--M_O banding vibrations respectively. The multiple bands observed at around 375cm^{-1}, 400cm^{-1} and 430cm^{-1} represent Fe^{+3}-O^{-2}, Mn^{+3}-O^{-2} and Nd^{+3}-O^{-2} stretching vibrations within the range 350cm^{-1} to 450 cm^{-1} representing the existence of different cations such as Nd^{+3}, Fe^{+3}, and Mn^{+3} at octahedral site could be distinctly seen in the spectra of γ irradiated samples [11-17]. The infra red spectra obtained for all gamma irradiated samples were very much identical to non radiated counterparts where in a very small shift of 2 cm^{-1} to 4 cm^{-1} was observed in the transmittance bands. This can be attributed to very small variations seen in bond lengths caused due to gamma radiation exposure.

6.4 Transmission electron microscopy (TEM)

Transmission electron microscopy proves to be a great experimental tool when it comes to critical observations and analysis which are to be carried out at nano scale. Figure 6.4.1 to Figure 6.4.3 show transmission electron micrographs and the particle size distribution histograms obtained for samples with composition $Mn_{0.6}Zn_{0.4}Fe_{2-x}Nd_xO_4$ and Figure 6.4.4 to Figure 6.4.5 show transmission electron micrographs and the particle size distribution histograms obtained for samples with composition $Mn_{0.65}Zn_{0.35}Fe_{2-x}Nd_xO_4$.

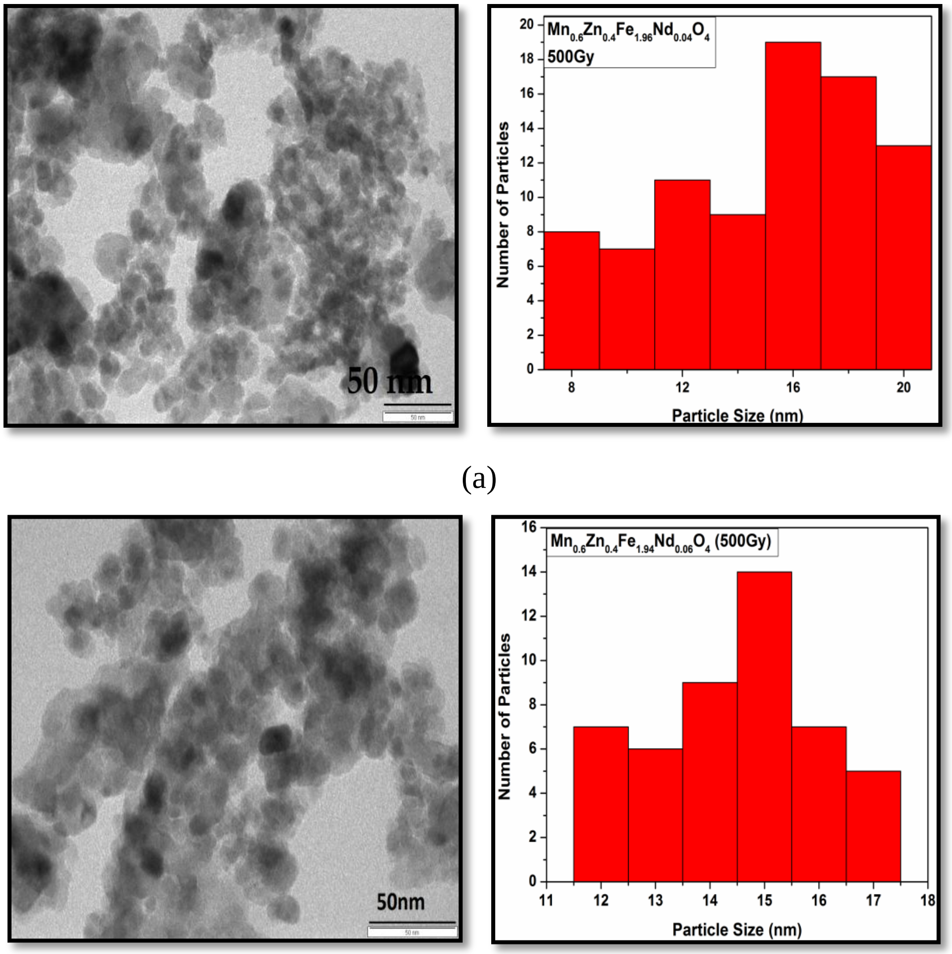

(a)

(b)

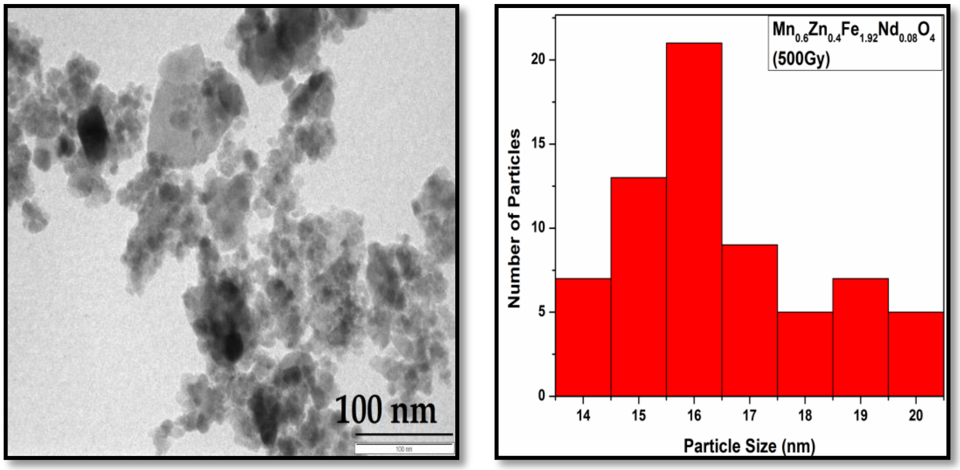

(c)

Figure 6.4.1 (a,b,c & d) Transmission electron micrographs and the particle size distribution histograms of $Mn_{0.6}Zn_{0.4}Fe_{2-x}Nd_xO_4$ irradiated with 500Gy

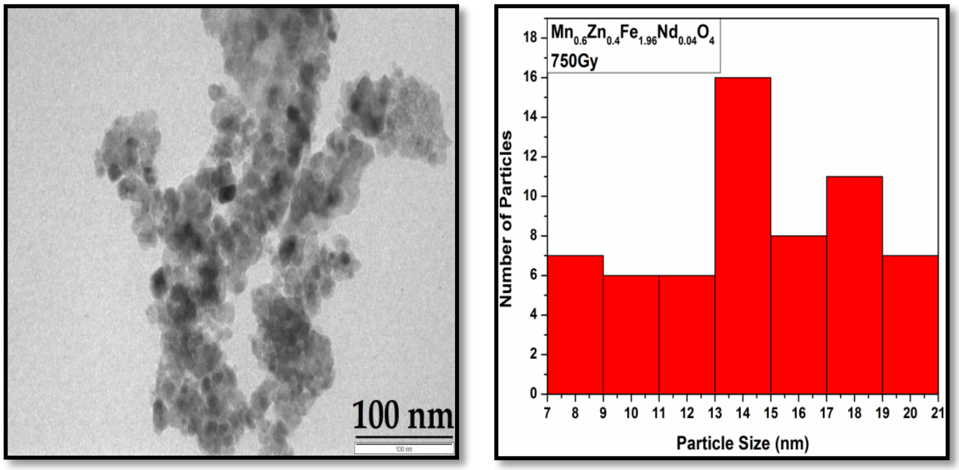

(a)

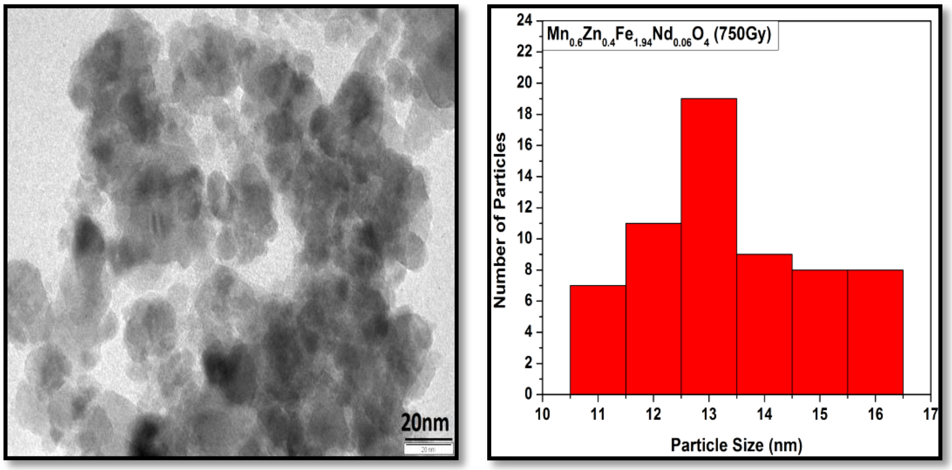

(b)

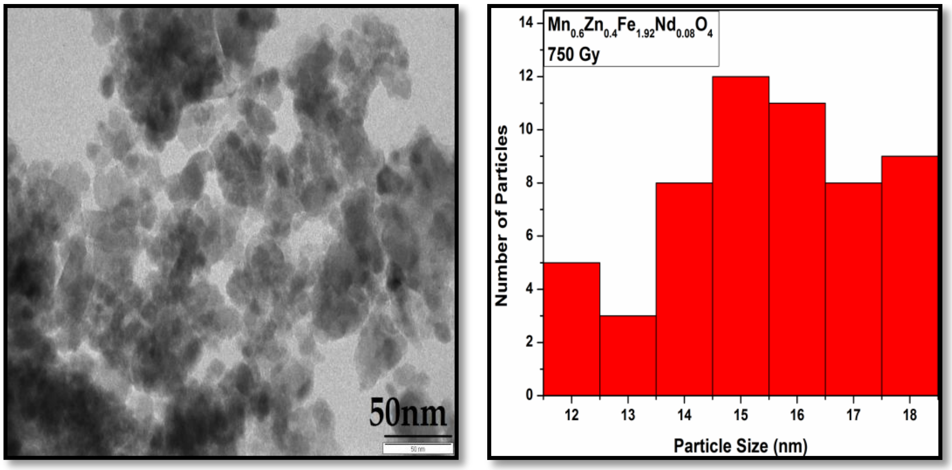

(c)

Figure 6.4.2 (a,b,c & d) Transmission electron micrographs and the particle size distribution histograms of $Mn_{0.6}Zn_{0.4}Fe_{2-x}Nd_xO_4$irradiated with 750Gy

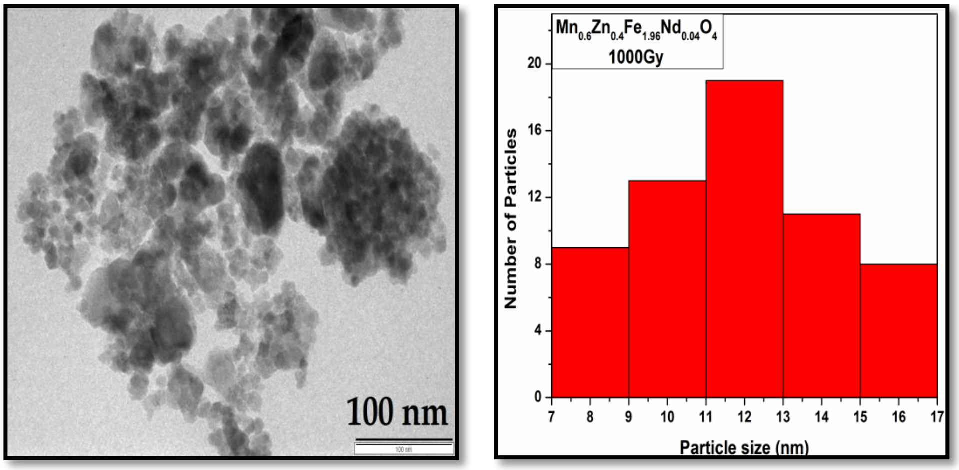

(a)

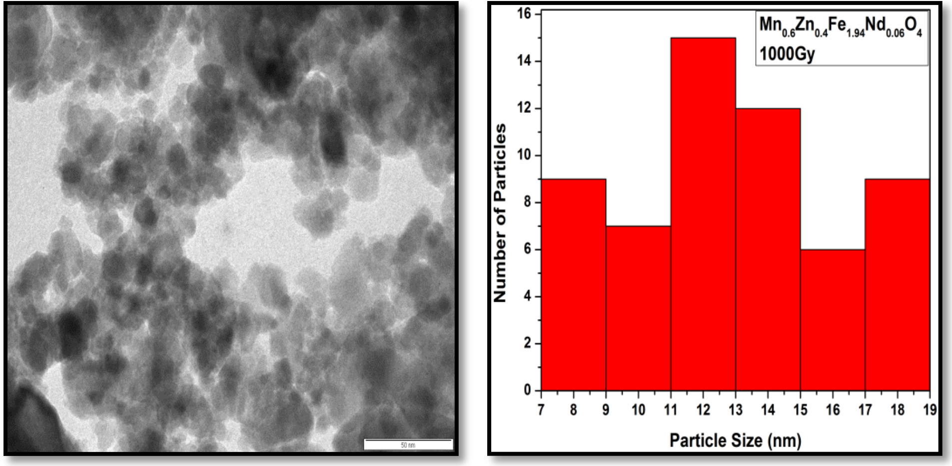

(b)

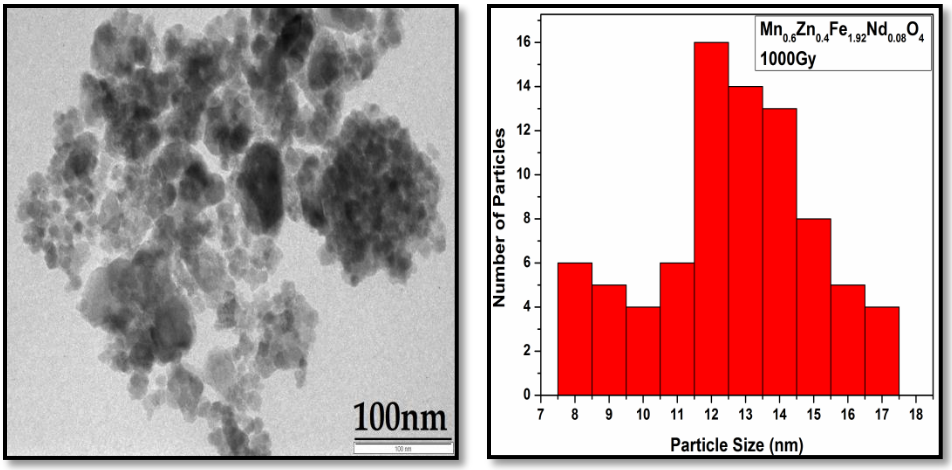

(c)

Figure 6.4.3 (a,b,c & d) Transmission electron micrographs and the particle size distribution histograms of $Mn_{0.6}Zn_{0.4}Fe_{2-x}Nd_xO_4$irradiated with 1000Gy

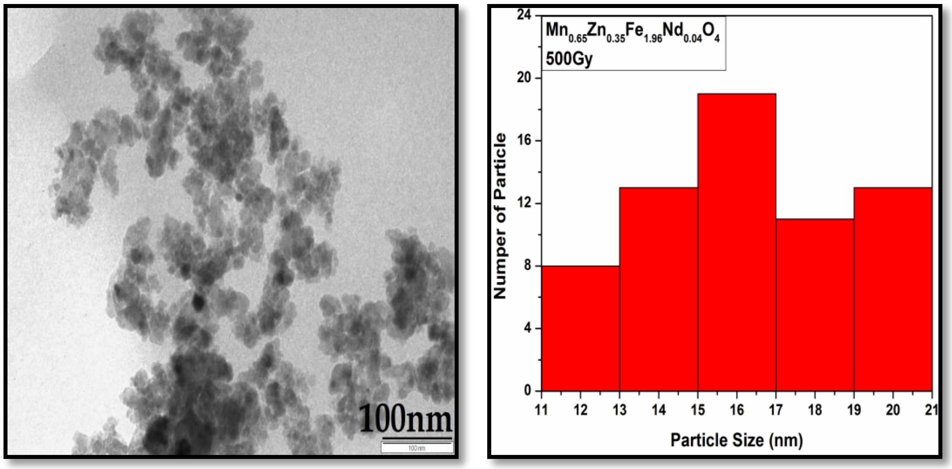

(a)

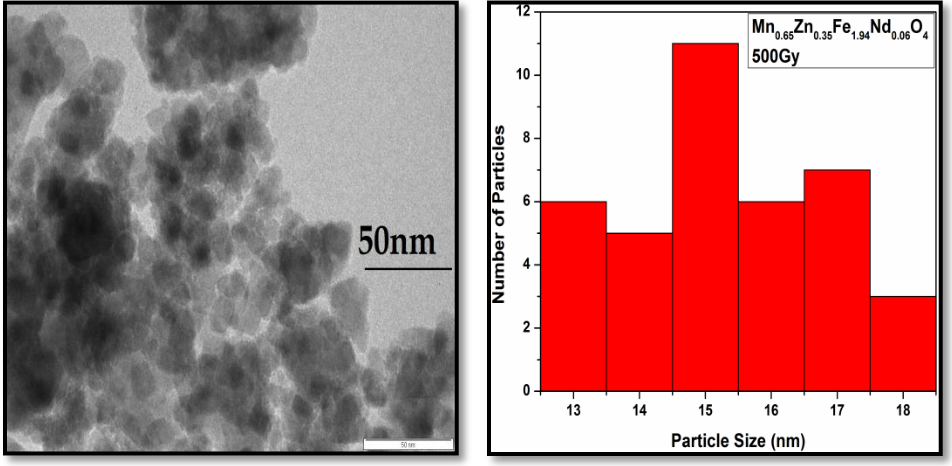

(b)

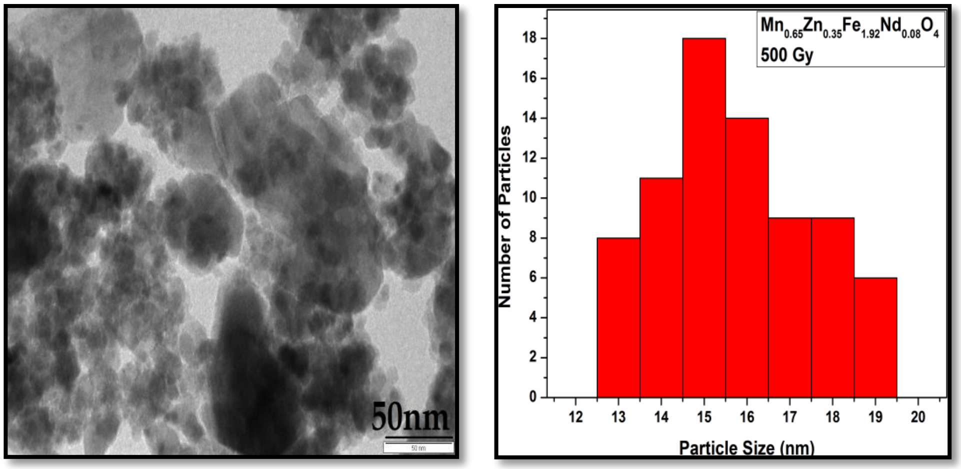

(c)

Figure 6.4.4 (a,b,c) Transmission electron micrographs and the particle size distribution histograms of $Mn_{0.65}Zn_{0.35}Fe_{2-x}Nd_xO_4$ irradiated with 500Gy

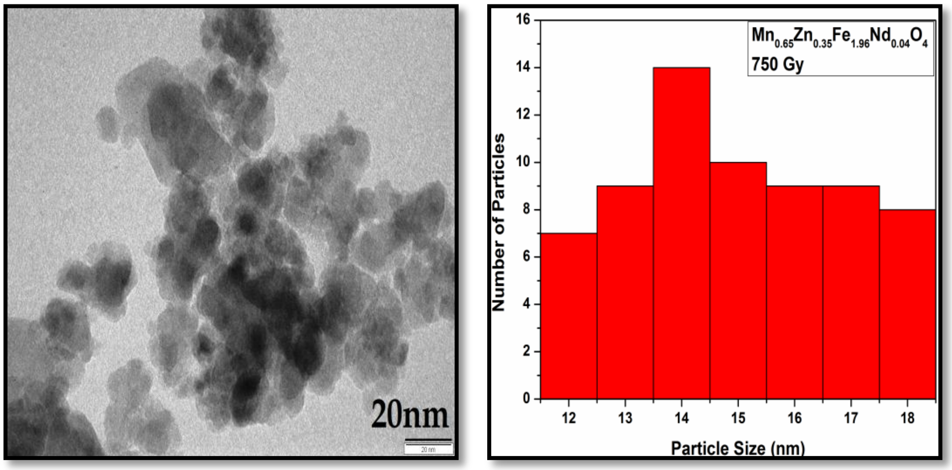

(a)

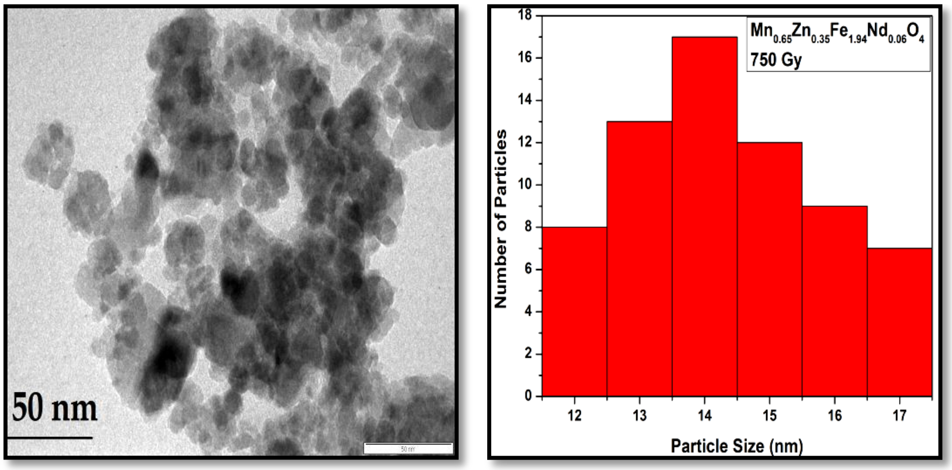

(b)

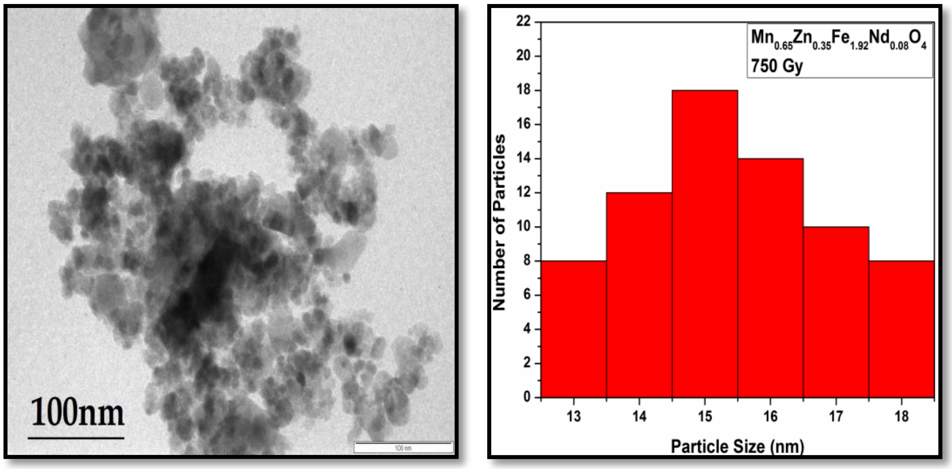

(c)

Figure 6.4.5 (a,b,c) Transmission electron micrographs and the particle size distribution histograms of $Mn_{0.65}Zn_{0.35}Fe_{2-x}Nd_xO_4$ irradiated with 750Gy

Table 6.4.1 Variation of particle size with Nd^{+3} concentrations for gamma irradiated $Mn_{0.6}Zn_{0.4}Fe_{2-x}Nd_xO_4$

Concentration Of Nd^{+3} ‘x’	500Gy Particle Size (nm)	750Gy Particle Size (nm)	1000Gy Particle Size (nm)
0.04	16±4	14±5	12±4
0.06	15±2	14±2	12±4
0.08	16±4	15±4	13±5

Table 6.4.2 Variation of particle size with Nd^{+3} concentrations for gamma irradiated $Mn_{0.65}Zn_{0.35}Fe_{2-x}Nd_xO_4$

Concentration Of Nd^{+3} ‘x’	500Gy Particle Size (nm)	750Gy Particle Size (nm)	1000Gy Particle Size (nm)
0.04	16±4	14±4	12±3
0.06	15±3	13±3	11±3
0.08	15±3	15±3	12±3

The values of particle size obtained from transmission electron micrographs for some of the gamma irradiated samples are listed in Table 6.4.1 and Table 6.4.2. From the micrographs and the particle size histograms it can be seen that there is an enhancement in the range of particle size as well as in the number of particles of various sizes. This may be attributed to the fact that there is a cracking of larger particles in to smaller particles due to the internal crystalline strain that is developed due to increase in the lattice size and unit volume size as a result of gamma radiation. From the Table 6.4.1 and Table 6.4.2 it can be seen that the particle size has reduced with gamma radiation and it further reduces from 16nm to about 12nm as the radiation dose is increased from 500Gy to 1000Gy. This fact also supports the fact that the crystalline strain increases with increasing gamma radiation dose there by breaking bigger particles in to smaller ones and developing disorder in form of amorphous material around the smaller particles which do not break. The particular analogy given in the proposed model that is strongly supported by other parameters like density, porosity, X-ray density, FWHM, crystallite size etc. seems to find favorable support from TEM as well, as there is increase in population of particles of lower size.

Thus from TEM results it is evident that γ radiation dose of increasing magnitude produces proportionate strain in the lattice by generating Fe^{+3} ions in high spin state with larger ionic radii (0.78 Å) at both tetrahedral site and the octahedral site [18-22].

Magnetic property exploration

6.5 Vibrating sample magnetometer (VSM)

Magnetic hysterisis loops obtained for γ irradiated $Mn_{0.6}Zn_{0.4}Fe_{2-x}Nd_xO_4$ and $Mn_{0.65}Zn_{0.35}Fe_{2-x}Nd_xO_4$ nanoparticles irradiated with 500Gy, 750Gy and 1000Gy obtained on VSM are shown in Figure 6.5.1 and Figure 6.5.2. Inserts in these figures show the central portion of the magnetic hysteresis loops which clearly indicate that the samples exhibit very low values of coercivity (H_C) and remnant magnetization (M_R) values. Figure 5.6.3 shows the variation of saturation magnetization (M_S) with increasing γ radiation dose.

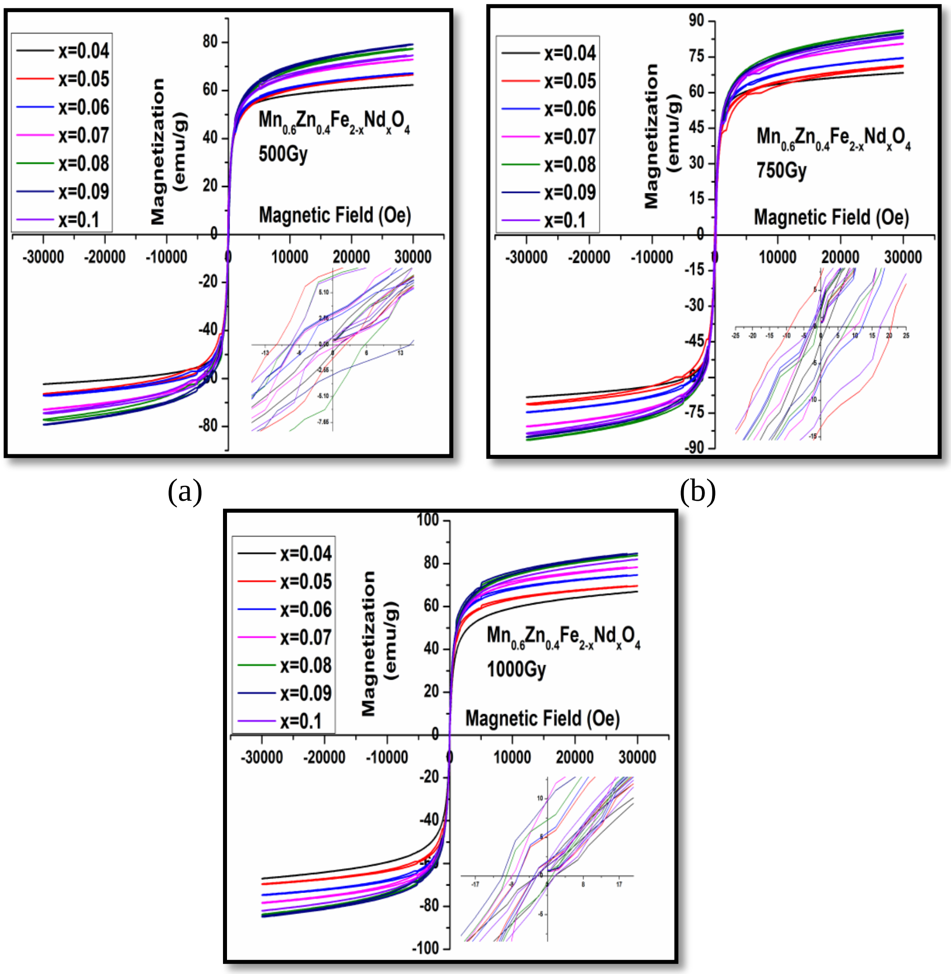

(a) (b)

(c)

Figure 6.5.1 Hysterisis loops for γ irradiated $Mn_{0.6}Zn_{0.4}Fe_{2-x}Nd_xO_4$ nanoparticles

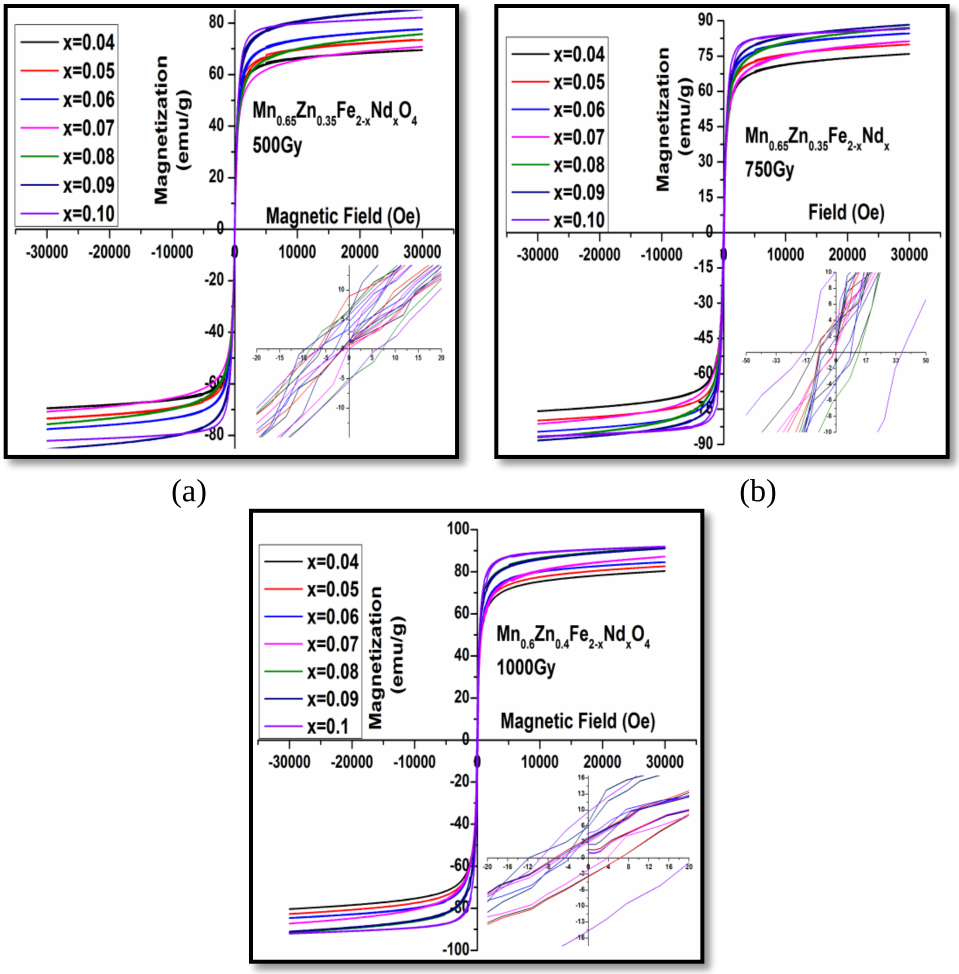

(a) (b)

(c)

Figure 6.5.2 (a&b) Hysterisis loops for γ irradiated $Mn_{0.65}Zn_{0.35}Fe_{2-x}Nd_xO_4$ nanoparticles

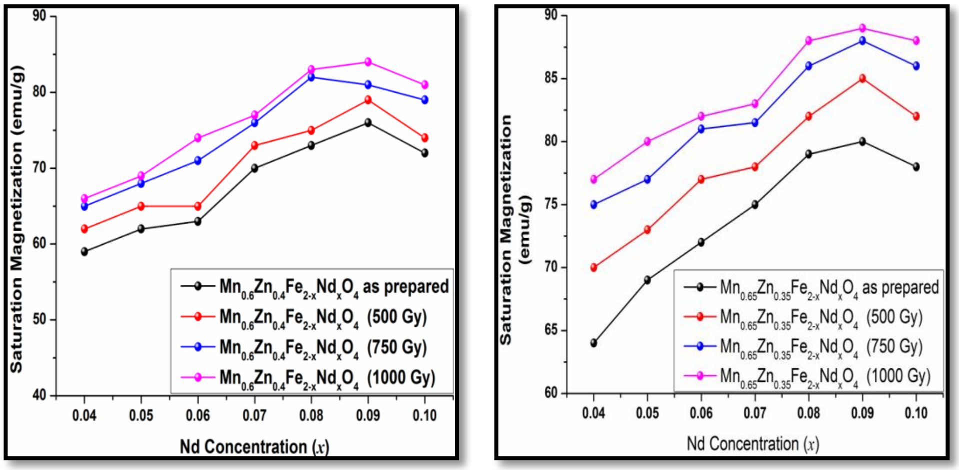

(a) (b)

Figure 6.5.3Variation of saturation magnetization (M_S) for γ irradiated $Mn_{0.6}Zn_{0.4}Fe_{2-x}Nd_xO_4$ and $Mn_{0.65}Zn_{0.35}Fe_{2-x}Nd_xO_4$ nanoparticles

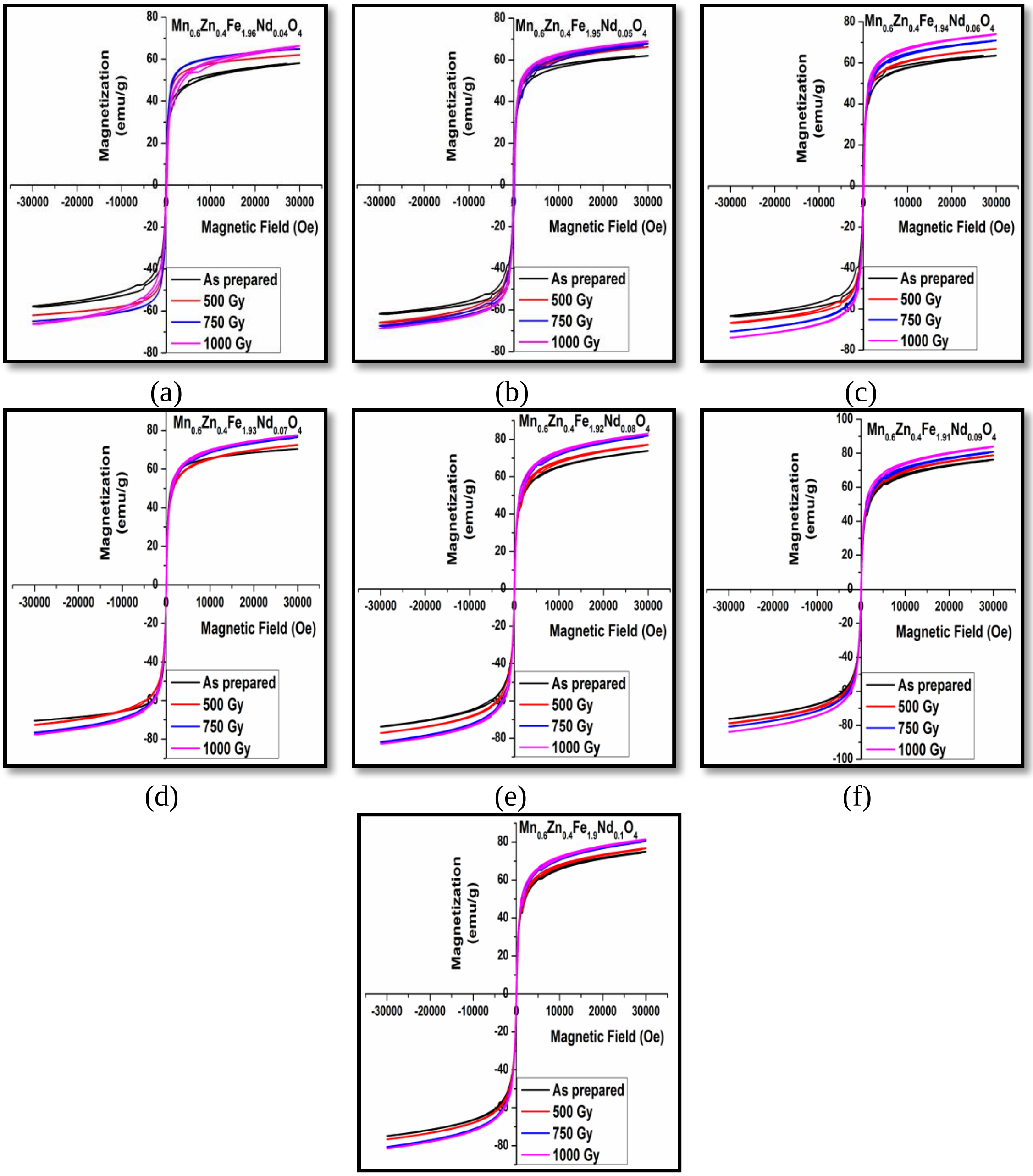

(a) (b) (c)

(d) (e) (f)

(g)

Figure 6.5.4 Hysterisis curves of as prepared and γ irradiated $Mn_{0.6}Zn_{0.4}Fe_{2-x}Nd_xO_4$ nanoparticles

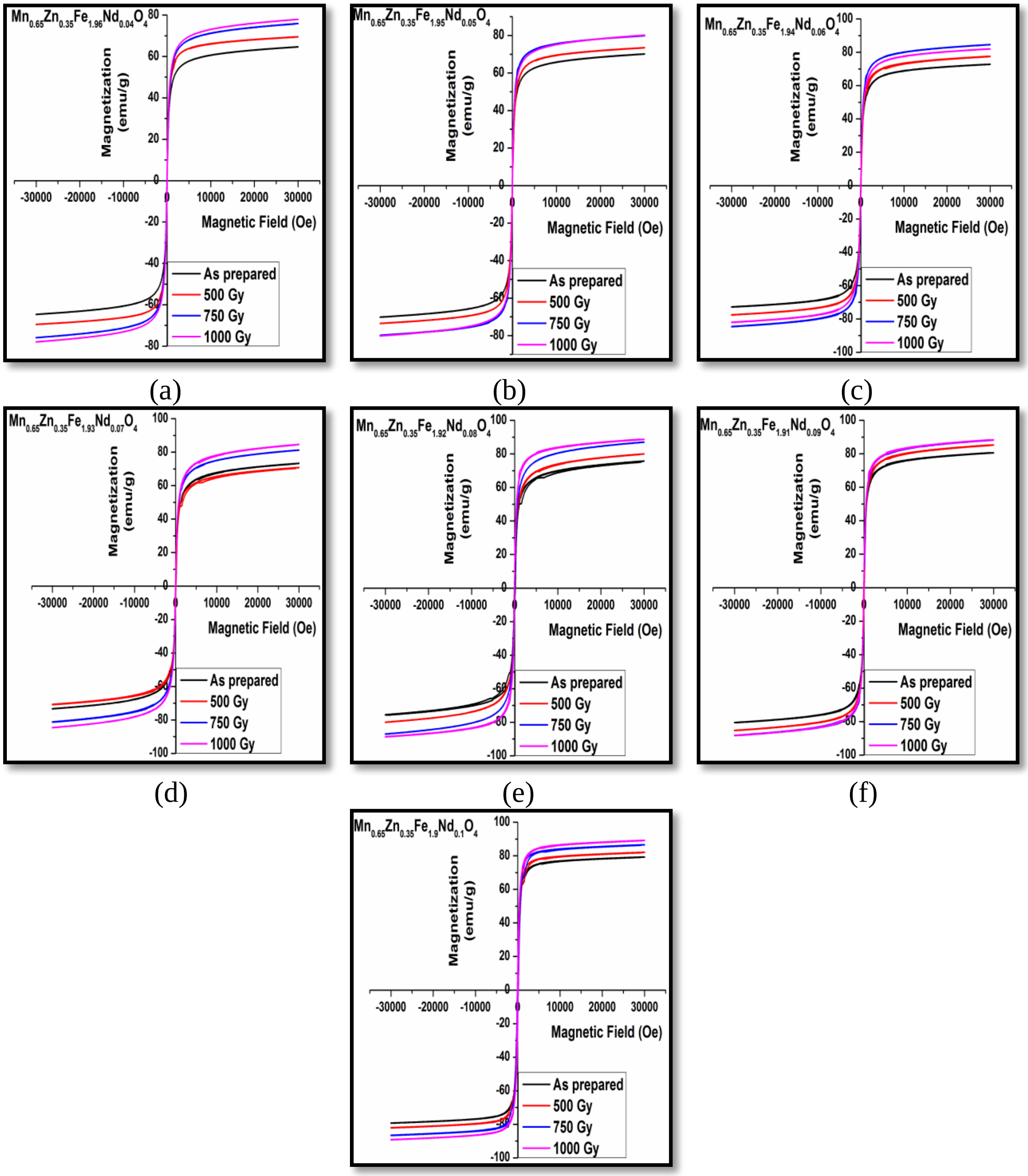

(a) (b) (c)

(d) (e) (f)

(g)

Figure 6.5.5 Hysterisis curves of as prepared and γ irradiated $Mn_{0.65}Zn_{0.35}Fe_{2-x}Nd_xO_4$ nanoparticles

From the Figure 6.5.3 it can be clearly seen that the saturation magnetization of the γ irradiated samples increases with increasing γ radiation dose. Exposure of ferrite nanoparticles to γ radiations of varying magnitude alters the Fe^{+2} /Fe^{+3} ratio at both octahedral and tetrahedral sites and increases the availability of Fe^{+3} in high spin state at both sites leading to enhancement in saturation magnetization [9].

Sample with x=0.04 of $Mn_{0.6}Zn_{0.35}Fe_{2-x}Nd_xO_4$ series show a minimum enhancement in M_S of 10 emu/g while the maximum enhancement of 20 emu/g was observed for x= 0.08 sample with maximum γ radiation dose of 1000Gy. Maximum value of saturation magnetization (M_S = 87 emu/g) was recorded for sample with x=0.09 for γ radiation dose of 1000Gy.

For $Mn_{0.65}Zn_{0.35}Fe_{2-x}Nd_xO_4$ series, minimum enhancement of 9emu/g was observed for x= 0.07 while the maximum increase of 15 emu/g was recorded for x= 0.04 with γ radiation dose of 1000Gy. Sample with x=0.09 showed the highest value of M_S= 96 emu/g with highest γ radiation dose as shown in Figure 6.5.5. Comparative plots of magnetic hysteresis curves of all the as prepared and gamma irradiated samples are presented in Figure 6.5.5 and Figure 6.5.4.

Table 6.5.1 Squareness ratio (M_R/M_S) for γ irradiated $Mn_{0.6}Zn_{0.4}Fe_{2-x}Nd_xO_4$

Nd^{+3} concentrations ‘x’	M_R/M_S Ratio for 500 Gy	M_R/M_S Ratio for 750 Gy	M_R/M_S Ratio for 1000 Gy
0.04	0.008	0.009	0.007
0.05	0.008	0.007	0.008
0.06	0.007	0.012	0.010
0.07	0.010	0.008	0.011
0.08	0.012	0.013	0.009
0.09	0.007	0.009	0.008
0.1	0.009	0.008	0.008

Table 6.5.2 Squareness ratio (M_R/M_S) for γ irradiated $Mn_{0.65}Zn_{0.35}Fe_{2-x}Nd_xO_4$

Nd^{+3} concentrations 'x'	M_R/M_S Ratio for 500 Gy	M_R/M_S Ratio for 750 Gy	M_R/M_S Ratio for 1000 Gy
0.04	0.007	0.011	0.009
0.05	0.008	0.006	0.013
0.06	0.008	0.008	0.010
0.07	0.009	0.007	0.011
0.08	0.010	0.009	0.008
0.09	0.008	0.009	0.008
0.1	0.007	0.011	0.010

Squareness ratios for γ irradiated $Mn_{0.6}Zn_{0.4}Fe_{2-x}Nd_xO_4$ and $Mn_{0.65}Zn_{0.35}Fe_{2-x}Nd_xO_4$ samples are listed in Table 6.5.1 and 6.5.2. It can be seen that the ratios lie within the superparamagnetic limit and one can conclude that γ irradiated samples exhibit superparamagnetic nature which may be considered as the consequence of particle size reduction of bigger and smaller particles due to the crystalline strain developed due to γ radiation exposure. Since there is regeneration of particles of smaller size by the two procedures mentioned in the model it also results in redistribution of cations at the two sites and hence this would contribute to change in all the magnetic properties of the samples. Accordingly increase in magnetic moment and hence the saturation magnetization M_S is attributed to redistribution of cations at two sites triggered due to increasing γ radiation exposure and increase in availability of Fe^{+3} ions in high spin state with larger magnetic moment at both the tetrahedral and the octahedral site [22,23].

Variation of magnetization as a function of temperature was determined for γ irradiated $Mn_{0.6}Zn_{0.4}Fe_{2-x}Nd_xO_4$ and $Mn_{0.65}Zn_{0.35}Fe_{2-x}Nd_xO_4$ nanoparticles over the temperature range of 50K to 385K at constant applied field of 750Oe. The field cooled (FC) and zero field cooled (ZFC) curves obtained for γ irradiated samples are shown in Figure 6.5.3 (a, b & c) and 6.5.4. (a, b & c).

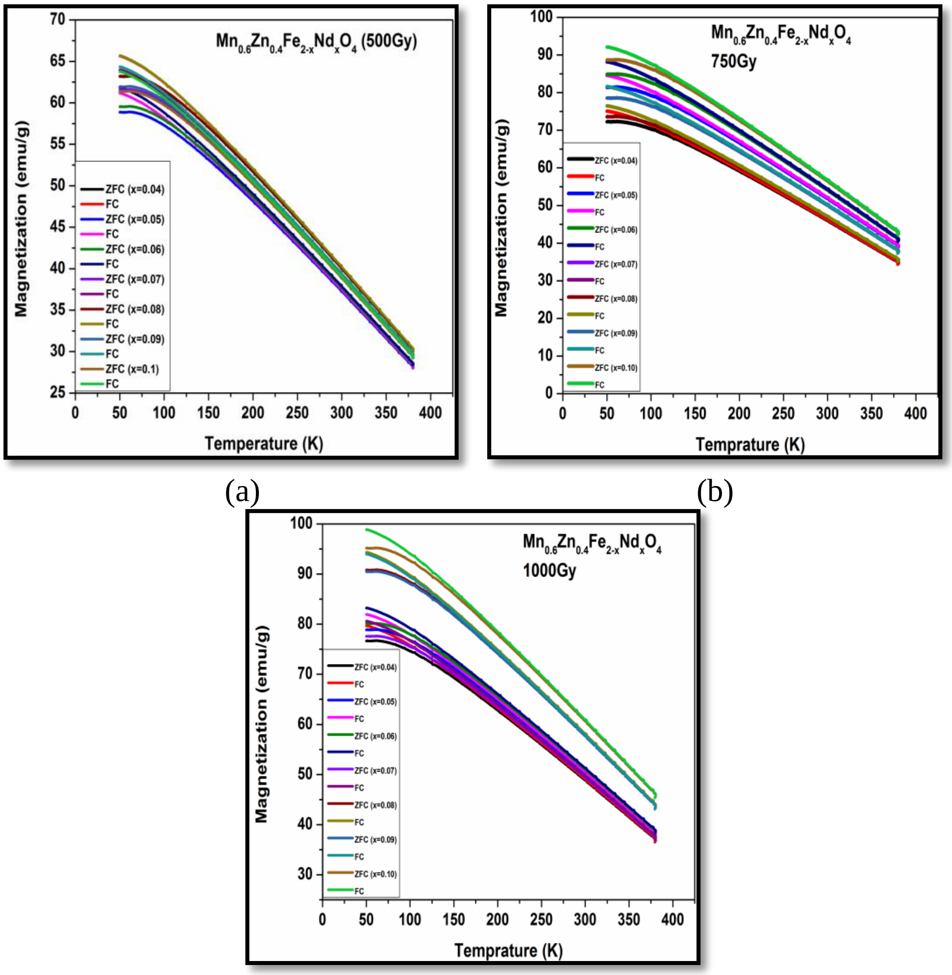

(a) (b)

(c)

Figure 6.5.6 (a, b & c) Field cooled (FC) and zero field cooled (ZFC) curves for $Mn_{0.6}Zn_{0.4}Fe_{2-x}Nd_xO_4$ nanoparticles

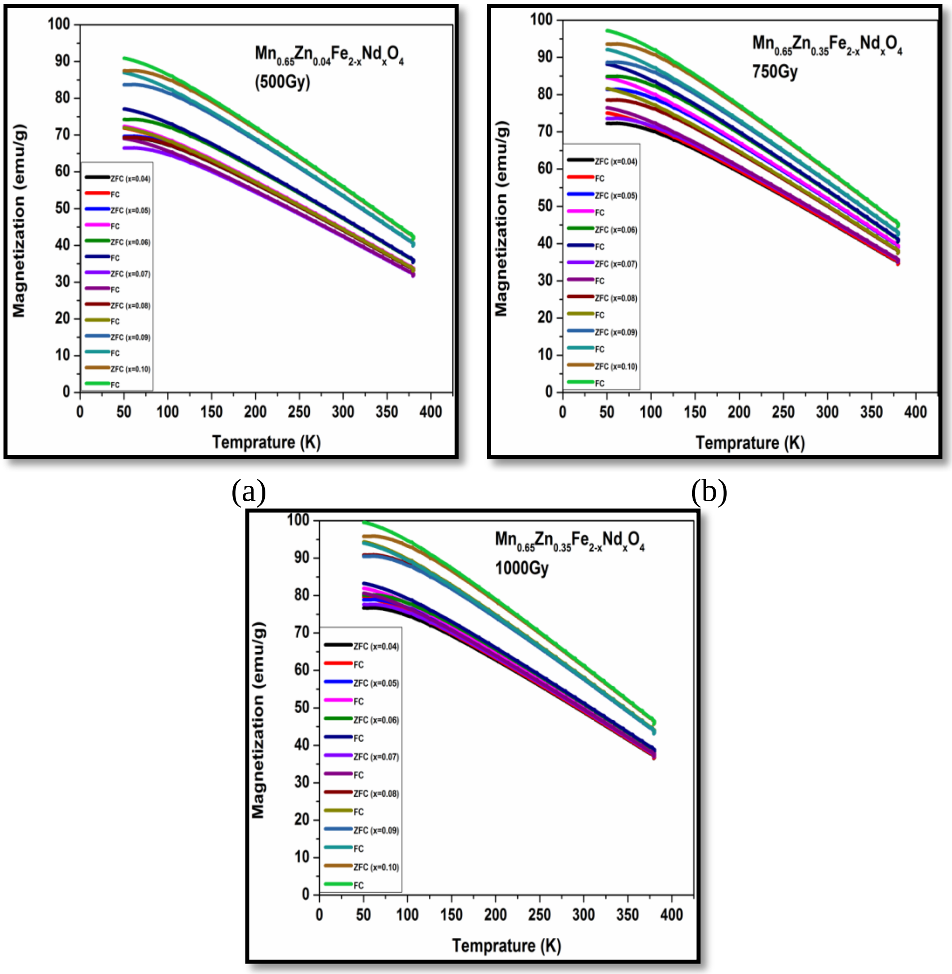

(a) (b)

(c)

Figure 6.5.6 (a, b & c) Field cooled (FC) and zero field cooled (ZFC) curves for Mn$_{0.65}$Zn$_{0.35}$Fe$_{2-x}$Nd$_x$O$_4$ nanoparticles

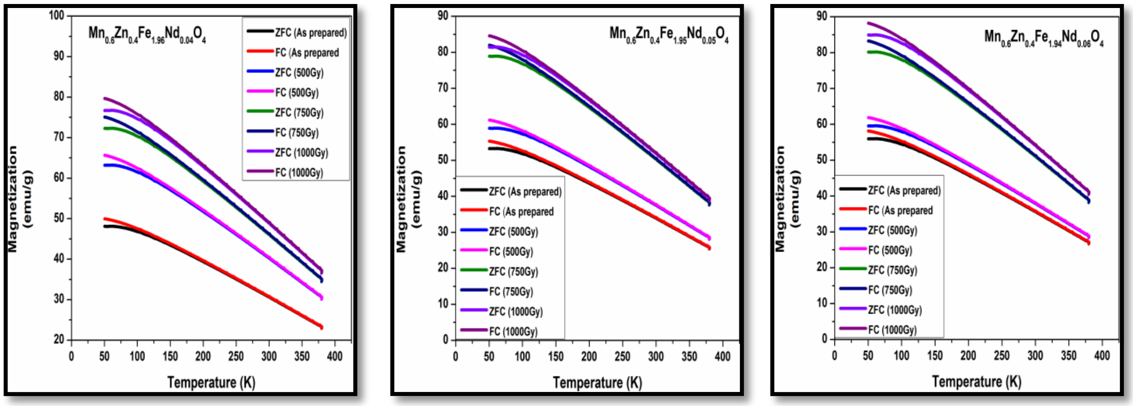

(a) (b) (c)

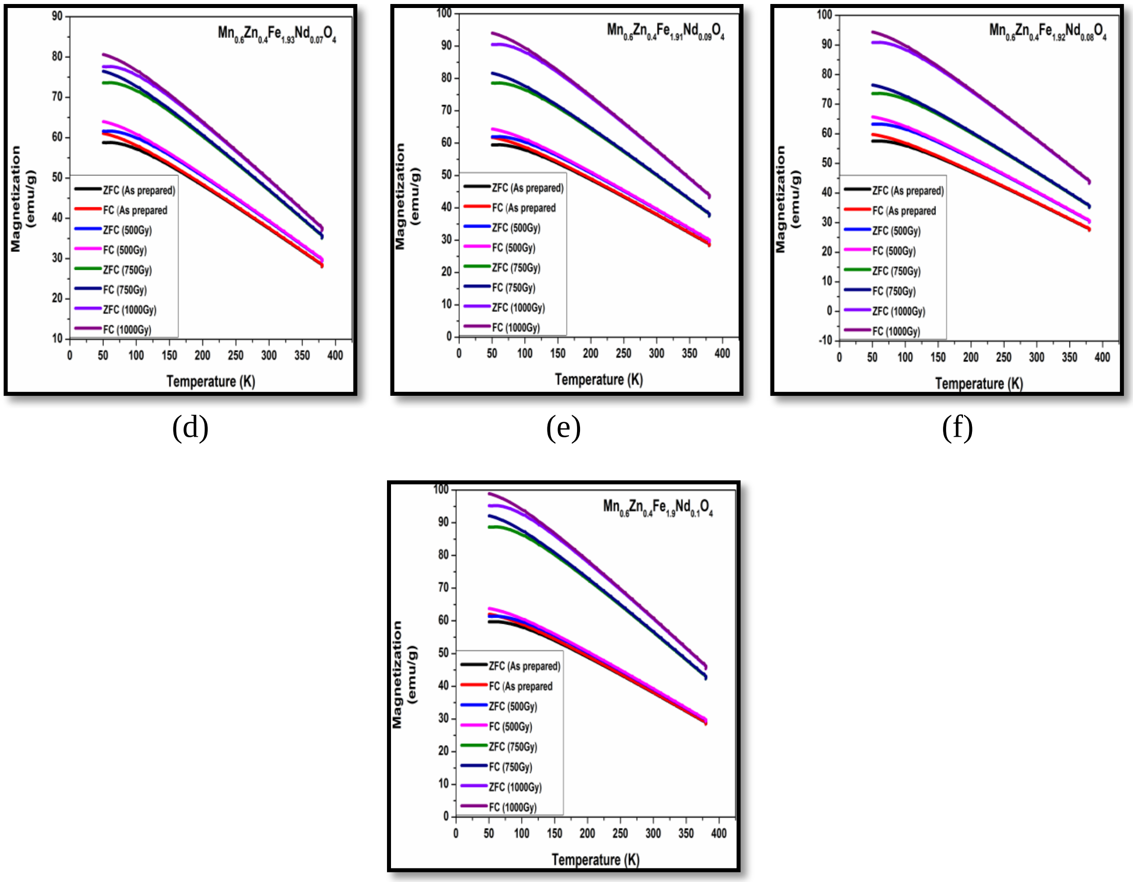

(d) (e) (f)

(g)

Figure 6.5.7 Field cooled (FC) and zero field cooled (ZFC) curves for as prepared and γ irradiated $Mn_{0.6}Zn_{0.4}Fe_{2-x}Nd_xO_4$ nanoparticles

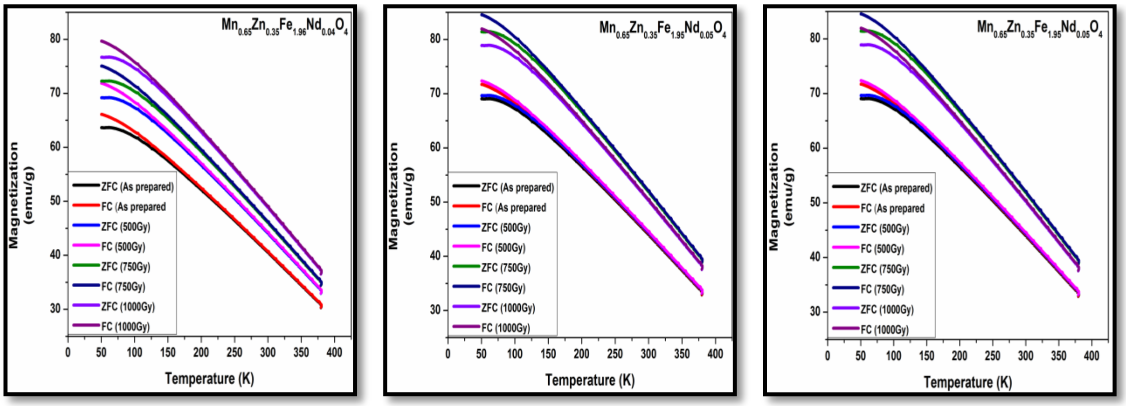

(a) (b) (c)

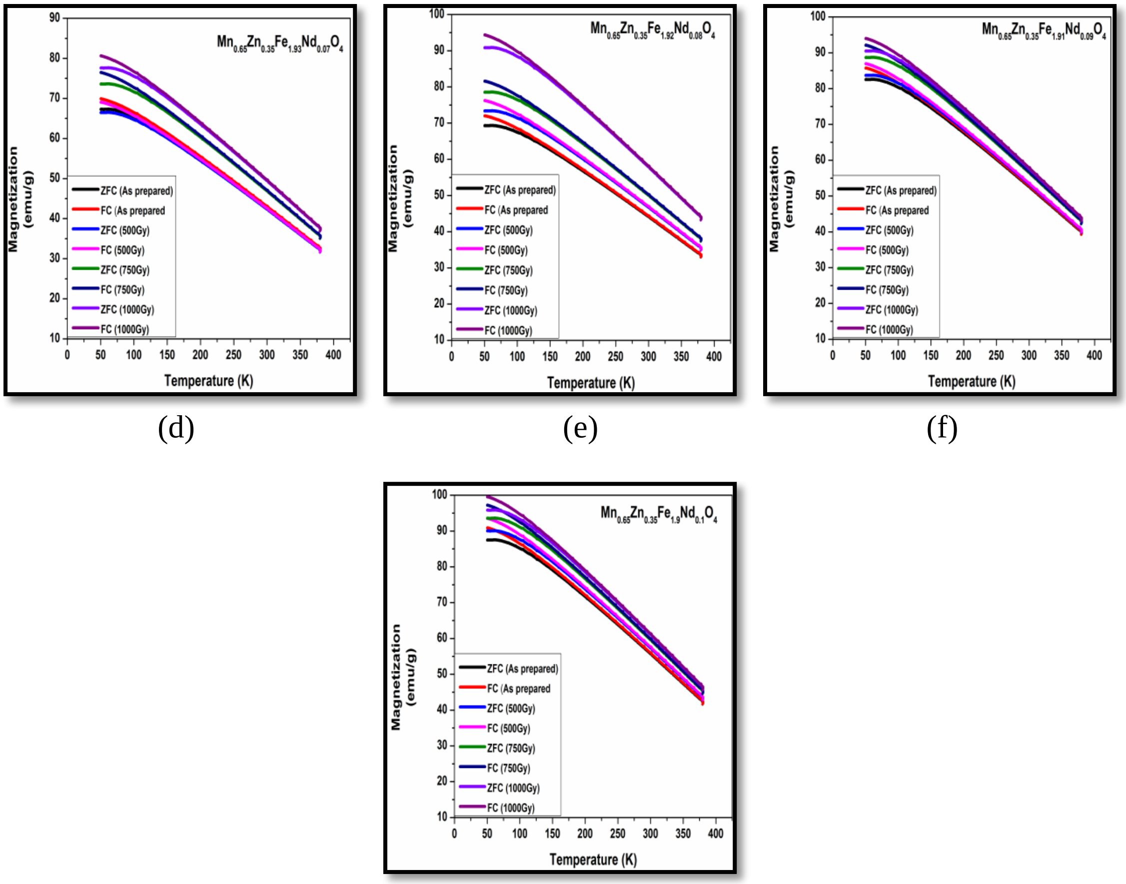

(d) (e) (f)

(g)

Figure 6.5.8 Field cooled (FC) and zero field cooled (ZFC) curves for as prepared and γ irradiated $Mn_{0.65}Zn_{0.35}Fe_{2-x}Nd_xO_4$ nanoparticles

It may be seen that the magnetization of samples increases with increasing gamma radiation dose. This increase in magnetization with increasing γ radiation dose can be attributed to increased concentrations of Fe^{+3} ions in high spin state at both tetrahedral sites and the octahedral sites which enhances the magnetic moment.

Figure 6.5.5 and Figure 6.5.6 represent comparative plots of magnetization as a function of temperature for as prepared and gamma irradiated sample. The values of temperatures T_{MAX} and T_{DIFF} obtained for gamma irradiated samples from FC and ZFC curve are presented in Table 6.5.3 and Table 6.5.4 where T_{MAX} is the blocking temperature of smaller particles in the sample while T_{DIFF} is the blocking temperature of larger particles present in the samples [24]. Together they define the range of blocking temperature for a given material which also means that the samples are inhomogeneous and contain particles of varying sizes which are extremely small in general as established by TEM results.

Table 6.5.3 Variation of T_{MAX} and T_{DIFF} obtained for gamma irradiated $Mn_{0.6}Zn_{0.4}Fe_{2-x}Nd_xO_4$ nanoparticles

Nd^{+3} concentration 'x'	500Gy		750Gy		1000Gy	
	T_{MAX} (K)	T_{DIFF} (K)	T_{MAX} (K)	T_{DIFF} (K)	T_{MAX} (K)	T_{DIFF} (K)
0.04	69	119	67	119	66	116
0.05	66	118	65	118	64	117
0.06	63	118	62	118	63	116
0.07	63	116	61	116	61	114
0.08	62	117	60	117	59	116
0.09	61	116	61	116	62	115
0.1	62	117	59	117	60	116

Table 6.5.4 Variation of T_{MAX} and T_{DIFF} obtained for gamma irradiated $Mn_{0.65}Zn_{0.35}Fe_{2-x}Nd_xO_4$ nanoparticles

Nd^{+3} concentration 'x'	500Gy		750Gy		1000Gy	
	T_{MAX} (K)	T_{DIFF} (K)	T_{MAX} (K)	T_{DIFF} (K)	T_{MAX} (K)	T_{DIFF} (K)
0.04	71	120	68	119	66	118
0.05	68	119	65	119	63	118
0.06	67	118	66	117	64	117
0.07	66	119	64	118	63	118
0.08	67	118	63	117	62	116
0.09	66	118	63	117	60	116
0.1	65	119	62	118	61	117

It can be seen from the table 6.5.3 and 6.5.4 that the temperature difference between T_{MAX} and T_{DIFF} is small for all samples. This difference actually gives the variation of blocking temperature for particles of various sizes in the material. A narrow temperature bandwidth is an indicator of the fact that particle size distribution in the samples is essentially small this is also evident from the particle size histograms obtained from TEM micrographs. The blocking temperature does not show any remarkable variation with increasing gamma radiation dose. For temperature below T_{MAX} which is the lowest blocking temperature, the magnetization remains constant which can be attributed to enhance anisotropy due to stronger inter particle interactions, making moments pinned to one another with the thermal energy becoming smaller to overcome the energy barriers. The magnetization of field cooled curves was seen to increase further below T_{MAX} which can be attributed to better magnetic ordering and enhanced magnetic character due to the dominance of Fe^{+3} ions in high spin state at both the octahedral and the tetrahedral sites in gamma irradiated samples. The magnetization curves for all gamma irradiated samples were observed to follow a decreasing trend for $T>T_{MAX}=T_B$ the blocking temperature obeying the Curie-Weiss law. The furcation observed in ZFC and FC plots beyond a particular temperature T_{DIFF} is indeed a characteristic observed in systems or samples containing superparamagnetic grains. It may be seen that similar behavior is observed in the plots obtained for all the samples. This fact suggests that the samples are made up of superparamagnetic grains which could be single domain or a mixture of single domain and a small fraction of multidomain grains.

6.6 Mössbauer spectroscopy

This is yet another tool very useful to investigate the magnetic environment at different sites. Figure 6.6.1 to Figure 6.6.6 show Mössbauer spectra of $Mn_{0.6}Zn_{0.4}Fe_{2-x}Nd_xO_4$ and $Mn_{0.65}Zn_{0.35}Fe_{2-x}Nd_xO_4$ nanoparticles recorded at room temperature in the velocity of ±11.5 mm/s using conventional Mössbauer spectrometer. Mössbauer spectra for the samples were also fitted with three sextets and a paramagnetic doublet. The presence of these sextets can be attributed to superexchange interaction between the magnetic ions at A– and B–sub-lattices.

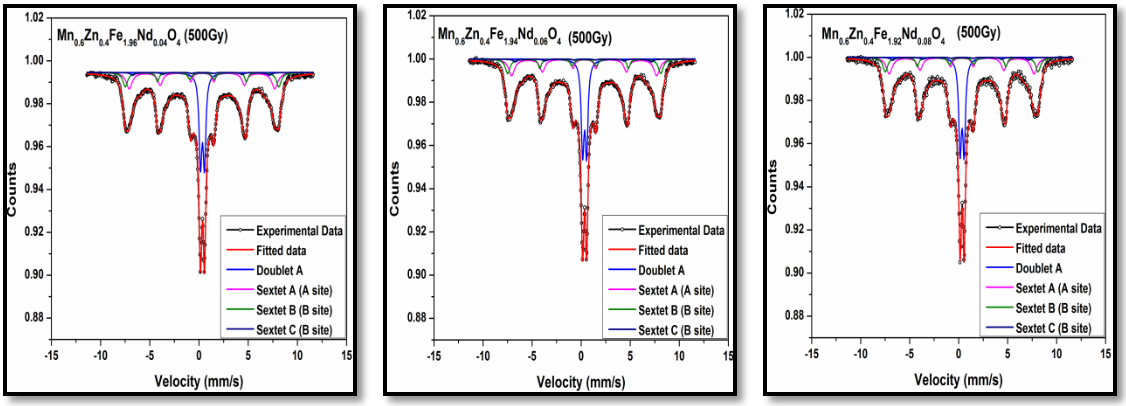

(a) (b) (c)

Figure 6.6.1 Mossbauer spectra for $Mn_{0.6}Zn_{0.4}Fe_{2-x}Nd_xO_4$ nanoparticles irradiated with 500Gy

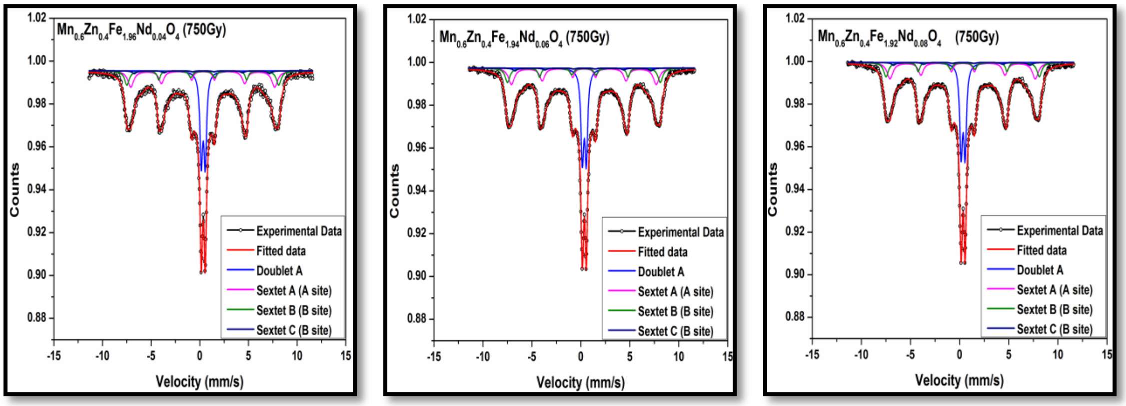

(a) (b) (c)

Figure 6.6.2 Mossbauer spectra for $Mn_{0.6}Zn_{0.4}Fe_{2-x}Nd_xO_4$ nanoparticles irradiated with 750Gy

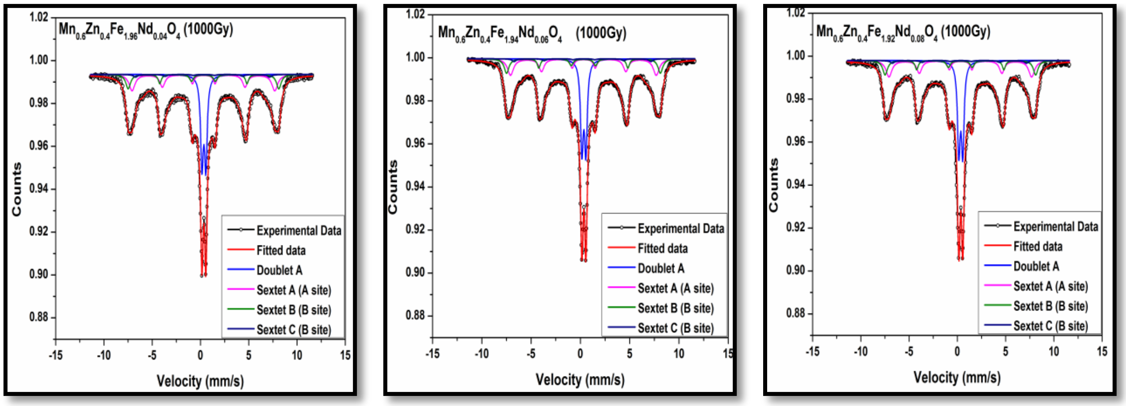

(a) (b) (c)

Figure 6.6.3 Mossbauer spectra for $Mn_{0.6}Zn_{0.4}Fe_{2-x}Nd_xO_4$ nanoparticles irradiated with 1000Gy

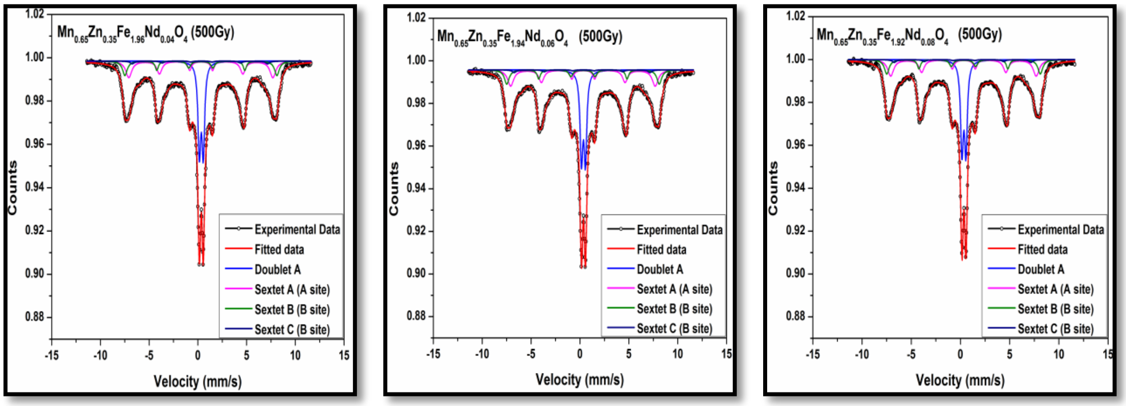

(a) (b) (c)

Figure 6.6.4 Mossbauer spectra for $Mn_{0.65}Zn_{0.35}Fe_{2-x}Nd_xO_4$ nanoparticles irradiated with 500Gy

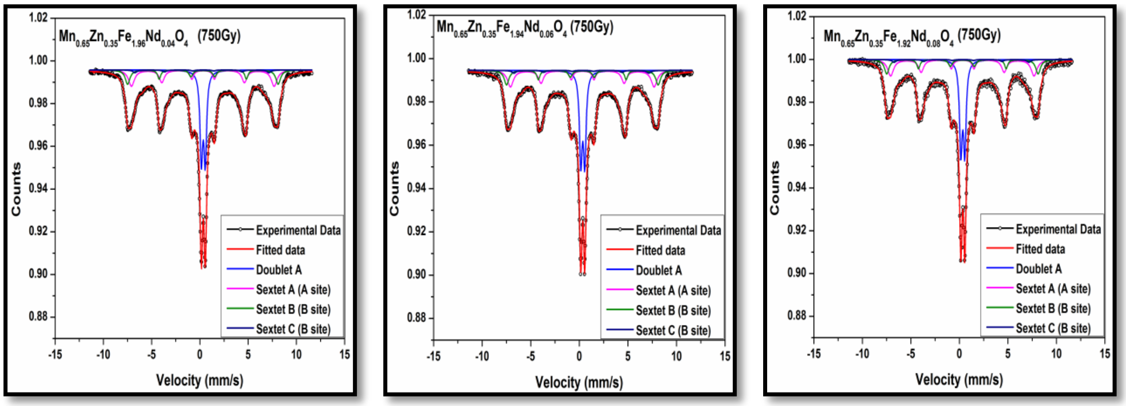

(a) (b) (c)

Figure 6.6.5 Mossbauer spectra for $Mn_{0.65}Zn_{0.35}Fe_{2-x}Nd_xO_4$ nanoparticles irradiated with 750Gy

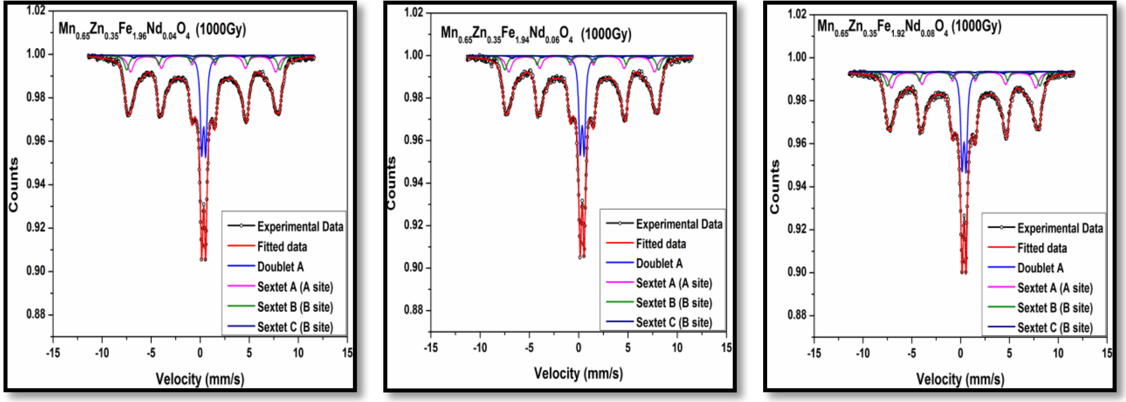

(a) (b) (c)

Figure 6.6.6 Mossbauer spectra for $Mn_{0.65}Zn_{0.35}Fe_{2-x}Nd_xO_4$ nanoparticles irradiated with 1000Gy

Table 6.6.1a Calculated values of isomer shift (IS), quadrupole splitting (QS) and hyperfine magnetic field for $Mn_{0.6}Zn_{0.4}Fe_{2-x}Nd_xO_4$ irradiated with 500Gy.

Sample	Iron site spectra	Isomer shift (IS) mm/s	Qdrupole splitting (QS) mm/s	Hyperfine field (Tesla)	Relative area (%)
X=0.04	Doublet (S. P.)	0.351±0.004	0.420±0.011	-	37.16
	Sextet A (Octa)	0.389±0.011	0.056±0.008	47.72±0.26	18.35
	Sextet B (Octa)	0.335±0.031	0.066±0.015	44.28±0.37	18.52
	Sextet C (Tetra)	0.287±0.025	0.030±0.013	36.21±0.51	25.97
X=0.06	Doublet (S. P.)	0.348±0.063	0.437±0.027	-	38.19
	Sextet A (Octa)	0.375±0.042	0.037±0.012	47.86±1.39	19.75
	Sextet B (Octa)	0.337±0.022	0.045±0.011	45.33±2.11	18.66
	Sextet C (Tetra)	0.288±0.031	0.052±0.016	35.35±1.39	23.41
X=0.08	Doublet (S. P.)	0.346±0.028	0.441±0.021	-	38.52
	Sextet A (Octa)	0.379±0.056	0.044±0.028	48.19±0.55	19.88
	Sextet B (Octa)	0.355±0.057	0.042±0.021	43.75±2.34	19.36
	Sextet C (Tetra)	0.291±0.033	0.046±0.023	34..21±0.98	22.24

Table 6.6.1b Calculated values of isomer shift (IS), quadrupole splitting (QS) and hyperfine magnetic field for $Mn_{0.6}Zn_{0.4}Fe_{2-x}Nd_xO_4$ irradiated with 750Gy.

Sample	Iron site spectra	Isomer shift (IS) mm/s	Qdrupole splitting (QS) mm/s	Hyperfine field (Tesla)	Relative area (%)
X=0.04	Doublet (S. P.)	0.342±0.012	0.436±0.009	-	37.98
	Sextet A (Octa)	0.391±0.008	0.066±0.012	47.83±0.35	18.73
	Sextet B (Octa)	0.337±0.039	0.054±0.017	44.37±0.11	18.06
	Sextet C (Tetra)	0.229±0.052	0.030±0.007	36.89±0.27	24.61
X=0.06	Doublet (S. P.)	0.356±0.015	0.438±0.015	-	38.21
	Sextet A (Octa)	0.386±0.036	0.034±0.018	48.23±2.31	19.55
	Sextet B (Octa)	0.383±0.021	0.043±0.009	46.72±3.10	19.35
	Sextet C (Tetra)	0.226±0.033	0.051±0.018	36.11±2.13	23.36
X=0.08	Doublet (S. P.)	0.349±0.025	0.444±0.013	-	38.73
	Sextet A (Octa)	0.383±0.053	0.045±0.019	48.96±1.58	20.31

	Sextet B (Octa)	0.331±0.046	0.041±0.009	43.75±0.59	19.45
	Sextet C (Tetra)	0.224±0.034	0.048±0.017	34..21±1.08	21.49

Table 6.6.1c Calculated values of isomer shift (IS), quadrupole splitting (QS) and hyperfine magnetic field for $Mn_{0.6}Zn_{0.4}Fe_{2-x}Nd_xO_4$ irradiated with 1000Gy.

Sample	Iron site spectra	Isomer shift (IS) mm/s	Qudrupole splitting (QS) mm/s	Hyperfine field (Tesla)	Relative area (%)
X=0.04	Doublet (S. P.)	0.351±0.026	0.429±0.015	-	39.21
	Sextet A (Octa)	0.386±0.015	0.056±0.018	47.99±0.35	19.55
	Sextet B (Octa)	0.337±0.019	0.049±0.021	44.36±1.32	19.34
	Sextet C (Tetra)	0.234±0.048	0.031±0.005	35.69±0.76	21.90
X=0.06	Doublet (S. P.)	0.349±0.011	0.434±0.008	-	39.43
	Sextet A (Octa)	0.388±0.024	0.037±0.025	48.96±1.65	19.55
	Sextet B (Octa)	0.346±0.011	0.046±0.011	45.63±1.11	19.35
	Sextet C (Tetra)	0.232±0.029	0.049±0.016	36.85±1.09	23.36
X=0.08	Doublet (S. P.)	0.336±0.016	0.425±0.022	-	39.77
	Sextet A (Octa)	0.385±0.066	0.048±0.018	48.96±1.36	19.86
	Sextet B (Octa)	0.342±0.026	0.053±0.011	43.75±0.59	18.69
	Sextet C (Tetra)	0.224±0.034	0.052±0.018	34..21±1.08	21.68

Table 6.6.2a Calculated values of isomer shift (IS), quadrupole splitting (QS) and hyperfine magnetic field for $Mn_{0.65}Zn_{0.25}Fe_{2-x}Nd_xO_4$ irradiated with 500Gy.

Sample	Iron site spectra	Isomer shift (IS) mm/s	Qudrupole splitting (QS) mm/s	Hyperfine field (Tesla)	Relative area (%)
X=0.04	Doublet (S. P.)	0.342±0.015	0.389±0.016	-	37.69
	Sextet A (Octa)	0.388±0.008	0.023±0.023	48.63±1.26	18.35
	Sextet B (Octa)	0.392±0.036	0.053±0.031	45.25±1.03	18.52
	Sextet C (Tetra)	0.292±0.016	0.042±0.016	36.96±1.36	25.97
X=0.06	Doublet (S. P.)	0.351±0.019	0.438±0.018	-	38.19
	Sextet A (Octa)	0.346±0.065	0.053±0.018	48.59±1.39	19.75
	Sextet B (Octa)	0.318±0.061	0.053±0.019	46.36±1.36	18.66

	Sextet C (Tetra)	0.286±0.009	0.036±0.015	36.35±0.09	23.41
X=0.08	Doublet (S. P.)	0.363±0.037	0.459±0.009	-	38.67
	Sextet A (Octa)	0.346±0.086	0.062±0.016	49.36±2.36	19.26
	Sextet B (Octa)	0.362±0.053	0.046±0.026	44.36±1.25	19.37
	Sextet C (Tetra)	0.299±0.021	0.038±0.011	33.16±2.56	22.70

Table 6.6.2b Calculated values of isomer shift (IS), quadrupole splitting (QS) and hyperfine magnetic field for $Mn_{0.65}Zn_{0.25}Fe_{2-x}Nd_xO_4$ irradiated with 750Gy.

Sample	Iron site spectra	Isomer shift (IS) mm/s	Qudrupole splitting (QS) mm/s	Hyperfine field (Tesla)	Relative area (%)
X=0.04	Doublet (S. P.)	0.353±0.011	0.435±0.011	-	37.98
	Sextet A (Octa)	0.386±0.025	0.068±0.009	48.83±2.36	19.25
	Sextet B (Octa)	0.328±0.026	0.046±0.028	45.23±1.39	19.36
	Sextet C (Tetra)	0.228±0.016	0.037±0.013	37.26±2.11	24.01
X=0.06	Doublet (S. P.)	0.359±0.035	0.426±0.045	-	38.21
	Sextet A (Octa)	0.388±0.026	0.053±0.023	49.66±1.36	19.55
	Sextet B (Octa)	0.378±0.015	0.026±0.016	48.36±1.59	19.35
	Sextet C (Tetra)	0.224±0.029	0.052±0.026	38.39±2.01	23.36
X=0.08	Doublet (S. P.)	0.355±0.016	0.422±0.009	-	38.73
	Sextet A (Octa)	0.384±0.026	0.052±0.009	50.36±2.22	20.31
	Sextet B (Octa)	0.341±0.056	0.046±0.012	48.22±1.18	19.45
	Sextet C (Tetra)	0.228±0.053	0.051±0.013	37.66±2.33	21.49

Table 6.6.2c Calculated values of isomer shift (IS), quadrupole splitting (QS) and hyperfine magnetic field for $Mn_{0.65}Zn_{0.25}Fe_{2-x}Nd_xO_4$ irradiated at 1000Gy.

Sample	Iron site spectra	Isomer shift (IS) mm/s	Qudrupole splitting (QS) mm/s	Hyperfine field (Tesla)	Relative area (%)
X=0.04	Doublet (S. P.)	0.351±0.026	0.429±0.015	-	39.21
	Sextet A (Octa)	0.386±0.015	0.056±0.018	49.96±1.13	19.55
	Sextet B (Octa)	0.337±0.019	0.049±0.021	46.32±0.98	19.34

	Sextet C (Tetra)	0.234±0.048	0.031±0.005	37.38±1.17	21.90
X=0.06	Doublet (S. P.)	0.349±0.011	0.434±0.008	-	39.43
	Sextet A (Octa)	0.388±0.024	0.037±0.025	50.23±2.36	19.55
	Sextet B (Octa)	0.346±0.011	0.046±0.011	49.46±2.52	19.35
	Sextet C (Tetra)	0.232±0.029	0.049±0.016	38.67±2.01	23.36
X=0.08	Doublet (S. P.)	0.336±0.016	0.425±0.022	-	39.77
	Sextet A (Octa)	0.385±0.066	0.048±0.018	51.23±1.25	19.86
	Sextet B (Octa)	0.342±0.026	0.053±0.011	49.55±1.11	18.69
	Sextet C (Tetra)	0.224±0.034	0.052±0.018	38.86±2.13	21.68

It may be seen that there is a increase in relative area of super paramagnetic doublet with increasing γ radiation dose. This provides a clear indication of enhancement in super paramagnetic behavior which is a characteristic observed in nanomagnetic materials when the reduction of particle size reaches below a critical limit. Out of remaining three sub-spectra, one corresponds to Fe ions occupying the tetrahedral site and remaining two sextets correspond to the octahedral Fe ion sites. The isomer shift (IS), quadrupole splitting (QS) and hyperfine field (H_{hf}) were calculated from the fitting of spectra. By comparing the values in Table 6.6.1 (a,b,c) and Table 6.6.2(a,b,c) with published data we can conclude that the Fe exists at both the octahedral and the tetrahedral site as Fe^{3+} that too in high spin state.

The hyperfine field at B site is observed to increase with increasing gamma radiation dose. This enhancement in hyperfine field can be attributed to lowering of Fe^{+2}/Fe^{+3} ratio due to increase of Fe^{+3} ions in high spin state. The hyperfine field at A-site was found to increase marginally due to transfer of Fe at tetrahedral site as a consequence of gamma radiation exposure. Increase in relative area of paramagnetic doublet with increasing gamma radiation dose at the expense of relative area of magnetic sextets indicates the enhancement in superparamagnetic behavior which can be attributed to the reduction of particle size as a result of gamma radiation exposure [26-29].

6.7 Relative permeability

Magnetic permeability of the material is very important for high frequency applications such as EM wave absorbers and inductor devices. Initial permeability of polycrystalline material depends on several factors such as average grain size, chemical composition of the material, nature of the grain boundaries etc. Permeability of samples under study was seen to be greatly affected by gamma radiation doses.

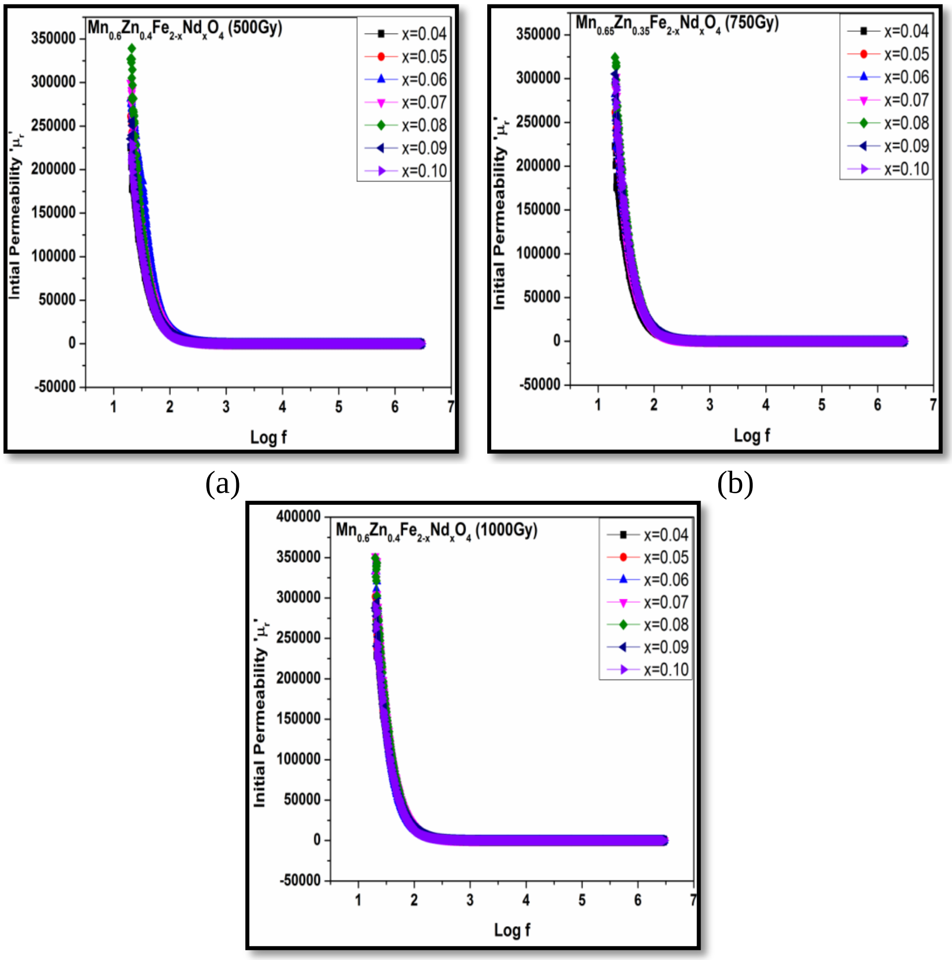

(a)

(b)

(c)

Figure 6.7.1 (a, b & c) Variation of relative permeability 'μ_r' for γ irradiated $Mn_{0.6}Zn_{0.4}Fe_{2-x}Nd_xO_4$ nanoparticles

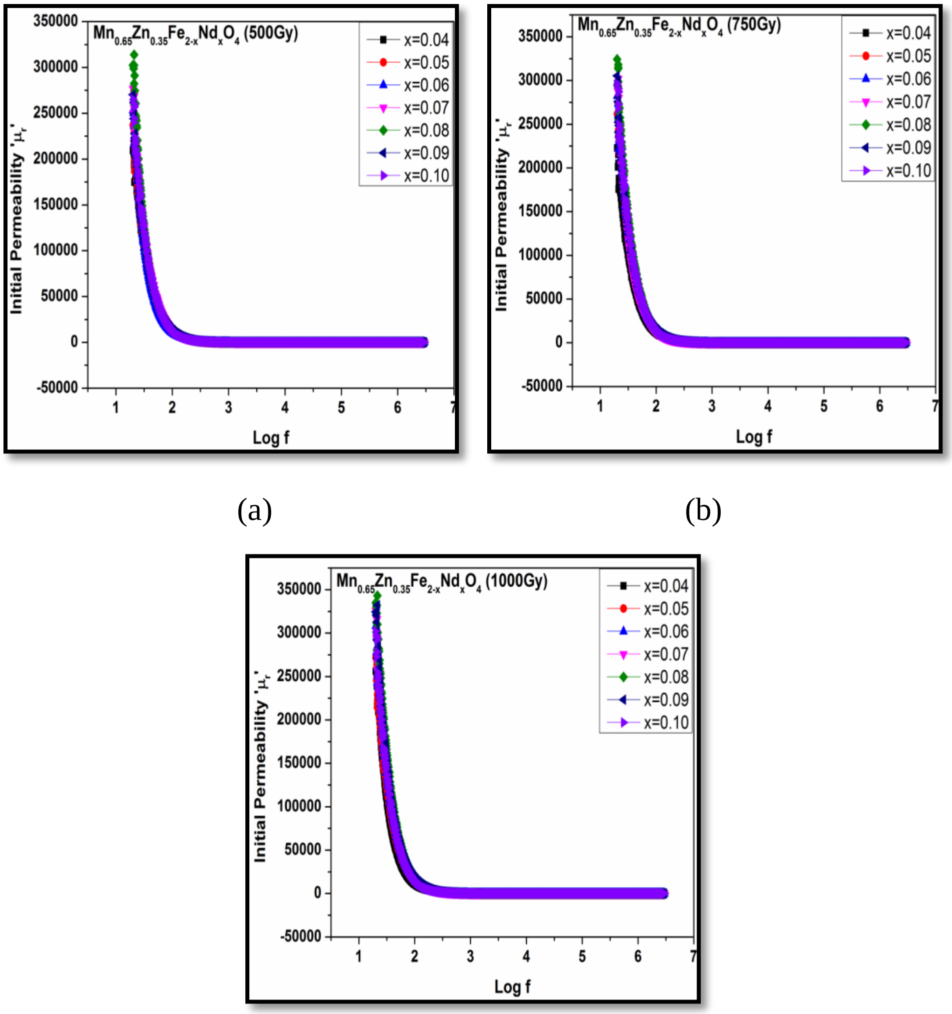

(a) (b)

(c)

Figure 6.7.2 (a, b & c) Variation of relative permeability ‘μ_r’ for γ irradiated $Mn_{0.65}Zn_{0.35}Fe_{2-x}Nd_xO_4$ nanoparticles

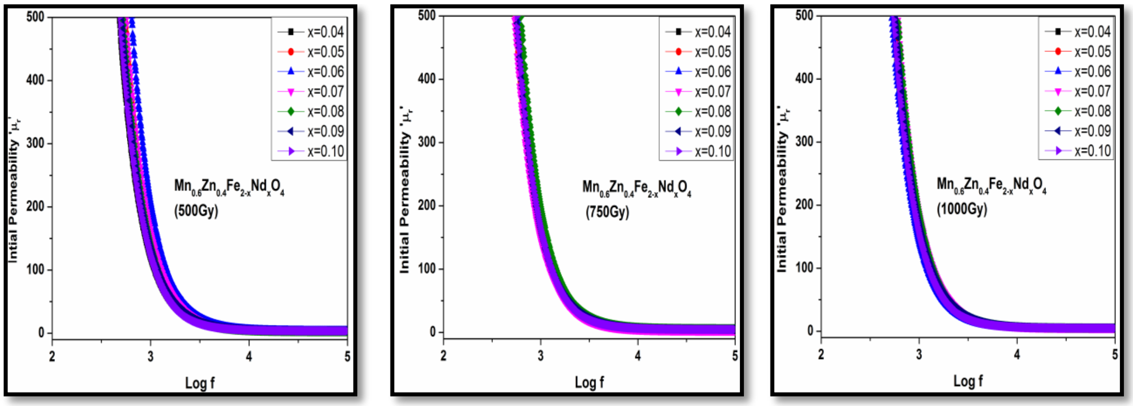

(a) (b) (c)

Figure 6.7.3 (a, b & c) Variation of relative permeability ‘μ_r’ of $Mn_{0.6}Zn_{0.4}Fe_{2-x}Nd_xO_4$ nanoparticles in frequency range of 100Hz to 100kHz

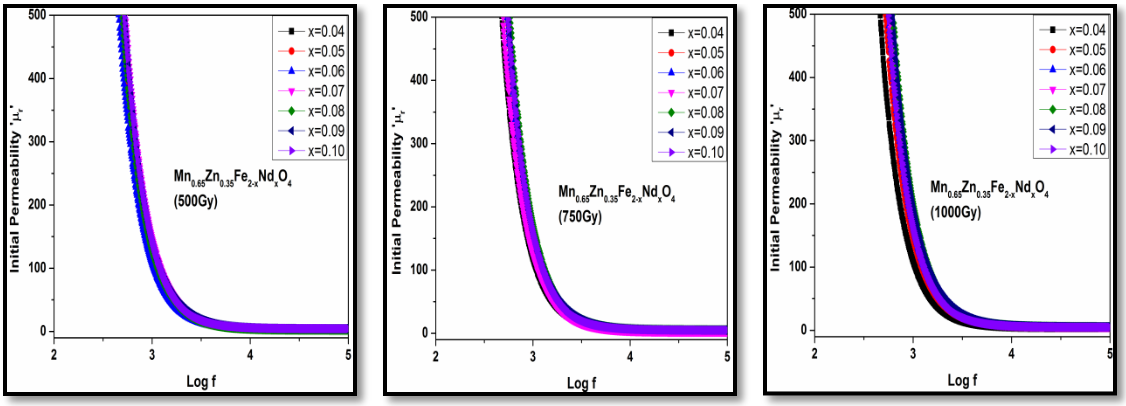

(a) (b) (c)

Figure 6.7.4 (a, b & c) Variation of relative permeability ‘μ_r’ of $Mn_{0.65}Zn_{0.35}Fe_{2-x}Nd_xO_4$ nanoparticles in frequency range of 100Hz to 100kHz

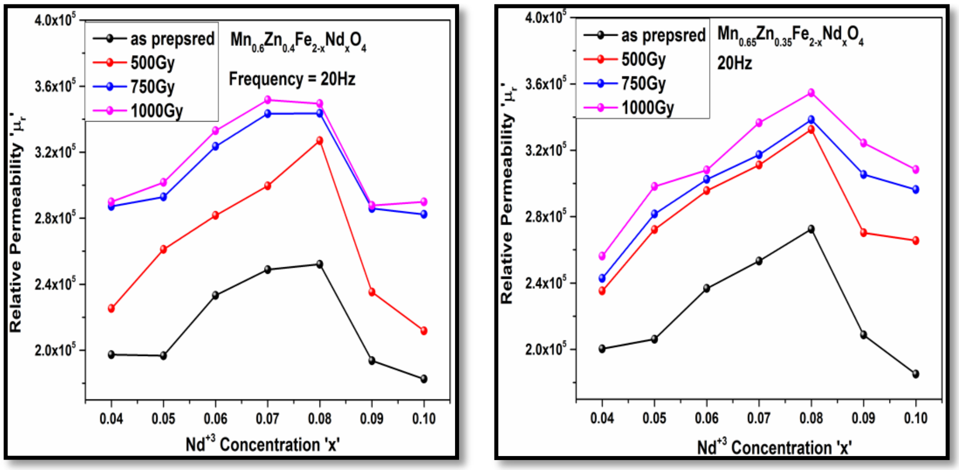

(a) (b)

Figure 6.7.5 (a & b) Variation of relative permeability ‘μ_r’ of gamma radiated $Mn_{0.6}Zn_{0.4}Fe_{2-x}Nd_xO_4$ and $Mn_{0.65}Zn_{0.35}Fe_{2-x}Nd_xO_4$ nanoparticles at 20Hz

Figure 6.7.1 and Figure 6.7.2 shows the variation of relative permeability ‘μ_r’ with frequency for γ irradiated $Mn_{0.6}Zn_{0.4}Fe_{2-x}Nd_xO_4$ and $Mn_{0.65}Zn_{0.35}Fe_{2-x}Nd_xO_4$ nanoparticles over the frequency range of 20Hz to 3MHz. An enlarged view of permeability variation in the frequency range of 1000Hz to 100 kHz is shown in Figure 6.7.3 and Figure 6.7.4. Samples were seen to exhibit permeability of the order 10^2 even at frequency of 1 kHz and decrease further to a constant low value beyond 10 kHz. Permeability of all the samples was seen to be greatly enhanced due to γ radiation exposure. Maximum enhancement of 1.1 $x10^5$ was observed for sample $Mn_{0.6}Zn_{0.4}Fe_{2-0.08}Nd_{0.08}O_4$ and an increase of $0.7x10^5$ was observed for sample $Mn_{0.65}Zn_{0.35}Fe_{2-0.08}Nd_{0.08}O_4$ both with gamma radiation dose of 1000Gy with is as shown in Figure 6.7.5. Reduction in grain size with increasing gamma radiation dose supports the domain wall motion resulting in a decrease in damping constant at lower frequencies. Increase in non conducting grain boundaries also provides better stability at higher frequencies [30,31]. The increasing trend in permeability of nanoparticles also indicate better magnetic ordering in the samples, which again can be attributed to alteration of Fe^{+2}/Fe^{+3} ratio at both the octahedral and tetrahedral sites and conversion of Fe^{+3} in to high spin state due to gamma radiation exposure which results in improved magnetic ordering to a great extent and lower volume fraction of defects within the crystallites. Permeability was observed to decrease rapidly with increasing frequency for all the samples as the materials are composed of single domain nanoparticle which posses lower stability towards higher frequencies being superparamagnetic in nature [32].

Electrical transport property exploration

6.8 D. C. Resistivity

The resistivity of a ferrite material is of particular importance when it comes applications especially in areas where power consumption and power dissipations are involved. For low power dissipation in addition to narrow magnetic hysteresis for lower eddy currents and low power dissipation the resistivity of the material could be moderately high. The DC resistivity (ρ) plots as a function of temperature for the samples $Mn_{0.6}Zn_{0.4}Fe_{2-x}Nd_xO_4$ and $Mn_{0.65}Zn_{0.35}Fe_{2-x}Nd_xO_4$ are presented in Figure 6.8.1 and Figure 6.8.2. Room temperature variation of resistivity values with γ radiation dose is shown in Figure 6.8.3 (a & b). The resistivity profiles gamma irradiated samples were observed to be very much identical to their un-radiated counterparts. However the resistivity values were observed to be a little lower after gamma irradiation. Like structural and magnetic properties, the variations produced in resistivity of these samples were also seen to be proportional to the gamma radiation dose absorbed by the samples.

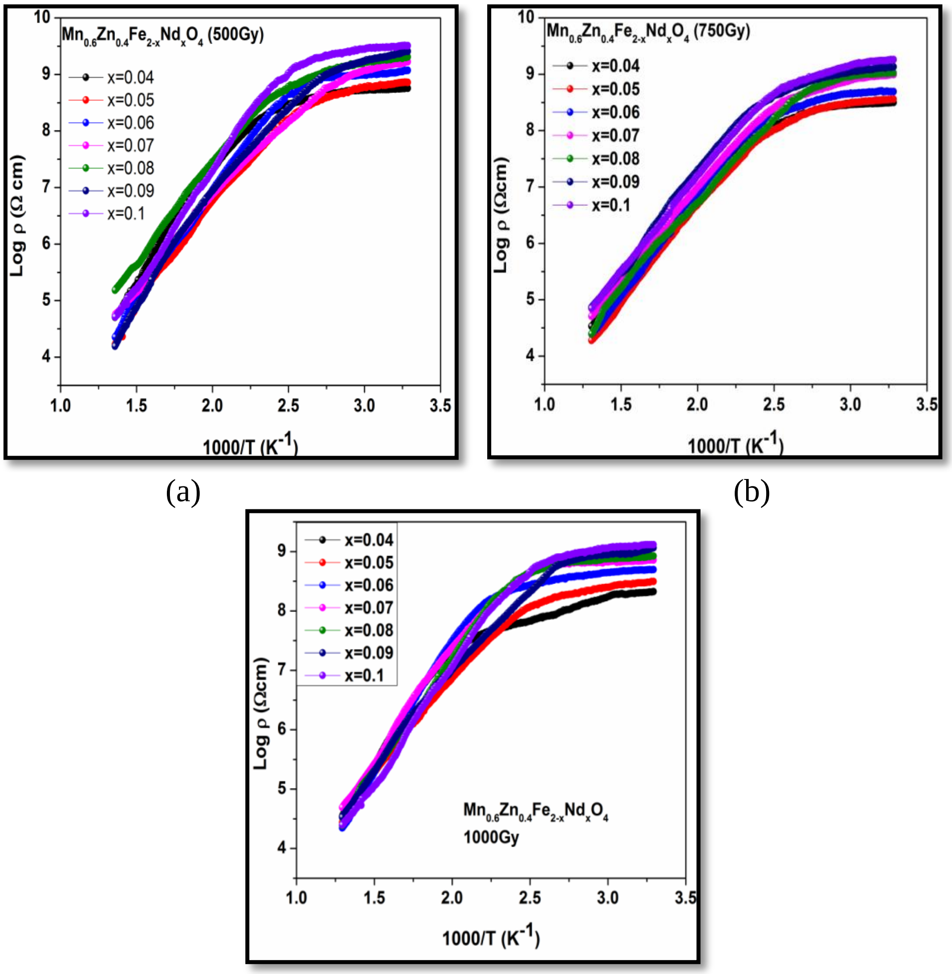

(a) (b)

(c)

Figure 6.8.1 (a, b & c) Variation of D.C. resistivity for γ irradiated $Mn_{0.6}Zn_{0.4}Fe_{2-x}Nd_xO_4$ nanoparticles

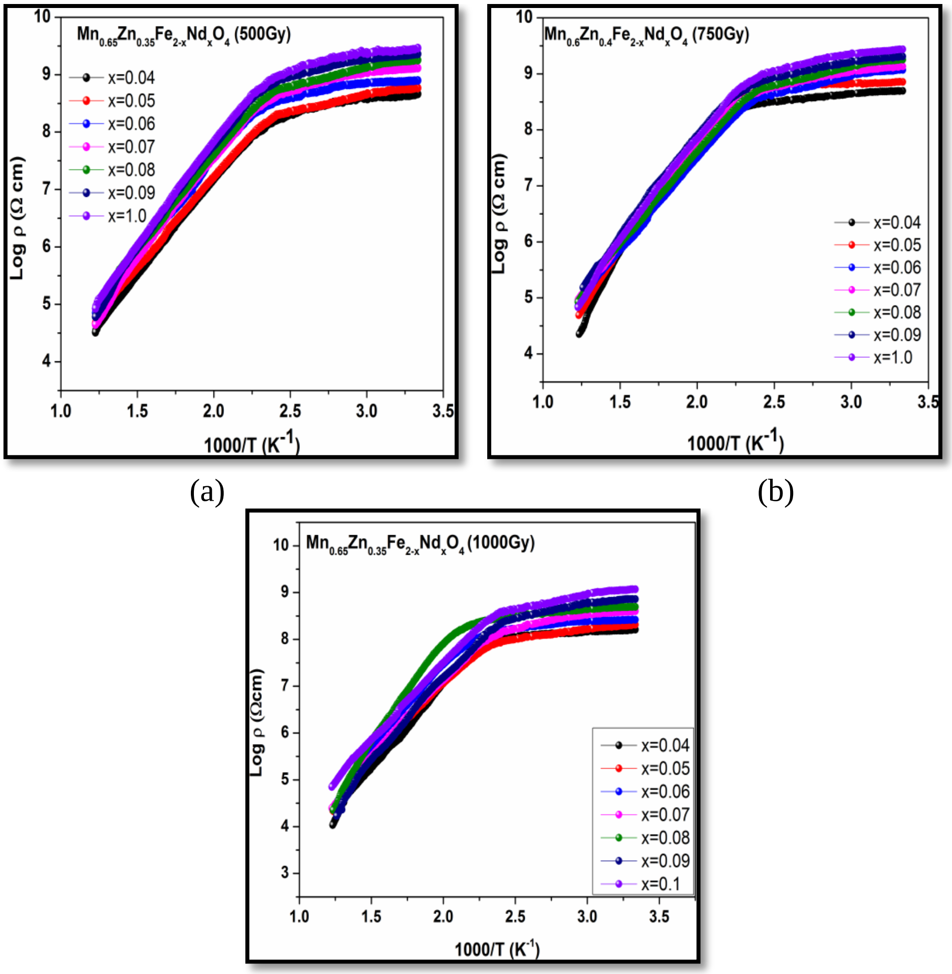

(a) (b)

(c)

Figure 6.8.2 (a, b & c) Variation of D.C. resistivity for γ irradiated $Mn_{0.65}Zn_{0.4}Fe_{2-x}Nd_xO_4$ nanoparticles

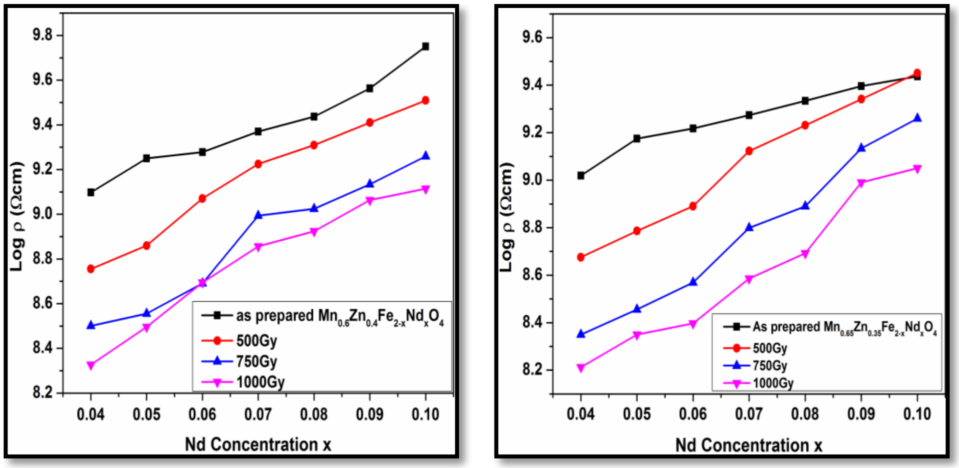

(a) (b)

Figure 6.8.3 (a & b) Variation of room temperature D.C. resistivity for γ irradiated $Mn_{0.6}Zn_{0.4}Fe_{2-x}Nd_xO_4$ and $Mn_{0.65}Zn_{0.35}Fe_{2-x}Nd_xO_4$ nanoparticles

Initial room temperature resistivity of all the gamma irradiated samples was seen to decrease with increasing gamma radiation dose. Resistivity of the ferrite material nanomaterials is generally governed by several factors such as particle size, grain boundaries, electronic charge hopping etc. Reduction in particle size as per the proposed model is expected to increases the contribution to the resistivity from non-conducting grain boundaries and increased amorphous content in the radiated materials. However increasing Fe^{+3} at both the site and rearrangement of cation distribution triggered due to gamma radiation exposure was seen to lower the resistivity thereby overcoming the increase from grain boundaries and amorphous material resulting in an overall decrease in resistivity. The change in Fe^{+3}/Fe^{+2} ratio at at both the sites and the alterations in cationic arrangement facilitates electronic exchange between $Fe^{+2} \Leftrightarrow Fe^{+3}$, $Mn^{+2} \Leftrightarrow Mn^{+3}$, $Mn^{+2} \Leftrightarrow Fe^{+3}$ etc. At higher temperatures dc resistivity is observed to decrease exponentially with raising temperature indicating semiconductor behavior in all the un-radiated and irradiated samples. It may be seen from the plots that the resistivity drops very sharply from its higher value from 10^8 to 10^4 within a temperature band of 441K to 773K which can be attributed to the increase in mobility of the charge carriers with increasing temperature. Activation energies of γ irradiated $Mn_{0.6}Zn_{0.4}Fe_{2-x}Nd_xO_4$ and $Mn_{0.65}Zn_{0.35}Fe_{2-x}Nd_xO_4$ samples are listed in tables 6.8.1a and Table 6.8.1b. Gradual decrease in activation energy E_a with increasing dose of gamma radiation can be attributed to the increase in electronic hoping rate due to variation in cation distribution and the above mentioned mechanisms. The activation energy values for $Mn_{0.65}Zn_{0.35}Fe_{2-x}Nd_xO_4$ samples were found to be marginally lower compare to the values obtained for samples $Mn_{0.6}Zn_{0.4}Fe_{2-x}Nd_xO_4$.

Table 6.8.1a Variation of Activation energy (Ea) in temperature range of 441K-773K resistivity plots of gamma irradiated $Mn_{0.6}Zn_{0.4}Fe_{2-x}Nd_xO_4$

Nd^{+3} concentrations 'x'	Activation energy (eV) (500Gy)	Activation energy (eV) (750Gy)	Activation energy (eV) (1000Gy)
0.04	0.18	0.17	0.17
0.05	0.18	0.18	0.17
0.06	0.20	0.19	0.18
0.07	0.19	0.19	0.18
0.08	0.20	0.18	0.18
0.09	0.21	0.20	0.19
0.1	0.22	0.21	0.19

Table 6.8.1b Variation of Activation energy (Ea) in temperature range of 441K-773K resistivity plots of gamma irradiated $Mn_{0.65}Zn_{0.35}Fe_{2-x}Nd_xO_4$

Nd^{+3} concentrations 'x'	Activation energy (eV) (500Gy)	Activation energy (eV) (750Gy)	Activation energy (eV) (1000Gy)
0.04	0.18	0.17	0.16
0.05	0.19	0.18	0.17
0.06	0.19	0.18	0.17
0.07	0.20	0.19	0.18
0.08	0.19	0.18	0.19
0.09	0.20	0.19	0.18
0.1	0.20	0.19	0.18

In high temperature region large amount of energy is supplied to the charge carriers and lowering of activation energy favors the conduction process as more electrons can be released in the conduction band. Trapped charges if any also take part in conduction process in this region as there is ample thermal energy available for the charge carriers there by reducing the resistivity further.

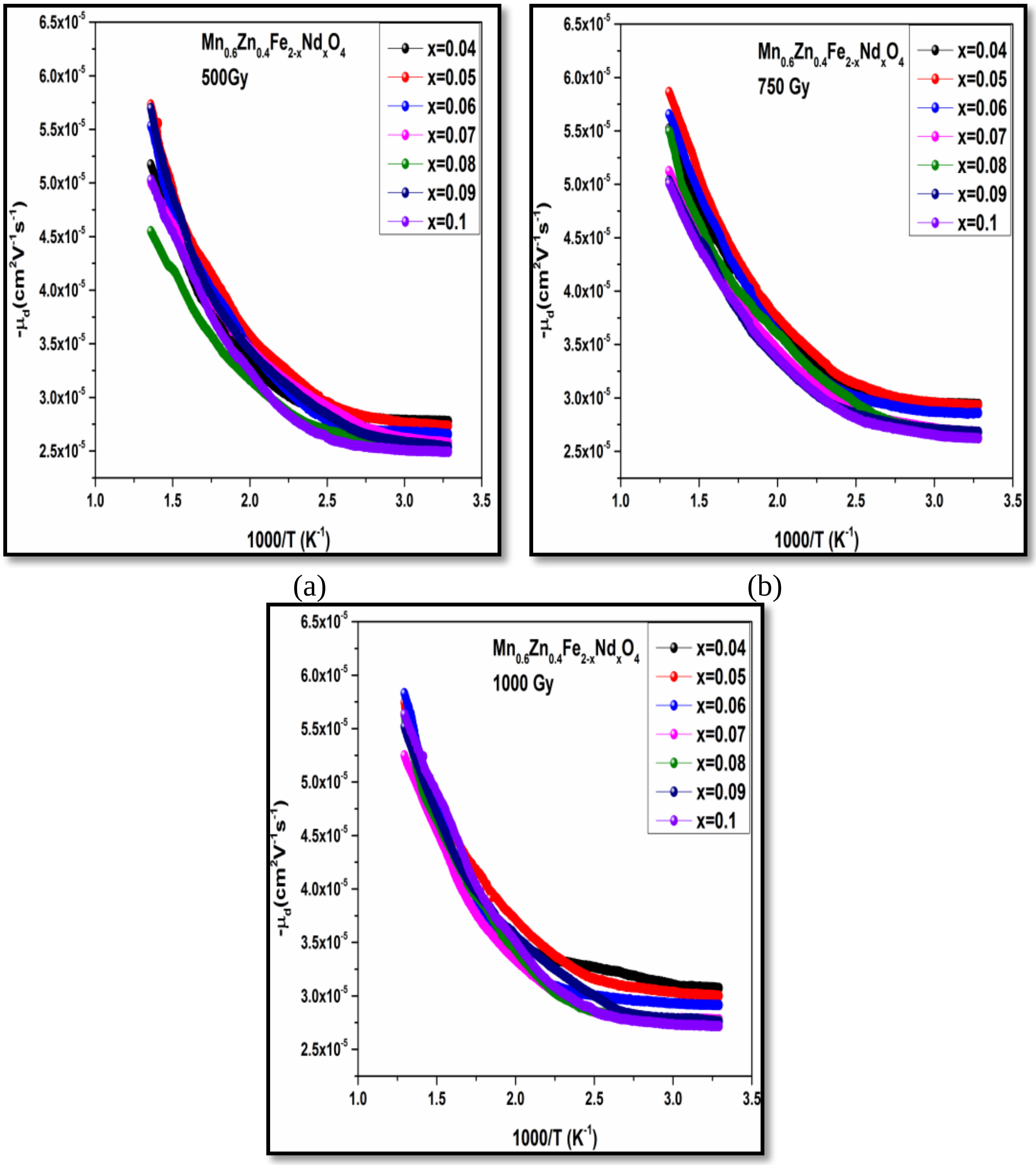

(a) (b)

(c)

Figure 6.8.4 (a & b) Variation of drift mobility of charge carriers with temperature for γ irradiated $Mn_{0.6}Zn_{0.4}Fe_{2-x}Nd_xO_4$ nanoparticles

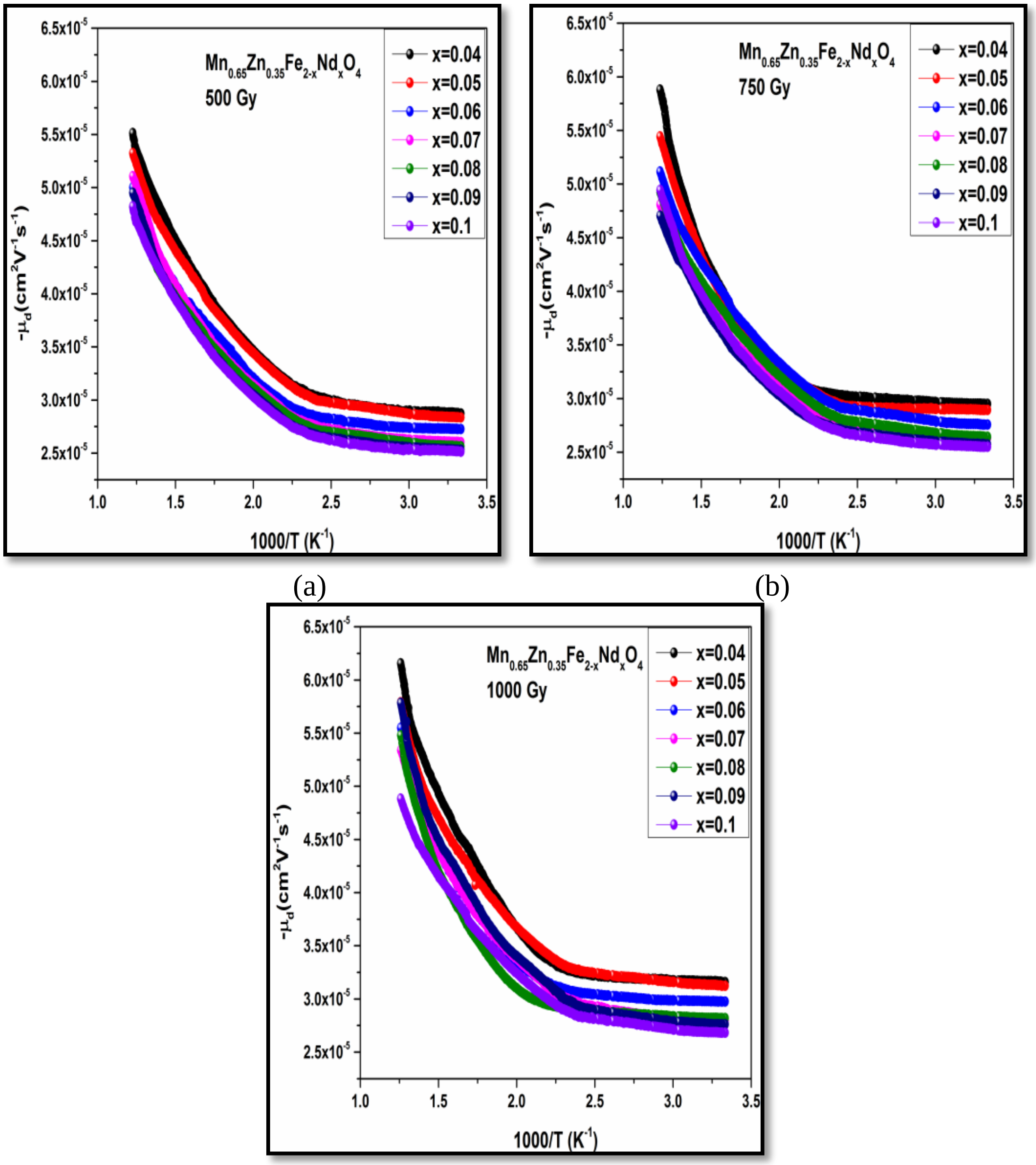

(a) (b)

(c)

Figure 6.8.5 (a & b) Variation of drift mobility of charge carriers with temperature for γ irradiated $Mn_{0.65}Zn_{0.35}Fe_{2-x}Nd_xO_4$ nanoparticles

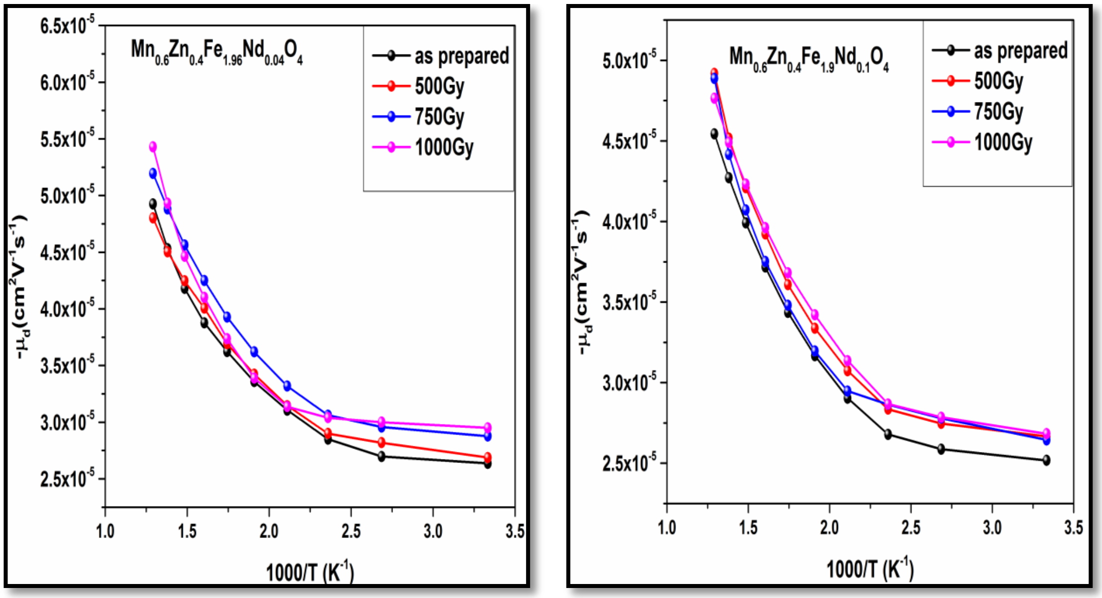

(a) (b)

Figure 6.8.6 Variation of drift mobility with temperature at different gamma radiation doses for $Mn_{0.6}Zn_{0.4}Fe_{2-x}Nd_xO_4$ (x=0.04 and x=0.01)

The plots of variation in drift mobility of gamma irradiated samples are presented in Figure 6.8.4 and Figure 6.8.5. Variation of drift mobility with temperature at different gamma radiation doses for $Mn_{0.6}Zn_{0.4}Fe_{1.96}Nd_{0.04}O_4$ and $Mn_{0.6}Zn_{0.4}Fe_{1.9}Nd_{0.1}O_4$ is presented in Figure 6.8.6. Mobility of the radiated samples was observed to increase with increasing gamma radiation dose. This increase in mobility can be attributed to increase in Fe^{+3} content at both the sites which facilitates the conduction process. Due to this enhancement in drift mobility of thermally activated charge carriers at higher temperatures the resistivity was seen to be lower [9, 33-37].

6.9 Dielectric constant variation with frequency

The plots for dielectric constant ‘ε’ as a function of frequency with increasing gamma radiation dose for $Mn_{0.6}Zn_{0.4}Fe_{2-x}Nd_xO_4$ and $Mn_{0.65}Zn_{0.35}Fe_{2-x}Nd_xO_4$ nanoparticles are shown in Figure 6.9.1 and Figure 6.9.2. The variation in dielectric constant of individual samples with increasing gamma radiation dose is shown in Figure 6.9.3 and Figure 6.9.4.

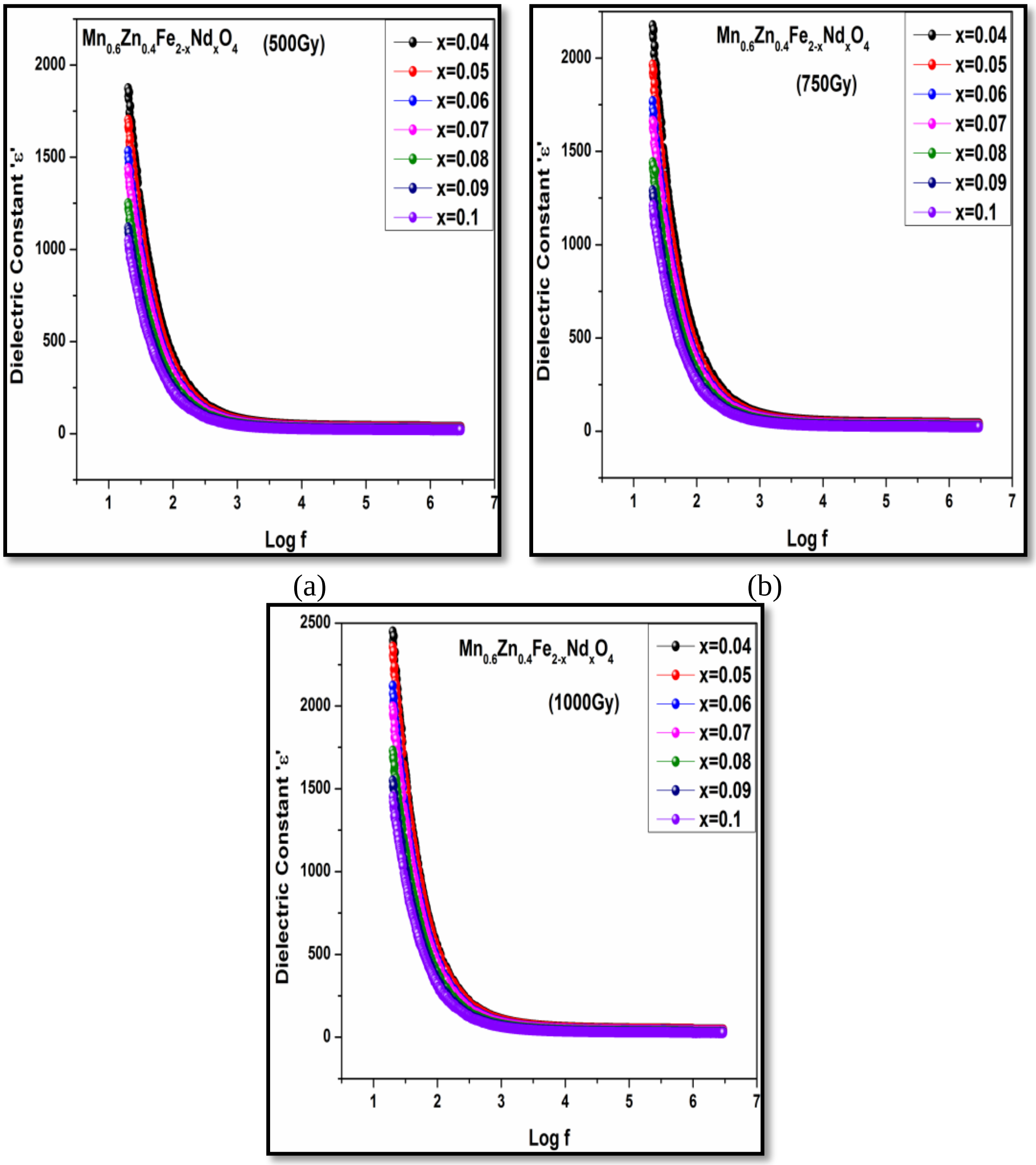

(a) (b)

(c)

Figure 6.9.1 (a, b & c) Variation of dielectric constant ‘ε’ for γ irradiated $Mn_{0.6}Zn_{0.4}Fe_{2-x}Nd_xO_4$ nanoparticles

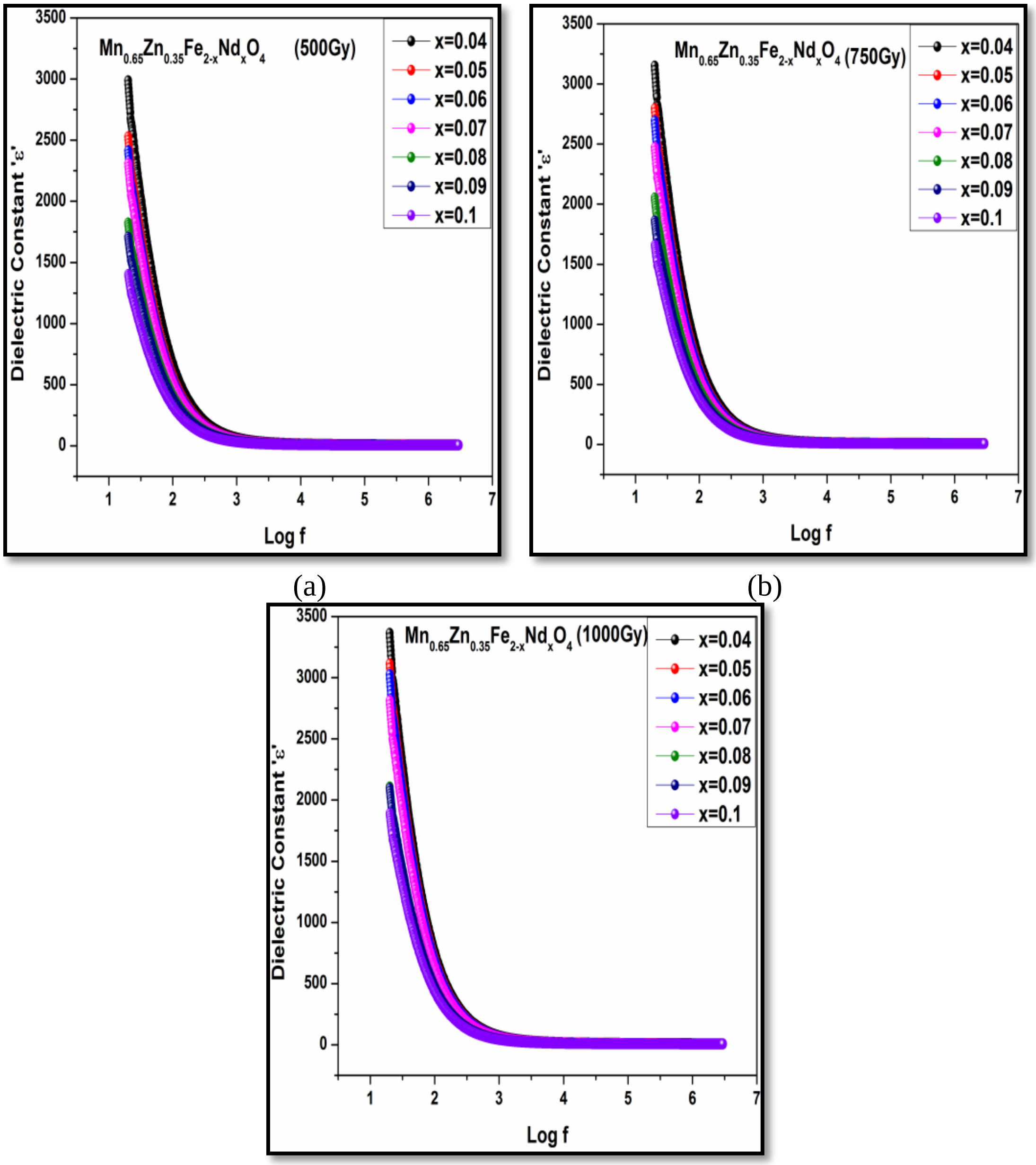

(a) (b)

(c)

Figure 6.9.2 (a, b & c) Variation of dielectric constant ‘ε’ for γ irradiated $Mn_{0.65}Zn_{0.35}Fe_{2-x}Nd_xO_4$ nanoparticles

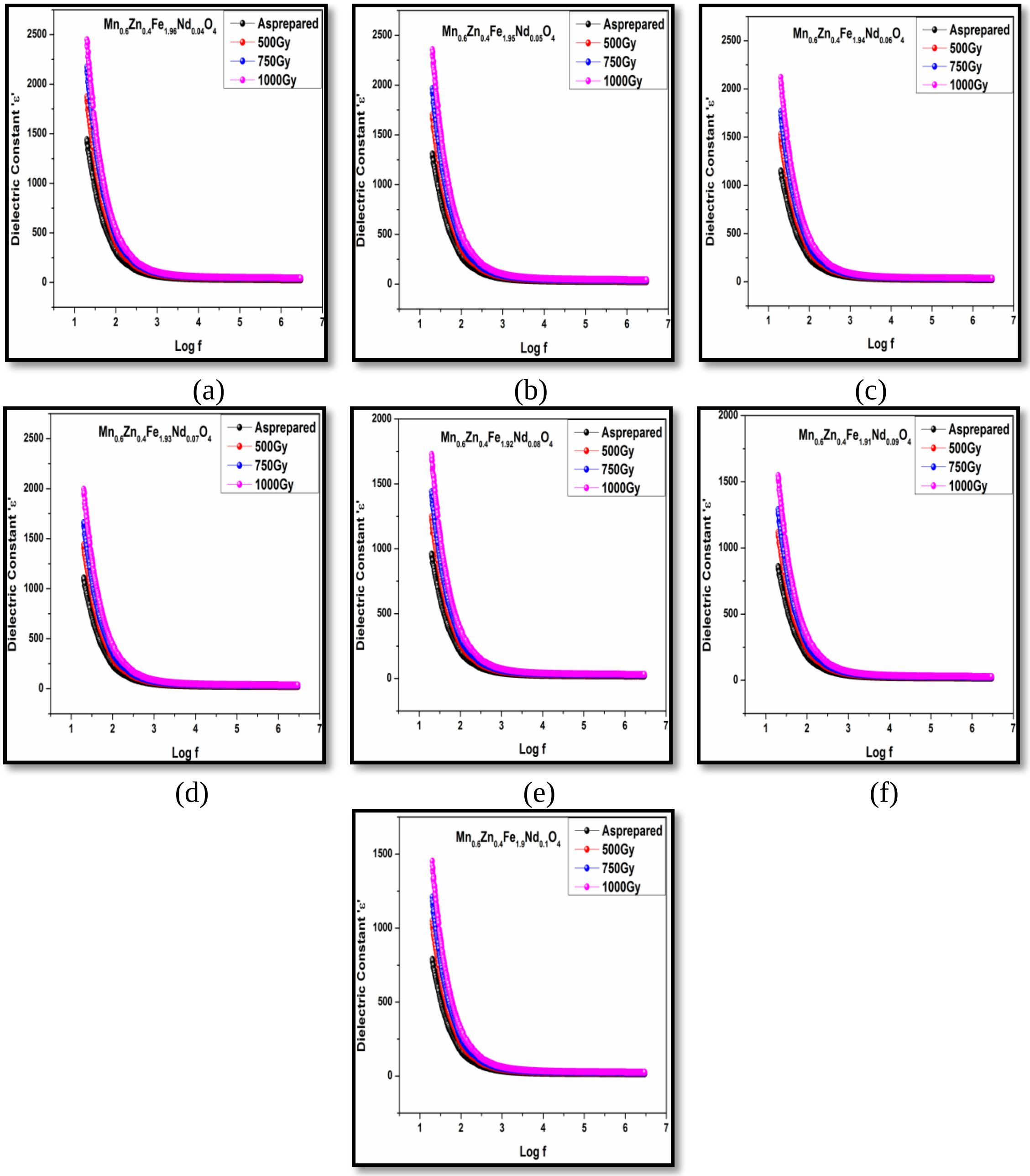

(a) (b) (c)

(d) (e) (f)

(g)

Figure 6.9.3 Variation of dielectric constant ‘ε’ with γ radiation dose $Mn_{0.6}Zn_{0.4}Fe_{2-x}Nd_xO_4$ nanoparticles

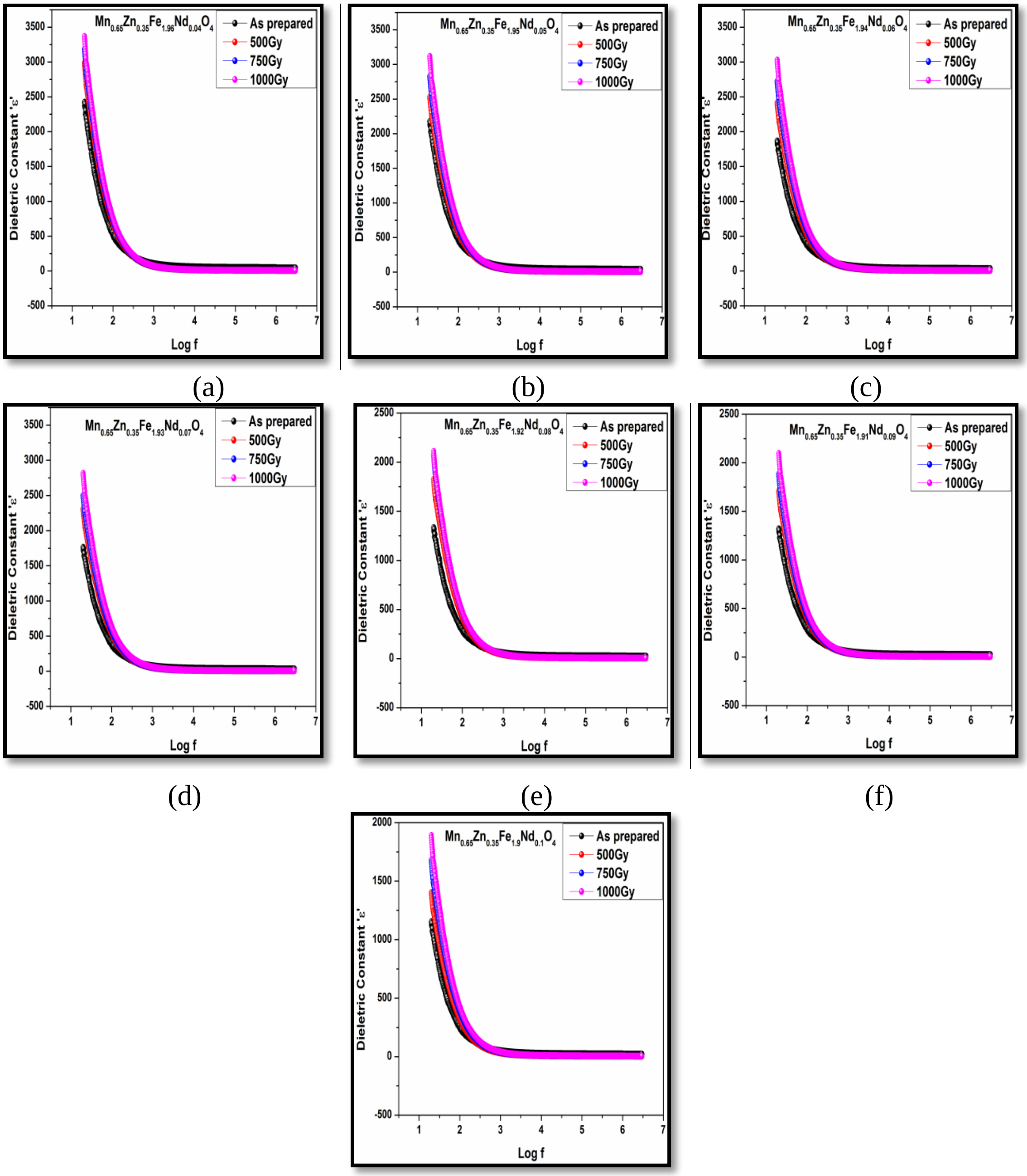

(a) (b) (c)

(d) (e) (f)

(g)

Figure 6.9.4 Variation of dielectric constant ‘ε’ with γ radiation dose $Mn_{0.65}Zn_{0.35}Fe_{2-x}Nd_xO_4$ nanoparticles

At lower frequencies the values of dielectric constant values are seen to increase with increasing gamma radiation dose. In particular if we compare non radiated and radiated $Mn_{0.6}Zn_{0.4}Fe_{2-x}Nd_xO_4$ series, sample with x=0.04 a maximum hike in dielectric constant of 1090 units while for sample with x=0.1 a minimum increase of 675 units was observed for highest gamma radiation dose of 1000Gy. A similar comparison of $Mn_{0.65}Zn_{0.35}Fe_{2-x}Nd_xO_4$ series shows a maximum increase of 870 units for x=0.04 sample and a minimum enhancement of 450 units for x=0.1sample for samples with a dose of 1000Gy. This enhancement can be attributed to the change in cationic rearrangement leading to a change in Fe^{+2}/Fe^{+3} ratios at both the tetrahedral and the octahedral sites triggered by gamma radiation exposure. Such cationic rearrangement improves electronic hopping mechanisms between various ions present in the lattice resulting in improved polarization causing an enhancement in dielectric constant [37-40]. At higher frequencies the dielectric constant values are found to approach towards very low values as usual. Beyond 1KHz frequency the values almost stop responding to the frequency variation by maintaining almost the lowest value at all frequency variations.

6.10 Dielectric loss variation with frequency

The plots of dielectric loss versus frequency at different Nd^{+3} concentrations for increasing gamma radiation doses are shown in Figure 6.10.1 and Figure 6.10.2. The samples with composition $Mn_{0.6}Zn_{0.4}Fe_{2-x}Nd_xO_4$ are found to exhibit higher dielectric loss values in comparison with the nanosamples with composition $Mn_{0.65}Zn_{0.35}Fe_{2-x}Nd_xO_4$.

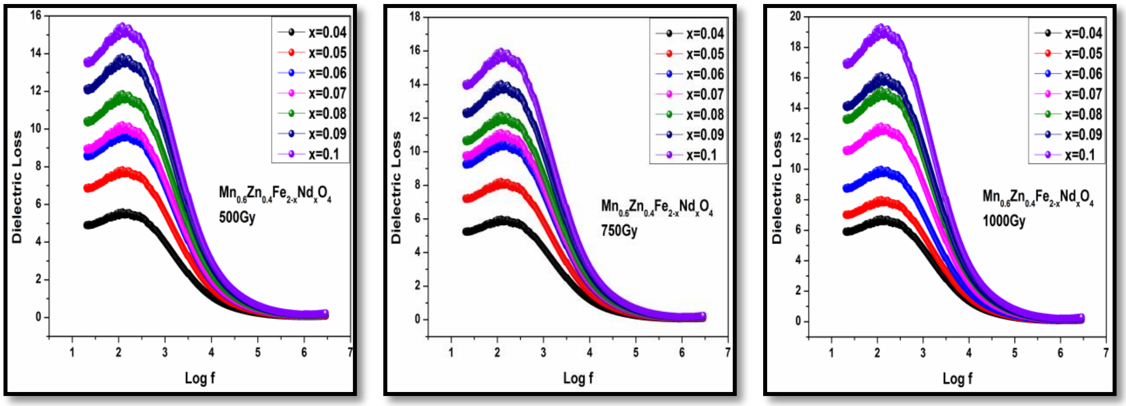

(a) (b) (c)

Figure 6.10.1 (a, b & c) Variation of Dielectric loss with frequency of γ irradiated $Mn_{0.6}Zn_{0.4}Fe_{2-x}Nd_xO_4$ nanoparticles

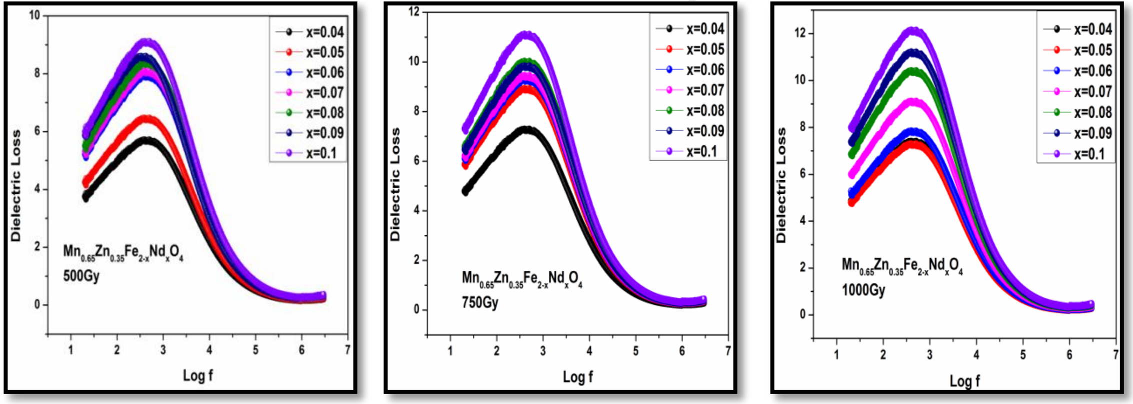

(b) (b) (c)

Figure 6.10.2 (a, b & c) Variation of Dielectric loss with frequency of γ irradiated $Mn_{0.65}Zn_{0.35}Fe_{2-x}Nd_xO_4$ nanoparticles

It was observed that dielectric loss increases with increasing gamma radiation dose for all the samples. This increase in loss with increasing can be attributed to the increased bond length as a consequence of gamma radiation exposure. The broad peak within the frequency range 100Hz to 1000Hz frequencies the loss tangent was seen for all the samples which occurs due to resonance effect between electron hopping frequency and applied field frequency (exact match of electron hoping between Fe^{+2} and Fe^{+3} ions and applied field frequency). Reduction of particle size also contribute to the loss as fine particle nature resulting in increased surface area along generation Fe^{3+} ions of larger ionic radii increases the amount of energy required for electronic exchange resulting in high loss. At higher frequencies the electronic exchange cannot follow the applied frequency and hence loss is found to decrease [41,42].

6.11 Dielectric constant variation with temperature

Variation of dielectric constant as a function of temperature at various frequencies for $Mn_{0.6}Zn_{0.4}Fe_{2-x}Nd_xO_4$ and $Mn_{0.65}Zn_{0.35}Fe_{2-x}Nd_xO_4$ nanoparticles is shown in Figure 6.11.1 and Figure 6.11.2 respectively.

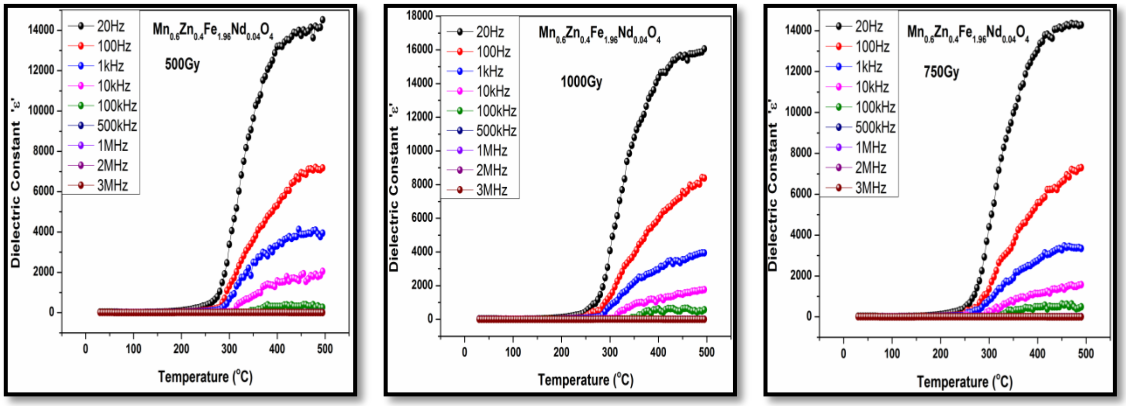

(a) (b) (c)

Figure 6.11.1 (a, b & c) Variation of Dielectric constant with temperature of γ irradiated $Mn_{0.6}Zn_{0.4}Fe_{1.96}Nd_{0.04}O_4$ nanoparticle

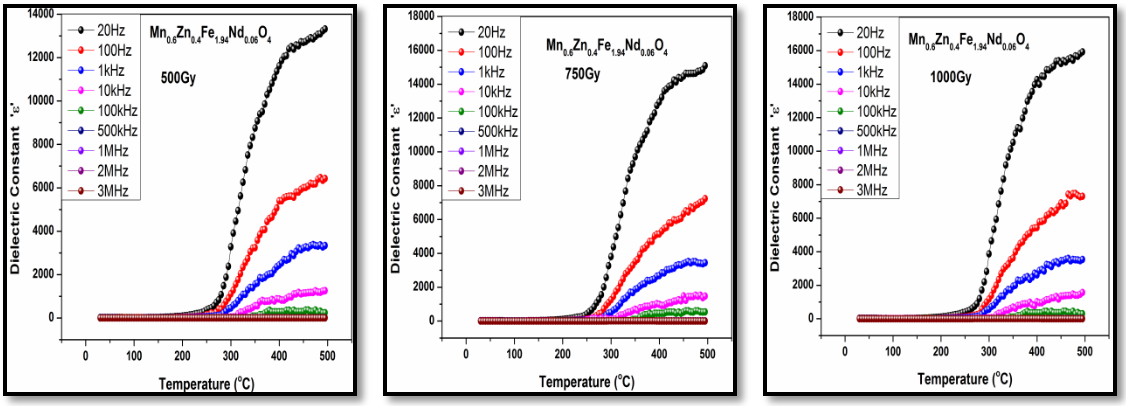

(a) (b) (c)

Figure 6.11.2 (a, b & c) Variation of Dielectric constant with temperature of γ irradiated $Mn_{0.6}Zn_{0.4}Fe_{1.94}Nd_{0.06}O_4$ nanoparticles

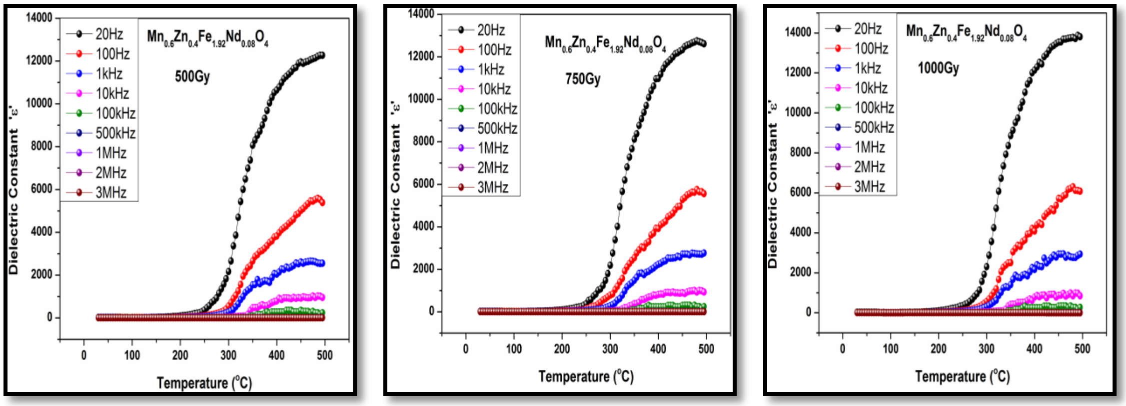

(a) (b) (c)

Figure 6.11.3 (a, b & c) Variation of Dielectric constant with temperature of γ irradiated $Mn_{0.6}Zn_{0.4}Fe_{1.92}Nd_{0.08}O_4$ nanoparticles

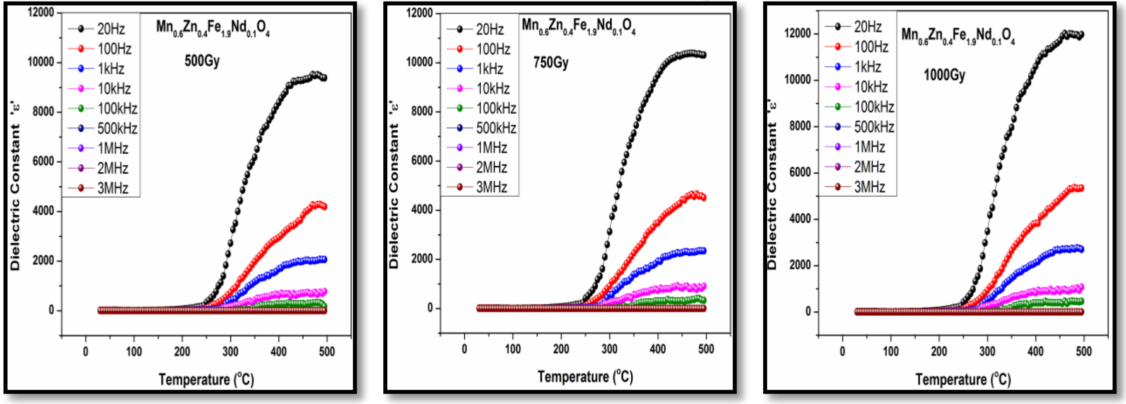

(a) (b) (c)

Figure 6.11.4 (a, b & c) Variation of Dielectric constant with temperature of γ irradiated $Mn_{0.6}Zn_{0.4}Fe_{1.9}Nd_{0.1}O_4$ nanoparticles

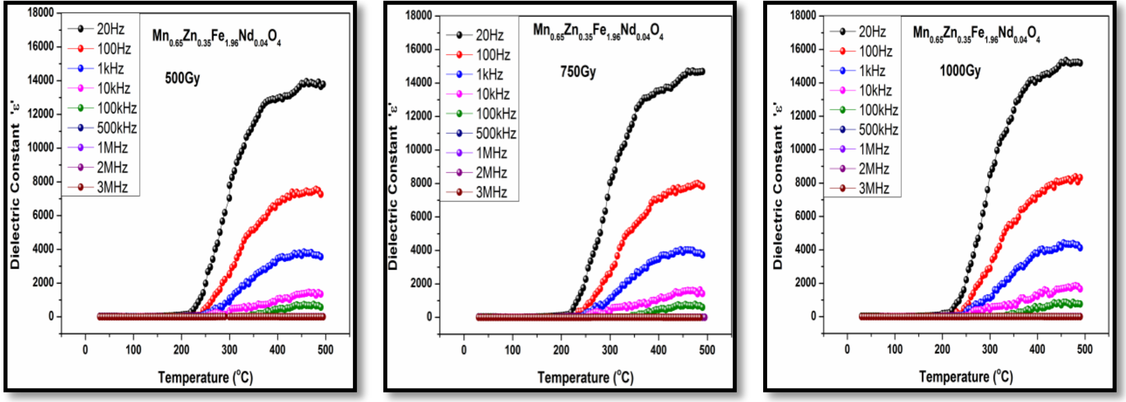

(a) (b) (c)

Figure 6.11.5 (a, b & c) Variation of Dielectric constant with temperature of γ irradiated $Mn_{0.65}Zn_{0.35}Fe_{1.96}Nd_{0.04}O_4$ nanoparticles

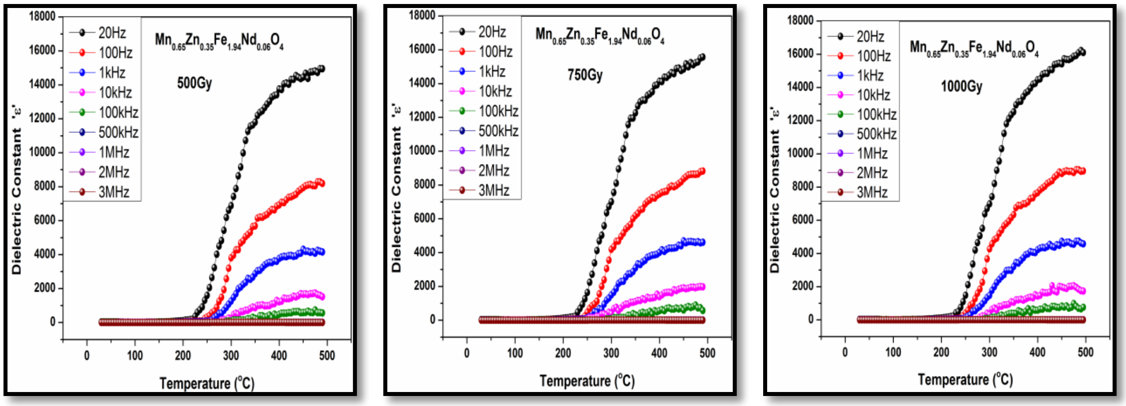

(a) (b) (c)

Figure 6.11.6 (a, b & c) Variation of Dielectric constant with temperature of γ irradiated $Mn_{0.65}Zn_{0.35}Fe_{1.94}Nd_{0.06}O_4$ nanoparticles

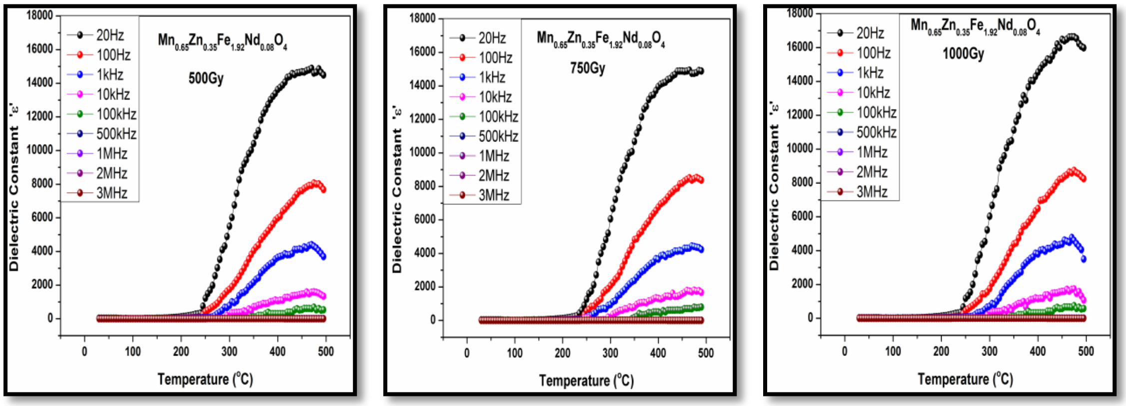

(a) (b) (c)

Figure 6.11.7 (a, b & c) Variation of Dielectric constant with temperature of γ irradiated $Mn_{0.65}Zn_{0.35}Fe_{1.92}Nd_{0.08}O_4$ nanoparticles

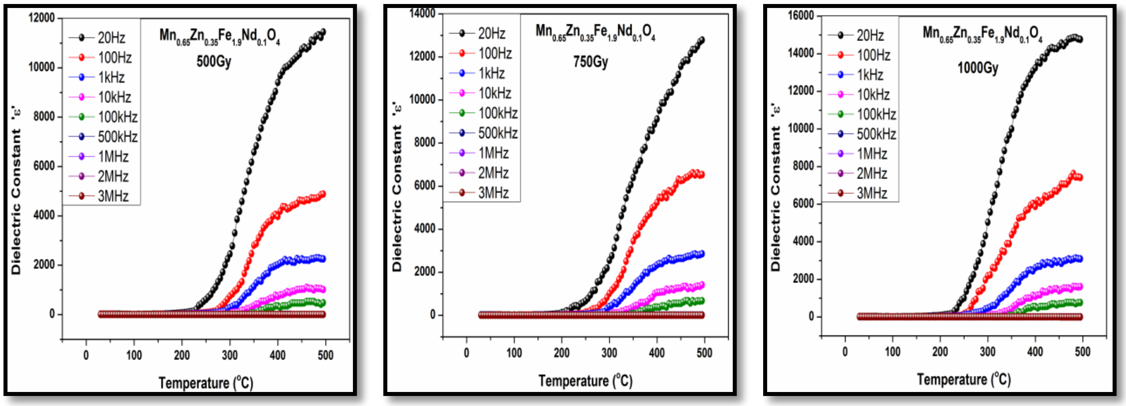

(a) (b) (c)

Figure 6.11.8 (a, b & c) Variation of Dielectric constant with temperature of γ irradiated $Mn_{0.65}Zn_{0.35}Fe_{1.9}Nd_{0.1}O_4$ nanoparticles

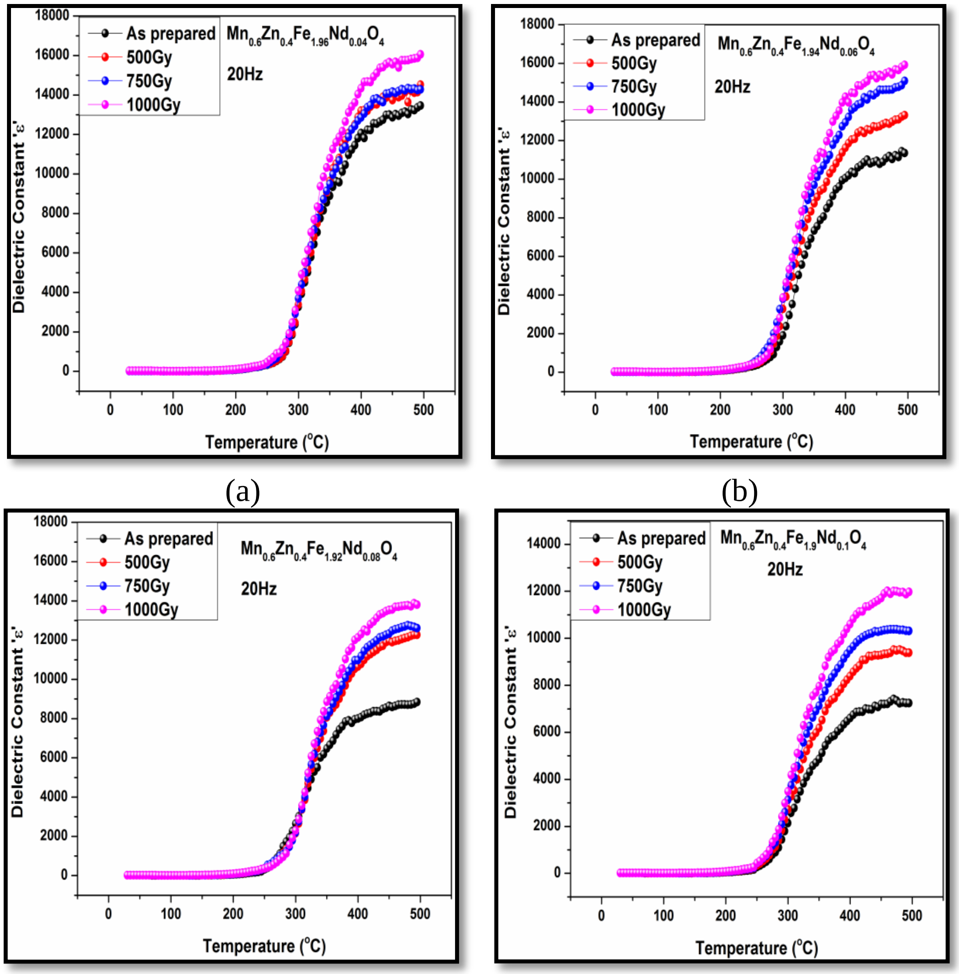

(a) (b)

(c) (d)

Figure 6.11.9 (a,b,c,d) Variation of Dielectric constant with temperature of γ irradiated $Mn_{0.6}Zn_{0.4}Fe_{2-x}Nd_xO_4$ nanoparticles at 20Hz

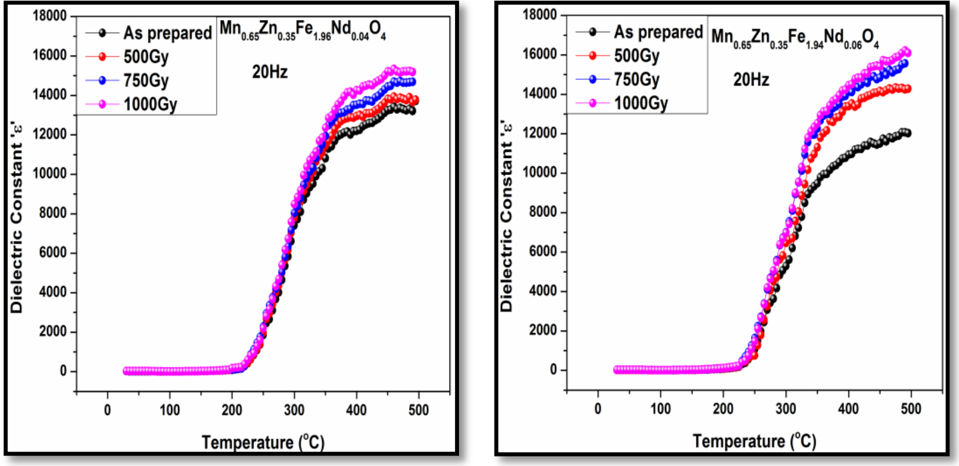

(a) (b)

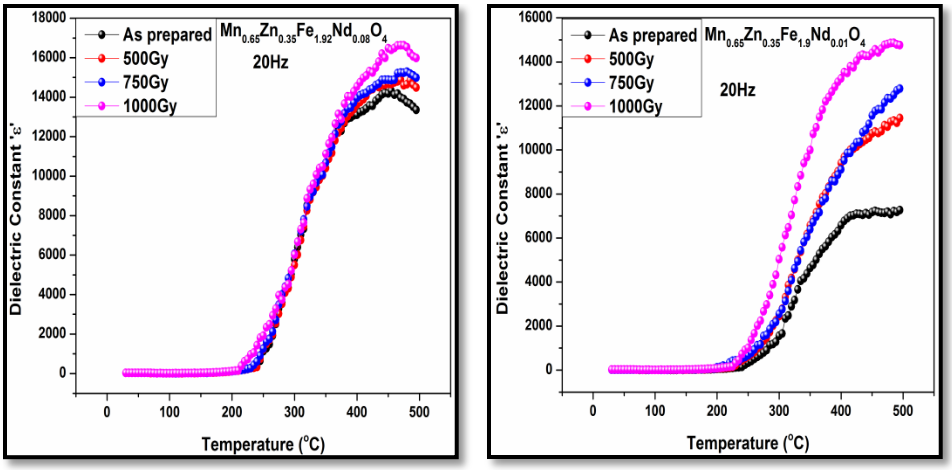

(c) (d)

Figure 6.11.10 (a,b,c,d) Variation of Dielectric constant with temperature of γ irradiated $Mn_{0.65}Zn_{0.35}Fe_{2-x}Nd_xO_4$ nanoparticles at 20Hz

Variation of dielectric constant with temperature for different gamma radiation doses at 20Hz for $Mn_{0.6}Zn_{0.4}Fe_{2-x}Nd_xO_4$ and $Mn_{0.65}Zn_{0.35}Fe_{2-x}Nd_xO_4$ is presented in Figure 6.11.9 and Figure 6.11.10.

All the gamma irradiated samples were seen to exhibit higher dielectric constant in comparison with the non radiated samples and the values were observed to increase with increasing gamma radiation dose. Samples are observed to exhibit low dielectric constant over the temperature range of 30°C to 160°C which is also evident from the resistivity plots where in samples show high resistivity in this temperature range. This can be attributed to low mobility of charge carriers. Beyond this temperature dielectric constant shows a gradual increase due to improved in charge carrier hopping rate which is supported by large amount of energy available at higher temperature along with other processes such as liberation of trapped charges. Exposure to gamma radiation alters the cationic arrangements at the tetrahedral and the octahedral site by altering the ratio of ferric and ferrous ions present at both the sites. This rearrangement was seen to be proportional to the magnitude of gamma radiation dose absorbed by the sample. As a result a proportionate increase in dielectric constant is seen in all the samples at higher temperatures. Altered cation distribution supports electronic charge hopping amongst Fe^{+2} /Fe^{+3}, Mn^{+2} /Mn^{+3} and Fe^{+2}/Mn^{+3} ions which results in better polarization and causes an enhancement in dielectric constant [43, 44].

6.12 Summary

Nanocrystalline rare earth doped manganese zinc ferrite materials with composition $Mn_{0.6}Zn_{0.4}Fe_{2-x}Nd_xO_4$ and $Mn_{0.65}Zn_{0.35}Fe_{2-x}Nd_xO_4$ (x=0.04, 0.05, 0.06, 0.07, 0.08, 0.09 and 0.1) were gamma irradiated with three different dose (500Gy, 750Gy and 1000Gy) obtained from Co^{60} source in order to investigate the effect of gamma radiation on structural, magnetic and electrical properties of these nanomaterials. From the analysis of X-ray diffraction data it was observed that all the samples exhibit cubic spinel phase. However reduction in diffraction peak intensities with broadening indicated increment of amorphous content with reduction in crystallite sizes in the samples as a consequence of gamma irradiation. Lattice parameters for both the series of nanosamples were observed to increase with increasing gamma radiation dose. This increase in lattice parameter can be attributed to the transformation of low spin Fe^{+3} ions (0.69Å) into larger ions of Fe^{+3} in high spin state (0.78Å). Structural parameters like mass density and X-ray density were observed to decrease with increasing gamma radiation dose while the porosity was observed to increase with increasing gamma radiation dose.

Cation distribution estimated from XRD data show transfer of Fe^{+3} from octahedral site to tetrahedral site compensated by the transfer of Mn^{+3} from tetrahedral site to octahedral site with increasing gamma radiation dose. From TEM micrographs and particle size distribution histogram clearly show a very narrow particle size distribution for for all $Mn_{0.6}Zn_{0.4}Fe_{2-x}Nd_xO_4$ and $Mn_{0.65}Zn_{0.35}Fe_{2-x}Nd_xO_4$ samples. Hysteresis loops obtained on VSM showed an increase in saturation magnetization with gamma radiation dose for all the samples. From the squareness values one can conclude that all the irradiated samples exhibit superparamagnetic nature. Rise in permeability values for gamma irradiated samples indicate better magnetic ordering due to increase in Fe^{+3} concentrations in high spin state at both the tetrahedral and the octahedral site. Room temperature DC resistivity of the samples is observed to decrease with increasing gamma radiation dose due to cationic rearrangement triggered by the gamma radiation exposure and change in ferrous and ferric ions ratio at octahedral and tetrahedral sites. At higher temperature resistivity was observed to decrease with increasing temperature depicting semiconductor like behavior. Dielectric constant as a function of frequency was observed to increase with increasing gamma radiation exposure. The dielectric loss was also seen to increase with increasing gamma radiation exposure. Variation of dielectric constant as a function of temperature at different frequencies showed an increase with increasing magnitude of gamma radiation dose for all the samples. The new values of parameters and properties obtained after irradiating the samples with gamma radiation did not alter or change even after storing the samples for long times. This confirmed that the changes produced in the samples were of permanent nature. In depth study and detailed analysis of all the properties has resulted in formulation of a model as mentioned in this chapter which could be linked in understanding of the changes produced in the samples. The model is simple and could be successfully and conveniently used to understand and explain all the persistent changes produced in the irradiated samples. The models also suggests that the changes produced are non reversible changes as it is not possible to get a larger crystal by putting together few or more crystals, so also one cannot get the order back once amorphous nature sets in due to break down of unit cells at the surface of a crystallite.

References

1. Pranav P. Naik, R. B. Tangsali, B. Sonaye, S. Sugur, Advanced Science Letters, Volume 22, (2016)pp752-758
2. Pranav P. Naik, R. B. Tangsali, B. Sonaye and S. Sugur, J. Nano. Adv. Mat. 3, No. 1, (2015) 1-7
3. Pranav P. Naik, R. B. Tangsali, B. Sonaye, S. Sugur, Journal of Magnetism and Magnetic Materials, 385(2015)377–385
4. Adil Gani, Tahir Gazanfar, Romee Jan, S. M. Wani, F. A. Masoodi, Journal of the Saudi Society of Agricultural Sciences (2013) 12, 109–115
5. L. Nalbandian, A. Delimitis, V.T. Zaspalis, E.A. Deliyanni, D.N. Bakoyannakis, E.N. Peleka, Microporous and Mesoporous Materials 114 (2008) 465–473.
6. P.P. Hankare, R.P. Patil, U.B. Sankpal, S.D. Jadhav, K.M. Garadkar, S.N. Achary, Journal of Alloys and Compounds 509 (2011) 276–280.
7. D.S. Mathew, R.-S. Juang, Chemical Engineering Journal 129, (2007) 51–65.
8. P. P. Naik, R. B. Tangsali, S. S. Meena, Pramod Bhatt, B. Sonaye, S. Sugur, Radiation Physics and Chemistry, 102 (2014) 147–152.
9. Pranav P. Naik, R. B. Tangsali, Journal of Alloys and Compounds, 723, (2017)266-275
10. K. Rama Krishna, K. Vijaya Kumar, Dachepalli Ravinder, Advances in Materials Physics and Chemistry 2, (2012) 185-191

11. S.M. Patange, S.E. Shirsath, G.S. Jangam, K.S. Lohar, S.S. Jadhav, K.M. Jadhav, Journal of Applied Physics, 109 (2011) 053909.
12. M. A. Amer, T. Meaz, S. Attalah, F. Fakhry, Journal of Magnetism and Magnetic Materials 401(2016)150–158
13. M. A. Amer, T. M. Meaz, M. El-Kestawy, A. I. Ghoneim, Journal of Magnetism and Magnetic Materials, 405(2016)137–144
14. M. A. Amer, Journal of Magnetism and Magnetic Materials 426 (2017) 771–778
15. M. A. Amer, A. Matsuda, G. Kawamura, R. El-Shater, T. Meaz, F. Fakhry, Journal of Magnetism and Magnetic Materials 439 (2017) 373–383
16. E. H. El-Ghazzawy, M. A. Amer, Journal of Alloys and Compounds 690 (2017) 293-303
17. L. Ben Tahar, L.S. Smiri, M. Artus, A.-L. Joudrier, F. Herbst, M.J. Vaulay, S. Ammar, F. Fie´vet, Materials Research Bulletin 42(2007) 1888–1896
18. R. Naik, A.V. Salker, Journal of Material Chemistry, 22(2012) 2740.
19. L. Zhao, H. Yang, X. Zhao, L. Yu, Y. Cui, S. Feng, Material Letters 60 (2006)1-6.
20. D.S. Mathew, R.-S. Juang, Chemical Engineering Journal 129, (2007)51–65.
21. A. Kale, S. Gubbala, R. Misra, Journal of Magnetism and Magnetic Materials 277, (2004)350–358.
22. Pranav P. Naik, R. B. Tangsali, S. S. Meena, Materials Chemistry and Physics 191,(2017) 215-224
23. S. K. Sharma, Ravi Kumar, V. V Siva Kumar, M Knobel, V. R. Reddy, A. Gupta, M Singh, Nuclear Instruments and Methods in Physics Research B, 248, (2006)37–41

24. J.P. Vejpravov, V. Sechovsk´y, WDS'05 Proceedings of Contributed Papers, Part III, (2005)518–523
25. S. S. Shinde, Sher Singh Meena, S. M. Yusuf, and K. Y. Rajpure, J. Phys. Chem. C 2011, 115, 3731–3736
26. K. Vasundhara, S. N. Achary, S. K Deshpande, P. D. Babu, S. S. Meena, A. K. Tyagi, J. Appl. Phys. 113, (2013) 194101.
27. S. R. Naik, A. V. Salker, S. M. Yusuf, S. S. Meena, J. Alloys Compd. 566, (2013) 54–61
28. Shalendra Kumar, A.M.M. Farea, Khalid Mujasam Batoo, Physica B, 403, (2008) 3604–3607
29. D. E. Dickson, F. J. Berry, Mo¨ssbauer Spectroscopy. Cambridge University Press, London, 1986, P 22
30. V. T. Zaspalis, V. Tsakaloudi, G. Kogias, EPJ Web of Conferences, 74, (2014)04004
31. K. Kondo, T. Chiba, S. Yamada, Journal of Magnetism and Magnetic Materials 254–255 (2003) 541–543
32. J. Hanuszkiewicz, D. Holz, E. Eleftheriou, V. Zaspalis, Journal of Applied Physics, 103, (2008) 103907
33. Ishtiaq Ahmad and Muhammad Tahir Farid, World Applied Sciences Journal, 19(4), (2012) 464
34. Ge-Liang Sun, Jian-Bao Li, Jing-Jing Sun and Xiao-Zhan Yang, Journal of Magnetism and Magnetic Materials, 281, (2004) 173
35. I. H. Gul, A. Maqsood, Journal of Alloys and Compounds 465, (2008)227

36. N.Y. Lanje, D.K. Kulkarni, Journal of Magnetism and Magnetic Materials. 234, (2001) 114
37. Manisha, V. Rane, D. Bahadur, Journal of Magnetism and Magnetic Materials. 192, 288-(1999)296
38. M. Asif Iqbal, M.U. Islam, Irshad Ali, Muhammad Azhar khan, Imran Sadiq and Ihsan Ali, Journal of Alloys and Compounds 586, (2014) 404
39. Chandra Babu, B, Naresh. V. Jayaprakash. B, S. Buddhudu , Ferroelectrics Letters Section Structural, Thermal and Dielectric Properties of Lithium Zinc Silicate Ceramic Powders by Sol-Gel Method Ferro Electrics letter, 38, (2011) 124
40. N. Rezlescu, E. Rezlescu, Dielectric properties of copper containing ferritesPhysics Status Solidi A. 23, (1974)575
41. B. Baruwati, K. M. Reddy, V. Sunkara, R. K. Manorama, O. Singh, J. Prakash , Applied Physics Letters 14, (2004)85
42. R. S. Devan, B. K. Chougule, Journal of Applied Physics 101, (2007) 014109
43. I.H. Gul, A. Maqsood, M. Naeem, M. Naeem Ashiq, 507, (2010)201
44. P.S. Jadhava, K.K. Patankarb, Vijaya Puri, Materials Research Bulletin 75 (2016) 162–166

CHAPTER 7

CONCLUSION

Nanocrystalline powders of rare earth (Nd^{+3}) doped manganese zinc ferrite materials with composition $Mn_{0.6}Zn_{0.4}Fe_{2-x}Nd_xO_4$ and $Mn_{0.65}Zn_{0.35}Fe_{2-x}Nd_xO_4$ (x =0.04, 0.05, 0.06, 0.07, 0.08, 0.09 and 0.1) were prepared using combustion method in order to investigate the effect of increasing rare earth concentrations on structural, magnetic and electrical properties of these nanomaterials. From the X-ray diffraction (XRD) patterns and data analysis, it was observed that the samples exhibit spinel structure. The structural parameters like lattice constant, mass density, X-ray density were observed to increase with increasing Nd^{+3} concentration which was due to occupancy of heavy and larger Nd^{+3} ion with ionic radii of 1.12Å replacing a smaller Fe^{+3} ionic radii of 0.69Å. Crystallite size of the samples was observed to decrease from 17nm to 12 nm for the samples belonging to $Mn_{0.6}Zn_{0.4}Fe_{2-x}Nd_xO_4$ series and vary from 18 nm to 15 nm for samples belonging to $Mn_{0.65}Zn_{0.35}Fe_{2-x}Nd_xO_4$ series. Porosity of the samples was also seen to decrease with increasing Nd^{+3} concentrations. Fourier transform infra red spectra showed all characteristic bands of ferrites. The cation-anion bond lengths and the distances between various cations were seen to increase as a consequence of Nd^{+3} doping. Cation distribution estimated from XRD data showed a transfer of $Fe^{+3/+2}$ ions from octahedral site to tetrahedral site with increasing the concentration of Nd^{+3} at the octahedral site. This transfer of $Fe^{+3/+2}$ ions was compensated by the transfer of $Mn^{+3/+2}$ ions to tetrahedral site.

Transmission electron micrographs confirmed the formation of nanoparticles within the narrow particle size distribution range of 15 nm to 18 nm for $Mn_{0.6}Zn_{0.4}Fe_{2-x}Nd_xO_4$ series and 20 nm to 17 nm for $Mn_{0.65}Zn_{0.35}Fe_{2-x}Nd_xO_4$ series of nanoparticles. Large agglomerates of nanoparticles were seen in SEM images for all the samples indicating a strong magnetic behavior, high surface charges and also due to other weak surface interaction such as the van der Waals forces. Hysteresis loops obtained on VSM showed an increase in saturation magnetization with increasing Nd^{+3} for x=0.04 to x=0.09 and decrease further for x=0.1. All samples exhibit negligible hysteresis loss. From the squareness values one can conclude that the samples with composition $Mn_{0.6}Zn_{0.4}Fe_{2-x}Nd_xO_4$ exhibit a mixed character of single domain and multi domain grains of different grain sizes all of which exhibit neat to superparamagnetic behavior while the samples with composition $Mn_{0.65}Zn_{0.35}Fe_{2-x}Nd_xO_4$ were clearly seen to exhibit superparamagnetic nature. Analysis of Mossbauer data showed the dominance of Fe^{+3} in high spin state at both the tetrahedral and the octahedral sites. Increase in relative area of paramagnetic doublet supported the fact that the particle size reduces with increasing Nd^{+3} concentrations resulting in enhancement of superparamagnetic fraction in the samples. Nanosamples were seen to exhibit very high room temperature DC resistivity of the order 10^9 Ω cm due to large surface area consisting of non conducting grain boundaries and low mobility of charge carriers. DC resistivity was observed to increase further with increasing Nd^{+3} concentrations. At higher temperature, resistivity of these samples was seen to decrease exponentially depicting semiconductor behavior. Dielectric constant as a function of frequency was observed to decrease with increasing frequency and attain constant value. It was also observed to decrease with increasing Nd^{+3} concentrations while the dielectric loss was observed to increase with Nd^{+3} concentrations. Dielectric constant was also observed to exhibit low values up to 160°C beyond which it was seen to increase with increasing temperature. Dielectric constant was found to decrease with increasing Nd^{+3} concentrations. The doped manganese zinc ferrite nanosamples were found to exhibit low loss in the temperature range of 30°C to 160°C beyond which the loss increases rapidly with increasing temperature.

In order to investigate the effect of high energy gamma (γ) radiation on various properties of these nanoparticles, the samples were exposed to three different doses (500Gy, 750Gy and 1000Gy) of gamma radiation using Co^{60} source. The samples were characterized using XRD, FTIR and TEM to study the structural medications introduced in the material as a result of gamma radiation exposure. Analysis of XRD data inferred that the samples retain spinel structure even after irradiating with gamma radiation dose of 1000Gy. However the intensity of diffraction peaks was seen to decrease with a broadening with increasing gamma radiation dose which is an indication of inclusion of amorphous nature and reduction in crystallite size. The crystallite size was also seen to decrease from 17 nm to 8 nm for $Mn_{0.6}Zn_{0.4}Fe_{2-x}Nd_xO_4$ series and 18 nm to 9 nm for $Mn_{0.65}Zn_{0.35}Fe_{2-x}Nd_xO_4$ with increasing gamma radiation dose. Lattice parameter for gamma irradiated samples was seen to increase resulting in enhancement in cell volume which was attributed to increase in the concentration of Fe^{+3} ions in high spin state due to gamma radiation exposure. Other structural parameters such as mass density and X-ray density were seen to decrease while porosity of gamma irradiated samples was showed an increasing trend with increasing magnitude of radiation dose. Cation distribution obtained for irradiated nanosamples showed further transfer of $Fe^{+3/+2}$ ions from tetrahedral site to octahedral site. This transfer was seen to be proportional to gamma radiation dose absorbed by the samples. The cation anion bond lengths and the distances between various cations were seen to increase further with increasing gamma radiation dose. Exposure to gamma radiation was also seen to favor magnetic properties of these nanomaterials. Saturation magnetization (M_S) was seen to increase up to 20emu/g for $Mn_{0.6}Zn_{0.4}Fe_{2-x}Nd_xO_4$ series and a maximum hike of 15emu/g was seen for the samples belonging to $Mn_{0.65}Zn_{0.35}Fe_{2-x}Nd_xO_4$ series.

From the squareness values one can conclude that all the irradiated samples exhibit superparamagnetic nature. Rise in permeability values for gamma irradiated samples indicate better magnetic ordering due to increase in Fe^{+3} concentrations in high spin state at both the tetrahedral and the octahedral site. Room temperature DC resistivity of the samples is observed to decrease with increasing gamma radiation dose due to cationic rearrangement triggered by the gamma radiation exposure and change in ferrous and ferric ions ration at octahedral and tetrahedral site. At higher temperature resistivity was observed to decrease with increasing temperature depicting semiconductor like behavior. Dielectric constant as a function of frequency was observed to increase with increasing gamma radiation exposure. The dielectric loss was also seen to increase with increasing gamma radiation exposure. Variation of dielectric constant as a function of temperature at different frequencies showed an increase with increasing magnitude of gamma radiation dose for all the samples. The changes produced in the irradiated nanosamples were tested for longevity by repeating the measurements after a span one month, three months and six months and were found to be of permanent nature with marginal variations within the experimental errors. Almost all the above variations in structural parameters and properties were supported and explained on the bases of hypothetical strain based model predicting the possible mechanisms for grain size reduction in increase of amorphous content which was very well supported by the particle size decrement observed in transmission electron micrographs as well as other variations seen in several properties.

It can be further inferred that irradiating manganese zinc ferrite nanosamples can be very effectively used as post synthesis technique to modify the structural, magnetic and electrical properties of these materials to enhance the performance of materials to suite desired applications. It is also reported that application of massive dose of Gamma radiation can also bring about permanent damage in the materials and destroy their useful properties.

7.1 Further Scope of Work

One can take up following ideas as research work in future for better understanding of these materials and opening new arenas of applications.

- Preparation of rare earth doped manganese zing ferrite thin films using various techniques like pulse laser deposition technique, RF sputtering technique etc. to study the response of these materials in the form of thin films towards different types and magnitudes of radiations on the bases of structural, magnetic and electrical property alterations.

- To formulate a theoretical model to predict the structural, magnetic and electrical character of rare earth doped manganese zinc ferrite nanomaterials in the powder form as well as in the form of thin films.

- To modify the composition of these material by doping different rare earth elements to increase the sensitivity of these materials in order to develop sensors such as radiation sensors, gas sensors etc.

PUBLICATIONS

1. Enduring Effect of Rare Earth (Nd^{+3}) Doping and γ- Radiation on Electrical properties of Nanoparticle Manganese Zinc Ferrite, **Pranav P. Naik**, R. B. Tangsali, Journal of Alloys and Compounds, 723, **(2017)**266-275.
2. Influence of Rare Earth (Nd^{+3}) Doping on Structural and Magnetic Properties of Nanocrystalline Manganese-Zinc Ferrite, **Pranav P. Naik**, R. B. Tangsali, S. S. Meena, Materials Chemistry and Physics 191,**(2017)** 215-224
3. Gamma radiation stimulated unwavering structural and magnetic refinements in $Mn_xZn_{1-x}Fe_2O_4$ nanoparticles, **Pranav P. Naik**, R. B. Tangsali, B. Sonaye, S. Sugur, Advanced Science Letters, Volume 22, **(2016)** 752-758
4. Effect of Rare-earth doping on Magnetic and Electrical Transport Properties of Nanoparticle Mn Zn Ferrite, M. Deepak Kumara, A. D'souzaa, M. Chatima, V. Naik, **Pranav P. Naik**, R. B. Tangsali, Advanced Science Letters, volume 22, **(2016)** 773-779
5. Study of Structural and Magnetic Properties of $Mn_{0.8}Zn_{0.2}Fe_2O_4$ Nanoparticles, Nidhi Tendulkara, Suvarna Patila, Vibhav Kuncalienkar, **Pranav P. Naik**, Mandakini Kundaikar, Satish Keluskar, Advanced Engineering Technology and Application, 5, No. 1, **(2016)**19-22
6. Synthesis of Uniform Size Superparamagnetic Grains of $Mn_xZn_{(1-x)}Fe_2O_4$ Ferrites by Precursor-Based Combustion Method**,** G. V. S. Kundaikar, R. B. Tangsali, V. J. Pissurlekar, J. S. Budkuley, **Pranav P. Naik,** J Supercond Nov Magn, 29, **(2016)** 789–794

7. Consequence of rare earth doping on structural and magnetic properties of $Mn_{0.6}Zn_{0.4}Nd_xFe_{2-x}O_4$ Nanoparticles, **Pranav P. Naik**, R. B. Tangsali, Advanced Nanomaterials: synthesis and applications (Academic reference series), ISBN: 978-93-85436-74-1, **(2015)** 103-106.
8. Sustained Augmentation in Electrical properties of $Mn_xZn_{1-x}Fe_2O_4$ nanoparticle s provoked by High Energy Gamma Radiation, **Pranav P. Naik**, R. B. Tangsali, B. Sonaye and S. Sugur, J. Nano. Adv. Mat. 3, No. 1, **(2015)** 1-7
9. Radiation induced structural and magnetic transformations in nano-particle $Mn_xZn_{(1-x)}Fe_2O_4$ ferrites, Journal of Magnetism and Magnetic Materials, **Pranav P. Naik**, R. B. Tangsali, B. Sonaye, S. Sugur, 385**(2015)**377–385
10. Gamma Radiation Roused Lattice Contraction effects investigated by Mössbauer spectroscopy in nanoparticle Mn-Zn Ferrite, **P. P. Naik**, R. B. Tangsali, S. S. Meena, Pramod Bhatt, B. Sonaye, S. Sugur, Radiation Physics and Chemistry, September **(2014)** Pages 147–152
11. Radiation stimulated permanent alterations in Structural and Electrical properties of core-shell Mn-Zn Ferrite Nanoparticles, **P. P. Naik**, R. B. Tangsali, S. S. Meena, Pramod Bhatt, B. Sonaye, S. Sugur, Journal of Nano research, vol 24**(2013)**, 194-202
12. Enrichment of magnetic alignment stimulated by γ-radiation in core-shell type nanoparticle Mn-Zn ferrite, **P. P. Naik**, R. B. Tangsali, B. Sonaye, and S. Sugur**, AIP** Conf. Proc. 1512, **(2013)** 354 doi: 10.1063/1.4791057

PAPERS PRESENTED IN INTERNATIONAL CONFERENCES

1. Presented a paper *(oral presentation)* entitled "Gamma radiation stimulated unwavering structural and magnetic refinements in $Mn_xZn_{1-x}Fe_2O_4$ nanoparticles" and won the **Best Paper Award** at 'NANOCON014' on 14 & 15 October 2014 at Pune Bharati Vidyapeeth University along with North Carolina A & T State University Greensboro-USA, Tuskegee University-Alabama (USA), The University of Tokushima-Japan and Centre of Materials for Electronics Technology (C-MET), India 3rd International Conference.
2. Presented a paper *(oral presentation)* entitled "Consequence of rare earth doping on structural and magnetic properties of $Mn_{0.6}Zn_{0.4}Nd_xFe_{2-x}O_4$ Nanoparticles" in an International conference on nanomaterials and nanotechnology (NANO 15) held at K. S. R. College of Technology, Tiruchengode, India during 7th -10th December 2015.
3. Presented a paper *(oral presentation)* entitled "Effect of gamma radiation on electrical properties of rare earth (Nd^{+3}) dopedManganese Zinc ferrite nanoparticles" in an International conference on nanoscience and nanotechnology forenergy applications (EAPP 2016) held at Sathyabama University, Chennai in association with Institute Jean Lamour, University of Loraine, France during 27th-29th June 2016
4. Presented a research paper *(oral presentation)* entitled "Radiation stimulated permanent alterations in Structural and Electrical properties of core-shell type Nanoparticle Mn-Zn Ferrite" in an international conference 'NANOCON 2012' organized with the theme 'NanoTechnology - Innovative Materials, Processes,

Products, and Applications' held during October 18-19, 2012, at Bharati Vidyapeeth University, Pune.

5. Presented a research paper *(oral presentation)* "Effect of Gamma Radiation on Structural and Magnetic Properties of $Mn_xZn_{1-x}Fe_2O_4$ Nanoparticles" in an International conference on Nanotechnology & Functional Material jointly organized by Sreenidhi Institute of Science & Technology and University of South Africa on January 4-7, 2012.

PAPERS PRESENTED IN NATIONAL CONFERENCES

1. Presented a research paper *(oral presentation)* on "Sustained Conductivity Augmentation due to structural adjustments in Core Shell Type $Mn_xZn_{1-x}Fe_2O_4$ Nanoparticles Provoked By Gamma Radiation" in a National conference NANO INDIA 2013 organized by CSIR-Nationa Institute for Interdisciplinary Science and Technology, Thrivananthapuram supported by Nano Mission, Department of Science and Technology, New Delhi during November 19-20, 2013.
2. Presented a poster entitled "Effect Of Rare Earth Doping On The Structural Parameters of Nanocrystalline Manganese-Zinc Ferrite", at 59th DAE symposium held at VIT Vellore, Tamilnadu during 16th to 20th December 2014
3. Attended National seminar on " Frontiers in Chemical and Material Sciences" organized by Department of Chemistry, Shivaji University, Kolhapur held during 16th to 17th January 2015.
4. Presented a paper *(oral presentation)* entitled "Effect of γ Radiations on Various Properties of Rare Earth (Nd^{+3}) Doped Mn-Zn Ferrite Nano-particles", at National level symposium on "Materials Characterization and Manufacturing (MCM 2016)" jointly organized by Department of Mechanical Engineering, Padre Concecao College of Engineering and Department of Physics, Goa University at Goa University, Goa, during 18th and 19th August 2016
5. Presented a research paper on "Sustained Conductivity Augmentation due to structural adjustments in Core Shell Type $Mn_xZn_{1-x}Fe_2O_4$ Nanoparticles Provoked By Gamma Radiation" in a National conference NANO INDIA 2013 organized by

CSIR-Nationa Institute for Interdisciplinary Science and Technology, Thrivananthapuram supported by Nano Mission, Department of Science and Technology, New Delhi during February 19-20, 2013.

6. Presented a research paper (Poster presentation) on “Enrichment of Magnetic Alignment Stimulated by γ-Radiation in Core-shell Type Nanoparticle Mn-Zn Ferrite” to DAE symposium 2012 at IIT Bombay, India.

WORKSHOPS ATTENDED

1. Attended DST -SERC School on “Advanced Functional Magnetic Materials” during February 3 –21, 2014 at Goa University.
2. Attended Winter school 2014 on Frontiers in Material Science held between 1st to 5th December 2014 at JNCASR organized by International Centre for Material Science, Jawaharlal Nehru Centre for Advanced Scientific Research, University of Cambridge, Sheikh Saqr Laboratory
3. Attended a two day workshop on “Application of X-Rays and Neutrons in study of condensed matter” organized by Indian association of physics teachers Goa regional council and Parvatibai Chowgule college of arts and science on 3rd and 4th September 2015.